



Expected sensitivity of the AugerPrime Radio Detector to the masses of ultra-high-energy cosmic rays using inclined air showers

Zur Erlangung des akademischen Grades eines
Doktors der Naturwissenschaften (Dr. rer. nat.)

von der KIT-Fakultät für Physik des
Karlsruher Instituts für Technologie (KIT)

und der

Universidad Nacional de San Martín (UNSAM)

angenommene

Dissertation

von

M.Sc. Felix Andreas Schlüter

aus Köln

Tag der mündlichen Prüfung: 20. Mai 2022
Erster Gutachter: Prof. Dr. Ralph Engel.
Zweiter Gutachter: Dr. Diego Ravnani
Betreuer: Prof. Dr. Tim Huege

Abstract

Despite enormous efforts in the last several decades, the origin of *ultra-high-energy cosmic rays* (UHECRs) – their acceleration sites and acceleration mechanism(s) – remains unidentified and is subject of active research. The progress made during that time, in particular by the Pierre Auger Observatory, established that significant advances in our understanding of the nature of UHECRs are only achieved with a better knowledge of their mass composition, i.e., through more precise measurements. To this end, the Pierre Auger Observatory is upgrading its large-aperture *Surface Detector* (SD) to enhance its mass sensitivity for the detection of the highest-energy cosmic rays ($E \gtrsim 4 \times 10^{19}$ eV). As part of this effort, the *AugerPrime Radio Detector* (RD) will consist of over 1600 dual-polarized radio antennas mounted on top of each of the SD's *water-Cherenkov detector* (WCD) stations. The RD will be measuring the electromagnetic radiation in the 30 MHz to 80 MHz frequency band produced by highly inclined air showers with zenith angles $\gtrsim 65^\circ$. Thus, the RD will allow us to determine the cosmic-ray energy by measuring the shower's electromagnetic component, which is largely independent of the cosmic-ray mass. In contrast, since most particles in highly-inclined air showers are absorbed in the atmosphere and do not reach the ground, the WCDs will mainly record muons from the muonic shower component, which is highly correlated to the cosmic-ray mass. The combination of that complementary information allows us to infer the cosmic-ray mass with high precision.

With this work, I have laid the foundation to process, reconstruct, and analyze data measured by the RD. To develop a signal and reconstruction model for the radio detection of inclined air showers, I have conducted comprehensive studies of the nature of the radio emission from inclined air showers by utilizing numerical CoREAS simulations. In particular, I have investigated the origin of the radio emission within the extensive particle cascades and studied the correlation between the emission strength and ambient conditions. Furthermore, I have identified and characterized a refractive displacement of the radio-emission footprints at the ground, caused by the propagation of the electromagnetic radiation through the Earth's atmosphere. This causes the radio emission from an 85° air shower to be displaced by about 1.5 km and thus has essential implications for the description of the radio-emission footprint and the interpretation of the reconstructed geometry for very inclined air showers with zenith angles above 80° . With that at hand, I have developed a signal model of the 2-dimensional lateral distribution of the radio emission in the 30 MHz to 80 MHz frequency band. This model enables the reconstruction of the (electromagnetic) shower energy with sparse radio-antenna arrays and an *intrinsic* resolution of below 5% without taking into account instrumental uncertainties. As the electromagnetic energy can be reconstructed without any dependency on the cosmic-ray mass, this model is suitable to perform precise studies of the mass(-composition) of UHECRs, for example, with RD-SD hybrid detections of the AugerPrime Observatory. In

addition, I have evaluated the possibility of improving this mass sensitivity by measuring the slant depth of the shower maximum X_{\max} with a newly-proposed interferometric reconstruction technique. I have worked out, that the RD does not meet the specifications for an accurate reconstruction of X_{\max} , and that a time synchronization between antenna stations of $\lesssim 1$ ns and a signal multiplicity of $\gtrsim 20$ are required to achieve accurate results.

With this theoretical framework, I have thoroughly studied the expected performance of the RD to detect and reconstruct inclined air showers and its potential to determine the mass(-composition) of UHECRs with RD-SD hybrid measurements. These studies utilize Monte-Carlo-generated air showers, perform end-to-end simulations of the RD instrumental response including measured noise, and a reconstruction of all relevant air shower observables with the here-developed signal model. I have found that the RD will be fully efficient to detect inclined air showers with zenith angles above 70° and energies above 6.3×10^{18} eV. For a 10-year operation period, the RD will collect over 3900 events with energies above 10^{19} eV and around 570 events for energies above 4×10^{19} eV. An accurate reconstruction of the shower energy with the RD is already possible for air showers measured with 5 radio antennas and zenith angles above 68° . For current assumptions on the instrumental response of the RD, I have obtained an expected energy resolution of well below 10% for energies above 10^{19} eV and find no bias in the reconstructed electromagnetic energy for air showers induced by different primary particles. This study is concluded with an assessment of possible systematic uncertainties. By combining the RD-reconstructed (electromagnetic) energy and the SD-reconstructed number of muons, I assessed the potential discrimination between different primary particle types and to measure the average mass composition of UHECRs. The separation for proton- and iron-induced air showers with zenith angles above 70° and electromagnetic energies above 10^{19} eV is quantified with a *figure of merit* $FOM \approx 1.6$. The (simulated) measurements of the mean muon number with the RD and SD were found to reproduce the injected mass compositions. Hence, RD-SD hybrid measurements carry the potential to extend such measurements currently performed with the Fluorescence Detector and SD to higher energies, and thereby, to distinguish between different astrophysical scenarios that could explain the nature of UHECRs.

With the reconstruction model and mass-composition analysis developed in this work, the Pierre Auger Observatory is well-prepared for the arrival of experimental data from AugerPrime of inclined air showers.

Zusammenfassung

Trotz intensiver Forschung in den letzten Jahrzehnten, konnte der Ursprung der ultrahoch-energetischen kosmischen Strahlung (UHECRs, aus dem engl. für *ultra-high-energy cosmic rays*) noch nicht zweifelsfrei identifiziert werden. Die in dieser Zeit erzielten Fortschritte haben deutlich gemacht, dass weitere Erkenntnisse über UHECRs nur mit einem verbesserten Wissen über deren Massenzusammensetzung erreicht werden können, d.h. es sind genauere Messungen dieser Zusammensetzung erforderlich. Zu diesem Zweck rüstet das Pierre Auger Observatorium seinen Oberflächendetektor (SD, aus dem engl. für *Surface Detector*) auf, um dessen Massensensitivität für Messungen der kosmischen Strahlung bei den höchsten Energien ($E \gtrsim 4 \times 10^{19}$ eV) zu verbessern. Teil dieses Upgrade ist der AugerPrime Radiodetektor (RD), der aus über 1600 doppelt polarisierten Radioantennen bestehen wird, die auf jedem Wasser-Cherenkov-Detektor (WCD) angebracht werden. Der RD wird die elektromagnetische Strahlung von stark geneigten Luftschauern mit Zenitwinkel $\gtrsim 65^\circ$ im Frequenzbereich von 30 MHz bis 80 MHz messen. Damit wird es möglich sein, die Energie der elektromagnetischen Schauer-Komponente ohne Abhängigkeit von der Masse der kosmischen Strahlung zu bestimmen. Im Gegensatz dazu werden die WCDs hauptsächlich Myonen aus diesen stark geneigten Schauern messen, da andere Teilchen in der Atmosphäre absorbiert werden, bevor sie den Boden erreichen können. Die Kombination dieser komplementären Informationen ermöglicht es, die Massen(-Zusammensetzung) der kosmischen Strahlung mit hoher Präzision zu bestimmen.

Mit dieser Arbeit habe ich die Grundlage für die Verarbeitung, Rekonstruktion und Analyse von Daten, die mit dem AugerPrime Radiodetektor aufgenommen werden, gelegt. Um ein Signal- und Rekonstruktionsmodell für die Radiodetektion von geneigten Luftschauern zu entwickeln, habe ich umfassende Studien über die Natur der Radioemission von geneigten Luftschauern mit Hilfe von numerischen Simulationen durchgeführt. Insbesondere habe ich den Ursprung der Radioemission innerhalb der ausgedehnten Teilchenkaskaden untersucht, die Korrelation zwischen der Emissionsstärke und den Umgebungsbedingungen untersucht, und eine durch die Ausbreitung der Radioemission in der Erdatmosphäre verursachte Verschiebung der Radioemission am Boden identifiziert und beschrieben. Letztere führt zu einer Verschiebung um etwa 1.5 km für Luftschauer mit einer Neigung von 85° und hat somit wesentliche Auswirkungen auf die Beschreibung des Radioemission und die Interpretation der rekonstruierten Luftschauer-Parameter für stark geneigte Luftschauer mit Zenitwinkeln über 80° . Basierend auf diesen Erkenntnissen, habe ich ein Modell für die 2-dimensionale Lateralverteilung der Radioemission von 30 MHz bis 80 MHz entwickelt, mit dem eine Rekonstruktion der (elektromagnetischen) Schauerenergie ohne Berücksichtigung von instrumentellen Einflüssen mit einer *intrinsischen* Auflösung von unter 5% möglich ist. Außerdem kann die elektromagnetischen Schauerenergie ohne Abhängigkeit von der Masse der kosmischen Strahlung bestimmt werden, was genaue Untersuchungen der Massen(-Zusammensetzung) von UHECRs erlaubt. Damit ist dieses Rekonstruktions-

modell besonders für den Einsatz mit dem RD geeignet, um in Kombination mit dem SD die Massenzusammensetzung der UHECRs zu bestimmen. Genaue Messungen der atmosphärischen Tiefe des Schauermaximums X_{\max} würden die Massensensitivität für Messungen mit dem RD verbessern. Daher habe ich eine interferometrische Rekonstruktionsmethode, die großes Potenzial bei geneigten Luftschauern verspricht, getestet. Meine Ergebnisse zeigen, dass der RD die Anforderungen für eine genaue Rekonstruktion von X_{\max} mit dieser Technik nicht erfüllt, und dass eine Zeitsynchronisation zwischen den Antennenstationen von $\lesssim 1$ ns und eine Signalmultiplizität von $\gtrsim 20$ erforderlich sind, um genaue Ergebnisse zu erzielen.

Mit diesem theoretischen Rahmen habe ich die Fähigkeit des RD zur Erfassung und Rekonstruktion von geneigten Luftschauern und das Potenzial zur Bestimmung der Massen(-Zusammensetzung) von UHECRs mit hybriden Messungen zwischen dem RD und SD untersucht. Diese Studien nutzen Monte-Carlo generierte Luftschauer, verwenden vollständiger Simulationen der instrumentellen Sensitivität des RD und einer Rekonstruktion aller relevanten Luftschauer-Parameter mit dem neu entwickelten Signalmodell. Meine Analyse zeigt, dass der RD bei geneigten Luftschauern mit Zenitwinkeln über 70° und Energien über 6.3×10^{18} eV voll effizient sein wird. Bei einer Betriebsdauer von 10 Jahren wird der RD über 3900 Luftschauer mit Energien über 10^{19} eV und etwa 570 Luftschauer für Energien über 4×10^{19} eV aufzeichnen. Eine genaue Rekonstruktion der Schauerenergie ist bereits für Luftschauer möglich, die mit 5 Radioantennen und Zenitwinkeln über 68° gemessen wurden. Mit den derzeitigen Annahmen zur instrumentellen Sensitivität habe ich eine Energieauflösung von deutlich unter 10% für Energien über 10^{19} eV und keine Verzerrung bei der Rekonstruktion der elektromagnetischen Energie für Luftschauer, die durch verschiedene Primärteilchen ausgelöst werden, erhalten. Diese Studie wird mit einer Bewertung möglicher systematischer Unsicherheiten abgeschlossen. Auf der Grundlage dieser Ergebnisse wird die Fähigkeit analysiert, durch Protonen oder Eisenkerne induzierte Luftschauer zu trennen und die durchschnittliche Massenzusammensetzung von UHECR zu messen, indem die RD-rekonstruierte Energie und die SD-rekonstruierte Anzahl von Myonen kombiniert werden. Die Trennung von durch Protonen oder Eisenkerne induzierte Luftschauer mit Zenitwinkeln oberhalb von 70° und elektromagnetischen Energien oberhalb von 10^{19} eV ist durch eine Trennstärke von $FOM \approx 1.6$ bestimmt. Des Weiteren ist es möglich, auf Grundlage der rekonstruierten Schauerparameter, die simulierte Massenzusammensetzung qualitativ zu reproduzieren. Das signalisiert das Potenzial, mit dem RD Messungen, die schon mit dem Fluoreszenz Detektor und dem SD ausgeführt werden, zu höheren Energien zu erweitern und damit zwischen astrophysikalischen Szenarien zu unterscheiden.

Mit dem hier entwickelten Rekonstruktionsmodell und der darauf aufbauenden Analyse der Massenzusammensetzung von UHECRs ist das Pierre Auger Observatorium nun bestens gerüstet für den Beginn der Messungen mit dem RD.

Resumen

A pesar de los enormes esfuerzos realizados en las últimas décadas, el origen de los *rayos cósmicos de ultra alta energía* (UHECR por sus siglas en inglés), al igual que sus fuentes y mecanismos de aceleración, siguen sin ser identificados y son objeto de intensa investigación. El progreso realizado por el Observatorio Pierre Auger durante este tiempo, en conjunto con otros experimentos, ha demostrado que revelar la naturaleza de los UHECRs solo será posible si se logra mejorar la precisión de las mediciones de la composición química de las partículas primarias. Con este fin, el Observatorio Pierre Auger está actualizando su *Detector de Superficie SD* para mejorar su sensibilidad a la masa de los rayos cósmicos de mayor energía ($E \gtrsim 4 \times 10^{19}$ eV). Como parte de este esfuerzo, el *Detector de Radio RD* de AugerPrime consistirá en más de 1600 antenas de radio dualmente polarizadas que se montarán en la parte superior de cada *detector de Cherenkov de agua* del SD. El RD medirá la radiación electromagnética en la banda de frecuencias 30 MHz a 80 MHz producida por las lluvias atmosféricas extendidas muy inclinadas, es decir con ángulo cenital $\gtrsim 65^\circ$. De esta manera, el RD nos permitirá determinar la energía de los rayos cósmicos midiendo la componente electromagnética de la lluvia, que es independiente de la masa del primario. Por el contrario, dado que la mayoría de las partículas en las lluvias muy inclinadas se absorben en la atmósfera y no llegan al suelo, los WCD registran principalmente la componente muónica de la lluvia, la cual sí es sensible a la composición de las partículas primarias. Esta técnica de detección híbrida nos permitirá inferir la masa de rayos cósmicos con una precisión nunca antes lograda.

En este trabajo senté las bases para procesar, reconstruir y analizar los datos medidos con el RD. Desarrollé modelos de señal y reconstrucción aplicables a la detección de la emisión de radio de las lluvias atmosféricas extendida inclinadas y realicé, a través de simulaciones numéricas, estudios exhaustivos de la naturaleza de dicha emisión. En particular, investigué el origen de la emisión de radio en cascadas extensas de partículas y estudié la correlación entre la intensidad de la emisión y las condiciones ambientales. Además, identifiqué y caractericé un desplazamiento refractivo de la huella de emisión de radio en el suelo causado por la propagación de la radiación electromagnética a través de la atmósfera terrestre, lo que hace que la emisión de radio se desplace aproximadamente 1.5 km para lluvias con una inclinación de 85° . Esto tiene un enorme impacto en la comprensión de las huellas producidas en la superficie terrestre por las emisiones de radio y la siguiente interpretación de los observables físicos reconstruidos. A partir de este resultado, desarrollé un modelo de señal de la distribución lateral bidimensional de la emisión de radio. Este modelo nos permite reconstruir la energía electromagnética de la lluvia con antenas de radio dispersas y con una resolución *intrínseca* por debajo del 5%, sin tener en cuenta las incertidumbres instrumentales. Además, dado que la energía electromagnética reconstruida no depende de la masa del rayo cósmico primario, este modelo es adecuado para realizar estudios precisos de la composición de masa de los UHECRs, por ejemplo, con la detección

híbrida RD-SD de AugerPrime. Además, evalué la posibilidad de mejorar la sensibilidad del RD a la masa de los rayo cósmicos, midiendo la profundidad atmosférica donde la lluvia adquiere su máximo desarrollo X_{\max} con una técnica de reconstrucción interferométrica recientemente propuesta. Concluí que el RD no cumple con la especificación para una reconstrucción precisa de X_{\max} , y que una sincronización de tiempo entre estaciones de antena de $\lesssim 1$ ns y una multiplicidad de señal de $\gtrsim 20$ es requerida para lograr resultados precisos.

Aplicando este marco teórico, estudié minuciosamente el rendimiento esperado del RD para detectar y reconstruir lluvias atmosféricas extendidas inclinadas y su potencial para iluminar nuestro conocimiento sobre la composición de masa de los UHECRs utilizando datos híbridos de AugerPrime. Usé simulaciones Monte-Carlo de lluvias, simulaciones del detector ajustadas a datos medidos, y una reconstrucción basada en un modelo de señal recientemente desarrollado para los observables físicos relacionados con la emisión de radio.

Encontré que el RD será 100% eficiente para detectar lluvias de aire inclinadas con ángulos cenitales superiores a 70° y energías superiores a 6.3×10^{18} eV. Durante un período de operación de 10 años, el RD recolectará más de 3900 eventos con energías superiores a 10^{19} eV y alrededor de 570 eventos para energías superiores a 4×10^{19} eV. Una reconstrucción precisa de la energía de la lluvia es actualmente posible con el RD para lluvias medidas con más de 5 antenas de radio y ángulos cenitales mayores a 68° . Con la respuesta instrumental esperada del RD, preveo una resolución de energía inferior al 10% para energías superiores a 10^{19} eV y no encuentro sesgo en la reconstrucción de energía electromagnética de las lluvias ni una dependencia con la masa de la partícula primaria. Este estudio finaliza con una evaluación de las incertezas sistemáticas. Combinando la energía reconstruida por el RD y el número de muones reconstruidos con el SD, evalué el potencial para medir la composición de masa promedio de los UHECRs, y el poder de discriminación de los distintos tipos de primario. La separación para lluvias atmosféricas inducidas por protones y hierro con ángulos cenitales superiores a 70° y energías electromagnéticas superiores a 10^{19} eV se cuantificó con una *factor de mérito* $FOM \approx 1,6$. Según las simulaciones, el RD y el SD tienen el potencial de extender las mediciones que se realizan actualmente con el detector de fluorescencia y el SD a energías y ángulos cenitales más altos, para obtener mediciones mejoradas de la composición de masa del UHECR y, a su vez, para distinguir entre los diferentes escenarios astrofísicos que explican la naturaleza de estas partículas.

Con el modelo de reconstrucción y el análisis de composición de masas desarrollados en esta Tesis, el Observatorio Pierre Auger se encuentra preparado para enfrentar los desafíos presentados por el gran volumen de datos experimentales que generará inminentemente su Detector de Radio.

Contents

Abstract	i
Zusammenfassung	iii
Resumen	v
Contents	vii
I. Introduction: Cosmic Rays, Extensive Air Showers, and the Pierre Auger Observatory	1
1. Introduction & Motivation	3
2. Ultra-high-energy cosmic rays & Extensive Air Showers	5
2.1. Cosmic Rays	5
2.1.1. Energy spectrum	6
2.1.2. Mass composition	7
2.1.3. Arrival directions	9
2.1.4. Origin and propagation	10
2.2. Extensive Air Showers	13
2.2.1. Particle cascades	13
2.2.2. Radio emission	16
3. Detecting Extensive Air Showers with the Pierre Auger Observatory	21
3.1. The Fluorescence Detector	23
3.2. The Surface Detector	23
3.2.1. Station design	23
3.2.2. Trigger concept	24
3.2.3. Event reconstruction	25
3.2.4. Energy calibration	27
3.3. The Auger Radio Engineering Array	28
3.4. The AugerPrime Radio Detector	29
3.4.1. Station design	30
3.4.2. Engineering Array	32
3.4.3. Calibration & Monitoring	33
3.5. The Auger simulation and reconstruction framework	34

II. Inclined Extensive Air Showers	37
4. Simulation of the radio emission from inclined air showers	39
4.1. CoREAS simulations of inclined air showers	40
4.1.1. Simulations with a star-shaped antenna array	45
4.1.2. Simulations for the AugerPrime Radio Detector	46
4.2. Radio emission from inclined air showers	49
4.2.1. Decomposition of the radio signal	50
4.3. Studies on the nature of the radio emission from inclined air showers	51
4.3.1. Atmospheric dependencies of the radiation energy in inclined air showers	51
4.3.2. Investigating the atmospheric depth from which the radio emission measured at ground originates	53
5. Refractive displacement of the radio-emission footprint of inclined air showers simulated with CoREAS	55
5.1. Apparent asymmetry in the lateral distribution of the radio emission	56
5.2. Displacement of the radio-emission footprints	57
5.2.1. Fitting the Cherenkov ring	59
5.2.2. Investigation of showers with a large geomagnetic angles	60
5.2.3. Comparison of the radio symmetry center displacement for different frequency bands	61
5.3. Interpretation of the displacement as due to refraction	62
5.3.1. Description of refraction using Snell's law	63
5.3.2. Refraction and its treatment in CoREAS	65
5.4. Conclusions	67
6. Signal model and event reconstruction for the radio detection of inclined extensive air showers	69
6.1. Treatment of the simulated radio emission from inclined air showers	70
6.1.1. Estimation of the energy fluence	71
6.1.2. High-frequency emission artifacts from particle thinning	71
6.1.3. Systematic core displacement due to refraction	73
6.2. Model for the radio-emission footprints	73
6.2.1. Geometrical early-late effects	74
6.2.2. Lateral distribution of the geomagnetic emission	76
6.2.3. Parameterization of the charge-excess strength	81
6.3. Reconstruction of inclined air showers with a sparse antenna array	84
6.3.1. Reconstruction of the electromagnetic shower energy	85
6.3.2. Reconstruction of the distance to the shower maximum	87
6.3.3. Reconstruction of air showers generated with a different high-energy hadronic interaction model	88
6.4. Discussion	88
6.5. Conclusions	90

7. Interferometric reconstruction of the depth of the shower maximum	93
7.1. Expected performance of air-shower measurements with the radio-interferometric technique	96
7.1.1. Simulations for interferometry	96
7.1.2. Interferometric reconstruction of the shower properties	98
7.1.3. Interferometric reconstruction of the depth of the shower maximum under realistic conditions	104
7.1.4. Interferometric reconstruction for higher frequency bands	107
7.1.5. Discussion	109
7.1.6. Conclusion	113
7.2. Interferometric reconstruction of the depth of the shower maximum with the Auger radio detectors	114
7.2.1. Simulations	114
7.2.2. Shower selection	115
7.2.3. Expected reconstruction performance for the RD	116
7.2.4. Expected reconstruction performance for AERA	117
7.2.5. Conclusion	119
III. Measuring inclined extensive air showers with the Radio Detector of the AugerPrime Observatory	121
8. Detecting and reconstructing inclined air showers with the AugerPrime Radio Detector	123
8.1. Simulations of AugerPrime events	124
8.1.1. Detector simulation	124
8.2. Signal reconstruction with the Radio Detector	128
8.3. Collectable number of events	131
8.3.1. Detection efficiency	131
8.3.2. Aperture	134
8.3.3. Number of events	135
8.3.4. Discussion	136
8.4. Reconstruction of inclined air showers with the Radio Detector	137
8.4.1. Arrival direction reconstruction	137
8.4.2. Reconstruction of the electromagnetic shower energy	139
8.4.3. Reconstruction of the cosmic-ray energy	147
8.4.4. Investigation of systematic effects in the energy reconstruction	149
8.4.5. Discussion	152
9. Evaluating the sensitivity of the AugerPrime Radio Detector to the masses of ultra-high-energy cosmic rays using inclined air showers	153
9.1. Reconstructing the number of muons from inclined air showers	153
9.2. Generation of realistic event sets for different astrophysical scenarios	155
9.3. Separation of proton- and iron-induced inclined air showers	157
9.4. Measuring the number of muons in inclined air showers	160

9.5. Conclusion	162
IV. Summary	163
10. Summary	165
V. Appendix	171
A. Appendix to Chap. 4	173
A.1. Extrapolating CoREAS pulses	173
A.2. Parameterizations of the mean number of muons and their fluctuations from simulated inclined air showers	174
B. Appendix to Chap. 6	175
B.1. Alternative approach for the decomposition of the geomagnetic and charge- excess emission	175
B.2. Variation in the LDF parameters for different atmospheric conditions . . .	175
B.3. Refined lateral shape of the charge-excess fraction parameterization . . .	176
B.4. Electromagnetic shower energy derived from CORSIKA simulations . . .	177
B.5. Reconstructing the electromagnetic shower energy for showers generated with Sibyll-2.3d	177
C. Appendix to Chap. 7	179
C.1. Calculation of the effective refractive index between two arbitrary locations in the atmosphere	179
C.2. Parameterization of the Cherenkov radius for the interferometric recon- struction of inclined air showers with the Auger radio detectors	180
C.3. Station multiplicity and event selection for the interferometric reconstruct- ion of inclined air showers with the Auger radio detectors	181
D. Appendix to Chap. 8	183
D.1. Simulation of the signal arrival direction at individual antennas	183
D.2. Measured radio-frequency interference	184
D.3. Azimuthal dependency of the RD detection efficiency	185
D.4. Goodness of the LDF fits with the RD	186
D.5. Estimation of the uncertainty for the reconstructed electromagnetic shower energy	187
D.6. Correction of the fit-estimated energy resolution	188
D.7. Estimating start values for the LDF fit	189
D.8. Offline configuration: Reconstruction sequence and modules	189

E. Appendix to Chap. 9	193
E.1. Selection for the discrimination between proton- and iron-induced air showers	193
E.2. Proton and iron separation with the depth of the shower maximum	194
F. List of Publications	196
G. Acknowledgment	199
Bibliography	200

Part I.

Introduction: Cosmic Rays, Extensive Air Showers, and the Pierre Auger Observatory

1. Introduction & Motivation

From far beyond our own galaxy, mysterious cosmic messengers are reaching us. These messengers are charged nuclei with tremendous energies, so-called *ultra-high-energy cosmic rays* (UHECRs). The pure amount of energy these particles possess, some of them have macroscopic energies exceeding 10^{20} *electron volt* (eV) [1], suggests that they must originate from the most violent and unique regions in our universe. Also, UHECRs are a powerful tool in particle physics as they allow scientists to study an energy regime inaccessible with even the most powerful particle accelerators on Earth [2].

Besides being so energetic, UHECRs are rare, at 10^{20} eV less than 1 particle per square kilometer and century is impinging on the Earth's atmosphere. Once an UHECRs reaches Earth it interacts with the nuclei of air molecules in the Earth's atmosphere. The interaction causes both, the cosmic ray and air nucleus, to fragment. The fragments created in this collision will interact with more nuclei and thus initiate an exponentially growing cascade of secondary particles which at its maximum can contain billions of particles, the so-called extensive air showers. To detect those air showers, scientists construct and operate observatories of astonishing dimensions. The largest experiment dedicated to the detection of extensive air showers initiated by UHECRs is the Pierre Auger Observatory located in the Mendoza Province, Argentina, next to the city of Malargüe [3]. The observatory combines different detections techniques that allow it to measure extensive air showers with unprecedented accuracy. The largest detector component, suitable to detect UHECRs at the highest energies above 4×10^{19} eV, is a 3000 km^2 *Surface Detector* (SD) array, an area almost seven and a half times the size of Köln. The SD consists of 1600 *water-Cherenkov detectors* (WCDs), aligned on a hexagonal grid with 1.5 km spacing, which register the Cherenkov light produced by through-going air shower particles. The large lateral dimensions of extensive air showers at the ground allows them to be measured simultaneously by several WCDs.

Although considerable progress has been made in the last 60 years by the UHECRs community and in particular by the Pierre Auger Observatory in the last two decades, which challenges our early picture of UHECRs, the most relevant questions regarding their origin "Where and how are they accelerated?" remains yet to be answered. This progress has made it clear that further substantial improvements to our understanding of UHECRs can only be achieved with more and better mass-sensitive data at the highest energies above 4×10^{19} eV [4]. To accomplish this, the Pierre Auger Observatory has instituted the AugerPrime Upgrade with the objective to improve the mass sensitivity of its Surface Detector with the installation of additional detector components [5].

The upgrade comprises, among other enhancements, the installation of 1600 dual-polarized radio antennas on top of each WCD [6]. The *AugerPrime Radio Detector* (RD) will measure the coherent, electromagnetic radiation produced by the secondary particles in extensive air showers. The strongly forward-beamed radio emission from inclined air

showers with zenith angles $\theta \gtrsim 65^\circ$ illuminates large elongated areas allowing the simultaneous detection with several radio antennas in coincidence with the water-Cherenkov detectors. Those hybrid measurements of radio antennas and WCDs yield highly complementary information which can be exploited to determine the mass(-composition) of UHECRs [7].

With this work, I am laying the foundation to process, reconstruct, and analyze data measured by the AugerPrime Radio Detector. To this end, I have studied the emission and propagation of the electromagnetic radiation in inclined air showers in detail, using numerical simulations of the radio emission, see Chaps. 4 and 5, respectively. Based on the gained knowledge, I have developed a signal- and reconstruction model for the radio detection of inclined air showers which enables the reconstruction of the shower energy with a minimal dependency on the UHECRs mass and an excellent intrinsic resolution, see Chap. 6. A measurement of the depth of the shower maximum would greatly improve the capability of the Radio Detector to estimate the mass(-composition) of UHECRs. Hence, I have evaluated an interferometric reconstruction algorithm to obtain the depth of the shower maximum from highly inclined air showers with radio-antenna arrays in general and for the RD in particular, and specified requirements for experiments to employ this technique, see Chap. 7.

Finally, I have thoroughly studied the performance of the Radio Detector to detect and reconstruct inclined air showers. This pilot study of the RD performance constitutes Monte-Carlo generated air showers, a complete end-to-end simulation of the instrumental response of the RD, and an event reconstruction of all relevant air shower parameters. The main objectives are to estimate the expected number of events the RD will detect in 10 years of operation and the resolution with which those air showers can be reconstructed, see Chap. 8. With those reconstructed air showers, I have studied the scientific potential of hybrid measurements of the RD together with the SD to determine the mass composition of UHECRs and to determine the primary-particle type of individual air showers, see Chap. 9. In chapter 10, I summarize my work.

In the following two chapters, 2 and 3, I will provide the necessary theoretical background of UHECRs and extensive air showers as well as a detailed description of the Pierre Auger Observatory. I will focus on the relevance of mass-composition data and how the mass of UHECRs can be inferred from measurements of extensive air showers. Special attention is given to the description of the emitted electromagnetic “radio” emission in inclined air showers. The description of the Pierre Auger Observatory and its AugerPrime upgrade will focus on the WCDs and RD.

2. Ultra-high-energy cosmic rays & Extensive Air Showers

Cosmic rays are charged, ionized nuclei that hit the Earth's atmosphere with a total rate of about 1000 particles per square meter and second [2]. Their energy varies greatly from just below 10^9 eV to as much as 10^{20} eV and beyond. While the energy increases, their flux drops rapidly: For each decade in energy the flux decreases by roughly 3 decades. Remarkably, over this entire energy range of over 11 decades, the spectrum can be described approximately with a single power law $N(E) \sim E^\gamma$ with $\gamma \approx -3$ [8]. The rapidly dropping flux and the shielding of the Earth's atmosphere which prevents (primary) cosmic rays from reaching the Earth's surface, mandates different detection techniques to observe lower- and higher-energy cosmic rays. At lower energies, $E \lesssim 1 \text{ TeV} = 10^{12}$ eV, cosmic rays have to be measured directly outside or very high up in the atmosphere with space- or air-borne experiments [9, 10]. These experiments are naturally limited by their aperture and thus lose sensitivity with energy. At very high energies, $E \gtrsim 1 \text{ PeV} = 10^{15}$ eV, the indirect detection of cosmic-ray-induced extensive air showers with large detectors at the Earth's surface becomes feasible [2]. In the context of this work, we give special attention to *very-high energy* (VHE) cosmic rays above 10^{15} eV and *ultra-high energy* (UHE) cosmic rays above 10^{18} eV in Sec. 2.1. Extensive air showers and in particular the emitted radio emission, will be described in Sec 2.2.

2.1. Cosmic Rays

Cosmic rays in general are known since the beginning of the 20th century [11]. In the past decades, a lot of new measurements [12, 13, 14] have driven the field of *ultra-high-energy cosmic rays* UHECRs and challenged an early simplistic picture of UHECRs being protons that originate from a few powerful nearby sources and replaced it with a more complex and nuanced one [4]. As a consequence, the most intriguing questions about their origin, "Where do they come from?" and "How are they accelerated?", remain yet to be answered. This evolving picture of UHECRs being composed of heavier nuclei from potentially a mix of source classes has raised awareness of the need for more precise mass composition data at the highest energies. The Upgrade of the Pierre Auger Observatory, currently under construction, has been proposed to tackle this issue (cf. Chap. 3).

In this section, we will briefly summarize our current understanding of cosmic rays and present recent measurements (of the energy spectrum Sec. 2.1.1, mass composition Sec. 2.1.2 and arrival directions Sec. 2.1.3). Our current knowledge about the origin of UHECRs, their acceleration site and propagation is summarized in section 2.1.4. Because

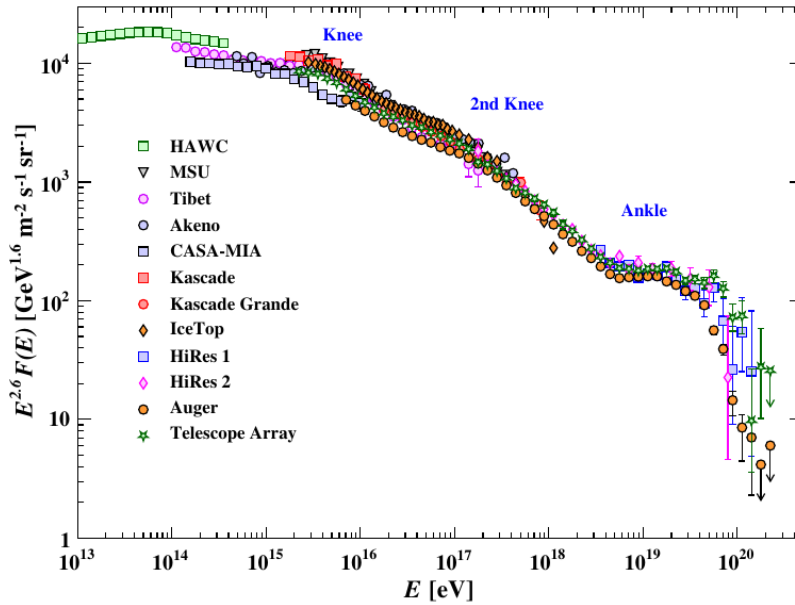


Figure 2.1.: All-particle cosmic ray flux at very high energies multiplied with $E^{2.6}$ as measured by various experiments. Several changes in the spectral index are clearly visible with good agreement between multiple experiments. Details in text. Figure from [18, Fig. 30.9].

of its relevance for this thesis, we will elaborate in more detail on the different approaches to measure the mass(-composition) of UHECRs with air-shower experiments in Sec. 2.1.2.

For the sake of compactness, we will mainly refer to measurements from the Pierre Auger Collaboration. Data of the other air shower experiment with sufficient aperture for the detection of UHECRs, the Telescope Array (TA), is mostly consistent with data from Auger within the quoted systematic uncertainties of both experiments [15, 16, 17].

2.1.1. Energy spectrum

In recent years, the energy spectrum of UHECRs has been measured beyond 10^{20} eV with remarkably accuracy [19]. Those measurements have revealed several features which prevent us from describing the spectrum by a single power law. The differential flux of cosmic rays at very high energies, measured by several experiments, is shown in greater detail in Fig. 2.1. The flux is multiplied by a factor of $E^{2.6}$ to better visualize changes in the spectral index γ . Although the data from different experiments exhibit a pronounced scatter, several features are clearly noticeable. The features, annotated in the figure, are the “Knee” at an energy of $E_{\text{Knee}} \approx 5 \times 10^{15}$ eV, the “2nd Knee” at an energy of $E_{2\text{nd Knee}} \approx 1.7 \times 10^{17}$ eV, the “Ankle” at an energy of $E_{\text{Ankle}} \approx 5 \times 10^{18}$ eV, and (not annotated) the “Suppression”, i.e., the apparent extinction of the cosmic-ray flux, starting at an energy of $E_{\text{Suppression}} \approx 5 \times 10^{19}$ eV [4]. Very recently, the most precise measurement of the spectrum at energies beyond the Ankle by the Pierre Auger Observatory [19] has revealed an additional feature between the Ankle and Suppression, the “Instep” at an energy of $E_{\text{Instep}} \approx 10^{19}$ eV. All those features describe a change in the spectral index $\gamma \in [-2.5, -3.3]$. The interpretation of those features remains an open question as they

can be the result of many properties of the nature of UHECRs. The acceleration and the escape from their acceleration site, the propagation as well as the distribution of their source(s) could all possibly affect the spectrum [4].

For example, it is generally assumed that UHECRs beyond 6×10^{18} eV are of extragalactic origin [20] (cf. Sec. 2.1.3). This suggests an interpretation of the Ankle as the transition between a galactic and extragalactic dominated spectrum. However, this requires an additional galactic cosmic ray “population” to bridge the gap between the *2nd knee*, which is commonly interpreted as the cut-off of an iron component accelerated in the shock front of supernova remnants (SNR)¹, and the Ankle [21]. If so, the lack of anisotropy in the arrival direction of cosmic rays with energies below the Ankle (assuming that a significant fraction of them must be protons) would be difficult to explain [5]. Thus, it is more likely that an extragalactic proton flux starts already at a lower energy of $\approx 10^{17}$ eV. This (again) opens-up the interpretation of the Ankle. In Ref. [22] the Ankle is explained with the pile-up of extragalactic higher-energy protons suffering from energy losses. However, this model can not easily explain the Auger data for mass composition (see next section, and discussion in [5, Sec. 2.2.1]).

The *suppression*, after conflicting measurements in the late 20th century, has nowadays been confirmed by different experiments. While an early prediction of this suppression, assuming a proton dominant flux, interpreted it as the consequence of catastrophic energy losses due to photo-pion production (i.e., GZK-Suppression cf. Sec. 2.1.4), with the indication of a heavier mass composition at these energies this interpretation is questioned by an interpretation which assumes that maximum-rigidity sources run out of power at these energies. It is nowadays clear, that a more detailed understanding of those features can only be achieved with a better understanding of the mass composition of UHECRs.

2.1.2. Mass composition

A detailed understanding of the mass composition of UHECRs is crucial for the interpretation of features seen in the energy spectrum. Furthermore, an accurate event-by-event mass estimation would even allow isolating light particles which, at the highest energies, could enable cosmic-ray astronomy.

Measuring the mass of cosmic rays is in general more challenging than a measurement of their energies or arrival directions. The statistical nature of the hadronic interactions between UHECRs and the nuclei of air molecules, cause so-called shower-to-shower fluctuations which cause a significant blurring of the signature of different primaries. Different techniques exist to estimate the mass of cosmic rays from indirect detection. The most common one is the measurement of the slant depth of the shower maximum X_{\max} (in units of g cm^{-2} , cf. Sec. 2.2). Air showers initiated by heavier particles develop, on average, earlier in the atmosphere and thus have a lower X_{\max} than showers from lighter particles.

Traditionally, fluorescence telescopes, which measure the entire longitudinal development of air showers directly from the emission of isotropic fluorescence light, are used to

¹ In this picture, the first *knee* is produced by a cut-off of protons accelerated in the same sources to the same maximum rigidity ($\equiv E/Z$ with E the energy and Z the charge number), hence iron nuclei have a 26 larger maximum energy than protons: a cut-off for protons at 5×10^{15} eV would imply a cut-off for iron at 1.3×10^{17} eV.

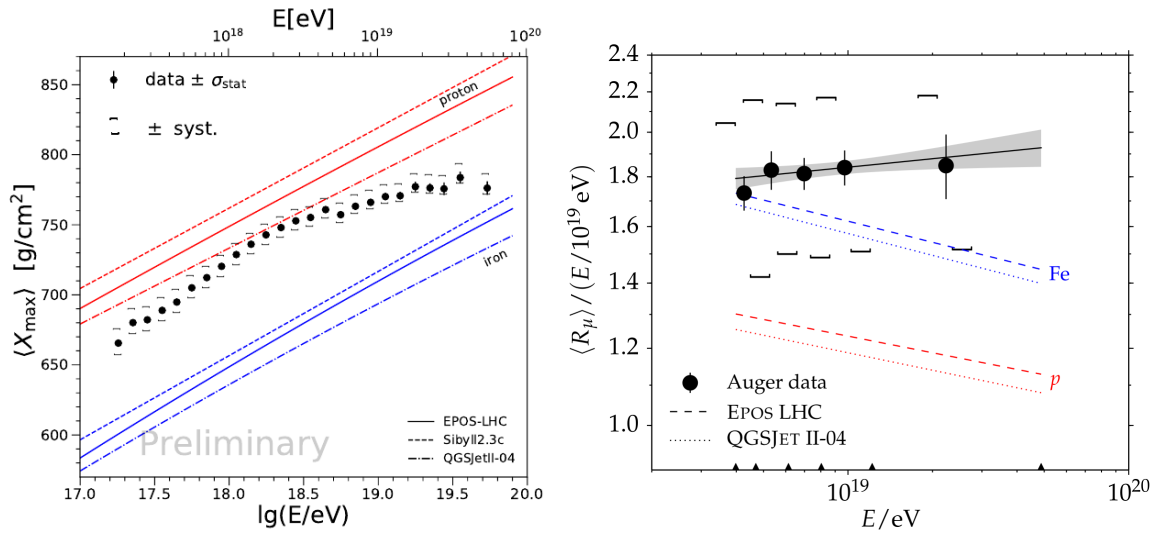


Figure 2.2.: *Left:* Measurement of $\langle X_{\max} \rangle$ as a function of the cosmic-ray energy by the Pierre Auger Observatory with hybrid events detected by the Fluorescence and Surface Detectors compared to theoretical predictions for protons and iron nuclei. Figure from [23]. *Right:* Measurement of the normalized mean muon content from inclined air showers measured in coincidence with the Auger Fluorescence and Surface Detectors. The data are in contradiction with the theoretical predictions. Figure from [24].

measure X_{\max} with high precision. The Pierre Auger Fluorescence Detector has measured X_{\max} with a resolution at lower energies of $\sim 25 \text{ g cm}^{-2}$ and $\sim 15 \text{ g cm}^{-2}$ at higher energies. The systematic uncertainty for this measurement is below 10 g cm^{-2} [25]. Fig. 2.2 (left) shows the $\langle X_{\max} \rangle$ measured by Auger together with the theoretical predictions from different high energy hadronic interaction models for a pure proton and iron composition. The data suggest a relatively light composition at lower energies around $\sim 10^{17.5} \text{ eV}$ which becomes slightly lighter with energy until $\sim 10^{18} \text{ eV} - 10^{18.3} \text{ eV}$. After this, the composition gradually becomes heavier with energy indicating a depletion of light elements from the UHECRs beam. Another observable to look at is the fluctuation $\sigma_{X_{\max}}$ as lighter particles have a greater statistical variance in their interaction. Also, $\sigma_{X_{\max}}$ is in agreement with a heavier composition at the higher energies [23]. However, at the very highest energies ($E \gtrsim 4 \times 10^{19} \text{ eV}$) the statistics available with fluorescence measurements are too limited to draw robust conclusions.

Recently, also digital radio-antenna arrays have demonstrated their capability to measure X_{\max} with compatible resolution. In contrast to fluorescence telescopes, those detectors measure the lateral profile of the radio emission at the ground which is found to be sensitive to the longitudinal development of the particle cascade as well. By matching the measured signal distributions to those obtained from Monte-Carlo simulations, experiments like Tunka-Rex [26], LOFAR [27], and AERA [28] have shown resolutions of 15 g cm^{-2} to 25 g cm^{-2} , however with larger systematic uncertainties.

A different approach to estimate the cosmic-ray mass relies on the measurement of the relative muon content R_{μ} in air showers. Air showers initiated by lighter cosmic rays have on average a weaker muonic component (i.e., are electron-rich) while heavier

elements produce more muons (are muon-rich) [2]. At the same time, R_μ increases with energy, hence to correctly interpret the mass(-composition) of cosmic rays from R_μ an independent measurement of the shower energy is required. To measure R_μ and the shower energy independently of each other, experiments have shielded a part of their detectors from the (much larger) electromagnetic shower component. The shielded detector units are measuring R_μ while the non-shielded units are used to reconstruct the energy. The KASCADE-Grande [29] experiment used lead/iron-shielded and non-shield scintillators to disentangle the muonic and electromagnetic shower components to categorize air showers into light and heavy. The design of the AugerPrime Upgrade is also focused on disentangling the two shower components to achieve mass sensitivity with its Surface Detector.

The same concept can be extended to hybrid detections of air showers with a radio detector which is only sensitive to the electromagnetic shower component and a completely shielded particle detector such as buried scintillator panels [30]. A combination of a radio detector with a particle detector also allows this concept to extend to larger zenith angles, i.e., highly inclined air showers. In such an air shower, most electromagnetic particles are stopped in the atmosphere and do not reach the ground. Hence, also non-shielded particle detectors measure muons while radio antennas register the emission produced by the electromagnetic cascade high up in the atmosphere [7]. This concept is already employed at Auger by combining measurements from the Fluorescence Detector and Surface Detector, cf. Fig. 2.2 (right), however only with limited statistics due to the limited exposure of the Fluorescence Detector (cf. Sec. 3.1). What is striking about Fig. 2.2 (right) is that the measurement from Auger is difficult to explain with the theoretical predictions from simulations (colored lines). At the highest energies, even a pure iron composition would stress the systematical uncertainty to be compatible. The apparent disagreement is known as “muon deficit” (in simulations) and has been reported by many experiments and different measurements [31]. The fact that the measured number of muons R_μ scales almost linearly with the energy (note the normalization of the y-axis) while simulations predict a scaling to the power of $R_\mu \sim E^b$ with $b \approx 0.9$ (cf. Secs. 2.2.1 and 4.1), hints to a change in compositions towards heavier elements with energy.

No data of hadronic interactions with an equivalent center of mass energy for cosmic rays beyond 10^{17} eV, taken in a controlled laboratory environment (such as a particle accelerator) exist. And at lower energies, data relevant for interactions in air showers, e.g., at large rapidities and for proton/pion and air nuclei projectiles, are rare or missing [32]. Hence, the models that predict those interactions in air shower simulations (such as QGSJet [33], Sibyll [34], or EPOS [35]), have to rely on extrapolating data from lower energies which introduces significant systematic uncertainties.

2.1.3. Arrival directions

The identification of the acceleration sites of UHECRs and thereby a more detailed understanding of the acceleration mechanism are among the most relevant and prevailing questions in high-energy astroparticle physics. In the past decade, the arrival directions of UHECRs have been intensively studied to find any kind of correlation on small or intermediate angular length scales with source(s) or class(es) of them. So far several indications

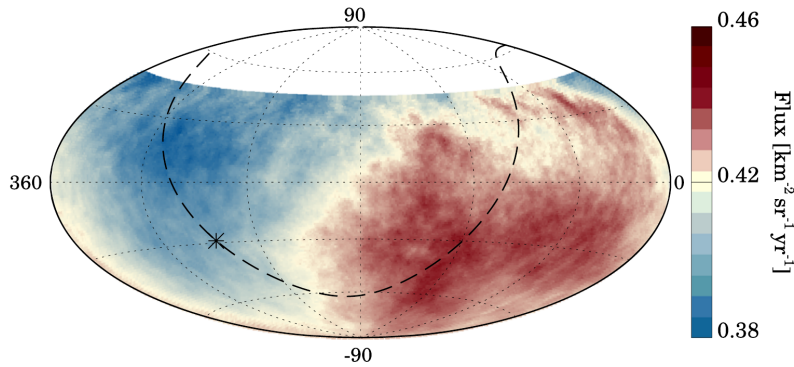


Figure 2.3.: Smoothed flux of cosmic rays with energies above $E \geq 8$ EeV in equatorial coordinates measured by Auger. The dashed line (star) indicates the galactic plane (center). The blank area indicates the directions which are not observed by the Auger Observatory. Figure taken from [20].

have been found, the most significant of them is a correlation with starburst galaxies found in Auger data [36], however none of them could be identified with the required 5-sigma statistical post-trial significance [4] for a discovery.

Searches for large-scale anisotropies are also performed. In 2018, the Pierre Auger Observatory reported a large-scale, dipole-like anisotropy in the arrival directions of UHECRs with energies above $E \geq 4$ EeV $\approx 10^{18.6}$ eV [20]. Fig. 2.3 shows the flux of UHECRs in equatorial coordinates. A clear excess in the flux of UHECRs in one direction accompanied by a suppression in the opposite direction is visible. The amplitude is measured with an amplitude of $d = 0.073^{+0.011}_{-0.009}$ and a significance of 6.6σ [37]. The non-correlation of the dipole orientation with the galactic plane and its center strongly suggests an extragalactic origin of ultra-high energy particles. Very recently an intriguing indication for a mass-dependent large-scale anisotropy, correlated with the galactic plane has been reported by Auger [38].

2.1.4. Origin and propagation

In this section, we summarize the most important aspects that govern the propagation of UHECRs. In the end, we present two competing (reference) scenarios for the origin of UHECRs which are tuned to describe the measured energy spectrum and mass composition data by Auger. However, due to the lack of more precise composition data at the highest energies, these models are only representative of a larger number of possible scenarios that can explain the Auger data.

Here, we focus on cosmic rays with energies beyond the Ankle which are believed to be of extragalactic origin. Hence, we summarize important details of the extragalactic propagation, a detailed summary of galactic propagation can be found in Ref. [2].

The primary interaction target for UHECRs during propagation is assumed to be the cosmic microwave background (CMB). The CMB interacts with ultra-high energy protons via *photopion-production*, i.e.,

$$p + \gamma \rightarrow p + \pi_0. \quad (2.1)$$

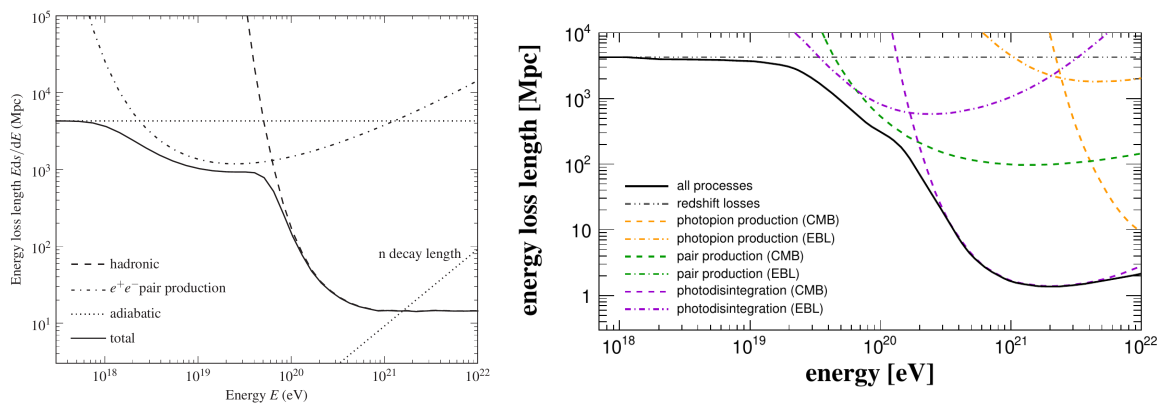


Figure 2.4.: *Left:* Energy-loss length for UHE protons due to the interaction with the CMB and other energy losses. Figure from [2]. *Right:* Energy-loss length for UHE iron nuclei due to the interaction with the CMB and EBL for different processes. Figure from [42].

The proton threshold energy for this interaction with a CMB-photon in its rest frame is $E_{p,\text{rh}} \approx 7 \times 10^{19}$ eV [2]. Hence, protons with energies beyond that would be strongly suppressed. This suppression is also referred to as the *GZK-Suppression* after Greisen, Zatsepin, and Kuzmin². In Fig. 2.4 (*left*) the energy loss length for protons as a function of the energy is shown. Besides neutral pions, also positively charged pion (together with a neutron) may be produced in this interaction. The pion would shortly afterward decay and produce at least one neutrino giving rise to the so-called cosmogenic neutrino flux.

For heavier nuclei, the interaction with the CMB via *photo-disintegration* is the most prominent interaction at higher energies³. By absorbing a photon, the nucleus gets into an excited state and decays during deexcitation into a daughter nucleus and at least one other nucleus/nucleon, i.e.,



In Fig. 2.4 (*right*) the energy loss length for iron nuclei as a function of the energy is shown. In this interaction no neutrinos are produced, hence the mass composition of UHECRs (at their source) has a great impact on the expected cosmogenic neutrino flux [41].

Due to the effect of both interactions, the maximum distance, i.e., horizon, from which cosmic rays at the highest energies can reach us is limited. This is commonly referred to as the *GZK-horizon*⁴ and has a radius of ~ 75 Mpc to 150 Mpc depending on the particle mass [2].

In Fig. 2.5 the description of the Auger all-particle spectrum with the spectra of 4 primaries is shown for energies above the Ankle. The description on the left side is referred to as the “maximum rigidity” scenario, the one on the right as the “photo-disintegration”

² Greisen [39] and Zatsepin and Kuzmin [40] independently predicted this suppression in the flux of ultra-high-energy cosmic ray (protons) shortly after the discovery of the CMB.

³ Also, heavier nuclei engage in photopion-production, however assuming that each nucleon carries the same amount of energy, the threshold energy for this interaction would increase linearly with the mass number A , i.e., $E_{A,\text{th}} = A E_{p,\text{rh}}$.

⁴ Although, strictly speaking, this term was invented for the horizon of UHE protons due to photopion production, it can be used for heavier nuclei which are first limited by photodisintegration and later by photopion production as well.

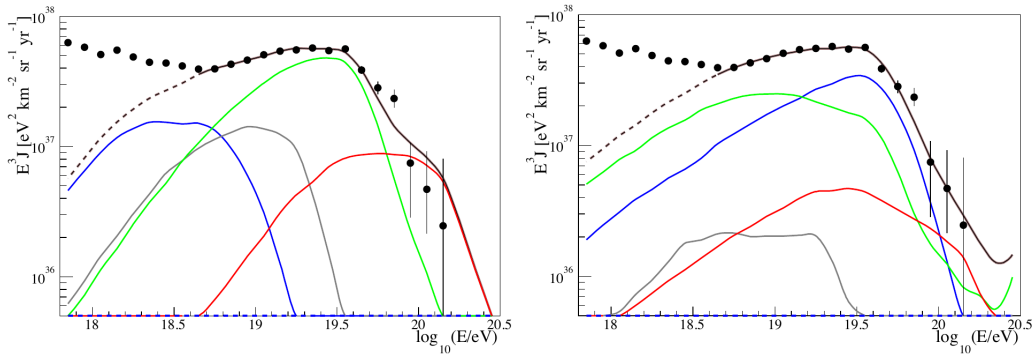


Figure 2.5.: All-particle spectrum measured by Auger (black dots) and described by the spectra of 4 different primaries, protons (blue), helium (gray), nitrogen (green), and iron (red) nuclei, for two different “mass-composition scenarios”. On the left, the primary particle spectra describe the maximum-rigidity scenario, and on the right, the photo-disintegration scenario. The particle spectra were obtained from model calculations with SimProp [43]. Figure from [5].

scenario. They are obtained using a model for a 4-primary spectrum at their sources and propagated using the simulation code SimProp [43] to Earth. The free parameters defining the source spectrum were tuned to the Auger-measured all-particle energy spectrum and mass composition, i.e., $\langle X_{\max} \rangle$ and $\sigma_{X_{\max}}$ (not shown). The free parameters are the maximum rigidity to which the sources can accelerate the particles (above which an exponential suppression of the spectra is assumed), the spectral index (all-particle spectra are assumed to have the same index), and mass composition at the source. For simplification, the distribution of sources is assumed to be homogeneous. Both presented scenarios refer to a different minimum and describe the features seen in the Auger data by completely different mass compositions at the sources (not shown) and at Earth.

The maximum rigidity scenario is characterized by a proton component at 5×10^{18} eV (with the cutoff at 7×10^{18} eV) which is naturally connected to the components of heavier nuclei which are shifted in energy (to the right) by $E_n = ZE_{\text{prot.}}$ with the charge number Z . The high energy end of the all-particle spectrum is described by iron nuclei (or similarly heavy ones) and the *suppression* is a consequence of the cutoff of the source spectrum rather due to energy losses during propagation. The source spectra are hard with $\gamma = 1$.

In the photo-disintegration scenario, UHECRs are accelerated beyond the threshold energy for photo-disintegration and the *suppression* is described by the energy loss of these particles. Heavier nuclei fragment and produce lighter ones which are shifted (to the left) in energy by the ratio of their masses. It is noteworthy that in this scenario almost no light particles are directly produced at the sources and that the source composition is dominated by particles in the nitrogen - silicon group. The injection spectra have an index of $\gamma = 2$ which is expected from Fermi acceleration.

In both cases, the protons are of extragalactic origin and linked to the spectra of heavier elements. None of the two scenarios describe the Ankle.

2.2. Extensive Air Showers

Extensive air showers (EAS), or short air showers, are large cascades of billions of secondary particles initiated in a collision of a high or ultra-high-energy cosmic ray and an air nucleus in the upper atmosphere. In this first hadronic interaction, a number of secondary particles are produced which themselves will produce more particles in further collisions forming the particle cascade. The entire particle content is concentrated in a “shower front” of only a few meters in thickness. After the particle cascade has reached its maximum in terms of particle numbers, this shower front has a lateral expansion of several square kilometers, depending on the cosmic-ray energy, which allows sparse particle detector arrays to detect air showers on the Earth’s surface. A brief summary of the particle cascade is given in the next section (Sec. 2.2.1). Besides the detection of the particle footprint with particle detectors, other detector types can be used to detect air showers. Examples are optical telescopes which measure the isotropic fluorescence or beamed Cherenkov light or radio antennas which measure emitted electromagnetic radiation in the MHz regime. The latter, which is of special interest in the context of this work, is described in some detail in Sec. 2.2.2.

2.2.1. Particle cascades

In the first interaction between a cosmic ray and an air nucleus, mostly hadrons such as charged and neutral pions are produced. The neutral pions will almost immediately decay into two photons which initiate the so-called electromagnetic (shower) component. The remaining charged pions remain in the hadronic component and further collide with more air nuclei. In each interaction, the produced neutral pions transfer energy into the electromagnetic component, and the energy of each hadron decreases until they eventually decay before colliding with other air molecules. The decay products are mostly muons which are accompanied by (muon-)neutrinos. The former give rise to the muonic shower component while neutrinos will not interact or decay nor be detected by air-shower detectors and therefore contribute to the so-called *invisible energy*. While the hadronic component is mostly extinct, very close to the cosmic-ray trajectory hadronic particles may reach ground. The muons will reach the ground over a large area and be detected by particle detectors.

The photons produced by the decay of the neutral hadrons will undergo pair-production while the produced electron-positron pairs will again radiate photons via bremsstrahlung. These alternating processes will repeat, while the number of particles in the electromagnetic cascade exponential increases, the energy of each particle decreases. Similar to the hadronic component, the electromagnetic component will increase until the energy of its particles drops below a critical energy $E_{\text{crit}} \approx 87 \text{ MeV}$ [2] and lose more energy due to ionization. This ionization leads to an excitation of the atmospheric nitrogen molecules which, during deexcitation, will emit isotropic fluorescence light, which is detectable during moonless nights.

This simplified picture of the different shower components and their interplay is illustrated in Fig. 2.6 (*left*). The reality is (unsurprisingly) more complex and more particles such as kaons, etas, protons, or neutrons are participating in the particle cascade [2].

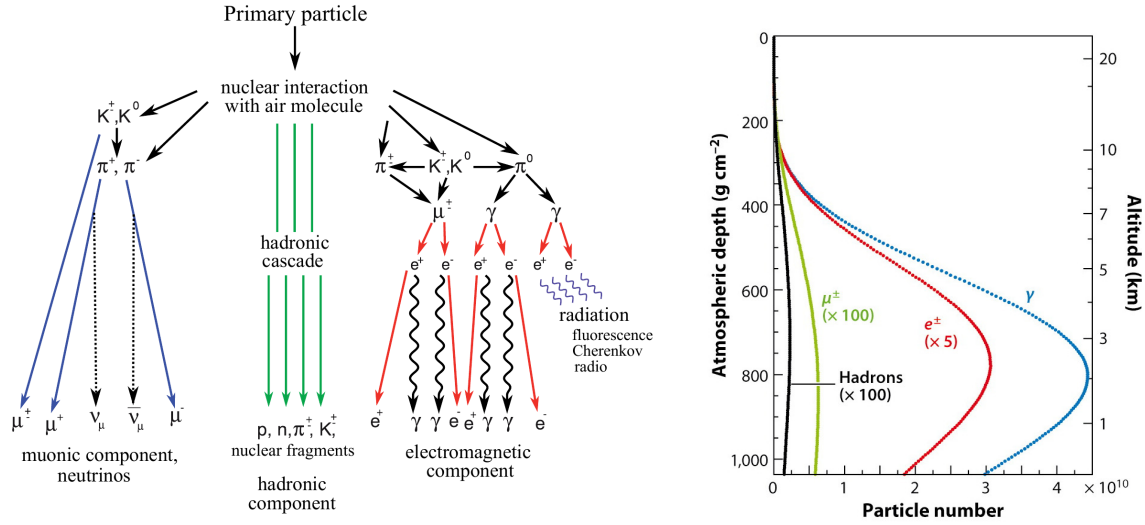


Figure 2.6.: *Left:* Illustration of the particle cascade of an extensive air shower with the characterization into 3 components, namely the muonic, hadronic, and electromagnetic. Figure from [44]. *Right:* Longitudinal particle profiles from a (simulated) vertical 10^{19} eV proton shower. Figure from [45].

During their propagation in the atmosphere, electrons and positrons emit electromagnetic waves which can be detected at the ground in the MHz regime as coherent radio emission. More details are given in the following section.

The longitudinal development of the different air shower components is shown for a simulated air shower in Fig. 2.6 (*right*). As it can also be derived from the above description, the hadronic component develops first. It “fuels” the electromagnetic component which comprises far more particles. Both components, however, after having reached their maximum, are diminishing. Lastly, the muonic component develops from the decay of low-energy hadrons. Unlike the other components, the muonic component remains relatively steady as the muons reach the ground before decaying or interacting. The plot also reveals the relative size of each component. The all-particle longitudinal profiles will closely follow that of the electromagnetic component, the noticeable maximum is referred to as the “shower maximum”. The slant depth X , i.e., the amount of matter the air shower traversed to this point measured in g cm^{-2} , is called X_{max} ⁵. Although the electromagnetic component decreases towards the ground, at a depth of 900 g cm^{-2} to 1000 g cm^{-2} it still dominates the particle footprint for cosmic-ray energies $\gtrsim 10^{18}$ eV. The Earth’s surface has a vertical depth of $\sim 1000 \text{ g cm}^{-2}$, the Pierre Auger Observatory located at an altitude ~ 1400 m a.s.l. is at a vertical depth of $\sim 860 \text{ g cm}^{-2}$. For non-vertical showers, the slant depth of the ground measured along the path of the air shower increases, however until around $\lesssim 60^\circ$ (the depth increases by a factor $\sim \cos^{-1} 60^\circ = 2$) the electromagnetic

⁵ Unlike in Fig. 2.6 (*right*), X_{max} often refers to the maximum of the all-particle energy deposit dE/dX in the atmosphere (due to ionization) rather than the particle multiplicity. Both distributions are closely correlated but not overlapping. Later in this work we refer to X_{max} as the maximum of the energy deposit profile.

component will still be significant. For even more inclined air showers muons will start to dominate the particles that reach the ground.

The longitudinal profiles shown in Fig. 2.6 (*right*) are computed using the numerical *Monte-Carlo* MC code CORSIKA [46]. Those fully numerical MC methods are the only possibility to predict the features of extensive air showers with high accuracy and especially can model the statistical nature of hadronic interactions which cause the shower-to-shower fluctuations. Also, analytical models to describe air showers exist, and although their practical applications are limited, they are successful in giving an accurate description of the average behavior of air showers. Furthermore, they are very helpful in understanding the consequences of different observables on the development of the particle cascade. The Heitler model [47] is used to describe electromagnetic particle cascades and an extension of it, the Heitler-Matthews model [48], can describe the hadronic shower component. Both models make the simplification that the particle cascades develop in discrete generations. At the end of each generation, the particles interact and produce a new generation of particles among which they split their energy equally. In the electromagnetic cascade (Heitler model) after one radiation length, $X_0 \approx 37 \text{ g cm}^{-2}$ each particle produces 2 new particles. Hence, the number of particles and their energy in each generation $n = X/X_0$ is given by $N(X) = 2^{X/X_0}$ respectively $E(X) = E_0/N(X)$. Given that the production of new particles stop when the energy of the particles drops below a critical energy $E(X) < E_c$ (this is the point at which the shower is at its maximum) the following relationships can be concluded:

$$N_{\max} \equiv N(X_{\max}) = E_0/E_c \sim E_0 \quad \text{and} \quad X_{\max} = \frac{X_0}{\ln 2} \ln(E_0/E_c) \sim \ln E_0. \quad (2.3)$$

For hadronic showers, the above formalism is slightly modified: In each interaction, n_{tot} particles are produced of which two-thirds are charged particles n_{ch} and one-third are neutral particles that escape into the electromagnetic cascade. From the above it is already apparent that most particles are contained in the electromagnetic component, hence: $N_{\text{em,max}} \approx N_{\max}$. The shower maximum is still governed by the electromagnetic cascade with the modification that the cascade develops faster as the primary energy E_0 is distributed among more particles

$$X_{\max}^{\text{had}} \approx \lambda_{\text{int}} + \underbrace{X_{\max}^{\text{em}}(E_0/(2n_{\text{tot}}))}_{\sim \ln E_0}. \quad (2.4)$$

The hadronic interaction length λ_{int} accounts for the fact, that the primary cosmic ray will penetrate the atmosphere before interacting. The number of muons produced by the hadronic component is given by the number of charged particles n_{ch}^n in the generation in which they reach their decay energy E_{dec} . From this follows that

$$N_{\mu} = (E_0/E_{\text{dec}})^b, \quad \text{with} \quad b = \frac{\ln n_{\text{ch}}}{\ln n_{\text{tot}}} \approx 0.82 \dots 0.9. \quad (2.5)$$

As the energy of UHECRs is much larger than the binding energy per nucleon in a nucleus $\sim 5 \text{ MeV}$, we can approximate the behavior of a nucleus with the mass number A and

energy E_0 with that of A protons with energies $E_h = E_0/A$. Using the above-established framework one obtains the following relationships ([2]):

$$N_{\text{em,max}}^A(E_0) = AN_{\text{em,max}}^p(E_h) \approx N_{\text{em,max}}(E_0), \quad (2.6)$$

$$X_{\text{max}}^A(E_0) = X_{\text{max}}(E_h = E_0/A), \quad (2.7)$$

$$N_{\mu}^A(E_0) = A^{1-\beta} N_{\mu}^p(E_0). \quad (2.8)$$

From the above equations, a few interesting conclusions can be drawn: I) The maximum number of electromagnetic particles does not change with the mass of the cosmic ray. This is in particular interesting w.r.t. the detection of radio emission which is mostly correlated to the number of electromagnetic particles in the atmosphere and thus not with the primary particle mass. II) The depth of the shower maximum as well as the number of muons varies with the mass of the primary particle, however the effects are not linear. And III) the variation of X_{max} and N_{μ} are anti-correlated, while X_{max} decreases for heavier nuclei N_{μ} increases.

2.2.2. Radio emission

Extensive air showers induce strongly beamed electromagnetic broadband pulses into the atmosphere which can be detected by ground-based radio antenna(s). With the advent of fast digital signal processing, the detection of air showers with those radio pulses has seen a renaissance in the 21st century [49].

This section will summarize and discuss the fundamental (microscopic) description of the electromagnetic radiation in the particle cascade of air showers (Sec. 2.2.2.1) as well as the macroscopic mechanisms which are understood to shape the signal distribution of the radio emission (Sec. 2.2.2.2). Here, we only discuss the radio emission from air showers. A more comprehensive summary is given in Ref. [49]. However, in recent years the radio emission from particle cascades in dense media, i.e., arctic ice, for the detection of UHE neutrinos has become a rapidly developing field. Many current and future experiments aim to detect cosmic particles from their in-ice radio emission [50, 51, 52, 53]. The shifted paradigm for the emission of radio waves in ice instead of air is excellently summarized in Ref. [54]. A good summary of the experimental activities in the detection of UHE cosmic rays and neutrinos is given in Ref. [55].

2.2.2.1. Simulation and microscopic description of the emission of electromagnetic radiation

The radio emission from extensive air showers originates from the acceleration of charged particles in the air shower cascades. Through scattering (of air molecules) or the influence of the Earth's magnetic field, the particles constantly change their direction, i.e., accelerate. As the radiated power strongly depends on the particle charge/mass ratio, almost the entire radiation originates from electrons and positrons [49]. Mathematically this is described by the Liénard-Wichert potentials which are derived from Maxwell's equations [56]. Two formalisms exist to describe the electromagnetic radiation from those acceleration processes, the "ZHS" [57, 58] and "endpoint" [59, 60] formalism. Both are

used in different Monte-Carlo air shower simulation codes and are, under appropriate conditions, mathematically equivalent⁶ [54, 61]. Here, we only give details to the endpoint formalism which is employed by the CoREAS [56] code which is used to simulate the radio emission from inclined air shower for this work, see Chap. 4. With the endpoint formalism, the electromagnetic radiation for each charged particle is calculated at the particle's (straight) track start- and endpoints. At each of those points the electric field vector $\vec{E}(\vec{x}, t)$ for an observer position \vec{x} in the direction \hat{r} and distance R from the point of emission is given by ([60]):

$$\vec{E}_{\pm}(\vec{x}, t) = \pm \frac{1}{\Delta t} \frac{q}{c} \left(\frac{\hat{r} \times [\hat{r} - \vec{\beta}^*]}{(1 - n\vec{\beta}^* \cdot \hat{r})R} \right). \quad (2.9)$$

$\vec{\beta}^*$ is the velocity vector of a particle (in units of the vacuum speed of light c) after an instantaneous acceleration from a startpoint (corresponds to the $-$ sign) or a before an instantaneous deceleration at an endpoint (corresponds to the $+$ sign). The Δt (gives the time resolution in the simulated signal) has to be larger than the timescale over which the acceleration/deceleration process occurs. n is the refractive index of the medium at the emission point. The total radio signal from an air shower at an observer position is the superposition of the emission from start- and endpoints of all tracks respectively from all charged electromagnetic particles of the entire particle cascade. To correctly sum up the signals of all particles, the propagation delay has to be taken into account which is given by $t = t_0 + (R\bar{n}/c)$. \bar{n} is the average refractive index along the (straight) line-of-sight between emission point and observer, i.e., $\vec{l} = R\hat{r}$.

So far, the SLAC T-510 experiment is the only one that aimed for experimental verification of the two formalisms ZHS and endpoint. Within the systematic uncertainties of this experiment, both formalisms are compatible with the measurement on the level of $\approx 5\%$ to 10% [62].

The numerical calculations based on the microscopic description of the electromagnetic radiation from single particles are very successful in describing the data from air showers (for example see Fig. 5 in Ref. [63]). However, a satisfactory understanding of the radio emission from extensive air showers and its correlation with air shower observables was only achieved with the development of a macroscopic description of the mechanisms which are responsible for the radio emission measured on the ground. This development has been accompanied and accelerated by the development of analytic and semi-analytic simulation codes for the radio emission [64, 65]. In the following section, we will discuss this macroscopic description.

2.2.2.2. Macroscopic description of the coherent radio emission at ground

The dominant contribution of the radio emission is believed to originate from the deflection of electrons and positrons due to the Earth's magnetic field. Due to their opposite charges, electrons and positrons are deflected parallel respectively antiparallel to the direction of the

⁶ In fact under certain circumstances, e.g., for emission in the direction of or close to the Cherenkov angle the endpoint formalism diverges. In those cases available implementations of the endpoint formalism use a "fall-back" to the ZHS calculation [56].

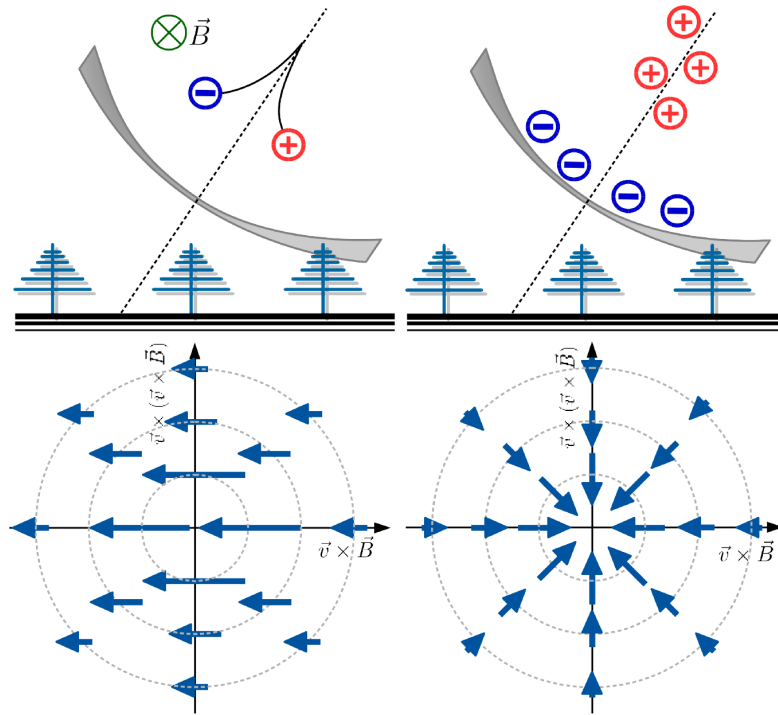


Figure 2.7.: Illustration of the two emission mechanisms, namely the geomagnetic (left) and charge-excess (right), for the electromagnetic radiation in air showers. On top a comic illustrates the macroscopic picture of an electron and positron pair creating a (time varying) current which leads to the observed emission. On the bottom the polarization pattern produced by both mechanisms is shown in a coordinate system with the x-axis pointing into the direction of the Lorentz force $\vec{v} \times \vec{B}$. Figure from [66].

Lorentz force $\vec{F}_L = e\vec{v} \times \vec{B}$ with the elementary charge e , the velocity vector of the particles \vec{v} and geomagnetic field vector \vec{B} . The early belief that those particles would travel on entire circular orbits and produce “geosynchrotron” radiation turned out to be inaccurate. In fact, the deflected particles will, depending on the surrounding air density, scatter or interact. Nonetheless, due to the deflection, a “transverse current” establishes. Due to the varying number of electrons and positrons in the shower front, the transverse current varies in time and induces a dipole-like emission with a polarization direction parallel to \vec{F}_L which is referred to as the “geomagnetic” emission. Both, the deflection by the electrons and positrons as well as the expected polarization pattern is illustrated on the left side of Fig. 2.7. It is worth highlighting, that, in fact, the time variance of the transverse current is responsible for the net emission at the ground [49].

A second mechanism that contributes to the emission at the ground is called “charge-excess” emission⁷. It is caused by a time-varying excess of negatively charged electrons in the shower front. The excess is caused due to additional electrons from the ionization of

⁷ Askaryan described this emission and the effect leading to it already in the 1961 [67], hence it is also often referred to as Askaryan emission.

the ambient air molecules and a depletion of positrons due to annihilation. The emission is linearly, inwards-radially polarized, cf. right side of Fig. 2.7.

Lastly, coherence effects shape the emission pattern at the ground. As the radio emission registered by observers is a superposition of the emission of billions microscopic emitters, the coherence of their waveforms defines the signal amplitude. As the shower front of EAS has a thickness of a few meters, coherence is generally conserved for signals below $\lesssim 100$ MHz (i.e., if the wavelength of the signals is of the same order as the shower front thickness). However, for a refractive atmosphere, the emission radiated under a specific direction, i.e., the Cherenkov angle, during the entire longitudinal development of the shower, arrives almost simultaneously respectively strongly temporally compressed at an observer. This improves the coherence within the radio pulse and increases the signal amplitude. This imprints the so-called Cherenkov ring into the emission pattern around the shower axis. A more qualitative and quantitative description of the Cherenkov ring as well as the superposition of geomagnetic and charge-excess emissions is given in Sec. 4.2. The temporal compression at the Cherenkov ring should not be confused with direct Cherenkov emission (in the radio regime) which in principle also exists but is too faint to be detectable [54]. Therefore, one can speak for the Cherenkov ring of an “Cherenkov-like” effect [49].

The temporal compression at the Cherenkov ring allows the detection of the radio emission from air showers (or in other media) at much higher frequencies than what is given by the aforementioned coherence criterion.

3. Detecting Extensive Air Showers with the Pierre Auger Observatory

The Pierre Auger Observatory is a (multi) hybrid-detector dedicated to the study of ultra-high-energy cosmic rays from the observation of extensive air showers. It is the world's largest observatory of its kind and, at present, features two large-aperture instruments. A *Surface Detector* (SD) array comprising 1600 *water Cherenkov detector* (WCD) stations on a hexagonal grid with a 1.5 km spacing which covers a total area of about 3000 km², and a *Fluorescence Detector* (FD) which consists of 24 optical telescopes situated at 4 sites overlooking the SD [3]. Figure 3.1 (left) shows a map of the observatory. It is located in the West of Argentina near the city of Malargüe (35.0° to 35.3° South, 69.0° to 69.4° West) on a high, flat mountain-plateau in the Andes called Pampa Amarilla at an altitude of around 1420 m above sea level. The site has a mass overburden of about 860 g cm⁻², the local geomagnetic field vector has an inclination and strength of -36° respectively 0.24 G.

Since its completion in 2008, the observatory has been continuously extended with smaller-scale devices to enhance its capabilities. The three *High Elevation Auger Telescopes* (HEAT) are co-located to the FD site Coihueco and observe the sky over the observatory at a higher elevation, thus being able to detect more shallow, i.e., less energetic, showers. The surface area in the HEAT field-of-view is instrumented with 61 additional WCDs on a denser 750 m spacing (SD-750), lowering the energy threshold for the SD. In parts of the 750 m-array, the *Auger Muon and Infill Ground Array* (AMIGA) allows accurate measurements of the pure muonic shower component with 30 m² buried scintillator panels (which are shielded from electromagnetic particles through 2.3 m of soil). Within the SD-750 is also an even denser subarray with a spacing of 433 m, SD-433, which lowers the energy threshold of the observatory further. The *Auger Engineering Radio Array* (AERA) comprises more than 150 dual-polarized radio antennas installed on an area of about 17 km². It has measures vertical air showers in coincidence with the SD in the energy range between $\sim 10^{17}$ eV to $\lesssim 10^{19}$ eV.

To accommodate the needs of an evolving science case and provide more mass-sensitive data at energies above 4×10^{19} eV, the observatory is currently undergoing a substantial upgrade. The upgrade aims to enhance the mass sensitivity with the measurements of the SD. The AugerPrime Upgrade comprises the installation of a 3.84 m² plastic scintillator panel on top of 1400 WCDs [5] and 1661 dual-polarized radio antennas above each WCD. With these upgraded detector stations, mass sensitivity is obtained through the separation of the muonic and electromagnetic shower components, cf. Sec. 2.1.2. The scintillator panels of the *Surface Scintillator Detector* (SSD), in combination with the WCDs, will exploit their different responses to muons and electromagnetic particles [69]. However, with increasing zenith angle, the size of the scintillator panels, projected into the shower frame, decreases. Hence, the SSD loses sensitivity for more inclined air showers with zenith angles

3.1. The Fluorescence Detector

The Fluorescence Detector detects faint fluorescence light emitted isotropically during the relaxation of air molecules that were excited by air shower particles. At 4 sites, each equipped with 6 telescopes, the FD observes the night sky over the SD. In Fig. 3.1 (left) each FD site and the field-of-view of each telescope is highlighted. The operation of the FD is restricted to fair weather, moon-less nights which limits its duty cycle to $\sim 14\%$ [3]. The observation of the fluorescence light allows for reconstructing the longitudinal development of air showers. The detected light curves describe the energy deposit of (mostly) the electromagnetic particles in the shower front and can be analytically described with the Gaisser-Hillas function [75]. An example light curve is shown in the top-right corner of Fig. 3.2: a clear maximum that coincidences with the shower maximum is visible which allows for reconstruction of the depth of the shower maximum X_{\max} . From the integration over the light curve, the calorimetric shower energy E_{cal} can be reconstructed. From E_{cal} the absolute shower energy E_{FD} is obtained by adding the “invisible” energy, i.e., the energy carried away by high energy muons and neutrinos, which is of the order of $\sim 12\%$ [76]. E_{FD} can be determined with relatively small systematic uncertainty. In particular, it is mostly independent of hadronic interactions at the highest energies, of which our knowledge is insufficient, cf. Sec. 2.2. The systematic uncertainty is dominated by uncertainties in the detector calibration and atmospheric conditions. Hence, the operation of the FD and the reconstruction of its data requires continuous calibration and atmospheric monitoring efforts [77]. Detailed studies yield an estimation of the systematic uncertainties of 14% on the reconstructed energy E_{FD} [3] and $< 10 \text{ g cm}^{-2}$ on X_{\max} [12]. The resolution on the energy is between 7.6 % to 8.6 % [78]. The resolution in X_{\max} depends on the energy: Below 1 EeV the resolution is about 25 g cm^{-2} , and improves to 15 g cm^{-2} for energies above 10 EeV [12]. The FD-reconstructed shower energy is used to cross-calibrate the SD (cf. Sec. 3.2.4 and Fig. 3.3 right) and thus the SD inherits the energy scale of the FD with its uncertainties.

3.2. The Surface Detector

The Surface Detector measures the Cherenkov-light emission from air shower particles which are passing through each of the 1600 water-Cherenkov detector stations. The WCD are located on a hexagonal grid with an equidistant spacing of 1.5 km and cover an area of roughly 3000 km^2 (cf. Fig. 3.1 left).

3.2.1. Station design

Each WCD station consists of a large, cylindrical water tank that hosts 12 000 l of purified water. The water tank has a diameter of 3.6 m and a height of about 1.6 m^1 . A picture of, an already upgraded, SD stations including WCD, SSD-panel, and RD-antenna is shown in Fig. 3.1 (right). The water tanks consist of a light-tight and UV-resistant polyethylene (plastic) which is capable to withstand the harsh environmental conditions of the Pampa

¹ The water level reaches a height of around 1.2 m.

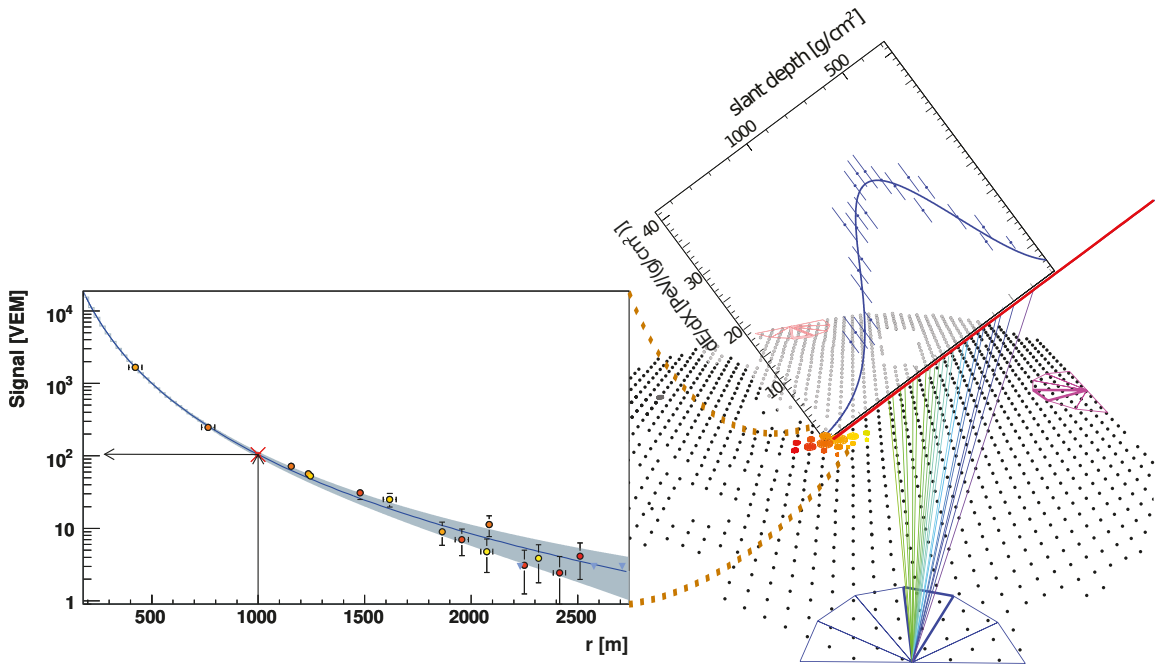


Figure 3.2.: Illustration of the hybrid detection of an extensive air shower with the SD and FD. The SD samples the lateral particle profile at ground (*left*), and the FD samples the longitudinal energy deposit in the atmosphere (*top right*).

and provides sufficient rigidity for people to stand on top of it² [79]. The water is contained in a sealed liner with a reflective inner surface which improves the light yield from passing air shower particles through reflection. This light is collected by three 9" photomultiplier tubes (PMT) installed at the top of the tank facing downwards. A significant advantage of this detector design is the uniform exposure for particles arriving from the whole sky. In addition, each WCD has a GPS receiver, communication antenna, onboard electronics for triggering and data acquisition³, and a 24 V power system which allows the WCD stations to run autonomously with a duty cycle of almost 100%. In the context of the AugerPrime Upgrade, also the station onboard electronic is upgraded: the *Unified Board* (UB) is replaced with the *Upgraded Unified Board* (UUB) which allows handling data from the additional detector components of the SSD and RD. The UUB provides all necessary information, triggers and GPS timing, as well as power to the RD frontend electronic.

3.2.2. Trigger concept

The SD trigger concept is of importance in the context of this work, as the RD will be triggered by the WCD stations⁴. The SD employs a hierarchical trigger concept with 3 different triggers (T1 - T3) being computed in real-time. The first two trigger stages, T1 and T2 are formed independently on each detector station. Based on the T2 information from all stations, considering spatial and temporal coincidence, an array trigger T3 is

² A fact, I have convinced myself about personally.

³ Collecting and transmitting air-shower data as well as monitoring data.

⁴ In the future, the implementation of a hybrid trigger using the information of the WCD and RD is possible.

formed. If the criteria for a T3 are met, data from stations with a T1 and T2 are requested and stored [80].

The purpose of the T1 and T2 is to reduce the number of registered signals in each detector station, which is dominated by atmospheric background muons passing through the detector at a rate of ~ 3000 Hz, to a sufficiently low rate of ~ 20 Hz (T2) which can be sent to the *Central Data Acquisition System* (CDAS) [80]. By dividing the station-level trigger into a T1 and T2 trigger one can record more data (all T1 and T2's) (and thus maintain a lower energy threshold) while fewer trigger information (only T2's) are sent to CDAS for a T3-decision⁵. Once a T3 trigger occurs, the data for all T2 stations and all T1 stations within 6 crowns⁶ of a T2 station and $30 \mu\text{s}$ from the T3 event time⁷ is requested and stored. The resulting rate of T3 events is ~ 0.03 Hz. Also, an FD trigger initiates the request for SD data. For very included air showers, two individual T3 may be formed for the same shower. If that happens both T3 events are later merged (off-line). Two additional triggers, T4 and T5, formed in an off-line reconstruction, are explained in the next section.

3.2.3. Event reconstruction

The WCD signal processing, calibration and reconstruction is described in detail in Refs. [82, 83]. The recorded signals are converted into units of *Vertical Equivalent Muon* (VEM), i.e., the signal a 1 GeV vertical through-going muon produces.

The attenuation of the electromagnetic particle cascade in the atmosphere as well as the magnetic deflection of muons greatly affects the particle distribution at the ground and thus is the signal distribution measured by the SD at higher zenith angles. Hence, different reconstruction algorithms are needed to describe the particle footprint for vertical and inclined air showers (with zenith angles below and above 60° respectively). Here, we only summarize the vertical reconstruction [83]⁸ in few words and give more attention to the inclined reconstruction [84].

With the reconstructed WCD signals, two additional trigger conditions, T4 and T5 are defined off-line. To satisfy a T4, the reconstructed signal arrival times need to agree with a plane shower front moving with the speed of light. The details are different for vertical and inclined air showers. For the latter, at least 3 nearby triggered stations need to be compatible with a shower front. Accidentally triggered stations (i.e., from random coincidence muons) are removed in an iterative “top-down selection” if their signal arrival times are not compatible with a shower front fitted to all other stations. An event is assigned with a T5 (also referred to as 6T5) if the air shower falls within the array for which the nearest WCD station and all 6 neighboring stations (first crown) were active at the time (that does not mean they have to be triggered). Also, here vertical and inclined air showers are treated differently: For a vertical shower, the condition is met if the “hottest” station, i.e., the station with the largest VEM signal, has 6 active stations around it. Due

⁵ Sending T2's occupies already around half of the bandwidth of 1200 bits per second [3].

⁶ Crowns refer to hexagons around a central station. The first crown comprises the 6 neighboring stations at a distance of 1.5 km, the second crown, which envelopes the first crown, already contains 12 stations with varying distances to the central station, and so on, cf. [81, Fig. 4.3]

⁷ Estimated from all T2 stations.

⁸ We refer to the *Observer* reconstruction detailed in this reference.

to the symmetry in the particle profile of vertical showers, this is sufficient to judge that the shower falls within an area of active stations. For inclined air showers, which imprint highly asymmetric particle profiles, this simple association is not possible. Hence, the reconstructed shower core position (explained below) is used to identify the nearest station.

As the first step in the reconstruction, the arrival direction of the air shower is reconstructed. From the T4 trigger decision, the arrival direction assuming a plane wavefront is already known. For improved accuracy (w.r.t. a plane shower front reconstruction), a spherical model to describe the shower front is used for inclined air showers. This model predicts the signal arrival time at each station from the distance between them and a point-like source. The accuracy of this reconstruction was derived from MC [84] and in a data-driven analysis [85] to be better than 0.5° .

On the left side in Fig. 3.2 the lateral signal distribution for a vertical air shower measured by the SD is shown. The signal of each WCD is expressed in VEM. To describe the signal distribution a (rotationally symmetric) lateral distribution function (LDF) is used. The shape of this LDF has been parameterized with a high-quality set of measured, well-sampled air showers. Because the shape is parameterized, only the parameter S_{1000} defined as the signal amplitude at a lateral distance of 1000 m is fitted⁹. S_{1000} is found to be correlated with the air shower energy and therefore is called “shower size”. With the constant intensity cut method, a zenith angle dependency on S_{1000} due to atmospheric attenuation is removed, and the shower size is converted into S_{38} [83]. This reconstruction is found to be fully efficient for vertical air showers with energies above 2.5×10^{18} eV. The resolution of the shower size is estimated from data and MC to be on the order of 15% at the lowest energies and 6% to 7% at the highest energies [19].

The particle footprint from inclined air showers is dominated by muons. The large geometrical distance between the shower maximum and the detector causes a significant magnetic deflection of the muons resulting in highly asymmetric footprints. An example of a simulated muon density profile from a very inclined air shower is shown in Fig. 3.3 (left). To describe the particle profile from inclined air showers, two-dimensional “muon-density maps” $\rho_{\mu,19}(\vec{r}, \theta, \phi)$ are constructed from simulations of proton-induced air showers with a primary energy of 10^{19} eV. They describe the mean muon density as a function of the position in the shower plane \vec{r} and air-shower arrival direction θ, ϕ . The maps were produced using CORSIKA with the high-energy hadronic interaction model QGSJetII-03 [33]. The WCD do not measure the muon density directly but the all-particle flux at the ground (in units of VEM). To convert this to a muon density two steps are needed: First, a (simulation-derived) correction factor (\equiv the zenith-angle and lateral-distance dependent ratio between the WCD signal from the electromagnetic and muonic component) for a remaining, non-negligible electromagnetic particle component is applied [84, Fig. 6]. Second, the parameterized WCD-response for an arbitrary number of muons is used to convert the corrected WCD signals into a number of penetrating muons and with the known size of the WCD to a muon density. With that, the muon density measured in each WCD ρ_{μ}^{meas} can be described by the muon-density map and a scaling factor N_{19} :

$$\rho_{\mu}^{\text{pred}}(\vec{r}) = N_{19} \rho_{\mu,19}(\vec{r}, \theta, \phi). \quad (3.1)$$

⁹ The parameterization depends on the zenith angle as well as on S_{1000} .

In a log-likelihood minimization, minimizing the difference between the measured and predicted muon densities, the scaling N_{19} and the shower core position, which governs the WCD station positions in the shower plane \vec{r} are determined. In this minimization also the arrival direction, i.e., θ and ϕ , is varied ¹⁰.

N_{19} refers to the relative number of muons in the air shower w.r.t. the number of muons in the reference maps. As the number of muons N_μ correlates with shower energy (cf. Eq. (2.5)), N_{19} serves as shower size and can be cross-calibrated with the FD-reconstructed energy¹¹. The MC-derived resolution for the reconstruction of N_{19} are above 15% for energies below 10 EeV and decrease to 5% for energies around 100 EeV. Given that N_μ varies not only with the energy but also with the primary particle mass (cf. (2.8)), inflicts a mass dependency on the energy derived from N_{19} . The reconstruction of inclined air showers (with zenith angle between 62° to 80°) is fully efficient for energies above 4×10^{18} eV [14].

Using the simulated muon-density at fixed energy and primary-particle mass as a reference implies the assumption that changing them will only change the absolute scale (i.e., N_{19}) but not the lateral shape of the maps. Furthermore, the (similar) assumption is made that the used simulations (which make use of a particular high-energy hadronic interaction model) reproduce the true shape of the muon-density profiles. It could be shown with simulations that this is true for varying primary particles, energies, and hadronic interaction models [86, 84].

With N_{19} the air shower muon content can be directly estimated. Combined with an independent reconstruction of the shower energy (from e.g., FD or RD), this allows to infer the mass(-composition) of the UHECRs (cf. Sec 2.1.2). In Chap. 9 we will evaluate the potential of coincidence measurements of inclined air shower with the SD and RD to study the mass(-composition) of the UHECRs.

3.2.4. Energy calibration

Air shower events recorded in coincidence with the FD and SD, such as the example event shown in Fig. 3.2, allow a cross-calibration between both detectors. This allows the absolute energy scale of measurements with the FD to be adapted for measurements with the SD also for events which are not detected in coincidence with the FD, for example during daytime. The cross-calibration constitutes the conversion of the shower size (S_{38} , N_{19}) which has no astrophysical relevance, to the total shower energy E_{SD} using a power law. Figure 3.3 (right) shows the correlation between the (unbiased) shower size estimator S_{38} and N_{19} for vertical respectively inclined air showers with the SD-1500 array as well as S_{35} for the SD-750 (vertical air showers only). Due to the cross-calibration, the SD-reconstructed energy inherits the systematic uncertainties of the energy scale of the FD. Without the FD, an absolute calibration of the shower size would need to rely on MC simulations and thus be subject to large theoretical uncertainties due to the insufficient understanding of hadronic interactions at the highest energies.

¹⁰ However, the thus obtained values are not stored and only the result from the shower front fit to the signal arrival times are used.

¹¹ Given that the atmosphere attenuation described by the simulation is “imprinted” in the muon-density maps, no CIC correction is needed for N_{19} .

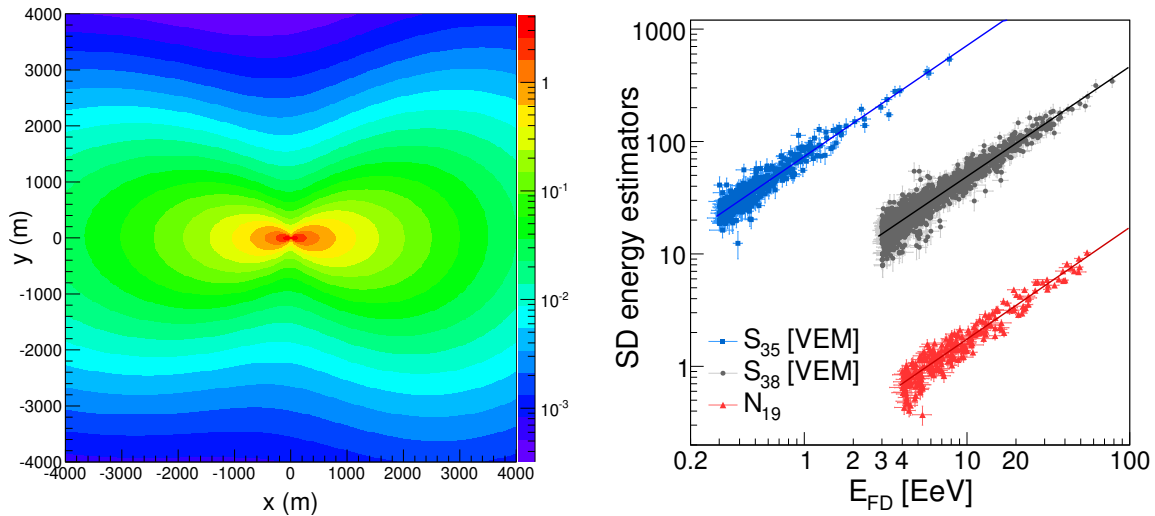


Figure 3.3.: *Left:* Contour plot of the muon density in the shower plane for a $E = 10$ EeV proton shower with a zenith angle $\theta = 84^\circ$ coming from East ($\phi = 0^\circ$), simulated with QGSJetII-03. The y-axis is oriented in the direction of the \vec{B} field projected onto the shower plane. Figure and caption adopted from [84]. *Right:* Correlation of the energy estimators S_{38} (SD-1500) and S_{35} (SD-750) for vertical air showers, and N_{19} inclined air showers, with the FD-reconstructed energy. S_{38} and S_{35} are given in VEM, N_{19} is dimensionless. Figure and caption adapted from [87].

3.3. The Auger Radio Engineering Array

The Auger Engineering Radio Array measures the electromagnetic radiation emitted by the electromagnetic shower particles in the 30 MHz to 80 MHz frequency band. It comprises more than 150 *radio-detector stations* (RDS) on an area of about 17 km². Co-located with the SD-750 array and overlooked by the Coihueco FD-site, AERA detects cosmic-ray induced air showers with energies above 10¹⁷ eV in coincidence with those detectors. As an engineering array, it has had a major role in demonstrating the application of the radio detection of air showers with (relatively) sparse autonomously operating¹² antennas for future large(r)-scale experiments [88, 71]. In this role, AERA makes use of different radio-antenna types, readout electronics, trigger concepts and is a “test-bed” for the development of various reconstruction algorithms as well. A comprehensive summary of the detector array is given in Ref. [66, Sec. 4.4]. Although designed for the detection of vertical air showers, AERA also demonstrated the ability to detect and reconstruct inclined air showers with a sparse antenna array [71], the technique which will be adopted by the RD. Studies of the muon content of those showers, measured in coincidence with the SD, are already undergoing [89], however suffer from the very limited aperture of AERA towards high-energetic inclined air showers.

Two antenna types are utilized in the majority of RDS and used for physics analyses: a *Log-Periodic Dipole Antenna* (LPDA) and an *active bowtie* called Butterfly. A picture of RDS with both antenna types is shown in Fig. 3.4 (*left* and *middle*). Each RDS has two antennas

¹² The RDS are solar-powered and most of them operate with wireless communication. However, to detect air showers they still rely on external trigger signals.

that are (orthogonally) aligned in East-West (EW) and North-South (NS) directions to allow a full reconstruction of the electric field vector (cf. Sec. 8.1.1). Furthermore, each RDS has a solar panel that powers a battery to allow operation during nights or cloudy days and readout electronics such as a *low-noise amplifier* LNA, filter-amplifier, and digitizer.

AERA was deployed in different stages and on grids with varying spacings: In 2011, 24 LPDA stations were deployed on a 144 m-spaced triangular grid. Those stations are cable-connected to a central in-field facility from which the data is sent via a direct communication link to the Coihueco FD site. In 2013, an additional 100 RDS were deployed with a grid spacing of 250 m and 375 m, this time using Butterfly antennas and wireless communication via an integrated communication antenna. Finally, in 2015, 29 Butterfly-stations on a 750 m grid completed the deployment.

Two different trigger concepts are employed in AERA. A subset of 40 RDS stations in the northeast of the array employs self-triggering, the remaining RDS are (mostly) externally triggered by the SD. The different trigger concepts mandate different onboard electronics. The external triggered RDS have a 4 GB ring buffer which allows to continuously store data for ~ 7 s for external triggers arriving with a latency. The self-triggering stations have small scintillator panels installed.

Several calibration campaigns were performed to allow an absolute energy reconstruction, similar to the FD. Those efforts comprise the calibration of the absolute gain using the omnipresent diffuse galactic emission as the reference signal [90, Sec. 6.2] [91, Sec. 4.2] as well as of the directional-dependent response pattern using a reference transmitter carried by an octocopter [92]. Those efforts inspire similar, currently ongoing efforts of the RD which are discussed in Sec. 3.4.3.

A “beacon” transmitter was installed at Coihueco which permanently transmits a reference signal at 4 frequencies between 58 MHz and 72 MHz to improve on the GPS timing¹³ of the RDS. A sub-nanosecond timing would enable interferometric reconstruction algorithms, cf. Chap. 7. The reference signal is recorded alongside the air shower signals and analyzed off-line to determine a temporal correction for each station and event. Thus drifts found in the GPS time tags can be corrected for and the overall resolution improved. An analysis of the beacon signals from commercial aircraft yield a timing resolution of the order of 2 ns [93].

In AERA also several *Short Aperiodic Loaded Loop Antennas* (SALLA) were deployed next to the aforementioned antenna types to study their performance and to cross-calibrate the antennas [94]. The SALLA antenna will be used for the AugerPrime Upgrade. A picture of one of these AERA-SALLAs is shown in Fig. 3.4 (right) next to a RD prototype antenna on top of a WCD.

3.4. The AugerPrime Radio Detector

The AugerPrime Radio Detector will detect inclined air showers with zenith angles above $\sim 65^\circ$ and energies above $\gtrsim 4 \times 10^{18}$ eV from radio pulses in the 30 MHz to 80 MHz frequency band. In coincidence with the SD, it will extend the aperture and sky coverage for mass-sensitive measurements of AugerPrime. With the installation of a dual-polarized SALLA

¹³ The timing accuracy from the GPS time-tagging is of the order of 5 ns to 10 ns.



Figure 3.4.: Pictures of 3 AERA antenna stations, each with a different radio antenna (from left or right): LPDA, Butterfly, (AERA-)SALLA. For LPDA and Butterfly the sensitive antenna elements are highlighted in blue.

antenna on top of each WCD station, the RD will be the world's largest radio detector array for the detection of UHECRs. With an instrumented area of about 3000 km^2 it will eclipse current experiments by 2 orders of magnitude.

The ability of the RD to detect and reconstruct inclined air showers and the study of the scientific potential of coincidence detections with the SD is the primary focus of this work. In Chap. 8, we perform a reconstruction of (simulated) inclined air showers detected with the RD using a signal- and reconstruction model developed in Chap. 6. In Chap. 9, we evaluate the potential to study the mass composition of UHECRs with the RD and SD and outline the capability of event-by-event mass discrimination.

The RD will make use of the existing infrastructure of the Pierre Auger Observatory and its Surface Detector which allow a very fast and cost-effective realization of the entire project. More details about the station design and integration into the SD are described in Sec. 3.4.1. A description of the currently operated engineering array (RD-EA) and the first results of the analysis of its data are given in Secs. 3.4.2 and 3.4.3.

3.4.1. Station design

The SALLA has two circular dipole elements which are connected via a resistor at the bottom and LNA at the top from which the signals are readout. The particular design including the resistor yields a wideband sensitivity adequate to measure the emission of air showers in the tens to a hundred MHz [95]. It also defines its directional sensitivity pattern. Due to the resistor mounted at the bottom, the antenna is relatively insensitive to reflected signals from beneath. Furthermore, the SALLA has a high(er) relative sensitivity towards signals coming with a zenith angle larger 60° (w.r.t. the other antennas employed at Auger) [96, Fig. 16]. In addition, the antenna is easy to manufacture and transport, and its design is lightweight and robust. Hence, the SALLA combines several favorable characteristics for the application in the RD.

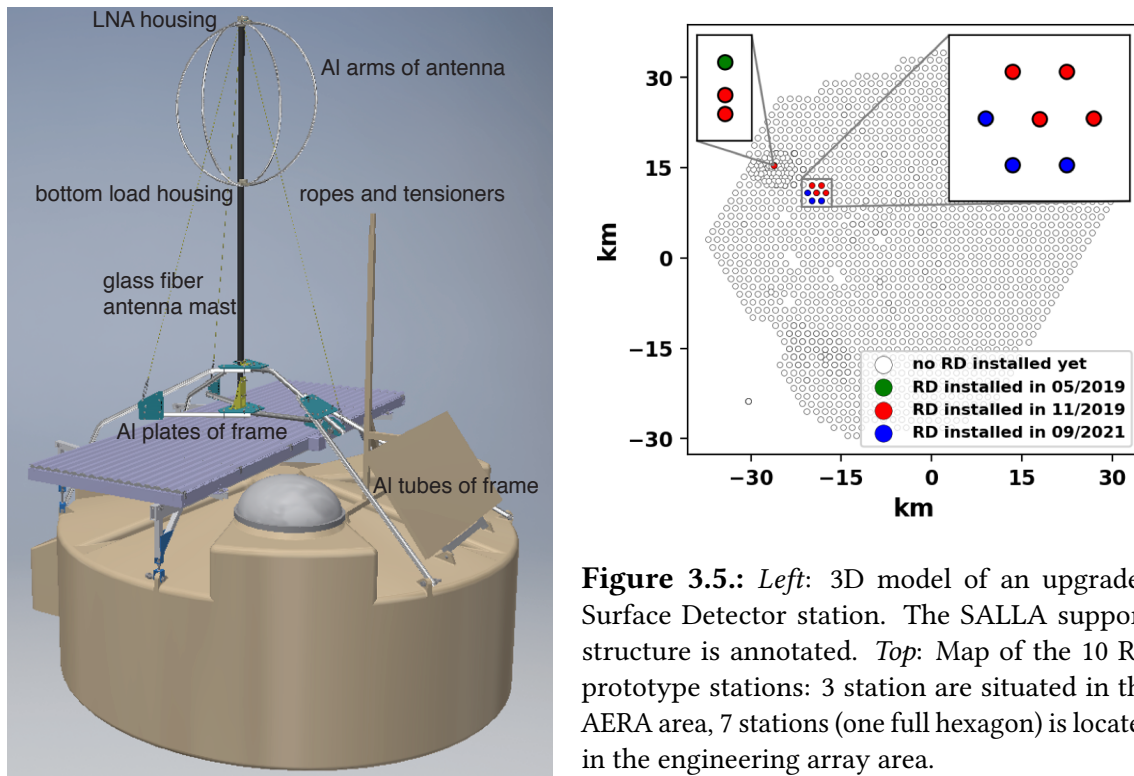


Figure 3.5.: *Left:* 3D model of an upgraded Surface Detector station. The SALLA support-structure is annotated. *Top:* Map of the 10 RD prototype stations: 3 stations are situated in the AERA area, 7 stations (one full hexagon) is located in the engineering array area.

Due to the resistor, only $\sim 10\%$ of the captured signal intensity is available at the input of the LNA [96]. Hence, adequate amplification is needed. Nonetheless, electronic noise is expected to be significantly lower than the omnipresent galactic background [95], cf. Sec. 3.4.3. Other advantages of the SALLA are a minimal group delay and pulse distortion [96]. The antenna was originally developed in the context of AERA [96] and later deployed at the Tunka-Rex experiment [97]. The antennas which will be employed in the RD were optimized for a better signal-to-noise ratio for air shower signals and better sensitivity to the diffuse galactic emission. In particular, the radius of the dipole elements was increased, the resistor load decreased, and the LNA design replaced [98].

The SALLA dipole elements are half-circuit tubes with a diameter of 1219 mm. The elements are made of aluminum with an oval cross-section with a thickness varying from 17 mm to 20 mm. Each antenna element has to be flat with a tolerance of 2 mm, their diameter is within a tolerance of ± 3 mm¹⁴ [100]. Each RD station will have 2 antennas (\equiv channels) which are aligned in EW and NS and connected to the same LNA and resistor which are protected by UV-resistant, injection-molded housings. Two diodes at the signal input, protect the LNA from lightning [101]. The LNA achieves the amplification and impedance matching between the antenna circuit and readout system with two 100 nH inductors and a 9:1 RF transformer. The resistor has a load of 392Ω and 240 nH [98]. The LNA and resistor housings are connected to a glass-fiber mast. Within the mast, a 6 m coaxial cable connects the antenna with the station electronics. Along the cable, 5 ferrites are installed to reduce the effect of the cable onto the antenna sensitivity. The mast is

¹⁴ Specification for the manufacturer. All aluminum parts, including the antenna elements, are produced by the company Giezen [99].

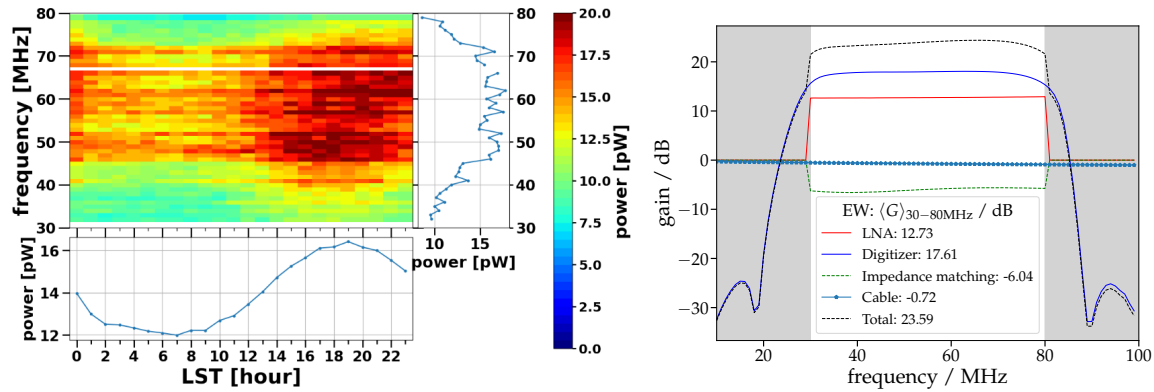


Figure 3.6.: *Left:* Spectral power of data recorded with a RD-EA station containing the diffuse galactic emission. The panel on the bottom shows the integrated power over all frequencies as a function of the *local sidereal time* LST while the panel on the right side shown the power as a function of the frequency integrated over the time. The modulation of the power as a function of the LST is from the transient galactic center and can be used for an absolute calibration. Figure from [102]. *Right:* Frequency-dependent response of the different components of the signal-processing chain in dB.

connected to an aluminum support structure which is fixed to the WCD tank at 3 points. Additional tension-wires connect the upper part of the mast with the base of the aluminum structure to reduce oscillation of the mast and antenna. The support structure and mast provide sufficient flexibility to correctly align the antenna w.r.t. the horizon and correct for eventual tilts of the tank and the ground surface respectively. An accuracy of 1° in the vertical alignment (w.r.t. the zenith) is needed. A 3D model of the mechanical structure of the entire upgraded station is shown in Fig. 3.5.

The shielded coaxial cable feeds the signal into the RD-frontend board which features a filter-amplifier, digitizer, and FPGA. The filter-amplifier enhances the signal in the 30 MHz to 80 MHz band with 17.6 dB, see Fig. 3.6 (*right*). The digitizer samples the amplified signal with 250 Ms per second and 12 bits. The data sent to CDAS for each antenna has a length of 2048 samples or 8192 ns. The frontend board is connected to the UUB via a digital extension port. From the UUB the RD-frontend board receives the trigger signal, power, and GPS timing. When a trigger occurs, RD data are sent via the UUB to CDAS alongside the data from WCD and SSD.

3.4.2. Engineering Array

In November 2019, an engineering array (RD-EA) with ten mechanical antennas was established at two locations at the observatory. A map of the RD-EA is presented in Fig. 3.5 (*top*), the color code refers to the installation dates of the read-out electronics. Seven antennas were also equipped with read-out electronics. Out of those, four stations were used to record air shower signals (those installed on a complete hexagon). In September 2021, the read-out electronics of all stations (including those which previously have had no read-out electronics) was updated.

The objective of the RD-EA is two-folded: Evaluate the durability and robustness of the mechanical and electronic parts in in-situ conditions, and, validate the functioning and performance of the components. For the latter, two questions are of particular interest: “Do we, unambiguously, measure air shower signals in coincidence with the SD?” and “Can we observe the sidereal modulation of the omnipresent diffuse galactic background emission?”. In Ref. [102], first data from the RD-EA were analyzed: Both, air shower signals and the galaxy emission were unambiguously detected by the SALLA antennas. As an example, Fig. 3.6 (*left*) shows the power of the galactic emission as a function of the local sidereal time and frequency as recorded by one of the RD-EA stations.

Furthermore, the RD-EA stations record ambient background noise which can be exploited in this work (Chaps. 8 and 9) to obtain a more realistic “picture” for future measurements of real events with the RD. More details on this are given in appendix D.2.

3.4.3. Calibration & Monitoring

The measurement of the diffuse galactic emission is of particular interest because it can be used to estimate the sensitivity of the RD stations and perform an absolute calibration by comparing the measured power with that of reference models. A preliminary calibration is performed in Ref. [102] and used later in this work to describe the absolute sensitivity of the RD, cf. Chap. 8. The frequency-dependent responses of the different components of the signal-processing chain as configured in Offline and used in Chaps. 8 and 9 are shown in Fig. 3.6 (*right*). The response of the LNA and impedance-matching are only given in the RD design frequency range of 30 MHz to 80 MHz (the real components have a non-zero response also outside this bandwidth). It should be noted that the hardware description of the RD is currently being refined (i.e., measurements or simulations of the responses of different components are updated). The description used in this work is the same as for the calibration in Ref. [102] but does not correspond to the most recent description, i.e., new measurements or better calculations of the response of single components are now available. However, applying the calibration (obtained with the same description) should mitigate any effects on the absolute sensitivity.

Besides the absolute gain/sensitivity of the antenna, its (relative) direction-dependent sensitivity “response pattern” is crucial for the reconstruction of air showers. Currently, extensive efforts are underway to properly simulate [103] and measure [104] this response pattern. In Fig. 3.7 a model of the SALLA antenna with WCD and SSD for the simulation code NEC-2 [105] is shown¹⁵.

For continuous monitoring of the diffuse galactic emission and state of the antenna, the FPGA in the RD-frontend board will be processing data which are sent via a 400 s-periodic monitoring data-stream. Currently, a fast Fourier-transformation algorithm is being developed to obtain, among other parameters, stacked histograms of the galactic emission in the frequency domain [106] for the galactic calibration.

¹⁵ Also, this model has been updated in the meantime featuring a hexagonal WCD model and more “wire”-elements for the SALLA. Note, that those changes to the directional-dependent SALLA response might not be completely compensated by the applied absolute calibration as measurements of the diffuse galactic emission are insensitive to small-scale angular changes of the directional response.

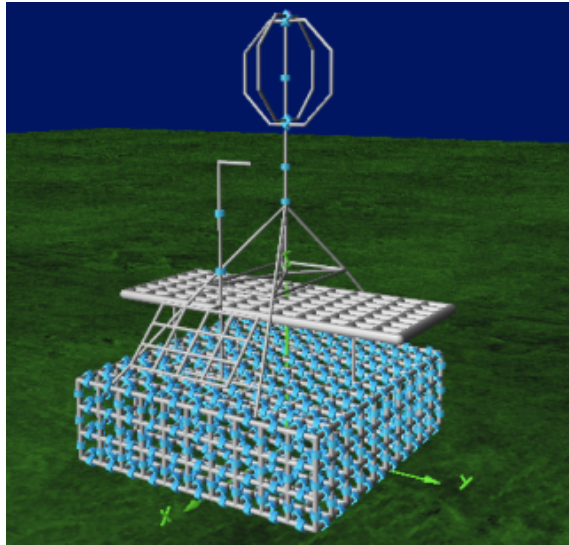


Figure 3.7.: NEC-2 model for the SALLA (including the WCD, SSD and RD-support structure) used in this work.

3.5. The Offline simulation and reconstruction framework

The Offline software package is the official Auger simulation and reconstruction framework [107]. It allows processing recorded and simulated data and simulations from all sub-detectors of the observatory. Its main purpose is the reconstruction of measured or simulated air shower events. For simulated events, it provides completed detector simulations of all Auger sub-detectors. Offline allows the read-in from various data formats for both, measured and simulated data. It provides its own data format which allows for storage of “intermediate” results to file and continuation of the detector-simulation/event-reconstruction in a subsequent run as well as a lightweight and standalone data format for high-level analysis *ADST*.

In Offline, the various simulation and reconstruction procedures are performed by *modules*: Each module serves a particular purpose, for example, the simulation of the directional response of the employed radio antenna or the reconstruction of the shower arrival direction. This allows an easy exchange of modules with similar purposes but different implementations. A specific application, e.g., the reconstruction of inclined air showers with the SD or a detector simulation of the RD, is defined by a *ModuleSequence* which chains together various modules. The configuration of each module and the detector is (mostly) supplied with static XML files. To execute Offline a user has to provide a *bootstrap.xml* which contains *configlinks* to the required configuration files (such as a *ModuleSequence.xml*). For time-dependent information, such as detector configuration or atmospheric conditions an interface for SQL databases is provided.

Internally Offline features two major data structures: the *Event* which hosts all recorded data as well as reconstructed observables and the *Detector* which hosts the (time-dependent) description/characteristics for each sub-detector as well as the atmosphere.

The functionality for the analysis of radio data with $\overline{\text{Offline}}$ is described in Ref. [108]. In chapter 8 the rich functionality of $\overline{\text{Offline}}$ is used to perform a complete detector simulation and event reconstruction for the RD. More details are given in that chapter.

Part II.

Inclined Extensive Air Showers

4. Simulation of the radio emission from inclined air showers

Parts of this chapter have been published in:

F. Schlüter and T. Huege

"Signal model and event reconstruction for the radio detection of inclined air showers"
[arXiv:2203.04364](https://arxiv.org/abs/2203.04364) (Publication to JCAP in process)

Simulations of extensive air showers are a vital tool in high- and ultra-high energy astroparticle physics. Many applications rely on those simulations: The development of signal models and reconstruction algorithms, the direct reconstruction of air shower observables (by comparing the measured signals with the ones predicted by simulations) as well as the interpretation of measured data. In this work, we use those simulations to study the nature of the radio emission in detail, to develop and evaluate reconstruction algorithms for the radio detection of inclined air showers, and to study the performance of the AugerPrime Radio Detector.

The simulations predict the signatures of air showers which are measurable with different detector techniques. For example, air shower simulations predict all particles reaching the ground which are measured by particle detectors, or they predict the energy deposit of air shower particles in the atmosphere from which one can estimate the fluorescence light which is registered by fluorescence telescopes. Of particular interest in the context of this work is the prediction of the radio emission on the ground which is emitted by electromagnetic particles during the air shower development and measured by radio antennas.

We use fully numerical, so-called Monte-Carlo (MC), algorithms to predict the full cascade of secondary particles in the atmosphere and calculate the emission and propagation of the electromagnetic radio emission. Although those algorithms require considerable computing resources, their accuracy is superior compared to analytic or semi-analytic approaches to simulating extensive air showers.

For the simulation of the cascades of secondary particles, we use the CORSIKA code [46] which was developed at KIT and is the de-facto standard for air shower simulations in the astroparticle physics community. The emission and propagation of the electromagnetic radiation from the secondary electromagnetic shower particles is computed by the "Corsika-based Radio Emission from Air Showers" CoREAS code [56]. CoREAS uses the "endpoint" formalism [59, 60] to calculate the electromagnetic radiation of each electron and positron in the particle cascade. From the point of emission, the electromagnetic radiation is

propagated to predefined observer positions at ground¹. In chapter. 5 of this work, the propagation of the electromagnetic emission in CoREAS is discussed in more detail.

An alternative to CORSIKA and CoREAS are the simulation codes AIRES [109] for the simulation of the particle cascades and ZHAireS [110] for the prediction of the radio emission. In ZHAireS, the radio emission is simulated using the “ZHS” algorithm [57, 58]. It has been shown, that the prediction of the total radio emission from both codes is in agreement on the level of $\sim 5\%$ [111].

One crucial paradigm change when it comes to the simulation of the radio emission from air showers w.r.t. the simulation of, e.g., the particle content at the ground, is the requirement to pre-define the positions at which the radio emission is predicted. The radio emission registered at a specific position is the coherent sum of the emission radiated from all electrons and positrons during the entire development of the particle cascade. The relative arrival timing of emissions at an arbitrary observer position has to be recalculated for each position. Hence, the number of observers for which the summed emission can be predicted is limited due to computational constraints as the propagation of the radio emission from one source location to each observer position requires a significant amount of the overall computing time. Another important consequence of this is, when aiming to simulate a realistic detector layout, each simulation is associated with a particular air shower position within the detector array. It is not possible to place the shower at arbitrary positions as it is possible when only looking at the particle content of the air shower.

In the following, we give details about the CORSIKA/CoREAS simulations generated in the context of this work. In particular, we will describe the different simulation sets which are used in this work to study the radio emission from inclined air showers and the performance of the RD. Additional simulations serving particular purposes are introduced in the following chapters (e.g., Chap. 6 and 7) as well. In Sec. 4.2 we give a qualitative description of the 2-dimensional lateral signal distributions of the radio emission from inclined air showers at the ground. We conclude this chapter with two studies of the nature of the radio emission from inclined air showers.

4.1. CoREAS simulations of inclined air showers

In the context of this work, we generated many sets of simulations, each of them addressing a different objective. In general, they can be categorized into two categories of simulations: The first category contains air showers simulated with unrealistic settings, e.g., with an unrealistic detector array layout. The most prominent example for this, are simulated air showers with observers situated on a dense, star-shaped antenna grid centered around the air shower impact point at the ground. The air shower impact point at the ground is defined as the intersection between the primary particle trajectory and the observation plane. It is commonly, and also in this work, referred to as “shower core”. Also, the air shower parameters, i.e., their arrival directions and energies, do not necessarily reflect what is expected in nature. The second category comprises simulated air showers with (more) realistic settings, e.g., with a realistic, sparse detector layout and an arrival direction

¹ In fact the position of the observers can be arbitrarily chosen, observers “floating” in the air are possible. However, typically we are interested in the radio emission at the ground.

distribution, which corresponds to what is expected for actual air shower events. Those simulations are used to validate the developed reconstruction algorithms and test their performance.

All simulations were performed with settings matching the ambient conditions at the Pierre Auger Observatory. This comprises the atmospheric conditions, the strength and orientation of the Earth’s magnetic field, and the observation level, i.e., the altitude or height above sea level of the plane at which the particle content of the cascade is stored and the radio observers are typically situated². The atmospheric conditions describe the atmospheric density- $\rho(h)$ and refractive index $n(h)$ profiles. The density profile is described with a 5-layer parameterization. The first four layers are described with exponential dependency between the density and the altitude, the fifth layer uses a linear function. In this work, unless specifically mentioned otherwise, we use the same profiles available in CORSIKA/CoREAS from a python implementation [112] or within `Offline`. The refractive index profile is determined by $\rho(h)$ and the refractive index at sea level $n_0 = n(0)$ via the Gladstone-Dale law:

$$n(h) = 1 + (n(0) - 1) \frac{\rho(h)}{\rho(0)} \quad (4.1)$$

with the refractivity being defined as $N(h) = n(h) - 1$. Of course, in reality, the atmospheric conditions over the Observatory are constantly changing, however, it is possible to accurately describe the average conditions on a monthly basis [113]. The strength and orientation of the magnetic field are also changing with time, however, the timescale for significant deviations is large. Nonetheless, the orientation will change for changing air shower positions within the Auger array. The observation level for all our simulations is at 1400 m a.s.l.

To simulate air showers for this work, we have used several, only slightly varying, versions of CORSIKA/CoREAS from v7.69 to v7.74 which all utilize pre-calculated tables of the integrated refractive index to speed up the simulation of propagation of the radio emission in inclined air showers (in the context of this work a python implementation of these tables were added to [112], more details are given in the appendix C.1). In all simulations, the low-energy hadronic interactions were calculated using UrQMD [114]. To calculate the high-energy hadronic interactions we use QGSJetII-04 [115] or Sibyll-2.3d [34, 116]. We chose these two models (over the third post-LHC model EPOS-LHC), as their predictions for X_{\max} and number of muons represent the extremes among those models, cf. Fig. 2.2 (left) for X_{\max} . For the simulation of the particle cascades, an electron multiple-scattering-length factor³ of 1 was used. It has been reported that lowering this parameter to 0.05 increases the total emitted radiation energy by 11% regardless of the zenith angle and energy [111]. Furthermore, we use particle-“thinning” [117] for the simulation of the particle cascades: Particles that are produced in an interaction with an energy below a threshold energy E_{th} are discarded and only a single particle remains in the simulation. This particle is assigned an appropriate *weight* w to describe the assembly of particles it “replaces”. If the weight exceeds a certain maximum w_{\max} , two or more particles

² Although, as mentioned, this can vary according to the purpose of the specific simulations.

³ CORSIKA keyword STEPFC.

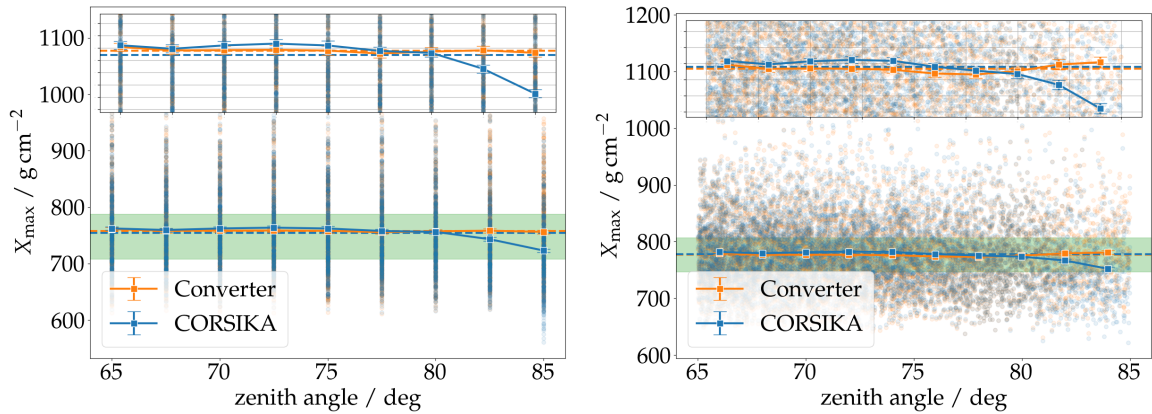


Figure 4.1: X_{\max} distributions as a function of the zenith angle from 2 different simulation sets (left with binned arrival directions and right with continuously distributed arrival directions) and with X_{\max} determined by CORSIKA (blue) or with a Gaisser-Hillas fit outside of CORSIKA (“Converter”, orange). The markers show $\langle X_{\max} \rangle_{\theta}$, the error bars indicate the uncertainty on the mean, i.e., σ/\sqrt{n} . The $\langle X_{\max} \rangle$ (for all zenith angles) is indicated by the dashed lines. The inset shows the range around $\langle X_{\max} \rangle$, the y -axis grid lines are separated by 10 g cm^{-2} . The $\langle X_{\max} \rangle_{\theta}$ from CORSIKA shows clearly an unexpected correlation with the zenith angle.

are kept in the cascade and the total weight split among them. For our simulations E_{th} and w_{max} are set relative to one parameter ϵ_{thin} : E_{th} resp. $w_{\text{max}} = E_0 \epsilon_{\text{thin}}$ with E_0 being the energy of the primary particle⁴. We generate simulations with ϵ_{thin} ranging from 5×10^{-6} to 1×10^{-7} . The effect of thinning on the simulation of the radio emission is discussed in Sec. 6.1.2. To obtain information about the longitudinal profile of the particle cascades we extract the longitudinal profiles of the particle numbers and energy deposits [118].

CORSIKA computes a Gaisser-Hillas (GH) fit to the energy-deposit table to determine the slant depth of the air-shower maximum X_{\max} . We found that this fit does not reliably work for air showers with zenith angles beyond 80° . Hence, we perform a 2-step χ^2 minimization ourselves to determine the depth of the shower maximum. The resulting X_{\max} distribution is uncorrelated with the zenith angle, as expected. Both X_{\max} distributions, determined by CORSIKA (blue) and by us (“Converter”, orange) are shown in Fig. 4.1 for two different simulation sets. For both simulation sets it can be seen that the mean X_{\max} calculated from CORSIKA decreases at the highest zenith angles (above 80°) as much as $\sim -30 \text{ g cm}^{-2}$. Inspecting some fitted GH profiles in CORSIKA at the highest zenith angles showed clearly that the fits failed, i.e., the fitted profiles do not describe the simulated profiles. Hence, in our analyses presented in Chapters 5, 6, and 7 which crucially rely on an accurate determination of MC X_{\max} , X_{\max} is estimated outside of CORSIKA. For our studies involving a real detector simulation using `Offline` in Chapters 8 and 9 we have relied on the CORSIKA estimated values to determine the signal arrival direction at each station (see Sec. 8.1.1). Although the bias in X_{\max} can be on the order of $\sim 30 \text{ g cm}^{-2}$ at the highest inclination, the relative effect on the relevant geometrical distance to shower maximum is rather small (cf. Fig. 6.12).

⁴ For determining w_{max} , the value of E_0 is used in units of GeV.

The simulation of the radio emission from air showers requires significant computational resources. While already the simulations of the particle cascades with up to several billion secondaries with CORSIKA require significant CPU power, the simulation of the radio emission multiplies the computation effort needed. The reason for this has already been outlined earlier, to predict the radio pulses at different observers, the emission and propagation of the electromagnetic radiation has to be repeated for each emission point and individual observer. Hence, the computational effort needed for the simulation of the radio emission scales linearly with the number of observers. For simulations with a realistic detector layout, the number of simulated observers increases with the zenith angle as the area for which the radio emission is detectable becomes larger and more observers are likely to register a strong signal. Furthermore, in inclined air showers, to simulate the propagation of the radio emission one has to consider the Earth’s curvature which increases the computational effort further, even with the pre-calculated tables of the integrated refractive index. In summary, the simulation of a single highly energetic and inclined air shower with more than 100 radio observers can require several hundred hours on a single CPU⁵. Hence, most simulations in this work have been generated using MPI-parallelization to cope with this enormous computational effort. MPI-parallelization means that single showers are subdivided into several sub-showers which are simulated independently of each other on different CPUs⁶. The particle content at the observation level (stored in the binary CORSIKA particle files) is stored for each sub-shower individually. To be able to process those showers with Offline, the sub-shower particle files have to be merged.

By the time we generated our showers, two scripts were available in the CORSIKA source code to merge those files: `concatcorsika.f` and `merge_corsika.cc`. In the context of this work, it was found that the former produces wrong results, i.e., the number of particles in the merged files does not agree with the sum of the sub-shower files, and was later removed from the source code. Consequently, we used the second script to merge the sub-shower particle files. A few other things have to be considered when working with MPI-generated simulations. Most importantly, the sub-shower particle files and consequently also the merged particle file contain an incorrect number for the “weighted number of muons arriving at observation level”. To be able to evaluate the performance of the WCD to reconstruct the muon content of inclined air showers, as well as to interpret the results of our analyses, this observable is crucial. Hence, to obtain it from MPI simulations, we manually count the number of muons contained in the merged particle file. We wrote an Offline-module for this purpose: *SimMuonCounter*.

One caveat of using MPI-parallelization is that the CORSIKA simulations were not running as stable as usual with only a single CPU. A potential cause for the experienced failures might be the fact that a CPU get assigned a sub-shower with no particles arriving at the ground (this can happen if the *PARALLEL*-options in CORSIKA were not optimal set for the number of used CPUs and simulated shower energy.). Hence, some generated simulation sets are incomplete which explains the odd number of showers. However, this does not affect any analyses with these simulation sets.

⁵ The “largest” shower simulated in this work, would have run for almost 800 h on a single CPU while the average is on the order of 60 h.

⁶ Of course that does not mean that the total CPU time decreases but the (running) time the simulations need to complete is significantly reduced.

4. Simulation of the radio emission from inclined air showers

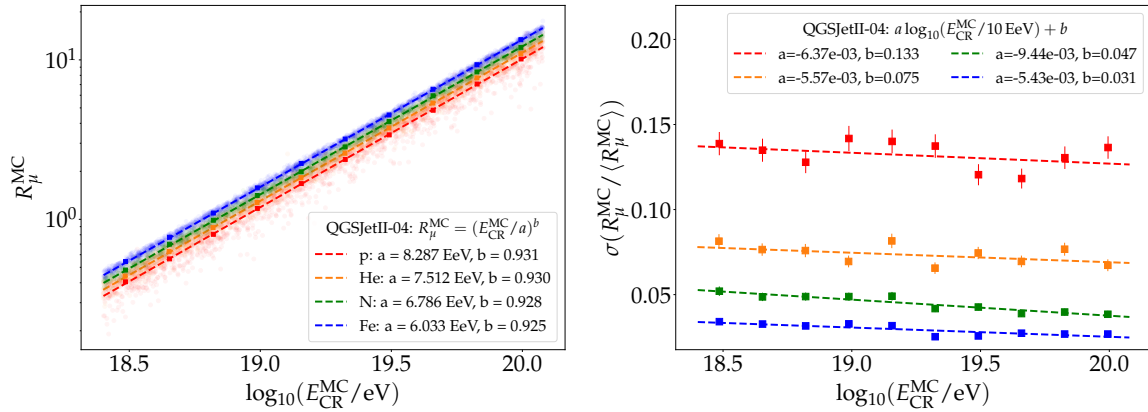


Figure 4.2.: *Left:* Normalized muon number at ground R_μ^{MC} from simulations of inclined air showers using QGSJetII-04 as a function of the cosmic-ray energy $E_{\text{CR}}^{\text{MC}}$. For each primary, the correlation between R_μ^{MC} and $E_{\text{CR}}^{\text{MC}}$ is described by a power law. *Right:* Corresponding relative physical fluctuations $\sigma(R_\mu^{\text{MC}} / \langle R_\mu^{\text{MC}} \rangle)$ in discrete bins as function of the energy. Error bars indicate statistical uncertainties. For each primary a linear model (with the logarithm of the energy) is fitted to the binned data.

To illustrate the muon content of our simulated air showers, we count the number of muons at the ground N_μ^{MC} and normalize it with an arrival-direction dependent reference muon-number $N_{\mu,19}^{\text{ref}}(\theta, \phi)$ which yields R_μ^{MC} . The dependency of $N_{\mu,19}^{\text{ref}}$ on the arrival direction allows to remove any dependency on R_μ^{MC} from the arrival direction. In Fig. 4.2 (*left*) R_μ^{MC} is shown for air showers induced by 4 different primaries and generated with QGSJetII-04. The reference muon-numbers $N_{\mu,19}^{\text{ref}}(\theta, \phi)$ are obtained from a spatial integration over the reference muon-density maps introduced in Sec. 3.2.3 [119], hence R_μ^{MC} can be directly compared to the reconstructed shower size N_{19} . On the right side the relative physical fluctuations for each primary are shown. Both observables are parameterized as a function of the energy. The functions for both observables and parameters for both hadronic interaction models are given in appendix A.2.

For most of our simulations, the CoREAS simulated traces have a length of 400 ns and a sampling frequency of 5 GHz. For some geometries, the non-band-pass filtered pulses are not fully contained within this 400 ns. This introduces a “cut-off” in the signal when zero padding the traces. Although this is not found to happen for pulses filtered to our desired band of 30 MHz to 80 MHz, when the zero-padded pulses are band-pass filtered, this cut-off introduces a second peak at the position of the cut-off which in some cases can dominate the air shower signals (in 30 MHz - 80 MHz). To avoid this, we employ an exponential model to extrapolate pulses such that the cut-off diminishes. A mechanism to do so has been implemented with python and in `Offline` and is explained in the appendix A.1.

Throughout this work, we will use the air shower observable d_{max} , the geometrical distance along the shower axis (the extrapolated trajectory of the primary particle) between the ground/observation plane and the shower maximum. It is being calculated for a given

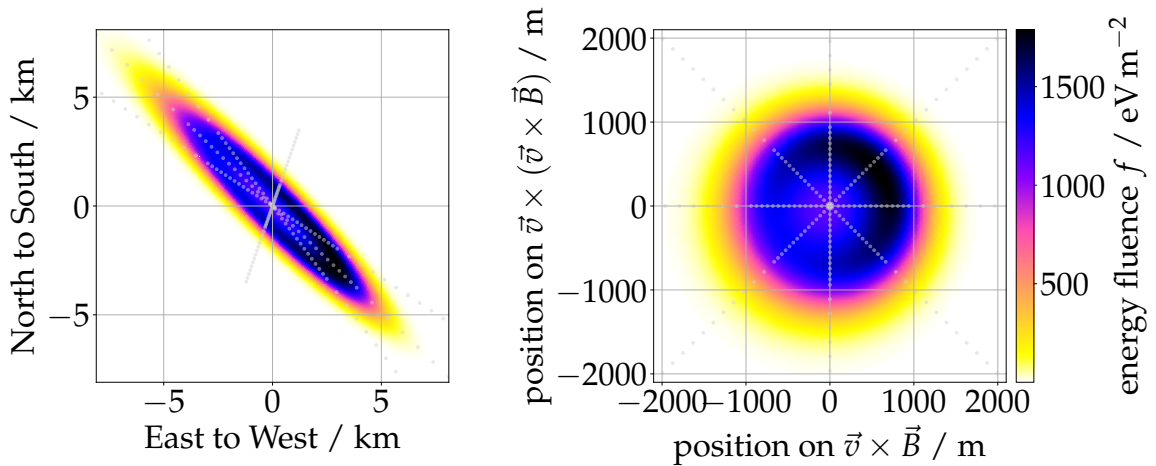


Figure 4.3.: Radio-emission footprint from an 80° CoREAS shower arriving from South-East for the energy fluence in the 30 MHz to 80 MHz band. The radio emission is simulated at 240 observer positions (indicated by the gray dots) and interpolated in between. *Left:* Radio-emission footprint shown in ground-plane coordinates with the shower incoming from the bottom-right. The footprint is largely elongated covering several tens of square kilometers and exhibiting strong asymmetries. *Right:* Radio-emission footprint shown in shower-plane coordinates. The footprint is fairly circular.

zenith angle, slant depth of the shower maximum X_{\max} , and altitude of the observation level with:

$$X_{\text{ground}} - X_{\max} = \int_0^{d_{\max}} \rho(\ell) d\ell. \quad (4.2)$$

X_{ground} is the atmospheric slant depth of the ground plane measured along the shower axis. $\rho(\ell)$ denotes the atmospheric density at the distance ℓ along the shower axis which is defined by the zenith angle. For inclined showers, the integral can only be solved numerically as the curvature of the atmosphere needs to be taken into account. In the first order d_{\max} scales with the zenith angle, and only to the second-order with X_{\max} .

4.1.1. Simulations with a star-shaped antenna array

Simulations with observers situated on a star-shaped grid (detector layout) are well suited for detailed studies of the radio emission at the ground, as they allow to easily decompose the radio emission into different emission mechanisms and study other features with high precision (cf. Sec. 4.2). An illustration of the radio emission at the ground from a star-shaped simulation is shown in Fig. 4.3. The colored background shows the radio emission interpolated from the emission simulated on the star-shaped grid. The observer positions are indicated by the gray dots.

For the main set of showers with observers on a star-shaped grid, we simulated 4309 proton and iron-induced air showers. The arrival direction of those showers was simulated with zenith angles from 65° to 85° equally spaced in 2.5° steps and 8 equidistantly spaced azimuth angles ϕ , i.e., coming from geomagnetic East ($\phi = 0^\circ$), North-East ($\phi = 45^\circ$), North ($\phi = 90^\circ$), etc. The simulated energies range from $18.4 \leq \log_{10}(E/\text{eV}) \leq 20.2$ in

$\log_{10}(E/\text{eV}) = 0.2$ equidistant steps. For each of these combinations and the two primaries, we generated 3 showers. The simulated atmosphere matches the conditions at the Auger Observatory in October (CORSIKA atmosphere ID 27) with a refractive index at sea level of $n_0 = 1 + 3.12 \times 10^{-4}$. We chose this atmosphere as it best represents the yearly average of the refractive index at the observatory [66, Fig. 3.21]⁷. The magnetic field strength and inclination were fixed to 0.2406 G respectively -35.9° . For the simulation of the particle cascade, the high-energy hadronic interaction model QGSJetII-04 and a particle thinning with $\epsilon_{\text{th}} = 5 \times 10^{-6}$ were used.

For each shower, the radio emission is sampled at 240 observer positions with the electric field “recorded” in the North-South (NS), East-West (EW), and Vertical (V) polarizations. The traces have a length of 400 ns and are sampled with 5 GHz. The observers are situated in the ground plane such that a star-shaped grid with 8 equidistant rays⁸ is formed in shower-plane coordinates. Alternatively, one could speak of observers on 30 concentric rings around the shower axis with 8 observers per ring. The radial spacing is denser close to the shower axis to sample the signal distribution within and around the Cherenkov ring more precisely, and sparser outside (cf. Fig. 4.3).

In addition to the 4309 simulations with the above configuration, we simulated proton showers with a fixed energy of $\log_{10}(E/\text{eV}) = 18.4$, the same binned arrival directions as above but with different atmospheric conditions. The atmospheric conditions match those of the Pierre Auger Observatory in February and June, as well as the US standard atmosphere⁹. For each atmosphere, we simulated 216 showers (one complete energy bin as described above but with only 160 observers (20 instead of 30 concentric rings) and a particle thinning of $\epsilon_{\text{th}} = 1 \times 10^{-6}$. Those two months represent both extremes in terms of density- and refractive index profile [113].

The star-shaped simulations are used in chapters 5 and 6.

4.1.2. Simulations for the AugerPrime Radio Detector

To evaluate the signal and reconstruction model, presented in a later chapter of this work, or to investigate the performance of the AugerPrime Radio Detector, we require simulations with the detector specific layout of the RD. Hence, the observers are situated at positions defined by the ideal layout of the SD array¹⁰. To be able to provide the (relative) observer positions to CoREAS we have to specify a position for the shower core within the ideal SD array. For the purpose of generating random core positions contained in the SD array together with all necessary input files for a CORSIKA/CoREAS simulation, we implemented the ExampleApplication `RdGenerateCoREASCardsWithoutEvent` in `Offline` alongside comprehensive changes to the module `RdREASSimPreparatorNG`. The core posi-

⁷ The figure in this reference shows the refractive index at the ground surface of the observatory at an altitude of ~ 1564 m. As input CoREAS requires the refractive index at sea level, hence we need to scale up the shown values using Eq. (4.1).

⁸ Those rays are also called “arms” in this work, for example in chap. 5.

⁹ CORSIKA atmosphere IDs for February: 19, June: 23, US standard: 1.

¹⁰ The ideal array defines the position of 1672 observers on a hexagonal array with the shape and size of the Auger Surface Detector array but with a perfect 1.5 km spacing, without any holes (missing stations), and a constant altitude of 1400 m

tion is drawn randomly within the central hexagon of a randomly chosen station¹¹. The chosen station has to have a full hexagon (crown) of 6 stations around itself¹² which satisfies the condition of having “contained” showers. For a given core position we only add observers within a geometry-dependent radius around the shower axis to the simulation instead of simulating signals for all 1672 observers for every shower. The exact algorithm how to select observers is detailed in the following section.

The air showers with the ideal SD array detector layout are generated with isotropic arrival directions for zenith angles within 65° to 85° , i.e., θ is uniformly distribution in $\sin^2 \theta$ and the azimuth angle is drawn from a uniform distribution between $\phi \in [0^\circ, 360^\circ)$. The air shower energies are uniformly distributed in $\log_{10}(E/\text{eV})$ which corresponds to a hard power-law spectrum with E^{-1} . While the simulated arrival direction distribution fits the expectation for the arrival directions of air showers with a flat detector, the simulated energy spectrum is much harder than what is expected from nature, $\sim E^{-3}$. We generate air showers induced by 4 different primaries: protons, helium-, nitrogen-, and iron nuclei. We use two different high-energy hadronic interaction models, QGSJetII-04 and Sibyll-2.3d and a thinning parameter $\epsilon_{\text{th}} = 1 \times 10^{-6}$. The atmospheric condition is the same as above, describing the condition at the Observatory in October. The magnetic field inclination changes depending on the core position within the array with a mean of -36.86° and a standard deviation of 0.14° . The magnetic field strength is almost constant with a mean of 0.2376 G and a standard deviation of 0.0004 G. For each primary and high-energy hadronic interaction module, we simulated ~ 2000 showers resulting in a total of 7972 QGSJetII-04 generated and 7998 Sibyll-2.3d generated showers.

The core positions of all those showers within the simulated array are shown in Fig. 4.4 (left). Each black dot corresponds to the position on a detector station/observer. Each red dot to the position of a simulated shower. On the right side of the same figure, an example footprint is shown.

In addition to that, we simulated an additional 8000 proton and iron induced showers with different atmospheric conditions. The showers were generated only with Sibyll-2.3d and a refined thinning with $\epsilon_{\text{th}} = 1 \times 10^{-7}$. Half of the simulations were performed with the atmospheric condition for February (Summer, CORSIKA ID 19, $n_0 = 1 + 3.36 \times 10^{-4}$) and the other half for June (Winter, CORSIKA ID 23, $n_0 = 1 + 3 \times 10^{-4}$).

4.1.2.1. Observer selection

For a static detector layout and random core positions, one has to decide for which antennas to simulate the radio emission. If the selection is too loose, i.e., one would simulate pulses for antennas that would not trigger and/or the radio emission would be too faint to be detectable, wasting a significant amount of computing resources which will limit the number of showers one can simulate. On the other hand, if the selection is too tight, one might miss simulating pulses for which a station could have detected a signal. In that case, we would negatively bias the analyses. Here, we employ a selection that is solely based on the shower’s arrival direction but not energy or shower maximum. We define a

¹¹ The central hexagon of a station marks the array for which any position within this hexagon is closest to the station.

¹² This excludes stations at the outer edge of the array.

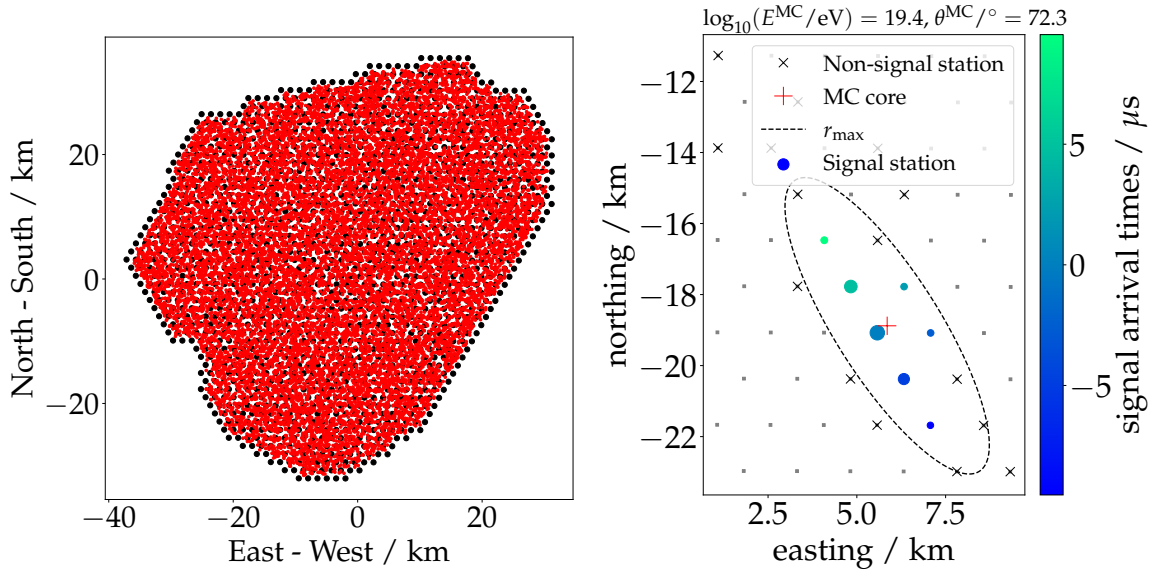


Figure 4.4.: *Left:* Simulated shower core positions (red dots) within the (simulated) ideal SD-array (each black dot refers to the position of the detector station). *Right:* Measured footprint of an inclined air shower simulated with the ideal SD-array. The color code indicates the arrival time of the radio signal, the size of the marker the signal strength measured at each antenna. For all stations within the drawn ellipsoid, a radio signal was simulated. The gray dots indicate stations without a WCD trigger. The “x” indicates stations with a triggered WCD but no detected radio signal (for stations with a simulated and without a simulated radio pulse). Details to the signal reconstruction are given in Chap. 8.

zenith-angle dependent maximum radius r_{\max} around the shower axis within which we simulate the signals for all observers. The maximum distance is determined as a multiple of the radius r_0 of the Cherenkov ring. The motivation behind this is that the size of the lateral signal distribution scales with r_0 , or in other words that the size of the lateral signal distribution in units of r_0 is, to first order, independent of the zenith angle. The calculation of r_0 is introduced in the next section. To estimate $r_{\max}(r_0)$, a fixed depth of the shower maximum of 750 g cm^{-2} regardless of the energy or primary particle is used. To ensure a minimal antenna multiplicity (> 3) a lower limit for r_{\max} of 1500 m is applied¹³, i.e.,

$$r_{\max} = \max(4 \cdot r_0, 1500 \text{ m}). \quad (4.3)$$

Both, the multiplication factor 4 and the lower constraint of 1500 m are configurable in the Offline-module and were set to ensure a sufficient signal multiplicity. For showers with a zenith angle $\theta \gtrsim 72^\circ$ the relation $4 \cdot r_0 > 1500 \text{ m}$ holds. Note that the radius r_{\max} refers to distance to the shower axis, i.e., the distance in the shower plane. The distance along the ground described by r_{\max} depends on the zenith angle and is larger than 1500 m.

¹³ In fact for a subset of 1000 QGSJetII, proton showers were generated without this lower limit. Hence, among those, 7 showers with a low zenith angle have fewer than 3 simulated pulses. If this matters for the analysis, those showers are rejected.

4.2. Radio emission from inclined air showers

The 2-dimensional lateral signal distribution at ground – “radio-emission footprint” – from a (simulated) 80° air shower coming from East is shown in Fig. 4.3 (*left*) in energy fluence (color-coded), i.e., the energy deposit per unit area, for 30 MHz to 80 MHz. The presented footprint is highly elongated along the shower direction covering a large area with a semi-major axis of ~ 10 km and a semi-minor axis of ~ 2 km, and exhibits strong asymmetries. The right panel in the same figure shows the radio-emission footprint in a shower-plane coordinate system. In this representation, the footprint is more circular. The coordinate system is defined by orthogonal unit vectors pointing into the directions $\vec{v} \times \vec{B}$, $\vec{v} \times (\vec{v} \times \vec{B})$, and \vec{v} , where \vec{v} is the direction of the primary particle trajectory (i.e., pointing exactly in the opposite direction of the shower axis), and \vec{B} pointing in the direction of the magnetic field vector¹⁴. A ring-like structure is visible in the emission pattern. This feature is due to the Cherenkov compression [49]: the radio emission emitted during the whole development of the air-shower particle cascade arrives temporally compressed at the ground for a characteristic axis distance depending on the refractive atmospheric conditions. This imprints a ring-like feature into the emission pattern as the strong temporal compression allows to have coherent signal contributions to high frequencies. The radius of this ring, i.e., the Cherenkov radius r_0 in a plane perpendicular to the air shower direction, can be roughly estimated with a cone that has its apex at the shower maximum with an opening angle equal to the local Cherenkov angle $\delta_{\text{Che}}(h = h_{\text{max}})$, for a point source that is moving with the speed of light $\beta = 1$, i.e.,

$$\begin{aligned} \delta_{\text{Che}}(h_{\text{max}}, n_0) &= \cos^{-1} (1/n(\rho(h_{\text{max}}), n_0)) \\ r_0 &= \tan (\delta_{\text{Che}}(h_{\text{max}}, n_0)) d_{\text{max}}(\theta, X_{\text{max}}, h_{\text{obs}}), \end{aligned} \quad (4.4)$$

with the height of the shower maximum above sea level h_{max} which can be calculated from the zenith angle and X_{max} or from the zenith angle and d_{max} (the latter introduces an explicit dependency on the altitude of the observation plane h_{obs}). The refractive index at the shower maximum $n(\rho(h_{\text{max}}), n_0)$ is calculated for a given n_0 using Eq. (4.1) and a model of the atmospheric density profile $\rho(h)$.

On top of this, a strong asymmetry along the $\vec{v} \times \vec{B}$ -axis (x -axis) is visible (cf. Fig. 4.3, *right*) which is known to originate from the superposition of geomagnetic and charge-excess emission [49]. However, the maximum of the signal distribution is offset from the $\vec{v} \times \vec{B}$ -axis which is unexpected from the interference pattern of the two emission mechanisms. In fact, the maximum is shifted towards the incoming direction of the shower. This deviation is associated with an asymmetry arising from a geometrical early-late effect [120]. In inclined air showers, the radio emission above the shower axis travels over longer distances between source and observer than below the axis. The intensity of the expanding radio emission scales with this geometrical distance. Consequently, below the shower axis, i.e., early in the shower, observers at the ground measure a higher signal intensity than observers late in the shower and thus an early-late asymmetry is imprinted in the radio-emission footprint.

¹⁴ \vec{B} points upwards at the location (latitude) of the Pierre Auger Observatory.

Besides the asymmetries arising from their superposition and the early-late imprints, the geomagnetic and charge-excess emissions independently are assumed to be rotationally symmetric. However, Refs. [121] and [122] report relative deviations in the energy fluence of the sub-dominant charge-excess contribution of $\lesssim 20\%$ which are attributed to shower-to-shower-like fluctuations in the particle cascades.

4.2.1. Decomposition of the radio signal

For an accurate description of the radio-emission footprints it is useful to decompose the emission into the geomagnetic and charge-excess contributions. The geomagnetic emission, which originates from pairs of electrons and positrons deflected in opposite directions in the Earth's magnetic field, thus creating a time-varying transverse current, is polarized in the direction of the Lorentz Force $\vec{F}_L \sim \vec{v} \times \vec{B}$ (in which the electrons and positrons are deflected). The charge-excess emission is due to a time-varying net excess of negatively charged electrons in the shower front and is radially polarized around the shower axis. Hence, for pulses of observers located on the $\vec{v} \times \vec{B}$ -axis the emission contributions from both mechanisms interfere maximally destructively for positions along the negative and maximally constructively for positions along the positive $\vec{v} \times \vec{B}$ -directions. In contrast, on the $\vec{v} \times (\vec{v} \times \vec{B})$ -axis the emission contributions from the two mechanisms are disentangled due to their polarization. For the decomposition of geomagnetic and charge-excess emission we first rotate the electric field traces simulated in the coordinate system (i.e., for the polarizations) [EW, NS, V] into the $[\vec{v} \times \vec{B}, \vec{v} \times (\vec{v} \times \vec{B}), \vec{v}]$ coordinate system. This allows us to calculate the energy fluence for each of these polarizations¹⁵ $f_{\vec{v} \times \vec{B}}$, $f_{\vec{v} \times (\vec{v} \times \vec{B})}$, and $f_{\vec{v}}$. Then we decompose the signal in one part originating from the geomagnetic f_{geo} and another part originating from the charge-excess f_{ce} emission, making use of the above-described polarization characteristics, i.e., (derived from [121, 123])

$$f_{\text{geo}}^{\text{pos}} = \left(\sqrt{f_{\vec{v} \times \vec{B}}} - \frac{\cos \phi}{|\sin \phi|} \cdot \sqrt{f_{\vec{v} \times (\vec{v} \times \vec{B})}} \right)^2 \quad (4.5)$$

$$f_{\text{ce}}^{\text{pos}} = \frac{1}{\sin^2 \phi} \cdot f_{\vec{v} \times (\vec{v} \times \vec{B})}. \quad (4.6)$$

Here, ϕ is the polar angle between the observer position and the positive $\vec{v} \times \vec{B}$ axis. The underlying concept of Eqs. (4.5) and (4.6) is the following: The strength of the charge-excess emission is solely estimated from the emission in the $\vec{v} \times (\vec{v} \times \vec{B})$ -polarization and the observer position in the shower plane. With the position, one can also estimate the charge-excess emission contribution to the emission in the $\vec{v} \times \vec{B}$ -polarization (which interferes with the geomagnetic emission). The disadvantage of this ansatz is obvious: close to or on the $\vec{v} \times \vec{B}$ axis ($\sin \phi \rightarrow 0$), no signal is polarized in the $\vec{v} \times (\vec{v} \times \vec{B})$ direction, while the term $1/\sin \phi$ diverges, hence the ansatz loses validity. A different ansatz that overcomes this problem but comes with other disadvantages is discussed in the appendix B.1. It has to be mentioned that the equations (4.5) and (4.6) assume that both emission contributions arrive simultaneously at an observer, i.e., without any phase shift. Such a

¹⁵ In the latter almost no signal is deposited since the radio emission in air constitutes transverse waves.

phase shift would give rise to a circularly polarized component in the incoming electric field which indeed has been seen in experimental data [124], i.e., there is a time delay between the pulses originating from the charge-excess and geomagnetic emission.

To quantify the fraction of circular polarization in the radio pulses we calculate the Stokes parameters I , Q , U , V following the procedure detailed in reference [124]. Since the relative strength of the charge-excess emission decreases with the zenith angle (cf. Sec. 6.2.3), the fraction of circularly polarized signal is small for most showers in our set. The determined time delay, following the procedure in Ref. [124], is within $\Delta t < 1$ ns for most observers and thus the above equations are applicable for the radio emission in the 30 MHz to 80 MHz band. To ensure that this holds, we only use showers with a geomagnetic angle $\alpha > 20^\circ$, i.e., the angle between the shower axis and the Earth's magnetic field vector¹⁶.

Note that for optimal decomposition, we placed observers at locations along the $\vec{v} \times \vec{B}$ -axis, orthogonal to that, on the $\vec{v} \times (\vec{v} \times \vec{B})$ -axis, and on the bisectors of those two axes (simulations with the star-shaped antenna grid).

4.3. Studies on the nature of the radio emission from inclined air showers

In the following two (sub-)sections, we present two studies of the nature of the radio emission in (inclined) air showers. In Sec. 4.3.1 the correlation of the radiation energy from the two emission mechanisms with the air density at the shower maximum is investigated. In Sec. 4.3.2 we present the result from a study of *sliced*-CoREAS simulations to investigate from which part of the shower development the radio emission (mostly) originates. In Chap. 5, the here-described simulations are used to study the propagation of the radio emission in the Earth's atmosphere and its consequences on the coherent signal pattern at the ground.

4.3.1. Atmospheric dependencies of the radiation energy in inclined air showers

For this study, we use the 4309 simulations with a star-shaped grid to derive the total radiation energy at the ground. To this end, we numerically integrate over the 2d-signal pattern of the radio emission. The signals simulated on a star-shaped grid are used to interpolate the energy fluence to arbitrary positions off-grid. We employ an interpolation based on a Fourier-decomposition in shower-plane coordinates [125]. In Ref. [121] the (total) radiation energy from air showers was found to correlate with the air density at the shower maximum. This scaling was attributed to the scaling of the geomagnetic emission and explained as follows: Due to the lower air density, the mean-free path length of the

¹⁶ Depending on the geographic latitude at which an experiment is hosted, the magnetic field direction and a radius of 20° around it affect the detection of inclined air showers or not. In the case of the Pierre Auger Observatory with a local magnetic field pointing upwards with a zenith angle of $\sim 54^\circ$, only air showers coming from close to the geomagnetic North are rejected.

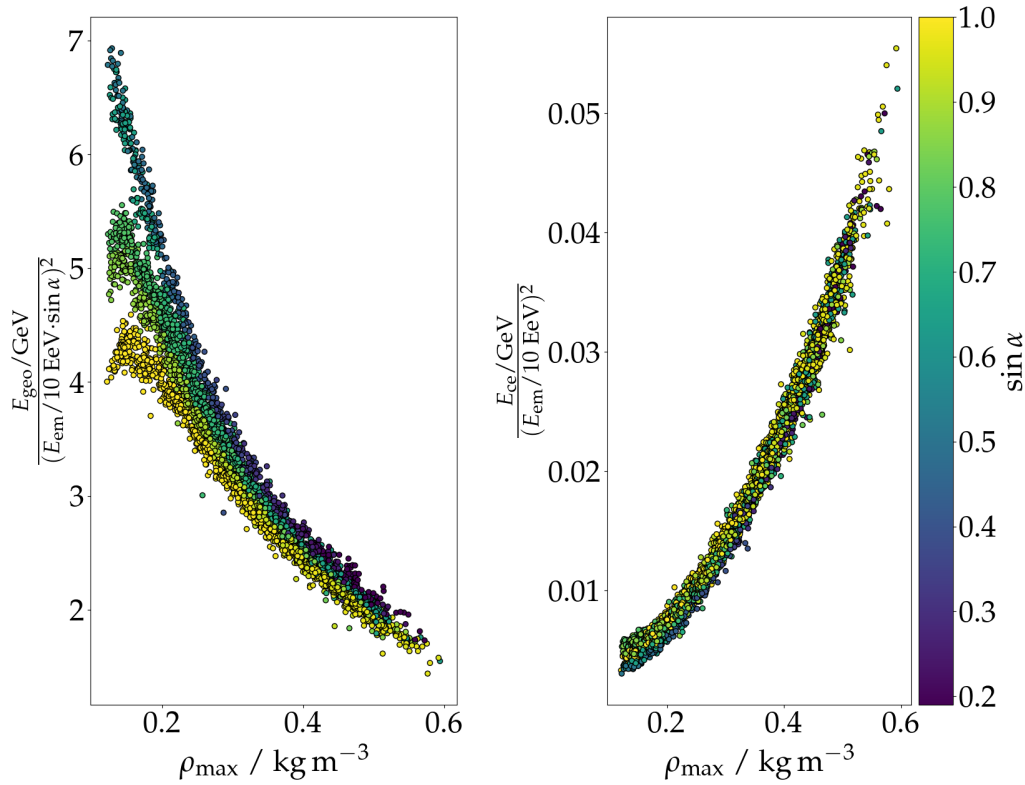


Figure 4.5.: Normalized geomagnetic (*left*) and charge-excess (*right*) radiation energy as a function of the local air density at the shower maximum ρ_{\max} . Notice the different y -axis scaling. For both emission mechanisms, the radiation energy is appropriately normalized to expose the correlation with ρ_{\max} . The orientation of the magnetic field w.r.t. the air shower arrival direction is indicated by the color code with the sine of the geomagnetic angle α .

electrons and positions is longer hence a transverse current can be established over large distances and time scales yielding an increased coherent emission. In Fig. 4.5 we show the correlation of the geomagnetic (*left*) and charge-excess (*right*) emission, derived using Eqs. (4.5) and (4.6), with the local air density at the shower maximum ρ_{\max} explicitly. For both mechanisms, the radiation energy is normalized with the electromagnetic shower energy E_{em} , Eq. (B.3), and, in the case of the geomagnetic emission, with the orientation of the magnetic field, to expose the correlation with ρ_{\max} .

For the dominant geomagnetic emission, we find an exponential correlation as reported in [121]. However, also an unexpected residual correlation with the orientation to the geomagnetic field is visible at lower air densities respectively higher zenith angles (indicated by the color-coded $\sin \alpha$). With $\sin \alpha$ scales the Lorentz force that acts on the electromagnetic particles and thus it is expected that the geomagnetic emission scales with it as well. In Ref. [54], a transition from a regime of time-varying transverse currents to a regime of synchrotron radiation is predicted for air showers developing in low air density in the presence of strong magnetic fields. We do not observe a clear transition in the phase space covered by our simulations (as it is also not expected), however, the residual correlation of the geomagnetic emission with the orientation of the geomagnetic

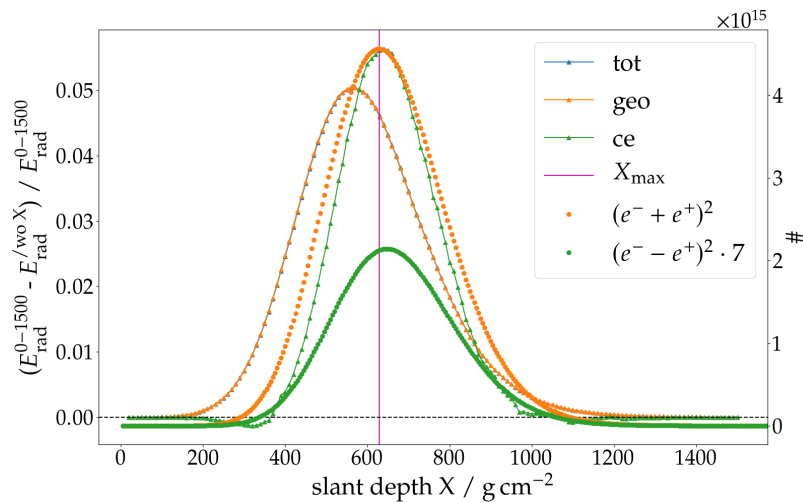


Figure 4.6.: Longitudinal profile of the radio-emission release in an 65° air shower. The y -axis shows the relative change in the radiation energy at the ground if all particles from a given *slice* are ignored for the computation of the radiation energy. The relative change is shown for the geomagnetic (orange), charge-excess (green), and overall (blue) radio emission separately. The profile of the total emission release follows closely that of the geomagnetic emission (and thus is hardly visible). The depth of the shower maximum is indicated for reference. The longitudinal profiles of the squared particle numbers of all electrons and positrons together $((e^- + e^+)^2)$ and excess electrons $((e^- - e^+)^2)$ are also shown (right y -axis).

field at lower air densities (cf. Fig. 6.10) might be explained by this transition. Another indication for the appearance of such a transition can be found in Ref. [126, Fig. 2]. It shows the density-scaling of the geomagnetic emission in ZHaireS-simulated air showers for the ambient conditions of the GRAND experiment [127] and exhibits a rapid decrease of the emission at lower densities while the correlation at higher densities is comparable to the results shown here. As the magnetic field at the GRAND site is much stronger than for the location of the Pierre Auger Observatory, common causation related to the magnetic field strength, i.e., the magnitude of the Lorentz force, seems reasonable.

The sub-dominant charge-excess emission also exhibits a significant correlation with ρ_{\max} . As expected, no correlation with the magnetic field (orientation) is observed. Only recently the correlation with ρ_{\max} has been reported in [126] using ZHaireS simulations. A naive explanation goes like this: Due to the decreased air densities, fewer ambient air molecules are ionized, and thus fewer electrons are “kicked out” and dragged within the shower front. As a consequence, a smaller negative charge excess builds up and the emitted radiation is weaker. However, deeper investigations are needed to establish that explanation.

4.3.2. Investigating the atmospheric depth from which the radio emission measured at ground originates

CoREAS allows separating the radio signals from different particles. That means that only the emission of particles fulfilling a certain condition such as their depth in the

atmosphere can be used to predict the signal in a certain observer. Furthermore, one can place many observers at the same position to obtain a detailed picture from where in the atmosphere the emission at this position originated. We refer to such simulation as *sliced*. The particles which contribute to a particular station can be filtered according to the position in the shower development, expressed in slant depth, their gamma factor (i.e., momentum), and their lateral distance to the shower axis [128]. Here, we use slices in slant depth to investigate from where in the shower most of the radio emission measured at the ground originates. In [121] a similar study was performed, however not with sliced simulations but with observers situated along several “observation planes” along with the shower development. They found that 1) the geomagnetic (and closely correlated the total) emission originates from slightly before the shower maximum with $\Delta X \approx 50 \text{ g cm}^{-2}$, i.e., from higher up in the atmosphere, and 2) that the charge-excess emission comes from even earlier $\Delta X \approx 90 \text{ g cm}^{-2}$. The latter result is challenged by [124, 129] which predict/find that the charge-excess emission, closely connected to the profile of the electron excess in the particle cascade, originates from after the shower maximum. The contradiction can be explained due to a non-adequate treatment of the coherence in the radio signal by the analysis in [121]. From the investigation of the total radiation energy at an observation plane with slant depth X , one obtains $E_{\text{rad}}(X)$ the radiation energy produced “so far”. However, emission produced later in the shower might not add coherently to the emission constituting $E_{\text{rad}}(X)$. Hence, to investigate from where in the shower development the contribution to the coherent emission at the ground is strongest, the procedure in [121] is inadequate. With sliced simulations a more appropriate procedure is possible. First, we sum together the signals from all individual observers at the same position whose signals correspond to different slices. With that, using again a star-shaped grid, the total radiation energy can be calculated $E_{\text{rad}}^{\text{tot}}$. Then we repeat the procedure but this time leaving out the signals from one slice, this yields $E_{\text{rad}}^{\text{without } X}$. Comparing $E_{\text{rad}}^{\text{tot}}$ and $E_{\text{rad}}^{\text{without } X}$ reveals the contribution of the signals from the slice X to the coherent signal at ground. We do that iteratively for each slice, the result is show in Fig. 4.6 (we only simulated slices within 0 g cm^{-2} to 1500 g cm^{-2} which should comprise the relevant parts of the electromagnetic particle cascade). With this approach, we find that the longitudinal profile of the charge-excess emission has its maximum at the shower maximum or slightly deeper. This follows the longitudinal profile of the numerical excess of electrons over positrons in the shower front (also shown) as predicted by [124, 129].

5. Refractive displacement of the radio-emission footprint of inclined air showers simulated with CoREAS

Parts of this chapter have been published in:

F. Schlüter, M. Gottowik, T. Huege, and J. Rautenberg

"Refractive displacement of the radio-emission footprint of inclined air showers simulated with CoREAS"

[Eur. Phys. J. C **80**, 643 \(2020\)](#)

To be able to exploit data of inclined air showers recorded with the AugerPrime Radio Detector, a detailed understanding of the signal distribution of their radio emission is crucial to accurately reconstruct the cosmic-ray properties of interest. As we have described in the previous chapter, the signal distribution of the radio emission at ground is affected by a strong asymmetry arising from the superposition of the geomagnetic and charge-excess emission caused by their individual polarization patterns [49]. For inclined showers with zenith angles larger than 60° an additional early-late asymmetry becomes relevant [120]. In Ref. [130] a previously unknown apparent asymmetry in the radio-emission footprint of inclined CoREAS simulations was observed which was presumed to be related to refraction of the radio emission in the atmosphere. In this chapter we explain and resolve this apparent asymmetry with a systematic offset of the radio-emission footprint with respect to the Monte-Carlo (MC) air shower impact point, i.e., the intersection between the MC shower axis and the ground plane. We express this offset as a displacement of the center of symmetry of the dominating geomagnetic radio emission from the Monte-Carlo impact point. We develop a method to determine the radio symmetry center without implying detailed knowledge of the lateral distribution function (LDF) of the radio-emission footprint. Furthermore, we present a model successfully describing the radio symmetry center displacement by the refraction of electromagnetic waves during their propagation through a refractive atmosphere based on Snell's law. In Ref. [131] the influence of the refractive index on the radio-emission footprint and thus the reconstructed depth of the shower maximum X_{\max} was studied. An important correlation of the reconstructed X_{\max} with the refractivity at the shower maximum was found. However, focusing on vertical showers effects on signal propagation were, so far, neglected.

Our investigation mainly refers to the frequency band of the radio emission from 30 MHz to 80 MHz. This frequency band is used by most current-generation large scale

radio detector arrays [132, 133, 97] as well as the AugerPrime Radio Detector. However, many next generation radio experiments [127, 134] aim to cover higher frequencies and a larger band, e.g. 50 MHz to 200 MHz for the proposed GRAND experiment [127]. In Sec. 5.2.3 we will therefore address the comparability of our results with this frequency band.

This chapter is structured as follows: In the following subsection we show that the additional apparent asymmetry in the lateral distribution of inclined showers found in Ref. [130] can be explained with a displaced radio symmetry center. In Sec. 5.2 we present a method to determine the symmetry center of the lateral distribution of the radio emission. Using a set of CoREAS showers, we establish a systematic displacement of the radio symmetry center with respect to the MC impact point. Furthermore, we investigate differences in the Cherenkov radius for geomagnetic and charge-excess emission. In Sec. 5.3 we present a model based on Snell’s law that successfully describes the displacement, and we discuss the treatment of the propagation of radio emission in CoREAS. Finally, we draw our conclusions in Sec. 5.4.

5.1. Apparent asymmetry in the lateral distribution of the radio emission

A qualitative description of the signal distribution of the radio emission from inclined air showers was already given in Sec. 4.2. The signal distribution exhibits strong asymmetries which are explained by the interference of geomagnetic and charge-excess emission and geometrical early-late imprints. While those effects are nowadays well-known to us, we can correct for them. For example, for observers situated on the $\vec{v} \times (\vec{v} \times \vec{B})$ -axis, both emissions are disentangled and should not exhibit any asymmetry from the interference between them. The early-late imprints can be corrected for with a geometrical correction consisting of a “projection into the shower plane” assuming a point source of the radio emission located at the shower maximum X_{\max} within 2% (cf. Sec. 6.2.1).

In addition to these nowadays well-known asymmetries, a further *apparent* asymmetry was observed in Ref. [130]. To further investigate this finding, we simulated one air shower with a zenith angle of 85° arriving from South for four different atmospheric refractive index profiles: two with a constant refractive index throughout the entire atmosphere and two with a refractive index profile according to Eq. (4.1) (i.e., $n(h) - 1 \sim \rho(h)$) with different refractive indexes at sea level. In Fig. 5.1 the lateral distribution of the radio signal along the $\vec{v} \times (\vec{v} \times \vec{B})$ axis is shown in terms of the energy fluence f with the unit eV/m^2 . In our notation the shower axis \vec{v} points in the direction of the primary particle trajectory and the magnetic field vector \vec{B} points to the north and upwards direction with an inclination of $\sim -36^\circ$. Thus, observers along the positive (negative) $\vec{v} \times (\vec{v} \times \vec{B})$ axis are early (late). Along this axis the geomagnetic and charge-excess contributions are decoupled by their polarization [121] and after a correction for geometrical early-late effects no asymmetry is expected. If the refractive index is set to a constant value of $n \equiv 1$ or $n \equiv 1.00003$ (approximately the value of $n(h_{\max})$ at the shower maximum for an air shower with a zenith angle of 85°) throughout the atmosphere, the signal distribution

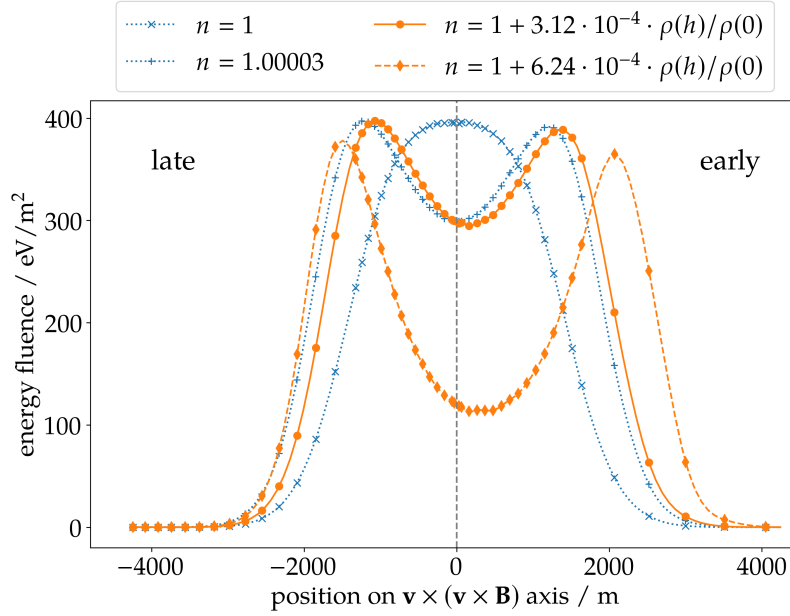


Figure 5.1.: Lateral distribution of the radio emission of an 85° air shower along the positive and negative $\vec{v} \times (\vec{v} \times \vec{B})$ axes with respect to the MC impact point. The energy fluence is expected to be symmetric on both axes. This is fulfilled for a constant refractive index n (blue lines), independent of its exact value. If the refractive index changes with height (orange lines), the LDF is not symmetric with respect to the MC shower axis. On closer look, a displacement of the symmetry axis rather than an asymmetry is observed. Figure updated from [130].

in the shower plane is symmetric along the positive and negative $\vec{v} \times (\vec{v} \times \vec{B})$ axes with respect to the MC shower axis. The exact value of the refractive index is not important for symmetry, but changes the shape of the LDF. With a changing refractive index following the density gradient in the atmosphere, an apparent asymmetry is observed, the LDF is not symmetric anymore with respect to the MC shower axis. This is enhanced when doubling the refractivity $n - 1$ throughout the atmosphere. It seems that for these simulations the symmetry axis is displaced from the MC shower axis in the direction of the positive $\vec{v} \times (\vec{v} \times \vec{B})$ axis rather than exhibiting an additional asymmetry. In the next subsection we will show that this displacement of the radio-emission footprint with respect to the MC impact point is eminent in all simulations. Thereby, we will illustrate the nature of this displacement which hints towards refraction of the radio emission. In Sec. 5.3 we will compare this displacement with a model calculation employing refraction of the radio emission in the atmosphere.

5.2. Displacement of the radio-emission footprints

We now analyze the apparent asymmetry introduced by the refractive index profile of the atmosphere in detail using the set of 4309 inclined air showers simulated with a star-shaped antenna grid and the October atmosphere introduced in Chap. 4. For each simulated shower we want to determine the symmetry center and evaluate its offset to the

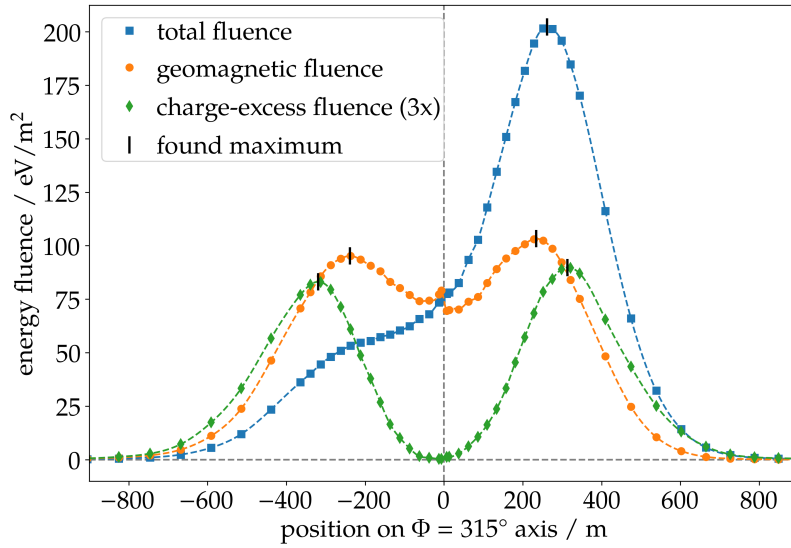


Figure 5.2.: Comparison of the geomagnetic, charge-excess and total energy fluence (cf. Eqs. 4.5 and 4.6) for a shower coming from North with a zenith angle of 65° . This corresponds to a geomagnetic angle with $\sin \alpha \approx 0.19$. The charge-excess contribution is multiplied by a factor of 3. Observers are shown on an axis with $\Phi = 315^\circ$, negative values corresponds to the $\Phi = 135^\circ$ axis. The found maxima are marked by black vertical lines on the LDF. For the geomagnetic energy fluence, a non-physical behavior can be seen close to the axis. This is an artifact of using the MC impact point as the radio symmetry center in the calculation.

MC axis. However by the time we investigated this matter, no validated LDF model was available to fit the symmetry center. Hence, we employ a purely geometrical approach to determine the symmetry center which does not assume any specific LDF: We fit a ring to the ring-like feature present in the radio emission at ground due to the temporal compression of the radio emission, i.e, the Cherenkov ring (cf. Sec. 4.2). The center of the fitted Cherenkov ring yields an estimation for the radio symmetry center.

This approach also yields an estimator for the radius of the Cherenkov ring. Its radius depends on the geometrical distance to the source region and on the refractivity in this region [131, 129]. Since geomagnetic and charge-excess emission were found to originate from slightly different regions in the atmosphere [121] it is expected that both emission contributions exhibit an independent Cherenkov ring. Hence, in the following we will describe the radio-emission footprint in terms of the geomagnetic energy fluence f_{geo} and charge-excess energy fluence f_{ce} separately (cf. Sec. 4.2.1 and Eqs. (4.5) and (4.6)).

In Fig. 5.2 an example shower with a small geomagnetic angle α (angle between the magnetic field axis and shower axis) is shown. For such showers with a weak geomagnetic emission the interference between geomagnetic and charge-excess emission impacts the position of the maximal fluence and can even completely suppress the Cherenkov ring in the negative $\vec{v} \times \vec{B}$ half-plane. Note that since the amplitudes of the electric field traces are interfering, the resulting asymmetry in energy fluence, e.g., the squared sum of the amplitudes, is accentuated. For the total fluence no ring can be estimated for signals with $\Phi = 135^\circ$. In contrast, the geomagnetic and charge-excess energy fluences

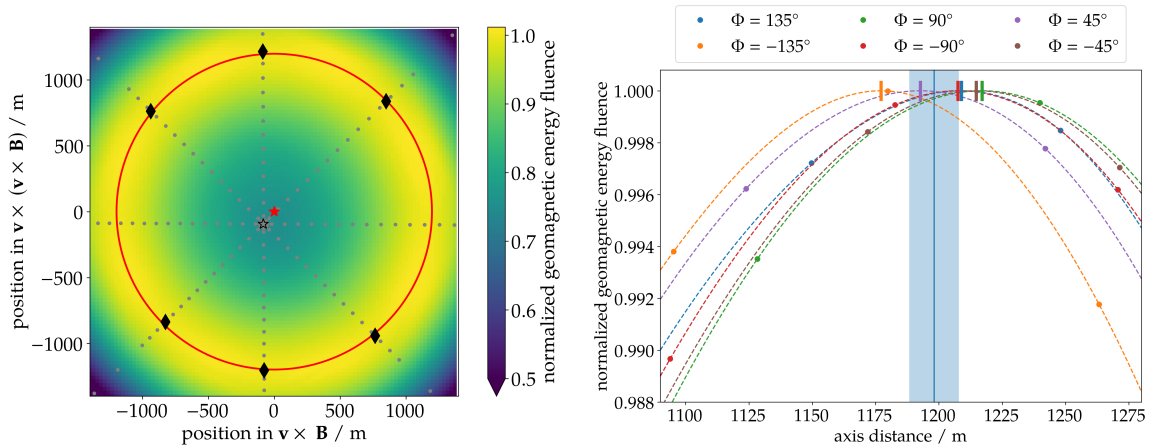


Figure 5.3.: Result of the iterative fit procedure to estimate the radio symmetry center. *Left:* 2D visualization of the fitted Cherenkov ring. For illustration purposes the background constitutes the cubic interpolation of the normalized geomagnetic energy fluence from signals around the Cherenkov ring. In red, the fitted Cherenkov ring and its center, the radio symmetry center, are shown. The black star marks the position of the MC impact point, gray dots show the positions of the simulated pulses. The positions of maximal geomagnetic energy fluence found for each arm of the star-shaped grid are denoted by the black diamonds. *Right:* 1D lateral distribution of the geomagnetic energy fluence for each polar angle of the star-shaped grid except for the $\vec{v} \times \vec{B}$ axis. Colored points denoted the calculated geomagnetic energy fluence for the simulated pulses. Their interpolation is shown by the dashed lines for each arm, the position of the maximum geomagnetic energy fluence is marked by the colored vertical line. The blue line and box denote the fitted radius of the Cherenkov ring and its uncertainty. The axis distances displayed on the x-axis are calculated using the fitted radio symmetry center.

individually exhibit a clear maximum. Note that for Fig. 5.2 the MC impact point was used for the calculation of the geomagnetic energy fluence which does not describe the true radio symmetry center as we will see later. The LDF described by f_{ce} exhibits a broader Cherenkov ring than f_{geo} which motivates to describe both features independently. Thus, in the following we will fit the Cherenkov ring to the individual footprints of the geomagnetic or charge-excess emission contributions.

5.2.1. Fitting the Cherenkov ring

Following Eqs. (4.5) and (4.6), the calculation of f_{geo} and f_{ce} depends on the location of the radio symmetry center via the polar angle Φ . Thus, it is not possible to find the locations of the Cherenkov ring on each arm of the star-shaped grid independently. Therefore, we fit the ring in an iterative process recalculating f_{geo} and f_{ce} in each step of the minimization. For this purpose the Cherenkov ring is described by the position along each arm of the star-shaped grid, for which the fluence is maximal. We found that with this definition, the Cherenkov radius is systematically underestimated w.r.t. the calculation of Eq. (4.4). This difference is illustrated in Appendix C.2. However, for the purpose of finding the center of Cherenkov ring the difference does not matter. These positions are found using a cubic spline interpolation along each arm of the star-shaped grid. For the minimization

process we employ the least squares method with equal weights for each ring position. The calculation of f_{geo} and f_{ce} following Eq. (4.5) and (4.6) becomes nonphysical for small values of $\sin \Phi$, hence the $\vec{v} \times \vec{B}$ axis is excluded. We note that pulses along this axis may not remain at $\Phi = 0^\circ$ respectively $\Phi = 180^\circ$ for the fitted center position and therefore the above equations could provide reasonable energy fluences using the true radio symmetry center position. Furthermore, an alternative approach to disentangle the radio emission from both mechanisms on the $\vec{v} \times \vec{B}$ axis, as detailed in appendix B.1, could be employed here. However, for simplicity and to avoid varying the number of data points during the fit, we do not try to ‘recover’ signals on the $\vec{v} \times \vec{B}$ axis and ignore them completely.

An example fit to the geomagnetic emission for an event with a zenith angle of 85° coming from North-West is shown in Fig. 5.3. The impact of the underlying interpolation function and the spacing of interpolated points used to find the maxima on each arm is found to be negligible for the obtained results. The displacement between the radio symmetry center and MC impact point is estimated to be 125 m in the shower plane. This is a small effect compared to the fitted Cherenkov ring radius of 1198 m, however, due to the high inclination this corresponds to a displacement of 1428 m on ground. The maximal difference between the Cherenkov radii, found on the individual arms, amounts to 40 m. The fit yields an uncertainty of the symmetry center displacement in the shower plane of 21 m.

Having two different Cherenkov rings, i.e., the ring in f_{geo} and f_{ce} , encoded in the total signal of $f_{\vec{v} \times \vec{B}}$ and $f_{\vec{v} \times (\vec{v} \times \vec{B})}$ with a similar strength, i.e., for showers with a small $\sin \alpha$, makes it challenging to disentangle them. Hence, in the following we will fit the Cherenkov ring and evaluate a displacement of the emission footprint of the dominating geomagnetic emission and only for showers with a larger geomagnetic angle.

5.2.2. Investigation of the radio symmetry center displacement for showers with large geomagnetic angles

For showers with a large geomagnetic angle, fulfilling $\sin \alpha > 0.25$, we determine the radio symmetry center displacement by a fit to the Cherenkov ring. This condition excludes 120 showers coming from North with a zenith angle below 70° . In total 4185 fits yield an accurate result and are analyzed in the following. We interpret our results as a function of “distance to X_{max} ”, i.e., the geometrical distance d_{max} between the shower max and core, cf. Eq. (4.2).

In Fig. 5.4 we summarize the observed displacement between MC impact point and radio symmetry center. In the ground plane, we find a displacement of more than 1500 m for the highly inclined showers (*left*). This is of the same order as the spacing of the detector stations for the radio upgrade of the Pierre Auger Observatory. To put the magnitude of the displacement into context we also express the offset in the shower plane as a fraction of the fitted radius of the Cherenkov ring which can go up to 15% (*right*). The presented displacement exhibits a pronounced scatter. The cosine of the azimuth angle, denoted by the color, shows that the found displacement depends on the shower arrival direction. The displacement is strongest for showers coming from West and weakest for East (given the inclination of the magnetic field of $\sim 36^\circ$ both directions translate to the

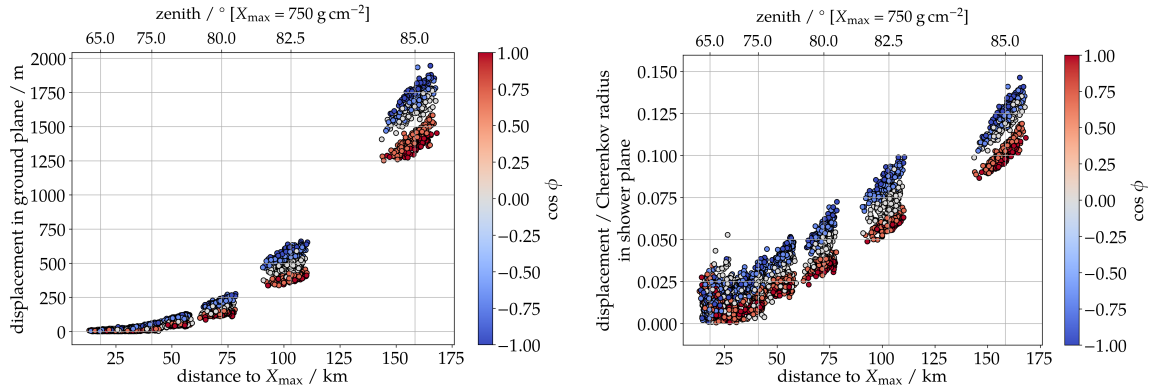


Figure 5.4.: *Left:* Displacement of the radio symmetry center with respect to the MC impact point in the ground plane as a function of distance to X_{\max} . *Right:* Displacement of the radio symmetry center with respect to the MC impact point in the shower plane normalized to the fitted radius of the Cherenkov ring as a function of distance to shower maximum. The color-coded cosine of the azimuth arrival direction illustrates an East ($\cos \phi = 1$) West ($\cos \phi = -1$) asymmetry.

highest $\sin \alpha$ values). This dependency is further investigated in Fig. 5.5 where we show the position of the fitted radio symmetry center on ground with respect to the MC impact point in the coordinate origin. We observe a displacement in the direction from which the shower is incoming, i.e., a displacement towards the shower maximum with a small rotation. The previously described scatter manifests as an East-West asymmetry. As the atmosphere in CoREAS simulations is rotationally symmetric these asymmetries in the displacement cannot be caused by atmospheric properties. An intuitive explanation is provided by the deflection of the charged particles in the Earth’s magnetic field. Given that the majority of shower particles is negatively charged, one can assume that the shower’s particle barycenter is displaced from the MC axis in the direction of the Lorentz Force for a negatively charged particle. Thus, the particle barycenter for showers from west would be displaced below the shower axis, i.e., towards west, while showers from east would be displaced above the shower axis, i.e., also towards west. Hence, this additional displacement already in the particle cascade would add up with the displacement due to refraction and could cause the observed asymmetry. However, further investigations are needed to establish this cause.

5.2.3. Comparison of the radio symmetry center displacement for different frequency bands

So far we have analysed the radio-emission for frequencies in the 30 MHz to 80 MHz band. This band is used by most current-generation radio experiments and in particular also by the upcoming large-scale Auger radio detector. We now determine the displacement of the symmetry center for footprints in the 50 MHz to 200 MHz frequency band. This is the target frequency band of the GRAND experiment [127], currently being in a proposal state, which is also focused on radio measurements of inclined air showers. In Fig. 5.6 the

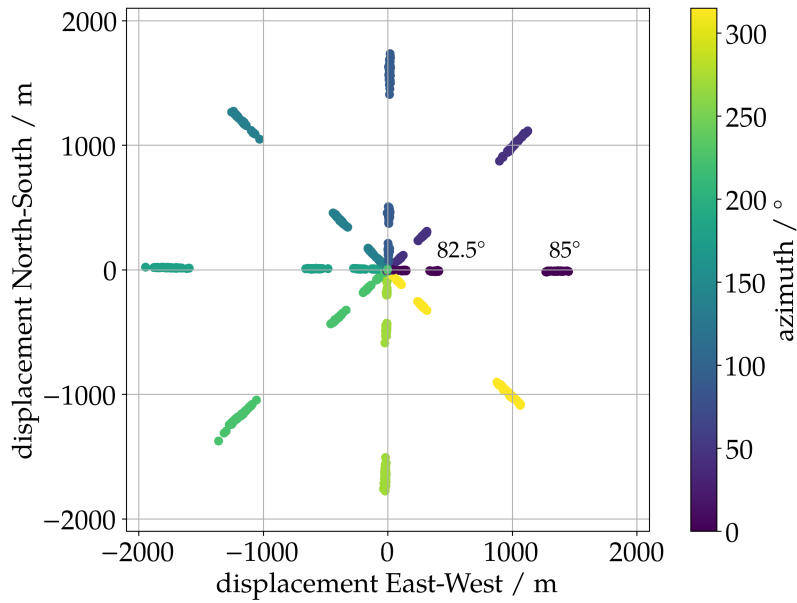


Figure 5.5.: Displacement of the radio symmetry center in the ground plane relative to the MC impact point in the coordinate origin. North is defined as geomagnetic North. The radio symmetry center is always displaced into the incoming direction of the showers. Hence, the clustering of points originates from the binned MC arrival direction of our set of simulations. For the two most inclined bins their MC zenith angle is annotated in the plot.

fitted symmetry center displacement (*left*) and Cherenkov radius (*right*) are shown for the two frequency bands.

We find no difference in the average behavior of the symmetry center displacement between the two frequency bands. The spread is smaller for higher frequencies as the Cherenkov ring is more pronounced and thus easier to fit. On average the fitted Cherenkov radius is $\sim 5\%$ larger for the higher frequency band. This trend is in agreement with [129] which showed the Cherenkov radius increasing with the frequency for vertical showers. This might be caused by differences in the geometrical distribution of the shower particles which primarily contribute to the radio signal in the considered frequency ranges. However, the exact origin of this deviation needs future investigations which are beyond the scope of this paper.

5.3. Interpretation of the displacement as due to refraction

We have shown that for simulations in an atmosphere with a varying refractive index the radio symmetry center is systematically displaced from the MC impact point. Now, we show that this displacement is in agreement with refraction of radio waves in a refractive atmosphere as described by Snell's law (cf. Eq. (5.1)). For this purpose we develop a model simulating the propagation of a single electromagnetic wave. Furthermore, we summarize and validate the treatment of the refractivity in CoREAS and discuss the validity of our model.

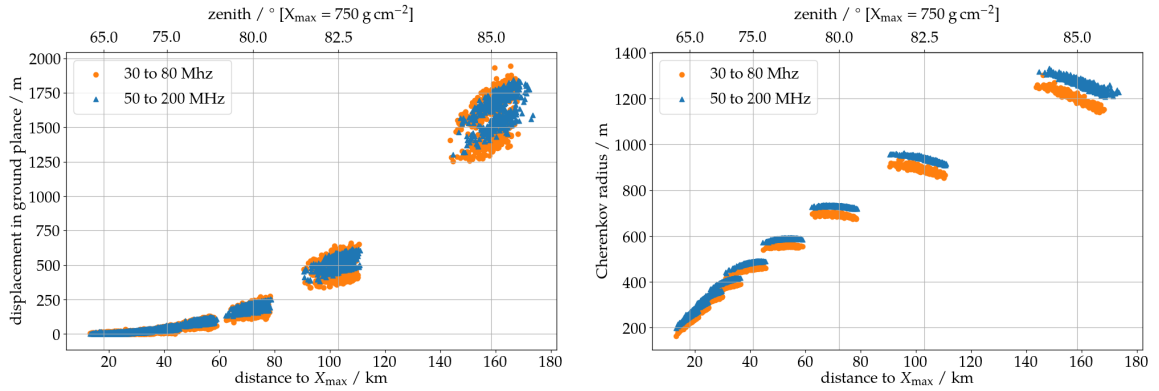


Figure 5.6.: *Left:* Displacement of the radio-emission footprint at ground for two different frequency bands. *Right:* Fitted radius of the Cherenkov ring in the geomagnetic emission for the two different frequency bands.

5.3.1. Description of refraction using Snell's law

We study the propagation of a single electromagnetic wave through the Earth's atmosphere described by a curved trajectory undergoing refraction according to Snell's law. For this purpose we assume discrete changes of the refractive index along the edges of imaginary curved layers throughout the atmosphere. The propagation within a layer with an upper edge height h_i is described by a straight uniform expansion with the phase velocity $c_n = c_0/n(h_i)$ given the refractive index as a function of the height above sea level $n(h)$. We adopt the refractive index as frequency-independent (i.e., non-dispersive) in the band from 30-200 MHz that we consider here. The change of direction between two layers with n_1 and n_2 is described in terms of the incidence angle (ϑ) from ϑ_1 to ϑ_2 following Snell's law

$$\frac{\sin \vartheta_2}{\sin \vartheta_1} = \frac{n_1}{n_2}. \quad (5.1)$$

The refraction is calculated in a curved atmosphere. The relationship between the geometrical distance from ground d_g and height above ground h_g is given for a zenith angle θ , observation level h_{obs} and the Earth's radius $r_{\text{earth}} = 6371$ km by

$$d_g^2 + 2(r_{\text{earth}} + h_{\text{obs}})(d_g \cos \theta - h_g) - h_g^2 = 0. \quad (5.2)$$

By solving this quadratic equation, one can calculate the height above sea level for every given distance to the ground by $h = h_g(d_g, \theta) + h_{\text{obs}}$. The refractive index for a given height $n(h)$ is calculated according Eq. (4.1) for the density profile $\rho(h)$ defined by the atmospheric model and the refractive index at sea level (n_0). We employ an atmospheric model with four exponential layers and one linear layer as used in CORSIKA/CoREAS, implementation from [66, 135]. Furthermore, to determine the incidence angle ϑ we account for the fact that the local zenith changes according to a spherical Earth w.r.t the zenith at the shower core. The thickness of each layer is set to 1 m assuring a high accuracy of the calculation¹.

¹ For simplicity of the algorithm is the thickness defined in a flat coordinate system, hence is the actual thickness (change in altitude) if the curved layers slightly varying.

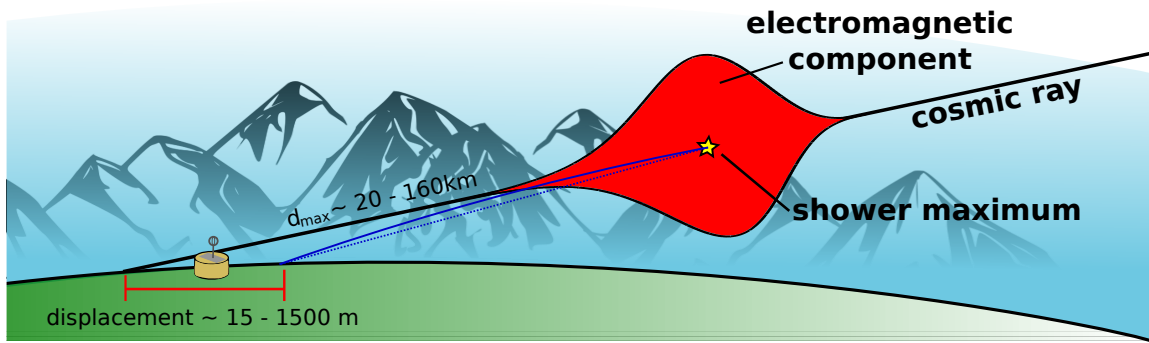


Figure 5.7.: Illustration for the refractive displacement in the atmosphere. The star illustrates the source, e.g., the shower maximum. The black line illustrates the MC shower axis, its intersection with the ground plane defines the MC impact point. The solid blue line illustrates a curved trajectory with same initial direction as the MC axis. The intersection of the curved trajectory with the ground defines the radio symmetry center. The deviation between the both intersections defines the displacement. The blue dotted blue line illustrates the straight line approximation for the curved trajectory. The arising curvature and symmetry center displacement are over-emphasized.

To predict the magnitude of a symmetry center displacement by refraction, we simulate the propagation of an electromagnetic wave along a bent trajectory with a starting point at a typical position for the shower maximum and an initial direction aligned to the direction of a shower (MC axis) towards the ground plane. The offset between the intersection of the bent trajectory with the ground plane and the intersection between a straight line with the initial direction of the electromagnetic wave and the ground plane is interpreted as the displacement. This approach is depicted in Fig. 5.7.

In Fig. 5.8 the predicted symmetry center displacement along the ground plane is shown as a function of the geometrical distance along the MC axis for shower geometries with a zenith angle between 65° and 85° . The orange line symbolizes the displacement for a source at a fixed slant depth of 750 g/cm^2 (e.g., shower maximum, average depth of maximum of our set of simulated showers). For a given slant depth, this distance translates to a zenith angle (top x-axis). Our model predicts a displacement of the order of 1.5 km for the most inclined showers at $\theta = 85^\circ$. In orange squares the displacement is shown for different slant depths between 620 g/cm^2 and 1000 g/cm^2 (typical range in our set of simulated showers) along the MC axis for 5 different zenith angles ($\theta = 65^\circ, 75^\circ, 80^\circ, 82.5^\circ, 85^\circ$). The model predictions are compared to the displacements determined from the CoREAS simulation set (colored circles: cf. Sec. 5.2, Fig. 5.4). The displacement is reasonably described by our model in terms of the overall magnitude (orange line) as well as the slope as a function of the source's slant depth (orange squares). In the bottom frame we show the absolute residuals between CoREAS displacement and refractive model. For their calculation we interpolated the model prediction along the orange squares to match the actual slant depth of the shower maximum of the simulated air showers. The residuals show no strong correlation with depth of shower maximum and increase up to $\sim 250 \text{ m}$ for the most inclined showers. Furthermore, our model predicts a displacement always towards the shower incoming direction. This corresponds to a refraction towards the ground, i.e., decreasing angle of incidence, which is given by a radially symmetric

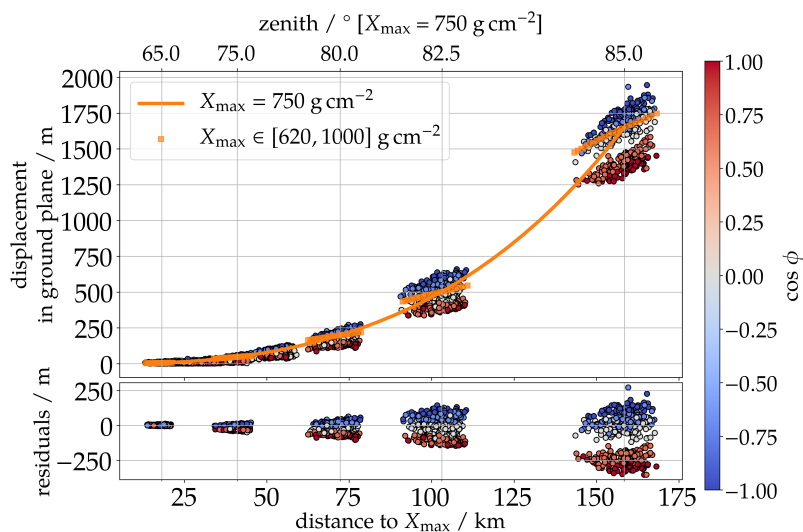


Figure 5.8.: Comparison between model-predicted and CoREAS-derived displacement of the radio symmetry center. The displacement is expressed within the ground plane. The orange line constitutes our model prediction for a source at a fixed slant depth of $X_{\max} = 750 \text{ g/cm}^2$ (translation to zenith angle on the top x-axis). The orange squares show the displacement as a function of the source slant depth (e.g. X_{\max}) for each given zenith angle (cf. top x-axis). The colored circles show the displacement determined from the CoREAS simulation set, cf. Fig. 5.4. The residuals are shown in the bottom frame.

atmosphere. In Fig. 5.5 this behavior was also observed for CoREAS simulations as the simulated showers exhibit a radio symmetry center displacement almost entirely in the incoming direction of the shower. As emphasized earlier, an East-West asymmetry as seen in CoREAS simulations, cf. Fig. 5.4 and 5.5, cannot be described by refractivity.

We verified that the impact of the atmospheric model, i.e. the density profile, is below 3% between the US Standard Atmosphere after Keilhauer and the Malargüe October atmosphere [118]. Comparing different observer altitudes we find no difference for the displacement as a function of d_{\max} . As already shown in Fig. 5.1, the refractivity at sea level has an influence on the predicted displacement. The yearly fluctuations of the air refractivity at the site of the Pierre Auger Observatory amount to 7% [121]. Varying N_0 over a range of $\pm 15\%$ we find the displacement to scale linearly with N_0 .

5.3.2. Refraction and its treatment in CoREAS

For the numerical calculation of the radio emission of an extensive air shower for an observer at ground, the refractive index has to be taken into account for two processes: First, in the generation of the radio emission for each particle. Second, in the propagation of each electromagnetic wave from a source to an observer. In CoREAS, the former is realistically included in the calculation of the radio emission from each particle using the endpoint formalism [59, 60, 56]. However, the treatment of the propagation is approximated. Since electromagnetic waves in the radio regime do not suffer from any significant attenuation effects while propagating through air, this propagation is described entirely

by two quantities. First, the geometrical distance (d), that the radio wave passes between source and observer, as the intensity of the emission scales with this distance. Second, the light propagation time (t_n) between source and observer which is of crucial importance as it governs the coherence of the signal seen by an observer from the full air shower. In CoREAS, t_n is calculated taking into account a refractive index dependent (phase-) velocity of the emission

$$t_n = \frac{1}{c} \int_{\text{source}}^{\text{observer}} n(h(\ell)) d\ell. \quad (5.3)$$

To calculate both quantities, CoREAS assumes a straight path between source and observer (cf. Fig. 5.7: blue dashed line). This approximation has implications for the geometrical distance between source and observer as a straight line underestimates the real distance along a curved trajectory. For the calculation of the light propagation time an additional implication arises from the fact that the average refractivity along a straight line varies from the refractivity along a curved trajectory. We find that the average refractivity and consequently the light propagation time is overestimated along straight trajectories.

We stress that the description of the propagation of the radio emission along straight trajectories in CoREAS is not in contradiction with the above-established refraction of the radio emission and the resulting displacement of the radio symmetry center in CoREAS simulations. In fact, the refraction of radio waves is a consequence of the fact that the propagation velocity changes with the refractive index c_n . It is in fact possible to achieve a displacement of the whole coherent signal pattern at ground by an accurate description of the light propagation time along straight trajectories, as we will demonstrate below.

To verify if the calculation along straight trajectories between source and observer is sufficiently accurate to calculate the radio emission seen from a full extensive air shower, we determine the geometrical distance and light propagation time following bent and straight trajectories (blue lines in Fig. 5.7) for several geometries. We simulate the propagation of an electromagnetic wave given incoming direction and atmospheric depth along a bent trajectory towards the ground plane. Once the trajectory intersects with this ground plane the process is stopped and d_{curved} and t_{curved} are calculated via a sum of d_i , t_{n_i} over all layers. Given the intersection and the initial starting point in the atmosphere, a straight trajectory is defined and d_{straight} and t_{straight} are calculated for comparison.

In Fig. 5.9 (left) the geometrical distance – compared between curved and straight trajectories in absolute terms of $d_{\text{curved}} - d_{\text{straight}}$, given the ambient conditions used for the employed simulation set. The comparison is shown as a function of the geometrical distance along the straight trajectory between source and observer. The source positions are set to be at an atmospheric depth of $X = 750 \text{ g/cm}^2$ for incoming directions with zenith angles between 65° and 85° . We obtain a maximal error of around 4 cm for the most inclined geometries with a path distance of $\sim 150 \text{ km}$. With a relative deviation of less than 1×10^{-6} , this approximation is completely suitable.

For the light propagation time, the relative difference for two source positions and one observer position between curved and straight trajectories $\sigma_t = \Delta t_{\text{curved}} - \Delta t_{\text{straight}}$ is of relevance as it governs the coherence of the total signal seen by a given observer. As we do not have an analytic description for curved trajectories, we can employ our model to find two source positions \vec{P}_1, \vec{P}_2 from which signals are emitted in two different directions $\hat{\theta}_1, \hat{\theta}_2$

which arrive via bend trajectories at the same observer position \vec{O} : $\vec{O}_2(\vec{P}_2, \hat{\theta}_2) - \vec{O}_1(\vec{P}_1, \hat{\theta}_1) = 0$. If we specify \vec{P}_1 , \vec{P}_2 , and $\hat{\theta}_1$ we can determine $\hat{\theta}_2$ via a root-finding algorithm. Besides evaluating light propagation time for the bend trajectories which connect \vec{P}_1 , \vec{P}_2 to \vec{O} , we do the same for straight lines and calculate σ_t . Fig. 5.9 (right) shows σ_t for different shower geometries (zenith angles) and configurations of \vec{P}_1 and \vec{P}_2 . The timing error σ_t between two sources which are located on one axis with a zenith angle between 65° and 85° and depths of 1000 g/cm^2 and 400 g/cm^2 is shown by the orange line. This slant depth range covers the bulk of the radiation energy release from the longitudinal development of an extensive air shower [121, Fig. 5]. In the most extreme case, the error in the relative arrival times for a source at the beginning of the shower evolution and a source at the end of the shower evolution, estimated using straight tracks, amounts to $\sigma_t \lesssim 0.1 \text{ ns}$. This is well below the oscillation time of electromagnetic waves in the MHz regime. The blue line in the same figure demonstrates the errors made for sources laterally displaced by a shift of $\pm 655 \text{ m}$ above and below the shower axis along an axis perpendicular to the shower axis at a depth of 750 g/cm^2 . This value was chosen such that it matches the Molière radius expected for a shower with $\theta = 85^\circ$ at $X_{\text{max}} = 750 \text{ g/cm}^2$ [136]. The errors due to the straight-line approximation for this source configuration are even much smaller.

While it may seem paradoxical on first sight that a calculation approximating propagation of electromagnetic waves along straight tracks can yield refractive ray bending, we have shown that the relevant calculation of relative arrival times is described well within the needed accuracy, i.e., is fully adequate for this purpose. We note that, similar to our findings, it was already found based on analytic calculations in reference [137, cf. Fig 9] that a straight-line approximation is sufficient for the calculation of relative arrival times of radio waves in extensive air showers.

Additionally, the refractive ray bending changes the incoming direction of the radio emission. This has implications for the reconstruction of the radio emission with real radio antennas as their response pattern is direction-dependent. We find a maximum change of direction of $\sim 0.14^\circ$, which is in agreement with [138]. This is below current experimental accuracy as well as the change in the incoming direction between early and late observers on the ground plane, estimated as $O(1^\circ)$ for a 85° shower.

5.4. Conclusions

We have established that the radio symmetry center is displaced with respect to the MC impact point in CoREAS simulations of inclined air showers. This displacement shows no significant dependence on the considered frequency band for non-dispersive refractivity. We have developed a model which reproduces this displacement quantitatively, describing it as a result of refraction of the radio waves during propagation in an atmosphere with a refractive index gradient. We have also discussed the validity of approximations made in CoREAS and shown that they are adequate to describe refractive effects in air-shower radio simulations. Furthermore, we have found indications that there are secondary effects causing additional scatter in the displacement of the radio symmetry center which is not related to the refractive index of the atmosphere or the atmosphere in principle but could be caused by the geomagnetic field.

5. Refractive core displacement

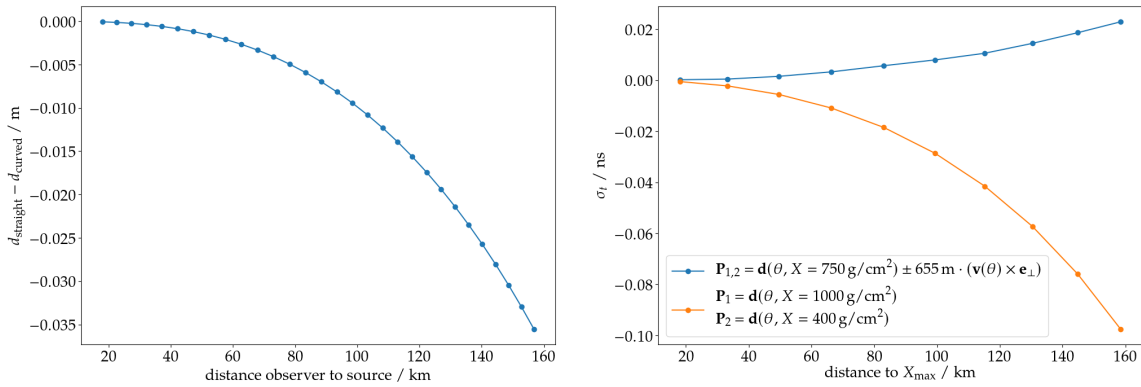


Figure 5.9.: *Left:* Difference in geometrical distance between a source at a depth of $X = 750 \text{ g/cm}^2$ and an observer at ground level for a straight-track calculation and curved-track calculation for zenith angles from 65° to 85° . *Right:* Difference in the relative arrival times calculated with curved and straight-track propagation $\sigma_t = \Delta t_{\text{curved}} - \Delta t_{\text{straight}}$ arising for two source positions and one observer position. Distance to X_{max} is calculated using a fixed depth of $X_{\text{max}} = 750 \text{ g/cm}^2$.

These findings have several implications towards the observation of cosmic rays with the radio detection technique. For the development of reconstruction algorithms (as in Chap. 6), assuming the MC impact point as symmetry center of the radio-emission footprint will disturb its lateral distribution, causing a mismodelling of the signal distribution. In observations the refractive displacement primarily has to be taken into account in the interpretation of the reconstructed shower geometry (as in Chap. 8). Considering hybrid detection and reconstruction, refractive displacement has to be taken into account when comparing/combining results across different detection techniques.

6. Signal model and event reconstruction for the radio detection of inclined extensive air showers

Parts of this chapter have been published in:

F. Schlüter and T. Huege

"Signal model and event reconstruction for the radio detection of inclined air showers"
[arXiv:2203.04364](https://arxiv.org/abs/2203.04364) (Publication to JCAP in process)

Exploiting the full potential of the radio detection of inclined air showers imposes the need of an accurate analytic description of the signal distribution of radio emission from those events. Such a model is indispensable for an accurate event reconstruction, i.e., reconstructing shower observables like the (electromagnetic) shower energy. While for air vertical showers (i.e., with zenith angles $\theta < 60^\circ$) several signal models of the radio emission at ground to reconstruct the shower energy have been proposed [139, 123] and used with experimental data [88], the understanding of inclined air showers has so far been much less mature.

For vertical showers, the lateral signal distribution of the radio emission is described based on the macroscopic interpretation of two emission mechanisms, the charge-excess (Askaryan) and geomagnetic emission [49]. Additionally, the proposed models for the radio emission at ground account for the temporal "Cherenkov" compression of the radio emission which causes an enhancement of the coherent emission at a characteristic distance around the shower axis forming an annulus in the emission pattern (Cherenkov ring). Both, the interference between the emission mechanisms and the Cherenkov ring are known to change with the ambient atmospheric conditions in the emission region of an air shower and hence change with the showers' zenith angles. An additional asymmetry due to geometrical projection effects becomes significant for zenith angles beyond 60° and further disturbs the radio-emission footprint of inclined air showers [120]. Thus, we need to develop new models to describe the radio-emission footprints of inclined air showers.

Here, we present a model which describes the 2-dimensional lateral signal distributions – "radio-emission footprints" – from inclined air showers in the 30 MHz to 80 MHz band. We describe the radio-emission footprints in energy fluence f [eV m^{-2}], i.e., the energy deposit per unit area, by an individual modeling of a symmetric signal distribution and additional effects introducing asymmetries, resulting in significantly asymmetric signal patterns. The symmetric signal distribution is associated with the geomagnetic emission

and can be described by a simple 1-dimensional lateral distribution function (LDF). Using a comprehensive set of CoREAS simulations we found that the shape of this LDF can be described with a single parameter d_{\max} the geometrical distance between shower core and the shower maximum. The additional effects causing “asymmetries” are associated with the interference of the geomagnetic emission and the sub-dominant charge-excess emission as well as with geometrical projection effects, so-called “early-late” effects. For both asymmetries, we find a description based only on d_{\max} and the position of an observer (i.e., the position of a radio pulse) in the shower plane. Hence, the entire radio-emission footprint is described by two observables, the geomagnetic radiation energy E_{geo} (spatial integral over the energy deposit of the geomagnetic emission at ground) regulating the total magnitude of the emission pattern and d_{\max} regulating the shape of the emission pattern. In addition to the aforementioned asymmetries, in this study we take into account the refractive displacement of the symmetry center of radio emission, which was introduced in the previous Chap. 5. From this model, we derive a robust and efficient reconstruction algorithm with 4 free parameters (E_{geo} , d_{\max} + 2 position coordinates). We have also implemented the module in the `Offline`-module `RdHASLDFitter`.

The model presented here is tuned to the ambient conditions of the Pierre Auger Observatory [140], located near the city of Malargüe, Argentina, in the Southern Hemisphere. This concerns the local magnetic field (strength and orientation), the observation height (altitude), and atmospheric conditions. The frequency band of 30 MHz to 80 MHz is used by most current-generation large-scale radio detector arrays [132, 133, 97] and in particular by the RD. However, many next-generation radio experiments [134, 127, 141] aim to cover higher frequencies and larger bands. In Sec. 6.4 we will discuss the adaptability of this model for different ambient conditions and frequency bands.

This article is structured as follows: In section 6.1, we discuss the sets of simulated showers used in this chapter and the treatment of the simulated radio signals. In the previous chapters we already gave a qualitative description of the highly asymmetric radio-emission footprints from inclined air showers. Now, in section 6.2 an analytic description of those footprints is presented. In section 6.3, this signal model is used to reconstruct the electromagnetic shower energy for simulations with a realistic, sparse antenna array. Finally, we discuss and conclude in sections 6.4 and 6.5.

6.1. Treatment of the simulated radio emission from inclined air showers

In this chapter we use 2 sets of simulated showers. In section 6.2, showers simulated with star-shaped antenna grids and different atmospheres are used to derive an analytic description of the radio-emission footprints. For the development of the model we only use showers with a geomagnetic angle $\alpha > 20^\circ$. This ensures a strong geomagnetic emission, whose modelling is central to our model and that the Eqs. (4.5) and (4.6) are valid (cf. Sec. 4.2.1). In section 6.3 the 15970 simulations with the RD detector layout and the Malargüe October atmosphere are used to evaluate the reconstruction of the electromagnetic shower energy with the here developed analytic model.

In the following subsections we will discuss a few technical aspects crucial for the development of the signal model.

6.1.1. Estimation of the energy fluence

To calculate the energy fluence f we sum over the squares of the electric field amplitudes in a 100 ns time interval centered around the peak. The peak is defined as the maximum of the quadratic sum of the Hilbert envelopes from all 3 polarizations. As we do not add noise to the simulated signals, we do not subtract the integrated power from a noise window (cf. second term in Eq. (8.3)). We decompose our signals as detailed in Sec. 4.2.1. This entails a rotation of the simulated traces into the $\vec{v} \times \vec{B}$ and $\vec{v} \times (\vec{v} \times \vec{B})$ polarizations using the MC shower arrival directions as well as employing Eqs. (4.5) and (4.6). The simulated pulses are band-pass filtered to the band of 30 MHz to 80 MHz with an idealized rectangle filter. A frequency resolution of ~ 100 kHz is ensured by zero-padding the traces to the required length.

6.1.2. High-frequency emission artifacts from particle thinning

To compute the radio emission from (inclined) air showers with reasonable computational effort, a technique called *thinning* is used [117]. This implies that particles produced in a single interaction and below a certain energy threshold are removed from the simulation except for one randomly selected particle. This particle is assigned a weight such that energy conservation is preserved. The probability for a particle to be selected is proportional to its energy. This dramatically reduces the number of particles to be simulated while correctly reproducing showers on average. Random particle fluctuations and thus shower-to-shower fluctuations are affected. However, if the energy threshold and the maximum weight a particle can be assigned with are chosen wisely, the effect is tolerable. For the simulation of the radio emission, *thinning* introduces another problem. Particles with large weights, which represent many particles, emit perfectly coherent radio waves while the actual ensemble of particles it represents would not radiate fully coherently. This effectively introduces artificially additional power in the radio emission at ground from the emission of single particles with large weights. For small lateral observer distances, this power is well below the actual coherent radio emission. However, for increasing lateral distances or when considering higher frequencies, i.e., with decreasing coherence, this artificial signal starts to significantly impact the simulated power and subsequently, the affected pulses need to be rejected.

In the left panel of Fig. 6.1, the spectra of two pulses are presented. The observer of one pulse is closer to the shower axis (*top*) and one further away (*bottom*). For both pulses, the spectra of the $\vec{v} \times \vec{B}$ - and $\vec{v} \times (\vec{v} \times \vec{B})$ -polarizations are shown, representing the signals of the geomagnetic and charge-excess emission contributions, respectively, as both observers are situated on the $\vec{v} \times (\vec{v} \times \vec{B})$ axis. The band of interest from 30 MHz to 80 MHz is highlighted. Both spectra show the same feature: A smooth exponential decay of the amplitude followed by a noisy plateau. While the first is expected for coherent emission, the latter is not and thus interpreted to be caused by thinning. While the pulse of the

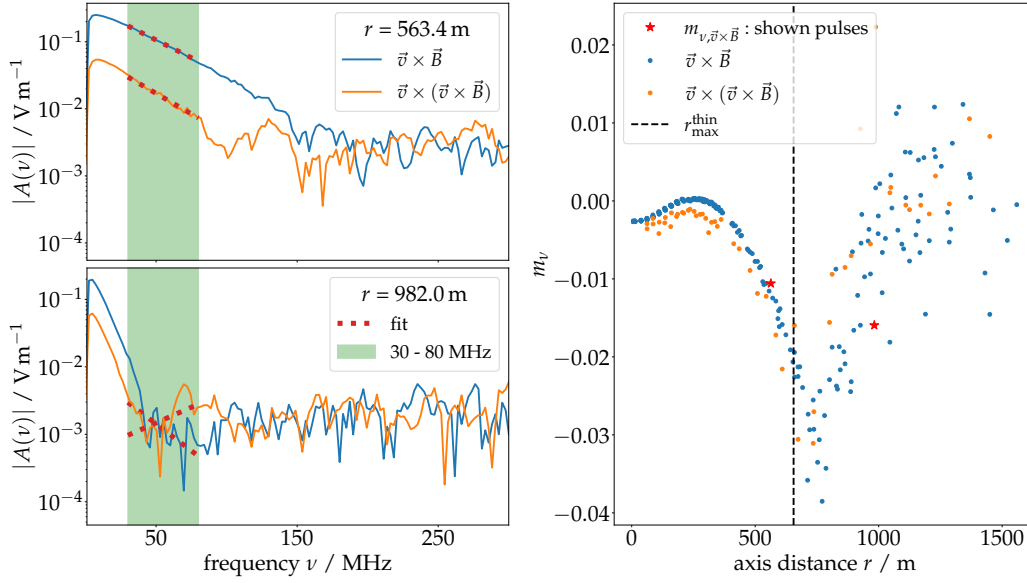


Figure 6.1: *Left:* Spectra of two simulated pulses of observers situated on the $\vec{v} \times (\vec{v} \times \vec{B})$ -axis at different distances to the MC shower axis (cf. legends). For each pulse the frequency content in the $\vec{v} \times \vec{B}$ and $\vec{v} \times (\vec{v} \times \vec{B})$ polarizations (i.e., geomagnetic and charge-excess emission for observers on the $\vec{v} \times (\vec{v} \times \vec{B})$ -axis) is shown. The greenish band highlights our frequency band of interest, the dashed red lines show fits according to Eq. (6.1) to the underlying spectra. *Right:* The fitted spectral slopes m_ν as a function of the lateral distance. For the $\vec{v} \times (\vec{v} \times \vec{B})$ polarization, only the slope from observers on the $\vec{v} \times (\vec{v} \times \vec{B})$ -axis and with an axis distance of at least 50 m are shown (because pulses of observers close to the shower axis or on the $\vec{v} \times \vec{B}$ -axis contain almost no signal in the $\vec{v} \times (\vec{v} \times \vec{B})$ -polarization, hence it does not make sense to calculate the slope and use it as a criterion to detect thinning). The slopes in the $\vec{v} \times \vec{B}$ polarization from the pulses presented in the left panels are highlighted with stars. The dashed, black line indicates the distance cut used to reject pulses affected by thinning (details in the text).

closer observer is not (or in the case of the $\vec{v} \times (\vec{v} \times \vec{B})$ -polarization only slightly) affect by the noise floor in the band of interest, the pulses of the observer further away from the shower axis show a significant disruption in both polarizations and thus have to be rejected from further analysis. To quantitatively examine whether a pulse is contaminated or not, we fit a first-order polynomial to the logarithmic spectrum in the frequency ν range between 30 MHz to 80 MHz, i.e.,

$$\mathcal{A}(\nu) = 10^{m_\nu \cdot \nu + b} \quad (6.1)$$

with a slope parameter m_ν and a constant b . The slope parameter m_ν as a function of the lateral distance for an example shower is shown in Fig. 6.1 (*right*). While the spectrum is almost flat ($m_\nu = 0$) on and around the Cherenkov ring, it is falling more steeply with increasing lateral distance as expected. Around 750 m a kink is visible. The lateral distance of the observer whose pulse in the $\vec{v} \times \vec{B}$ polarization has the steepest slope, defined as r_{\min} , is identified, after which the disruption in the considered band becomes considerable. In a conservative selection for the following study (the parameterization of the charge-excess fraction in Sec. 6.2.3) we consider the pulses of all observers with a lateral distance smaller

than $0.85 r_{\min}$ as clean, pulses of observers with a larger lateral distance as contaminated by thinning artifacts for both polarization. For the example event, the dashed line indicates this criterion. The considered maximum lateral distance per shower scales in first order with the zenith angle and just slightly with the energy (This is expected since energy-dependent weight limitation was used [117] to simulate the air showers). For highly inclined showers, observers with lateral distances of over 2 km are still considered. With this selection, the number of considered observers decreases from 240 to around 160 per simulated shower.

For fitting the lateral distribution of the geomagnetic emission (cf. Sec. 6.2.2), we consider all observers (even the ones with pulses affected by thinning artifacts), but assign an appropriate uncertainty to all signals, effectively reducing the impact of weak signals, to avoid any bias from affected pulses.

6.1.3. Systematic core displacement due to refraction

Recently, an additional “apparent” asymmetry in the radio-emission footprint of inclined air showers had been reported [130]. In Chap. 5 we show that this “apparent” asymmetry can be explained and resolved by a displacement of the whole radio-emission footprint from the MC core position. This core displacement is explained by the refraction of the radio emission during propagation in Earth’s atmosphere. Here, we account for it by allowing the radio core, i.e., the coordinates of the radio symmetry center, to vary from the MC core. The coordinates are found fitting the lateral signal distribution, cf. Sec. 6.2.2. The displacement also implies that the distance between the symmetry center of the radio emission and the shower maximum changes w.r.t. d_{\max} , which is defined as the distance between the MC shower core and the shower maximum. However, this effect is below 1% for all zenith angles and thus ignored in the following.

6.2. Model for the radio-emission footprints

The complex asymmetry pattern in the radio-emission footprints from (inclined) extensive air showers can be described by the interference of the two known macroscopic emission mechanisms, the geomagnetic and charge-excess (Askaryan) emission, and a ring-like feature around the shower axis which is due to Cherenkov-like time compression as already demonstrated for vertical showers. In Ref. [123], the lateral distributions of vertical showers were described individually the geomagnetic and charge-excess emission. For inclined air showers, the relative (and absolute, see Sec. 4.3.1) strength of the charge-excess emission decreases, making it difficult to obtain an unbiased estimation of the charge-excess emission from measured data, i.e., in the presence of ambient noise. Hence, our model relies primarily on the modeling of the dominant geomagnetic emission. Of course, we have to account for the interference of the geomagnetic and charge-excess emission contributions. Therefore, we define a charge-excess fraction (Sec. 6.2.3) to subtract the charge-excess emission from the emission in the $\vec{v} \times \vec{B}$ -polarization. After that subtraction, we are left with the geomagnetic emission f_{geo} which is distorted by a geometrical early-

late asymmetry. After removing this early-late signature, we describe the then symmetric geomagnetic emission with a 1-dimensional (rotationally symmetric) LDF.

In the following, we first formulate and evaluate the asymmetry correction for the early-late signature on the emission pattern of inclined air showers, Sec. 6.2.1. Second, we parameterize the shape of the early-late corrected geomagnetic emission with an appropriate 1-dimensional LDF, Sec. 6.2.2. And finally, we parameterize the charge-excess fraction in Sec. 6.2.3.

6.2.1. Geometrical early-late effects

For non-vertical showers, observers at the ground which are below the shower axis will measure the radio emission at an “earlier” stage of the shower development than observers above the shower axis. Given that for inclined air showers at ground level, the total radiation energy has already been released, the radio emission at an earlier stage, i.e., at a shorter distance to the emission region, will have a higher intensity and consequently, an early observer will measure a stronger signal (cf. Fig. 6.2) than a late observer. Additionally, an early and late observer with equal axis distance will not have the same off-axis or viewing angle, i.e., not the same angle between the line-of-sight from a point-like emission source (assumed to be at X_{\max}) to the observer and the shower axis. Both effects will introduce an asymmetry in the lateral distribution of the emission as a function of the axis distance. To correct for these effects and eliminate the asymmetry, we, on the one hand, project the observer positions (their axis distances) onto the plane perpendicular to the shower axis intersecting with the core, i.e., the shower plane, and on the other hand, correct for the spherical propagation between early and late observers by scaling their signals to the positions in the shower plane. Thereby, we assume the radio emission to expand spherically from a point-like source at the shower maximum with the distance d_{\max} to the shower plane, hence the electric field amplitudes scale with the inverse of d_{\max} and thus $f \sim d_{\max}^{-2}$. With this ansatz, the necessary corrections for an observer at the position \vec{x}_i can be derived [120]. With the correction factor

$$c_{\text{el}_i} \equiv \frac{d_{\max} + \vec{x}_i \cdot \vec{e}_v}{d_{\max}} = 1 + \frac{z_i}{d_{\max}} \quad (6.2)$$

the necessary correction are described by the following equations

$$f_i = f_{\text{raw}_i} \cdot c_{\text{el}_i}^2, \quad r_i = \frac{r_{\text{raw}_i}}{c_{\text{el}_i}}. \quad (6.3)$$

The factor c_{el_i} is smaller than 1 for early observers (z_i is negative because \vec{e}_v points into the direction of the shower particles) and larger than 1 for late observers. Note that due to the notation of \vec{v} and \vec{B} , observers in the positive $\vec{v} \times (\vec{v} \times \vec{B})$ direction are early and observers in the negative $\vec{v} \times (\vec{v} \times \vec{B})$ direction are late. With this projection into the shower plane, equal axis distances correspond to equal viewing angles and signals measured at the same distance between the point-like source and observers (for equal axis distances).

To evaluate the early-late correction, we have simulated an extra set of 17 showers which have observers on a star-shaped grid in the ground plane (equivalent to showers

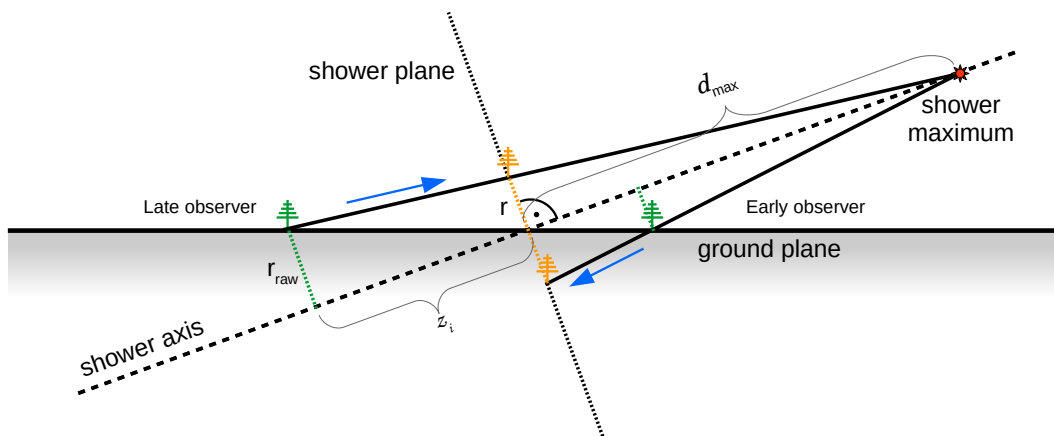


Figure 6.2.: Illustration of an inclined air shower with an early and late observer. To correct for early-late asymmetries, we *project* signals measured at ground plane (indicated with green antenna symbol) along the line of sight from antenna to shower maximum into the shower plane (yellow). See text for details.

described in Sec. 4.1.1) and additional observers on a star-shaped grid situated in the shower plane, i.e., in a plane perpendicular to the shower axis¹. The positions of the observers in the shower plane were chosen such that they correspond to the early-late correct shower-plane coordinates of the observers in the ground plane².

In practice, these effects become relevant for sparse arrays only beyond a zenith angle of 60° and imprint an early-late asymmetry in the radio-emission footprint. In Fig. 6.3 (left) the lateral distributions for a 80° shower with observers, simulated both in the ground and shower planes, are shown. The lateral distribution for the observers in the shower plane (orange circles) has no early-late asymmetry imprinted and is much more narrow than the distribution for the observers in the ground plane (green squares). The early-late corrected lateral distribution simulated at the ground (blue triangles) shows a good agreement with the distribution directly simulated in the shower plane. In the bottom panel, the ratio between the corrected ground signals and shower plane signals shows only a slight degradation for large axis distances.

A more quantitative comparison is given in Fig. 6.3 (right) which presents the ratio between corrected and directly simulated signals³ across all 17 showers with zenith angles ranging from 65° to 85° as a function of the lateral distance. The axis distance is normalized to the Cherenkov radius r_0 expected for these showers (cf. Eq. (4.4)). As seen in the previous example, the accuracy decreases for larger axis distances. The inset shows a histogram of the presented data. The overall correction is better than 5%.

¹ In fact “floating” in the air or being underground.

² To construct the two star-shaped grid so that their coordinates match X_{\max} has to be known. In fact, we took already simulated showers, added the second star-shaped grid and re-simulated them

³ Observers with $c_{el} = 1$, i.e., which are situated exactly perpendicular to the air shower axis, are removed from the analysis.

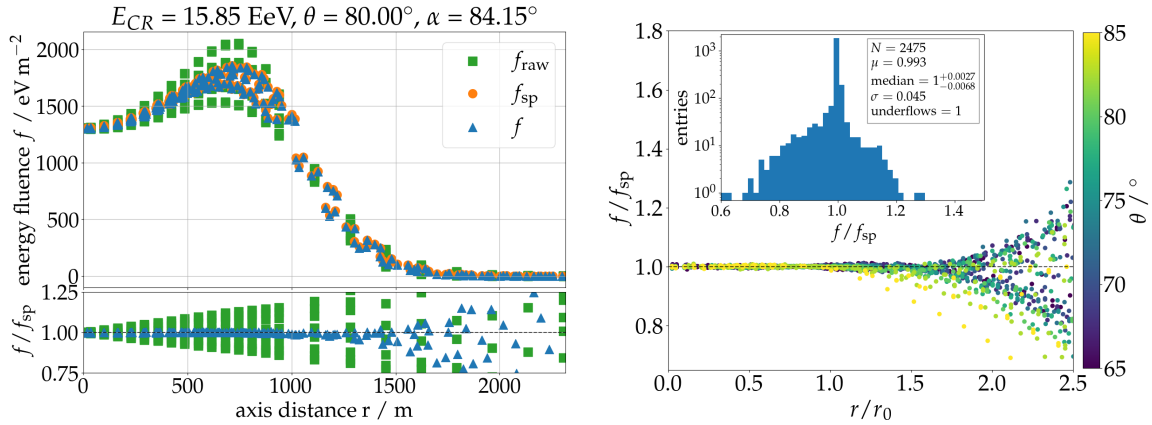


Figure 6.3.: Comparison of the energy fluences f_{sp} simulated directly in the shower plane and energy fluences f simulated in the ground plane followed by early-late correction to the shower plane. *Left:* As a function of energy fluence. *Right:* As a function of axis distance normalized to the axis distance of maximum energy fluence. Inset: Histogram of the deviation between simulated and corrected fluence.

6.2.2. Lateral distribution of the geomagnetic emission

While the total radio signal exhibits asymmetries, the purely geomagnetic emission is assumed to be rotationally symmetric after geometrical projections effects have been removed. It can thus be described by a 1-dimensional LDF. In Refs. [123, 97], the LDF describing the geomagnetic emission of vertical showers is modeled using a quadratic polynomial in an exponential, i.e., a Gauss curve. This functional form is adequate to describe the Cherenkov ring, i.e., the initial rise in energy fluence which is followed by an exponential decay⁴. For more inclined showers, the Cherenkov ring increases in radius, causing a more subtle increase of the emission strength close to the shower axis. For those signal distributions we did not achieve satisfying results describing them with a Gauss. In previous iterations of our model, we used a polynomial of the 3rd order in an exponential to account for this more subtle increase. This LDF could describe the region around the Cherenkov ring better but decayed too rapidly at larger axis distances, undershooting the simulated signal distribution. Now, to accommodate for the larger and more faint Cherenkov ring and improve the description at larger axis distances, we extend a Gauss by the addition of a sigmoid. The sigmoid modifies the LDF within the Cherenkov ring and allows for a less drastic decrease of the emission towards the shower axis (cf. Fig. 6.4). The combination of a Gauss and sigmoid yields a function f_{GS} with 7 parameters, an amplitude f_0 , and 6 parameters defining the shape of the LDF r_0^{fit} , σ , $p(r)$, a_{rel} , s , and r_{02} :

$$f_{\text{GS}}(r) = f_0 \left[\exp \left(- \left(\frac{r - r_0^{\text{fit}}}{\sigma} \right)^{p(r)} \right) + \frac{a_{\text{rel}}}{1 + \exp(s \cdot [r/r_0^{\text{fit}} - r_{02}])} \right]. \quad (6.4)$$

⁴ Such an LDF describes vertical showers only if the detector is sufficiently far from the emission region, otherwise the shower is not fully developed and the distribution of the radio emission changes. This is not a problem for inclined air showers as here detector and shower are always sufficiently far from each other.

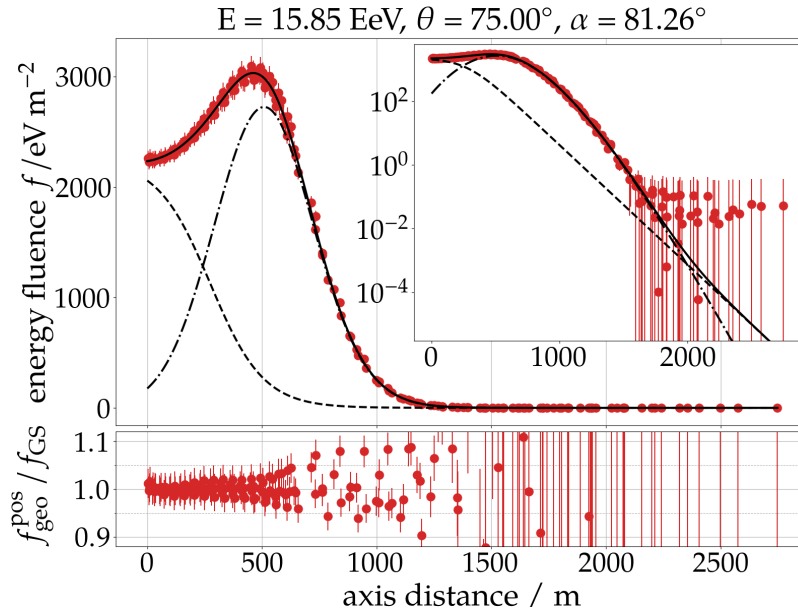


Figure 6.4.: Lateral distribution of the geomagnetic emission in terms of its energy fluence (red markers). The distribution is accurately described by the LDF $f_{\text{GS}}(r)$ which is the sum (solid line) of a Gaussian (dashed-dotted line) and a sigmoid (dashed line). The bottom panel shows the relative deviation between the true and fitted LDF. The tail of the lateral distribution exhibits a nonphysical flattening due to thinning which is compensated for by setting appropriate uncertainties.

An example fit of this function is shown in Fig. 6.4 demonstrating an overall good agreement until very large axis distance when thinning dominates. The tail (here at around 1000 m) is now more accurately described than before [142]. However, for even larger axis distances of around 1500 m or more, the LDF does not follow the distribution anymore. This flattening of the simulated distribution is not expected for the coherent radio emission from extensive air showers but is rather the result of thinning (cf. Sec. 6.1.2).

The lateral profile of the geomagnetic emission shown in Fig. 6.4 is obtained using Eq. (4.5) and after applying the early late correction. Furthermore, while fitting f_{GS} to the distribution we allow for a shift of the core coordinates which impacts the Eqs. (4.5) and (6.2) to compensate for refractive displacement. Hence, we recalculate the geomagnetic emission and early-late correction in each iteration of the fitting procedure (for fixed d_{max}). For fitting we use the *lmfit* python package [143] and a χ^2 minimization. To avoid any bias in the fitting of f_{GS} due to the thinning noise in the tail of the signal distribution, we assign (relatively) large uncertainties to these signals (cf. the large error bars in that figure),

$$\sigma_{f_{\text{geo}}} = 0.03 f_{\text{geo}} + 10^{-4} f_{\text{geo}}^{\text{max}}. \quad (6.5)$$

With this uncertainty model, the reduced $\chi^2/\text{n.d.f.}$ -distribution for all showers has a mean around 1.

The Gauss-parameters⁵ r_0^{fit} and σ can be interpreted as the position, i.e., radius, and width of the Cherenkov ring. However, it should be noted that r_0^{fit} does not coincide

⁵ $p(r) \sim 2$.

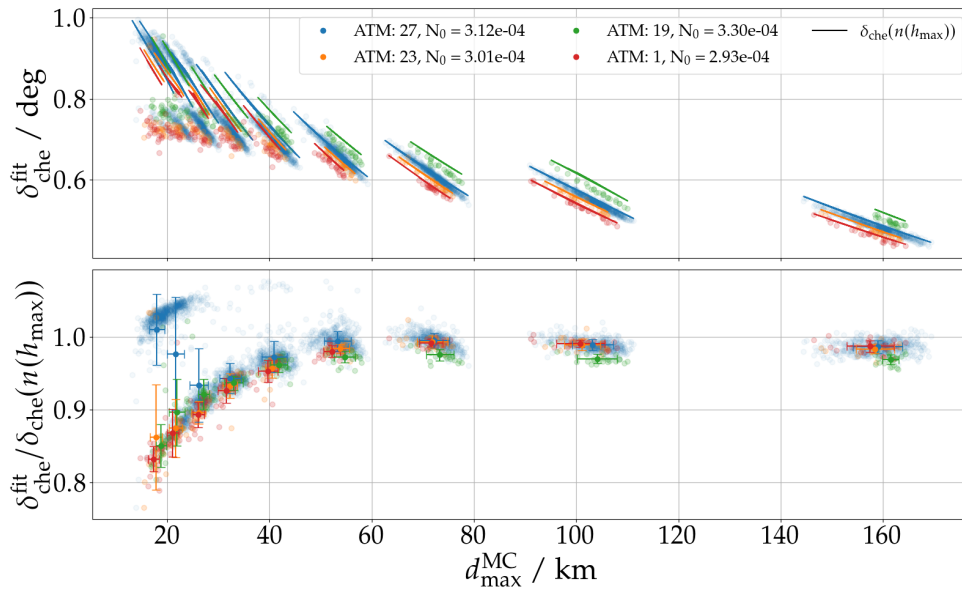


Figure 6.5.: Top: Cherenkov angle δ_{Che} as calculated from the refractive index n at shower maximum by Eq. (4.4) (lines) compared to the angle $\delta_{\text{Che}}^{\text{fit}}$ calculated from r_0^{fit} extracted from fitting Eq. (6.4) to individual showers (points). Simulations with four different atmospheric models are shown (pre-defined in CORSIKA 7, with refractivity at sea level set to the value quoted as N_0). Bottom: Deviation between fitted and calculated values. The profiles show the mean and standard deviations of the fitted values.

with the axis distance exhibiting the maximum signal strength, in fact it is slightly larger. This is plausible as the emission pattern is a superposition of a decaying exponential function and the ring-like feature. The exponent of the Gaussian, $p(r)$, is fixed to 2 for axis distances smaller than r_0^{fit} but can decrease for larger axis distances to accommodate a slower exponential decay (see Eq. (6.7)). This allows for a better description of the tail of the LDF and was already introduced in Ref. [123]. a_{rel} regulates the relative amplitude of the sigmoid term with respect to the Gauss term. The parameters s and r_{02} define the shape of the sigmoid term.

While it is no problem to fit an LDF with 7 free parameters (+ 2 core coordinates) to a well-sampled simulated event, in experimental data the signal multiplicity is generally much lower. Furthermore, measured signals are subject to uncertainties and start values for the fit parameters are uncertain. Hence, it is desirable to reduce the number of parameters, i.e., exploit the correlation between the fit parameters and shower observables. Thereby, one constrains, e.g., the shape of the LDF to physically reasonable forms. We investigate the correlation of all fit parameters (but f_0) with d_{max} (this includes an implicit dependency on the zenith angle, atmospheric model, and observation height). To investigate the correlation with d_{max} for the different fit parameters, we first fit f_{GS} with all parameters (but fixing $s = 5$) to the lateral profiles of all showers in our dedicated simulation set. We fix the slope of the sigmoid $s = 5$ as this ensures that the sigmoid is only dominant within the Cherenkov ring, as desired, and to generally simplify the following procedure and stabilizes the fitting. Then we pick a parameter and parameterize its correlation to

d_{\max} . Next, we fit all our showers again but this time fixing the chosen parameter to its parameterization and inspecting a next parameter. We repeat this procedure until all parameters are parameterized.

First, we investigate how the radius of the Gaussian r_0^{fit} relates to d_{\max} . In Fig. 6.5, the opening angle of a cone defined by d_{\max} (height) and r_0^{fit} (radius of the base), i.e., $\delta(r_0^{\text{fit}})^{\text{fit}} = \tan(r_0^{\text{fit}}/d_{\max})$ is shown (top panel) as a function of d_{\max} (dots). The prediction for the Cherenkov angle δ_{Che} at the shower maximum according to Eq. (4.4) is shown as well (lines). Both the fitted values δ^{fit} and the theoretical prediction are shown for 4 different simulated atmospheres (for more information about the simulated atmospheres see appendix B.2). The bottom panel shows the relative deviation between fitted and predicted angles. The comparison shows an overall remarkable agreement for larger zenith angles and different atmospheres. For lower zenith angles, a systematic deviation can be found. However, it is possible to use $r_0(d_{\max})$ (Eq. (4.4)) instead of fitting r_0 , without losing significant accuracy. We carefully checked that the remaining free parameters sufficiently compensate for the deviations introduced when using the predicted value of r_0 . In the following, we refer to r_0 as the Cherenkov radius.

Next, we parameterize $\sigma(d_{\max})$. The left panel in Fig. 6.6 shows the values derived for $\sigma(d_{\max})$ when fitting all showers with r_0 fixed to Eq. (4.4) and the slope $s = 5$ (blue circles). The red markers illustrate the mean and standard deviation (vertical error-bars, the bin sizes are indicated by the horizontal error-bars) of the fitted data. The green line shows our parameterization for σ ,

$$\sigma = \left(0.132 \cdot \left(\frac{d_{\max} - 5 \text{ km}}{\text{m}} \right)^{0.714} + 56.3 \right) \text{ m}. \quad (6.6)$$

We normalize the function with the term “ $d_{\max} - 5 \text{ km}$ ” to decrease the statistical fluctuations in the fitted parameters. However, this restricts the parameterization to values of $d_{\max} > 5 \text{ km}$. $d_{\max} < 5 \text{ km}$ is very unlikely for hadron-initiated air showers with zenith angles $\theta > 60^\circ$ as it would require depths of $X_{\max} > 1200 \text{ g cm}^{-2}$. And also for neutral particles for which a $d_{\max} < 5 \text{ km}$ is not difficult to imagine, this limitation does not matter as air showers which are closer than 5 km will, regardless of the zenith angle, illuminate an area too small for a measurement with sparse arrays. The uncertainties of the fitted data are statistical, estimated from the χ^2 -minimization of the LDF fit. They can not explain the deviation of single data points from the parameterization. It can not be excluded that those points represent an alternative minimum. However, the global minimum can be easily identified with the parameterization by the vast majority of the data. To obtain the optimal parameter for the parameterization in Eq. (6.6) we employed again a χ^2 -minimization, this time using the *iminuit* python package [144].

The same procedure is now applied consecutively to the parameters $p(r)$ (resp. b), a_{rel} , and r_{02} , in this order and always describing the previously parameterized parameters by their respective parameterizations found in the previous iteration. Their distributions are shown in Fig. 6.6 and their parameterizations are given by Eqs. (6.7) - (6.9):

$$p(r) = \begin{cases} 2 & r \leq r_0 \\ 2 \cdot (r_0/r)^{b/1000} & r > r_0 \end{cases}, \quad b = 154.9 \cdot \exp\left(-\frac{d_{\max}}{40.0 \text{ km}}\right) + 64.9, \quad (6.7)$$

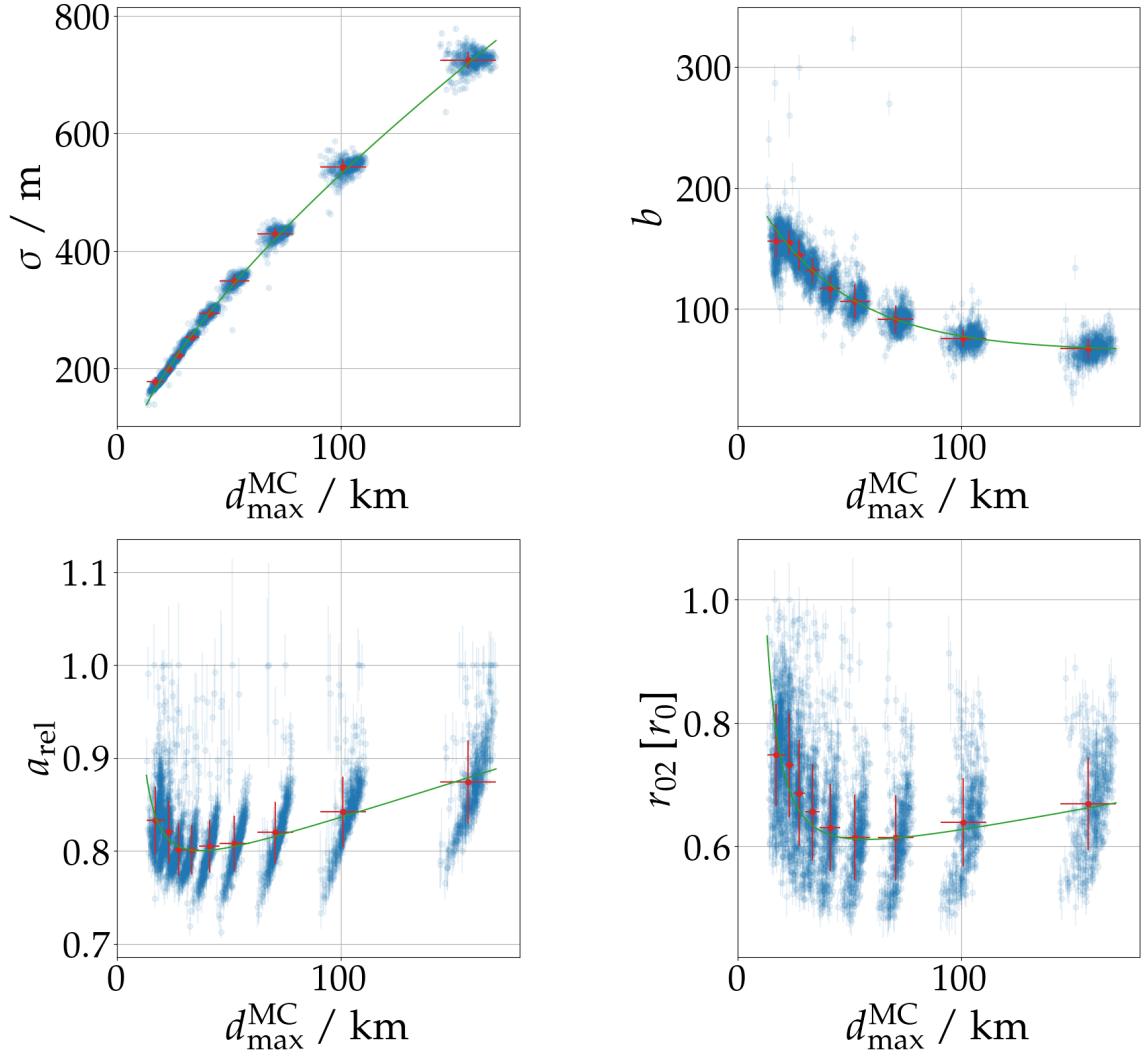


Figure 6.6.: Parameterizations according to Eqs. (6.6) - (6.9) (green lines) compared with the fit values for individual simulations (blue points) as well as their profiles (red points; means and standard deviations).

$$a_{\text{rel}} = 0.757 + \frac{d_{\text{max}}}{1301.4 \text{ km}} + \frac{19.8 \text{ km}^2}{d_{\text{max}}^2}, \quad (6.8)$$

$$r_{02} = 0.552 + \frac{d_{\text{max}}}{1454.2 \text{ km}} + \frac{66.2 \text{ km}^2}{d_{\text{max}}^2}. \quad (6.9)$$

In the distributions for a_{rel} and r_{02} , an additional trend, not described by the parameterizations, is significant. Within one zenith angle bin, a steep increase of the corresponding parameter from deep to shallow showers is apparent. The matter is further discussed in Sec. 6.4, for now we choose to only describe the correlation of all parameters with d_{max} .

We also verified the fit results for different atmospheres. We found that the October atmosphere used here describes the mean well. More information and plots regarding this aspect can be found in appendix B.2.

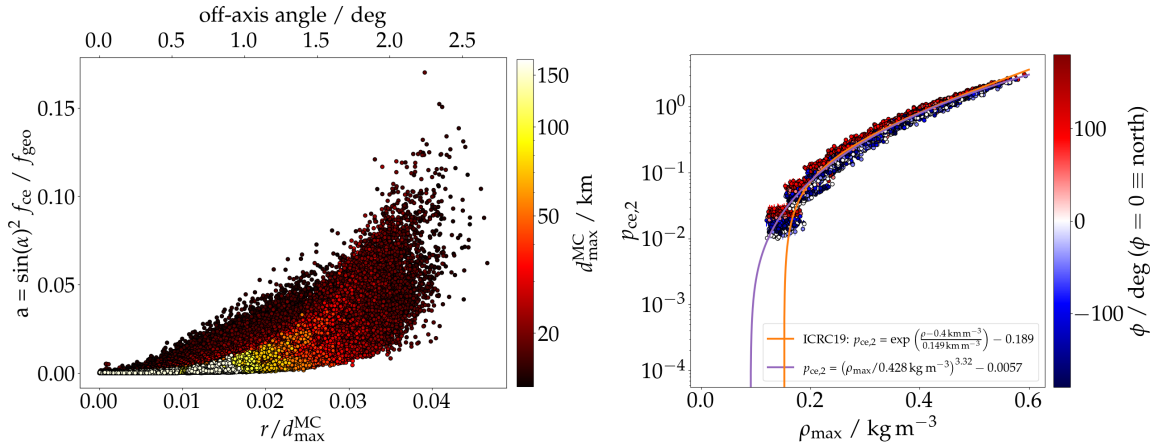


Figure 6.7.: *Left:* Lateral distribution of the charge-excess fraction a_{ce} (cf. Eq. (6.10)) for all showers with zenith angles from 65 to 85°. Pulses affected by thinning (cf. Sec. 6.1.2) and on the $\vec{v} \times \vec{B}$ axis are excluded. The lateral distance is normalized with d_{\max} . For small angles, this translates to the off-axis angle (the values in degree are annotated at the top). The color code shows d_{\max} and highlights a dependency on the shower geometry. *Right:* Optimized density scaling of the charge-excess fraction as a function of the air density at the shower maximum ρ_{\max} . The color code denotes the shower arrival direction. Lines are explained in the text.

6.2.3. Parameterization of the charge-excess strength

So far, we have determined the geomagnetic emission from the simulated pulses using Eq. (4.5) based on the known polarization characteristics of both mechanism. Thereby, the estimation of the charge-excess emission relies on the emission measured in the $\vec{v} \times (\vec{v} \times \vec{B})$ -polarization which for inclined air showers is weak. This makes it difficult to obtain an unbiased estimate of the true emission in the presence of ambient, thermal, Galactic, or anthropogenic noise. Hence, we follow an alternative approach where we define and parameterize the charge-excess fraction to determine the geomagnetic emission. With the following definition⁶ for the charge-excess fraction

$$a_{ce} \equiv \sin^2 \alpha \cdot f_{ce} / f_{geo}, \quad (6.10)$$

where α is the geomagnetic angle accounting for the scaling of the geomagnetic emission, one can derive an expression for f_{geo}

$$f_{geo}^{\text{par}} = \frac{f_{\vec{v} \times \vec{B}}}{\left(1 + \frac{\cos(\phi)}{|\sin \alpha|} \cdot \sqrt{a_{ce}}\right)^2}, \quad (6.11)$$

which solely depends on the (dominant) emission in the $\vec{v} \times \vec{B}$ -polarization. In the following, we use CoREAS simulations to derive a parameterization for a_{ce} .

In addition to aforementioned advantage, using a parameterization yields to other benefits: First, a parameterization allows to exploit the known dependency of the charge-excess

⁶ We note that this deviates from the definition based on amplitude ratios often used by other authors.

emission to the shower geometry and depth of the shower maximum. Second, assuming that both the geomagnetic and charge-excess emission contributions are rotationally symmetric, the parameterization can also be used to subtract the charge-excess emission for pulses of observers close to or on the $\vec{v} \times \vec{B}$ -axis.

We extract the charge-excess fraction from the simulated pulses with Eqs. (4.5) and (4.6). As mentioned earlier, these equations lose validity for observers close to the $\vec{v} \times \vec{B}$ -axis⁷. Hence, we only consider observers with $|\cos(\phi)| < 0.9$. Furthermore, we select only pulses that are not affected by thinning (cf. Sec. 6.1.2). In Fig. 6.7 (left) the lateral distribution of the charge-excess fraction for all selected pulses of all showers is shown. The lateral distance is given in terms of the off-axis or viewing angle, and d_{\max} is color-coded. The following behavior can be observed: First, the overall strength of the charge-excess emission decreases with increasing distance to the shower maximum ($\sim \theta$). Second, it increases with increasing lateral distance. The former can be explained by the following: The emission strength of at least the geomagnetic emission depends on the mean free path length with which the electromagnetic particles traverse the atmosphere. With a larger mean free path, equivalent to traversing a less dense environment, negatively and positively charged particles can drift further from each other before interacting, thus resulting in a stronger geomagnetic emission. For a given slant depth, the density at the shower maximum, near which most emission originates, is smaller (the mean-free-path length higher) for larger zenith angles (larger distances to the shower maximum). This phenomenon has been studied in simulations for the total energy release between both emission mechanisms in Ref. [121] and could be shown in data as well [145]. In contrast, the charge-excess emission increases with the density as shown in Sec. 4.3.1 and hence decreases with the zenith angle, d_{\max} respectively. The latter behavior has already been reported in Refs. [97, 146]. To find an appropriate description for the lateral distribution of a_{ce} we inspect its distribution appropriately normalized with the air density at the shower maximum ρ_{\max} (to remove any dependency on the scaling of the radio emission with the density). Based on this, we describe the lateral distribution of the charge-excess fraction with a linear model in off-axis angle, e.g., the axis distance divided by the distance to the shower maximum, to remove the dependency on the specific shower geometry. Furthermore, we add an exponential correction term to describe the lateral distribution. Those considerations led to the ‘‘ICRC19’’-parameterization of the charge-excess fraction, cf. Ref. [142]:

$$a_{ce}^{\text{ICRC19}} = \underbrace{0.373 \cdot \frac{r}{d_{\max}}}_{\text{off-axis angle} \equiv p_{ce,0}} \cdot \underbrace{\exp\left(\frac{r}{762.6 \text{ m}}\right)}_{\text{exp. correction} \equiv p_{ce,1}} \cdot \underbrace{\left[\exp\left(\frac{\rho_{\max} - \langle \rho_{\max} \rangle}{0.149 \text{ kg/m}^3}\right) - 0.189\right]}_{\text{density scaling} \equiv p_{ce,2}}, \quad (6.12)$$

lateral profile

Here, we present a refined version of this parameterization. First, we substitute the term describing the scaling of the charge-excess fraction with the air density by a single parameter $p_{ce,2}$ which is optimized fitting $f_{\text{geo}}(a_{ce}(p_{ce,2}))$ (Eq. 6.11) to f_{GS} . The parameters

⁷ With the approach of decomposition explained in appendix B.1, one can determine f_{geo} and f_{ce} on the $\vec{v} \times \vec{B}$ -axis. However, this approach comes with its own disadvantages and is not used here.

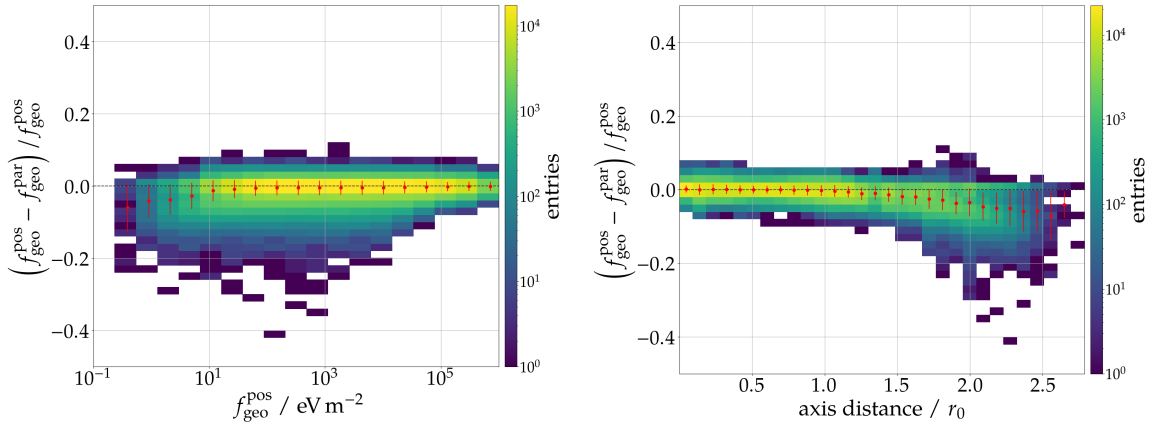


Figure 6.8.: Comparison of the geomagnetic energy fluence $f_{\text{geo}}^{\text{par}}$ determined with the parametrization and the geomagnetic energy fluence $f_{\text{geo}}^{\text{pos}}$ calculated from the signal polarization at each simulated position. The overall agreement is better than 2% with a mild degradation for low fluences (left panel) and distant observers (right panel).

of f_{GS} are fixed to the optimal values found in Sec. 6.2.2 before the parameterizations and only the normalization f_0 can vary with $p_{\text{ce},2}$. Fig. 6.7 (right) shows the correlation of $p_{\text{ce},2}$ fitted for all showers with ρ_{max} . The purple curve shows our new description given by

$$p_{\text{ce},2} = \left(\frac{\rho_{\text{max}}}{0.428 \text{ kg m}^{-3}} \right)^{3.32} - 0.0057. \quad (6.13)$$

The functional form is rather ad-hoc but describes the data better than the exponential function used at the ICRC19 [142] which is shown by the orange curve. Also, this function can become negative, and thus implausible, for low air densities but does so later, i.e., $\rho_{\text{max}} > 0.09 \text{ kg m}^{-3}$ than the exponential model ($\rho_{\text{max}} > 0.15 \text{ kg m}^{-3}$). This allows to extend the parameterization to zenith angles beyond 85° . ρ_{max} can be determined from d_{max} for a given atmospheric model and zenith angle, and thus does not introduce a new observable/fit-parameter. Similarly, the remaining terms of the previous parameterization describing the lateral profile of the charge-excess fraction were refined (see appendix B.3).

Finally, we can re-formulate the charge-excess fraction as a function of the lateral distance of an observer and d_{max} for a given zenith angle, observation height, and atmospheric model.

$$a_{\text{ce}} = \underbrace{\left[0.348 - \frac{d_{\text{max}}}{850.9 \text{ km}} \right] \cdot \frac{r}{d_{\text{max}}} \cdot \exp\left(\frac{r}{622.3 \text{ m}}\right)}_{\text{refined lateral profile}} \cdot \underbrace{\left[\left(\frac{\rho_{\text{max}}}{0.428 \text{ kg m}^{-3}} \right)^{3.32} - 0.0057 \right]}_{\text{refined density scaling}}. \quad (6.14)$$

It is worth mentioning that asymmetries in the lateral distribution of the charge-excess emission reported in Ref. [122] and attributed to shower-to-shower fluctuations can not be described. This introduces an irreducible but modest scatter of the charge-excess fraction (see evaluation is the next paragraph). On top of this, an additional dependency on the (azimuthal) arrival direction is apparent in Figs. 6.7 (right) and B.2, highlighted

by the color code, especially for the highest zenith angles (at which the overall relative strength of the charge-excess emission is lowest). This correlation is not yet understood and hence not described. However, it might be related to a so far, unexpected dependence of the geomagnetic radiation with the orientation of the geomagnetic field vector which was discussed in Sec. 4.3.1. However, due to the low relative strength of the charge-excess emission compared to the geomagnetic emission, the remaining scatter does not significantly deteriorate the accuracy as the following evaluation shows.

To evaluate the accuracy of parameterization Eq. (6.14), we compare the geomagnetic energy fluence determined with Eq. (6.11) using the parameterization in Eq. (6.14), called $f_{\text{geo}}^{\text{par}}$, with the fluence directly inferred from the simulated pulses using Eq. (4.5), labelled $f_{\text{geo}}^{\text{pos}}$. Since both emission mechanisms are already disentangled along the $\vec{v} \times (\vec{v} \times \vec{B})$ axis, i.e., $f_{\text{geo}}^{\text{par}} = f_{\text{geo}}^{\text{pos}} = f_{\vec{v} \times \vec{B}}$, the corresponding observers are excluded from the evaluation to not artificially embellish the evaluation. In Figure 6.8, the agreement between $f_{\text{geo}}^{\text{par}}$ and $f_{\text{geo}}^{\text{pos}}$ as a function of $f_{\text{geo}}^{\text{pos}}$ (left) and as a function of the lateral distance from the shower axis (right) is shown. The number of entries in each bin is color-coded on a logarithmic scale. The red markers show mean and standard deviation in each vertical column. The overall resolution is 2% with a negligible bias.

6.3. Reconstruction of inclined air showers with a sparse antenna array

So far, we have related the shape of the signal distribution (the symmetric LDF as well as the asymmetry corrections) to d_{max} . What remains is the absolute normalization f_0 . It is easy to see that this parameter correlates with the overall emitted (geomagnetic) radiation energy E_{geo} . To be more precise, the 2d spatial integral over the whole emission footprint at the ground corresponds to the overall emitted radiation energy. We can rewrite the LDF to explicitly correlate the signal distribution to the total geomagnetic radiation energy E_{geo} :

$$f_{\text{geo}}(r, E_{\text{geo}}, d_{\text{max}}) = E_{\text{geo}} \frac{f_{\text{GS}}(r, d_{\text{max}})}{2\pi \int_0^{5r_0} f_{\text{GS}}(r, d_{\text{max}}) r \, dr} \quad (6.15)$$

with $f_0 = 1$ set to unity. The integral in the denominator has to be solved numerically. The maximum integration distance of $5 r_0$ is sufficiently large to evaluate the integral and not lose any significant signal while the calculation being numerically robust and efficient. Now we can describe the entire radio-emission footprint with two fit parameters only, E_{geo} and d_{max} (+ two core coordinates). E_{geo} is strongly correlated with the electromagnetic shower energy E_{em} and hence can serve as energy estimator (for the definition of E_{em} see appendix B.4). To improve the correlation with E_{em} , we compensate for the second-order scaling of E_{geo} with the geomagnetic angle and air density at the shower maximum (following the logic established in Ref. [121]) and obtain a corrected geomagnetic radiation energy S_{geo} :

$$S_{\text{geo}} = \frac{E_{\text{geo}}}{\sin^2(\alpha)} \cdot \frac{1}{(1 - p_0 + p_0 \cdot \exp(p_1 \cdot [\rho_{\text{max}} - \langle \rho \rangle]))^2}. \quad (6.16)$$

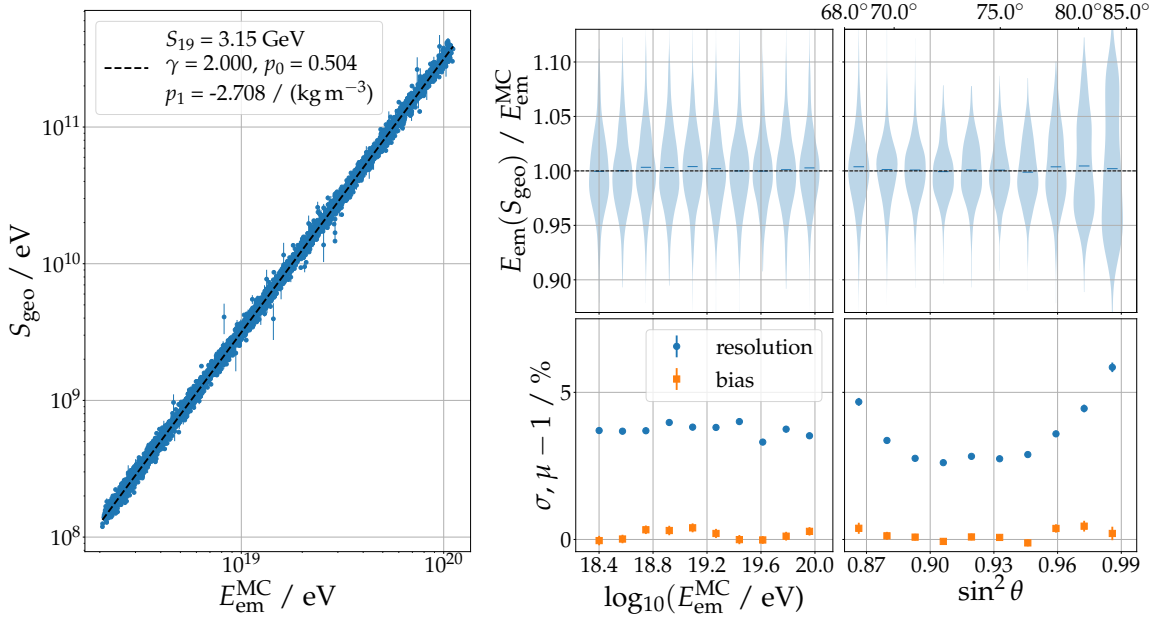


Figure 6.9.: Reconstruction of the electromagnetic shower energy E_{em} for the QGSJetII-04-generated showers. *Left:* Scatter plot of the radio-reconstructed electromagnetic shower energy as a function of the true electromagnetic shower energy. Legend indicates fit parameters according to Eq. (6.17). Bias and resolution (bottom panels) of the reconstructed electromagnetic energy are shown as a function of the true energy (*middle*) and zenith angle (*left*). The full distributions are illustrated in the top panels.

The constant $\langle \rho \rangle = 0.3 \text{ g cm}^{-3}$ reflects a typical air density at the shower maximum of an inclined air shower with $\theta \sim 75^\circ$. Finally, we can correlate S_{geo} and E_{em} using a power-law:

$$E_{\text{em}} = 10 \text{ EeV} \left(\frac{S_{\text{geo}}}{S_{19}} \right)^{1/\gamma}. \quad (6.17)$$

The normalization with $\langle \rho \rangle$ has direct implications on the value of S_{19} which can be interpreted as the geomagnetic radiation energy for a 10 EeV cosmic ray air shower with an air density at its shower maximum of $\rho_{\text{max}} = 0.3 \text{ g cm}^{-3}$.

6.3.1. Reconstruction of the electromagnetic shower energy

Now we use our second set of simulations, with a realistic detector layout and distribution of arrival directions, to reconstruct E_{em} and evaluate the performance of the signal model introduced in the previous sections. We reconstruct the showers with the fully-parameterized function $f_{\text{geo}}(r, E_{\text{geo}}, d_{\text{max}})$, i.e., Eq. (6.15), with the 4 free fit parameters E_{geo} , d_{max} , and two core coordinates. We minimize the following function:

$$\chi^2 = \sum_{i=0}^N \left(\frac{f_{\vec{v} \times \vec{B}, i} - f_{\vec{v} \times \vec{B}}^{\text{pred}}(\vec{x}_i, E_{\text{geo}}, d_{\text{max}})}{\sigma_{f_{\vec{v} \times \vec{B}, i}}} \right)^2. \quad (6.18)$$

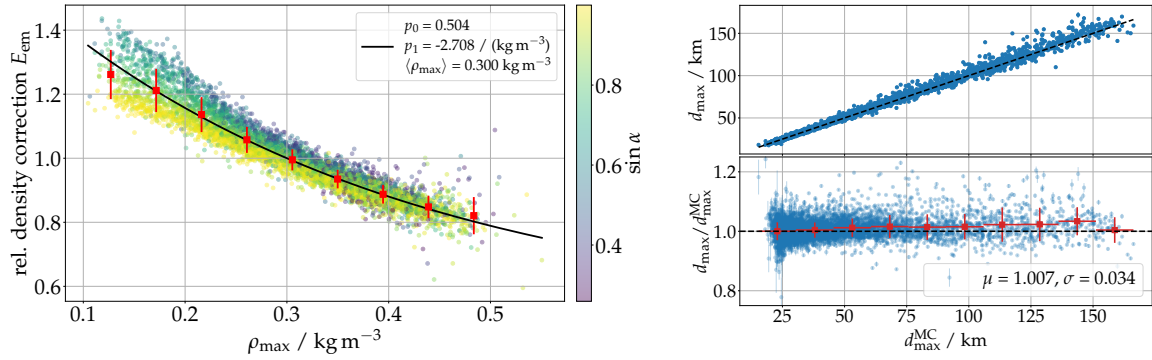


Figure 6.10.: *Left:* Fitted density correction according to Eq. (6.16) (black line) shown together with the normalized geomagnetic radiation energy from all selected showers (colored, transparent markers) together with their binned mean and standard deviation (red markers). With the normalization $y/\langle y \rangle$, y according to Eq. (6.20), any relative dependency to the energy and magnetic field should be removed. However, a remaining dependency on the geomagnetic angle is visible, especially for low densities (high zenith angle). *Right:* Comparison between fitted and true distance to the shower maximum d_{\max} . For the fit, the true arrival direction, i.e., zenith angle, to which d_{\max} is most sensitive to, is used. The correlation (top) between reconstructed and true d_{\max} and the resolution (bottom) are good.

Hence, instead of correcting or “symmetrizing” $f_{\vec{v} \times \vec{B}} \rightarrow f_{\text{geo}}^{\text{meas}}$ and comparing it to the predicted LDF f_{geo} , we add the asymmetry corrections introduced here inversely to f_{geo} and obtain a prediction for $f_{\vec{v} \times \vec{B}}$:

$$f_{\vec{v} \times \vec{B}}^{\text{pred}}(r, E_{\text{geo}}, d_{\max}) = f_{\text{geo}}(r, E_{\text{geo}}, d_{\max}) \left(1 + \frac{\cos(\phi)}{|\sin \alpha|} \cdot \sqrt{a_{\text{ce}}} \right)^2 c_{\text{el}}^2 \quad (6.19)$$

with r is the early-late corrected axis distance. The benefit of re-writing the minimization is that $\sigma_{f_{\vec{v} \times \vec{B}, i}}$ in an experimental setup is typically directly available from the reconstruction procedure of the recorded antenna signals while $\sigma_{f_{\text{geo}}}$ would need to be determined first.

For the following reconstruction of E_{em} , we select only QGSJetII-showers with a zenith angle $\theta > 68^\circ$ and at least 5 simulated observers (no requirements on the signal strength of the simulated pulses are imposed). For those 6210 showers we select 6194 showers with a good reconstruction quality. All parameters in Eqs. (6.16) and (6.17), S_{19} , γ , p_0 , and p_1 are determined in a combined fit of the reconstructed (fitted) E_{geo} and ρ_{\max} (determined given the fitted d_{\max}) to the true E_{em} . Their values are given in Tab. 6.1. The correlation between S_{geo} and E_{em} (left panel) as well as the achieved reconstruction accuracy (right panels) are shown in Fig. 6.9. The ratio $E_{\text{em}}^{\text{rec}}/E_{\text{em}}^{\text{MC}}$ is shown once as a function of the true electromagnetic energy $E_{\text{em}}^{\text{MC}}$ (middle) and once as a function of the true zenith angle (right). The top panels show the full distributions in discrete bins while the bottom panels show the achieved bias (μ) and resolution (σ). The reconstruction accuracy does not depend on the energy with a resolution of below 5% for all energies. The right panels demonstrate a minor degradation of the energy resolution for the lowest and highest zenith angles. This evaluation includes 160 shower with a geomagnetic angle $\alpha < 20^\circ$. Although their reconstruction accuracy is slightly worse than for other showers, they

are still reconstructed with reasonable accuracy and in particular including them had no significant effect on the calibration parameters in Tab. 6.1.

The fitted relative density correction for E_{em} according to Eq. (6.16) is illustrated in Fig. 6.10 (left). The fitted geomagnetic radiation energy for each shower, shown in the same figure by the transparent markers is normalized in such a way that only the correlation with air density remains, i.e., the y-axis shows $y/\langle y \rangle$ for

$$y = \frac{\sqrt{E_{\text{geo}}/\text{GeV}}}{(\sin \alpha^{\text{MC}} \cdot E_{\text{em}}^{\text{MC}}/10 \text{ EeV})}. \quad (6.20)$$

A significant correlation is visible which is well described by the fitted exponential model (cf. Eq. (6.16)). Note that the exponential is not directly fitted to these data but in a combined fit with Eq. (6.17)). The found correlation agrees well with the one found in Ref. [121], although the different $\langle \rho \rangle$ prevents a direct comparison of the fitted parameters. The color code shows the sine of the geomagnetic angle and highlights the same unexpected residual correlation which was already discussed in Sec. 4.3.1

Fig. 6.11 shows the ratio $E_{\text{em}}^{\text{rec}}/E_{\text{em}}^{\text{MC}}$ as a function of the MC X_{max} for each shower (blue dots). The binned mean and standard deviation (error bars) are highlighted by the red markers (the uncertainties on the means are indicated by the error caps). A bias with X_{max} is visible: for increasing X_{max} , the reconstructed electromagnetic energy is increasingly underestimated. The overall distributions of X_{max} and $E_{\text{em}}^{\text{rec}}/E_{\text{em}}^{\text{MC}}$ are shown as histograms at the top and right axes, respectively. A potential X_{max} -dependent bias in the energy reconstruction is delicate as it could yield a primary-particle dependent bias. However, the majority of events are contained within $X_{\text{max}} < 900 \text{ g cm}^{-2}$ for which the bias is below 5% (as demonstrated by the histograms)⁸. Furthermore, we did not observe any significant bias in the electromagnetic energy reconstruction between the different primaries. Nonetheless, in a future iteration of this reconstruction this could be improved as discussed in Sec. 6.4.

6.3.2. Reconstruction of the distance to the shower maximum

In Fig. 6.10 (right), the reconstructed d_{max} is compared to its true value. The comparison shows an overall good accuracy with no significant bias and a resolution of $\sim 3\%$ which does not significantly depend on the zenith angle. It should be mentioned that the superb reconstruction accuracy of d_{max} achieved here is mainly driven by using the true arrival direction in the reconstruction. In a realistic, experimental setup, where the arrival direction for inclined air showers is only known with a typical accuracy of $\lesssim 0.5^\circ$ [84]⁹, the reconstruction accuracy will decrease (more than what we would expect for the electromagnetic energy E_{em}). From an estimation of d_{max} it is possible to also estimate the depth of the shower maximum X_{max} . The potential for this is discussed in Sec. 6.4.

⁸ The X_{max} -distribution depends of course on the energy spectrum of the simulation set. The simulated spectrum is much harder than what is seen in nature, hence larger energies, i.e., deeper shower, are overrepresented here.

⁹ The detection of the air-shower front from radio emission does not suffer from Poisson fluctuation (as it is the situation with the detection of particles), hence a more accurate reconstruction of the shower arrival directions is likely possible.

Table 6.1.: Parameters of Eqs. (6.16) and (6.17) determine in a combined fit.

S_{19}	γ	p_0	p_1
3.1461 GeV	1.9997	0.5045	-2.7083 / (kg m ⁻³)

6.3.3. Reconstruction of air showers generated with a different high-energy hadronic interaction model

We repeated the same evaluation of the air-shower reconstruction with the Sibyll-2.3d-generated air showers. To reconstruct the electromagnetic energy E_{em} , the parameters γ , p_0 , and p_1 are fixed to allow a direct comparison of the S_{19} parameter. S_{19} decreased by less than 2% from 3.15 GeV to 3.10 GeV for the Sibyll showers as compared with the QGSJetII showers. It is worth stressing that this change is not due to differences in the prediction of the muonic shower component between both hadronic interaction models. The achieved resolution is very comparable between showers from both interaction models with the exception that the resolution for air showers with zenith angle $\theta < 70^\circ$ for Sibyll showed a small degradation in resolution ($\sigma_{E_{em}}^{Sibyll}(\theta < 70^\circ) \lesssim 7\%$ as compared to $\sigma_{E_{em}}^{QGSJet}(\theta < 70^\circ) \lesssim 5\%$, see Fig. B.3 in appendix B.5). The other results, e.g., the reconstruction of d_{max} and the E_{em} reconstruction bias with X_{max} remain practically unchanged.

6.4. Discussion

Besides the electromagnetic shower energy, the distance of the shower maximum is an observable of (great) interest as it can be used to determine the slant depth of the shower maximum X_{max} . X_{max} is of special interest as it is commonly used to infer the mass composition of cosmic rays. The distance to the shower maximum d_{max} is reconstructed with a superb accuracy of $\sigma_{d_{max}}/d_{max} = 3\%$ as shown in Fig. 6.10 (right)¹⁰. However, small (relative) changes in d_{max} correspond to large (absolute) changes in X_{max} . Even with a relative d_{max} resolution of 3%, the absolute resolution for the depth of the shower maximum is $\sigma_{X_{max}} \geq 50 \text{ g cm}^{-2}$ at $d_{max} \geq 75 \text{ km}$ (cf. Fig. 6.12). This leads to the conclusion that the sensitivity of the shape of the lateral signal distribution at ground to X_{max} is rather limited due to the large distance between shower maximum and detector and the (relatively) small variations in d_{max} induced by variations of X_{max} . While this is unfortunate for obvious reasons, when one wants to estimate the shower (i.e., cosmic-ray) energy it is advantageous as it minimizes the dependency of the LDF to the cosmic-ray mass.

The observed X_{max} -dependent bias in the energy reconstruction can be resolved, to a large degree, by describing the secondary correlation of X_{max} with the LDF parameters a_{rel} or r_{02} , cf. Fig. 6.6. The secondary correlation can be explained by the ambiguity of d_{max} for different zenith angles and X_{max} values. An elegant solution to resolve the ambiguity is the introduction of a linear term with d_{750} the distance between shower core and a fixed slant depth of 750 g cm^{-2} , in the parameterizations of a_{rel} or r_{02} . However, when doing

¹⁰ While we intentionally do not probe a realistic scenario such as one is faced with when using measured data, it is worth mentioning (again) that the true arrival direction (zenith angle) is used, with which d_{max} is mostly correlated.

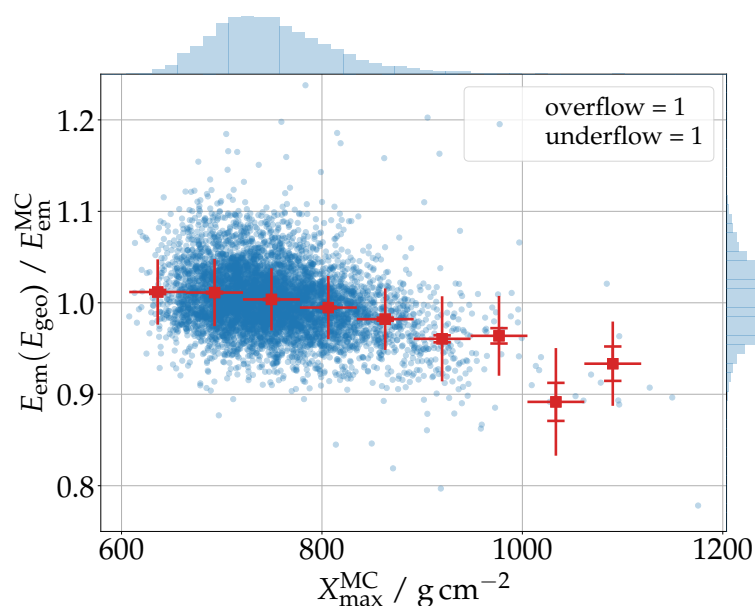


Figure 6.11.: Scatter plot of $E_{\text{em}}(E_{\text{geo}})/E_{\text{em}}^{\text{MC}}$ as a function of X_{\max} . Red markers show mean and standard deviation (error-bars; error-caps signify uncertainty of the mean). An X_{\max} dependent bias is apparent. The distributions of X_{\max} and $E_{\text{em}}^{\text{rec}}/E_{\text{em}}^{\text{MC}}$ are illustrated by the histograms on the top and right sides of the panel, respectively.

so, we found an implausible kink in the distribution of the fitted d_{\max} distribution with simulations from the validation set, and for this reason, the fact that we do not observe a significant primary-particle dependent bias and the sake of simplicity we decided to not include such a term in the parameterizations. However, if needed in the future, our model can be improved by a more thorough study of these secondary correlations.

The model presented here for the radio emission from inclined extensive air showers in the frequency band of 30 MHz to 80 MHz is tailored to the ambient conditions of the Pierre Auger Observatory. While the general concept and considerations should transform well to other experiments, i.e., other ambient conditions and frequency bands, like GRAND, the explicit parameterizations require revisions. For example, it is known that the Cherenkov ring is more prominent at higher frequencies [147], hence a re-parameterization of the shape of the 1-d LDF seems necessary. Relying on atmospheric models for the parameterization of the charge-excess emission and parts of the LDF parameters reduces the dependency on a particular set of ambient conditions. However, the explicit use of the axis distance in the parameterization of the charge-excess fraction and LDF model carries a dependency on the observation altitude. We consequently normalized our parameterizations to showers arriving perpendicular to the Earth’s magnetic field, hence changing orientations of the magnetic field should not affect the model. In Ref. [121], the scaling of the (geomagnetic) emission with the strength of the Earth’s geomagnetic field was investigated and found to be $E_{\text{geo}} \sim B^{1.8}$. This scaling should apply to our model as well. However, if it comes to a transition between from the regime of time-varying transverse currents to a regime of synchrotron radiation as predicted in [54] and discussed in Sec. 4.3.1,

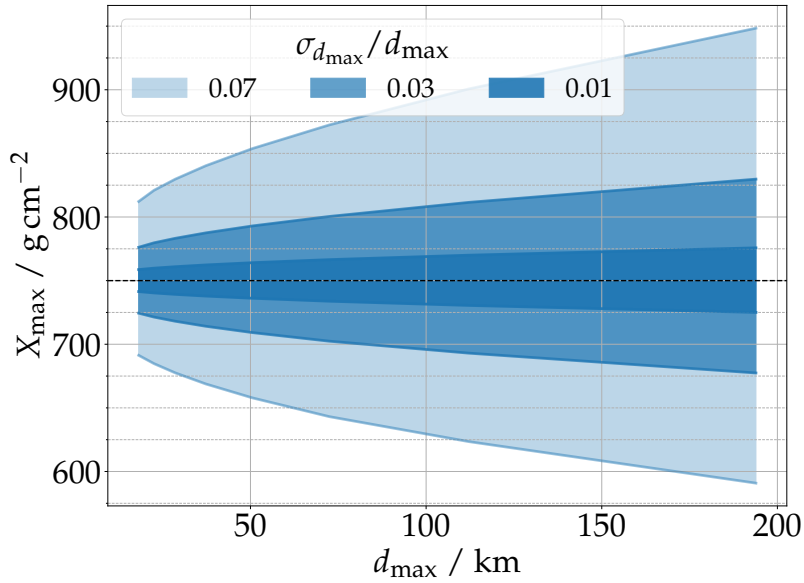


Figure 6.12.: Translation of the relative uncertainty $\sigma_{d_{\max}} / d_{\max}$ in an absolute deviation (uncertainty) of X_{\max} . The shaded areas indicate the negative and positive deviation from a nominal $X_{\max} = 750 \text{ g cm}^{-2}$ (black dashed line) for the relative uncertainties $\sigma_{d_{\max}} / d_{\max} = 1\%$, 3% , and 7% as a function of d_{\max} corresponding to the zenith angle range from 65° to 86° .

a re-parameterization of at least the charge-excess fraction and density correction are necessary.

The here performed reconstruction of the electromagnetic energy using the developed signal model corresponds to an idealized case and hence the achieved resolution can be considered the intrinsic resolution of the method for air showers reconstructed with a sparse antenna array. In measured data, neither the true arrival direction nor the precise signals from the antennas are known perfectly. Ambient and internal noise, an inaccurate detector description (especially of the directional response pattern of the antennas), and other effects will affect the signals reconstructed for each antenna. A detailed study of all those effects is conducted in Chap. 8 and has been presented at the ICRC21 [148].

In addition to its application in an event reconstruction, this signal model can also be used to predict the radio emission in 30 MHz to 80 MHz from inclined air showers of a given set of energies and arrival directions. This allows studying different aspects of the detection of inclined air showers, for example the effect of the observer spacing on the detection efficiency, when no time- and CPU-consuming Monte-Carlo simulations are available.

6.5. Conclusions

Measuring inclined air showers with radio antennas is of particular interest for two reasons. First, their large footprints allow us to instrument huge areas with sparse antenna arrays. Large areas are necessary to be able to observe the spectrum of cosmic rays at the highest energies. Second, inclined air showers observed in coincidence with radio and particle

detectors offer the unique potential to measure the muonic shower component (with the particle detector) and electromagnetic shower component (with the radio detector) independently of each other. The combination of this complementary information yields a strong sensitivity towards the mass of the cosmic ray. For a precise study of the mass composition of UHECRs, the energy resolution provided by the radio detector is of critical importance. The here presented model enables a robust and accurate reconstruction of the electromagnetic shower energy from the radio emission in the 30 MHz to 80 MHz regime from inclined air showers with sparse radio-antenna arrays. The intrinsic resolution is below 5% with no bias ($< 1\%$) on the primary particle. The model relies on an explicit modeling of the dominant, rotationally symmetric geomagnetic emission as well as effects which disturb this symmetric emission and lead to the highly asymmetric pattern we expect from inclined air showers. Those asymmetries are associated with the interference of the charge-excess emission with the geomagnetic emission as well as the imprint of geometrical early-late effects. We exploit correlations between the model parameters and shower observables to minimize the number of free parameters. The final model only relies on two free parameters, the distance between detector and the shower maximum d_{\max} and the geomagnetic radiation energy E_{geo} , plus two coordinates for the location of the impact point of the air shower. This allows a reliable fit of the signal distribution and thus efficient event reconstruction. This model will be used to reconstruct inclined air showers detected by the AugerPrime Radio Detector. Its performance is studied under realistic conditions, i.e., assuming experimental and instrumental uncertainties, in Chap. 8.

While the signal model enables a precise reconstruction of the electromagnetic shower energy, the sensitivity to the depth of the shower maximum X_{\max} from the reconstructed geometrical distance to the shower maximum d_{\max} is limited. An accurate reconstruction of X_{\max} would strengthen the sensitivity to the masses of UHECRs of measurements with the RD. In Chap. 7, an interferometric reconstruction of X_{\max} , which promises accurate results, especially for very inclined air showers, is evaluated.

The presented concept for the signal model is applicable for a variety of radio experiments trying to reconstruct inclined air showers. The described procedure can be used to tune the model parameterizations to match with different ambient conditions as well as different frequency bands relevant for any specific experiment.

7. Interferometric reconstruction of the depth of the shower maximum

Parts of this chapter have been published in:

F. Schlüter and T. Huege

"Expected performance of interferometric air-shower measurements with radio antennas"
[PoS \(ICRC21\) 228](#)

F. Schlüter and T. Huege

"Expected performance of air-shower measurements with the radio-interferometric technique"
[JINST 16 P07048 \(2021\)](#)

F. Schlüter and T. Huege

"Evaluating the Potential of radio-interferometric measurements with the Auger Radio Detectors"
[GAP2020-055 \(2020\), Internal Document of the Pierre Auger Collaboration](#)

An accurate reconstruction of X_{\max} for inclined air showers in addition to the measurement of the energy content of the electromagnetic cascade by the same radio antennas and the muonic content by ground-particle detectors would provide excellent sensitivity to the mass composition of cosmic rays [7, 149] and could thus provide key information in the quest for the origin of UHECRs. In particular, the anti-correlation between X_{\max} and size of the muonic shower component w.r.t. the cosmic-ray mass, yields an excellent discriminative power to distinguish between air showers induced by different cosmic-ray primaries. Furthermore, in inclined air showers the radio-emission footprint is spread over large areas thus enabling the observation of air showers with sparse antenna arrays [70, 71]. This allows one to instrument large areas ($> 1000 \text{ km}^2$) to detect ultra-high-energy cosmic rays with energies up to $\sim 100 \text{ EeV}$, soon to be realized with the AugerPrime Radio Detector. However, established radio-based X_{\max} reconstruction algorithms have only been validated and applied to vertical air showers. Those traditional methods which rely on the shape of the lateral signal distribution at ground are likely to lose accuracy due to the large distance between shower maximum and detector (cf. Chap. 6 and in particular Fig. 6.12). In Ref. [150], the so-called radio-interferometric technique (RIT) is developed and successfully applied to air shower simulations with an idealized detector (zenith-angle dependent dense antenna array, perfect time synchronization between antennas and perfectly known antenna locations) to reconstruct the shower axis and depth of the shower

maximum X_{\max} with high accuracy. A superb resolution of better than 0.04° ($< 0.2^\circ$) in the arrival direction and 3 g cm^{-2} (10 g cm^{-2}) in X_{\max} for inclined (vertical) showers is demonstrated.

In this chapter, we investigate whether the promising results achieved in Ref. [150] for simulations with an idealized detector can be confirmed for air showers measured with realistically dimensioned air shower detector arrays, i.e., coarse discretely spaced antenna¹ arrays, as needed to instrument the required large fiducial areas, and an imperfect time synchronization between antennas not connected by cables. The primary objective of this study is to investigate the application of RIT for inclined air showers with sparse antenna arrays, where the potential is largest in terms of exposure, achievable X_{\max} resolution and complementarity to ground-based measurements, and to formulate prerequisites for the application of RIT.

Radio signals from extensive air showers exhibit wave phenomena which interferometric reconstruction can exploit. An example for such phenomena is the nowadays well-established Cherenkov ring which results from higher coherence of the radio emission at a particular distance for the shower axis due to a stronger temporal compression of the signals emitted by billions of shower particles in an atmosphere with a non-unity refractive index.

Interferometric techniques expose this coherence in the radio emission. Thereby, both the signal's amplitude and phase information are used, while traditional reconstruction methods of extensive air showers rely on the amplitude information only. Interferometric techniques are standard in radio astronomy, where sources are at infinity and hence all antennas receive the same signal with a planar wavefront. Application to radio emission from extensive air showers is more challenging, as the sources are typically nearby, are extended, and the emission from different parts of the shower propagates through different parts of the atmosphere (\equiv integrated refractive index).

Previously, interferometric techniques for cosmic-ray detection have been used successfully in the LOPES experiment to identify coherent air-shower radio pulses amongst strong and time-correlated radio-frequency interference, to estimate the energy of the primary particle, and to provide an image of the intensity distribution on the sky from which the arrival direction can be determined [151]. They have also been employed to determine the depth of shower maximum from LOPES data [152, 153] with an experimental accuracy worse than 100 g cm^{-2} but potential in pure simulations to reach an accuracy as good as 30 g cm^{-2} . Attempts to apply interferometric techniques to ground-based radio arrays with a larger extension than the small-scale LOPES experiment, for example within the Auger Engineering Radio Array, had not been successful [154], presumably because the then-made assumption that antennas see identical signals no longer holds for larger arrays. Another experiment routinely using interferometric techniques to identify and reconstruct air-shower radio emission is ANITA [155]. Finally, real-time interferometric triggering is also being investigated for particle showers in ice [156] and air [157].

¹ With “antenna” we refer to an antenna(-station) consisting of at least two orthogonally aligned antennas allowing to determine the full 3-dimensional electric field of the incoming radio emission. In the context of air-shower simulations “antenna” refers to a location at which the radio pulse is sampled.

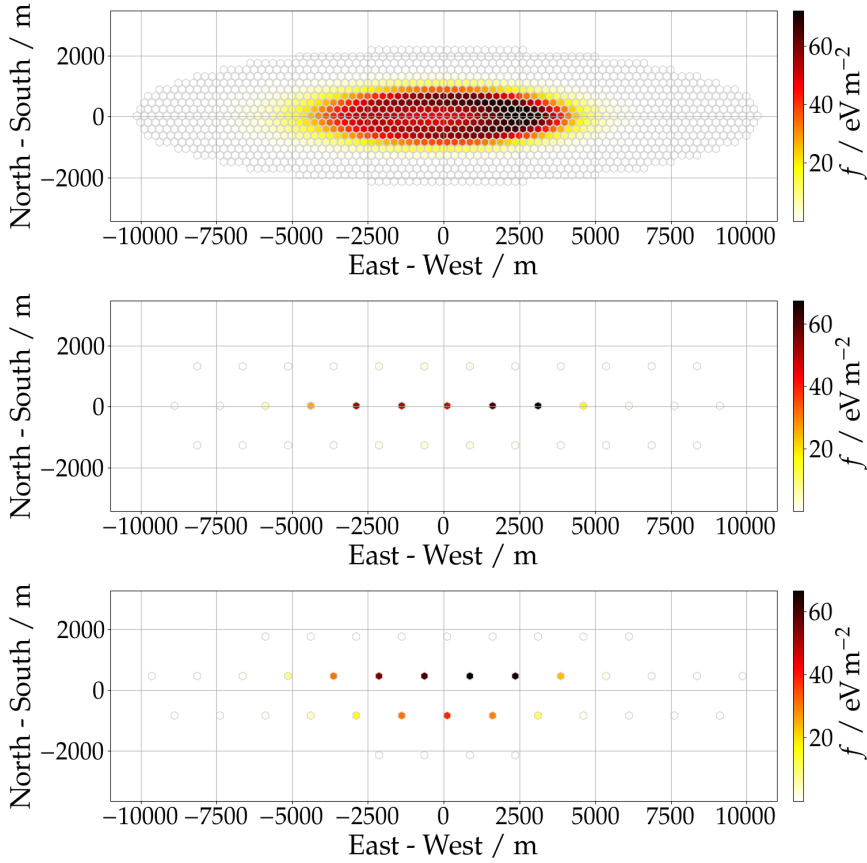


Figure 7.1.: *Top:* Radio-emission footprint of a 77.5° zenith-angle air shower coming from east measured with a dense 250 m array. The energy fluence f , i.e., energy deposit per square meter, is color coded. The footprint exhibits the typical Cherenkov ring. *Middle:* Same shower measured with a sparse 1500 m (sub-)array with the same central antenna. *Bottom:* Same shower measured on a 1500 m (sub-)array with a different central antenna.

For interferometry, the signal arrival times and the antenna positions have to be known very accurately to preserve the coherence within the measured signals. In Ref. [150], the authors quote that the timing accuracy has to be better than a quarter of the signals' oscillation period, e.g., $\sigma_t = \sqrt{\sigma_{t_{\text{signal}}}^2 + (\sigma_{\vec{x}_{\text{antenna}}}/c)^2} < (4 \cdot \nu)^{-1} \sim 5 \text{ ns}$ at a frequency of $\nu = 50 \text{ MHz}$. Furthermore, they report that a maximum inaccuracy of $\sigma_t = 3 \text{ ns}$ yields accurate results. In Ref. [158] a much more restrictive coherence criterion for the same frequency band is concluded: a twelfth of the period or $\sigma_t < 1 \text{ ns}$ at 80 MHz (this corresponds to 1.667 ns at 50 MHz). Air shower experiments which aim to instrument large areas rely on self-powering detector stations with wireless communication. Thus, the time synchronization between those stations, achieved with GPS clocks, is typically of the order of a few nanoseconds ($\sigma_t \sim 5 \text{ ns}$ to 10 ns) [159]. However, with specialized hardware such as a phase-stable beacon transmitter this might improve to the order of a nanosecond ($\sigma_t \lesssim 1 \text{ ns}$) [158, 160]. The antenna positions can be determined within $\sim 10 \text{ cm}$ with differential GPS surveys. Thus, for measurements of the radio emission below $\lesssim 100 \text{ MHz}$ the contribution of $\sigma_{\vec{x}_{\text{antenna}}}$ to σ_t can be ignored. However, for frequencies of

several hundred MHz the $\sigma_{\vec{x}_{\text{antenna}}}$ can become significant. Thus verifying which coherence criterion is sufficient is crucial for the design and planning of an experiment which aims to employ interferometric reconstructions.

The investigation presented here mainly refers to the frequency band of the radio emission from 30 MHz to 80 MHz. This frequency band, also used in Ref. [150], is used by most current-generation large scale radio detector arrays [132, 133, 97] as well as the upcoming AugerPrime Radio Detector. Additionally, we investigate the performance achievable with higher frequency bands, in particular 50 MHz to 200 MHz as proposed for the GRAND experiment [127] and 150 MHz to 350 MHz for even higher frequencies such as those accessible by the upcoming SKA-Low array [161, 162] or the IceCube Radio Surface array [141]. Furthermore, we investigate how an inaccurate knowledge of the atmospheric refractivity profile affects the reconstruction.

In section 7.1 we study the performance of the interferometric reconstruction with generic, sparse, hexagonal antenna arrays. In particular, we are investigating the effect of an inaccurate time synchronization in combination with the antenna multiplicity. For equidistantly-spaced antenna arrays this antenna multiplicity is governed by the radio-emission footprint size (which is strongly correlated to the air shower zenith angle) and antenna spacing of the array. Other effects, like the impact of ambient noise, i.e., radio-frequency-interference, or trigger algorithm (which would impact the antenna multiplicity) are not considered and only briefly discussed in Sec. 7.1.5.

In section 7.2 the interferometric reconstruction is tested specifically for the Auger radio detectors RD and AERA. In addition to simulating a time jitter we also study the effect of ambient noise (for AERA) and particle triggers (for the RD).

7.1. Expected performance of air-shower measurements with the radio-interferometric technique

This section is structured as follows. First, we elaborate on the shower simulations used in this work. In section 7.1.2 we describe the reconstruction of the shower axis and X_{max} with RIT. Furthermore, in Sec. 7.1.2.3 the effect of inaccuracies in the knowledge of the atmospheric refractivity on the reconstruction is shown. In Sec. 7.1.3.1 we evaluate RIT for inclined air showers with different zenith angles measured with a 1.5 km-spaced antenna array. The effect of an inaccurate time synchronization between antennas for different detector layouts, i.e., antenna arrays with different spacings is investigated in Sec. 7.1.3.2. In Sec. 7.1.4 the reconstruction in the higher frequency bands is evaluated. Finally, we discuss the obtained results in Sec. 7.1.5 and conclude in Sec. 7.1.6.

7.1.1. Simulations for interferometry

We evaluate the potential of RIT using two different sets of CoREAS simulations. The first set contains a subset of 1902, proton and iron induced, showers with an antenna grid matching the configuration of the ideal Auger Surface detector, introduced in Chap. 4. The showers were generated with QGSJetII-04 and with the October Malargüe atmosphere. The second set contains 50 proton showers simulated on a very *dense* hexagonal grid with

Table 7.1.: The number of reconstructions n_{rec} performed on the dense simulations, i.e., the amount of all unique sub-arrays for all 50 showers, and average number of antennas on each sub-array $\langle n_{\text{ant}} \rangle$ for the different array spacings.

spacing / m	250	500	750	1000	1250	1500
n_{rec}	50	200	450	800	1250	1800
$\langle n_{\text{ant}} \rangle$	1342	336	149	84	54	37

an antenna spacing of 250 m and was simulated with the same settings as the first set (hadronic interaction models, atmospheric condition, thinning, ...).

To study the reconstruction performance for different detector layouts, i.e., array spacings, simulations with a very *dense* grid, which can be divided in several sub-arrays with larger antenna spacings, are suitable. Since the computational cost for each shower scales almost linearly with the number of simulated pulses we need to limit our phase space of densely sampled, simulated showers. Thus, we simulate 50 proton showers with only one energy $\log(E/\text{eV}) = 18.4$, one zenith angle $\theta = 77.5^\circ$ and two azimuth angles $\phi = 0^\circ$ (arriving from geomagnetic east) and $\phi = 30^\circ$ (arriving from north of east), for each of which we simulate 25 showers. For a hexagonal array which is invariant for rotations of 60° , showers from 0° and 30° cover the two extreme cases of a shower falling into the array exactly parallel to a line of antennas and with the largest possible angle between two lines of antennas. Pulses are simulated on a grid with 250 m spacing and a maximum axis distance of 2235.6 m around the core. This amounts to $\lesssim 1350$ pulses per shower. The core location relative to a central antenna is randomly distributed. The pulses are simulated on a horizontal plane with an altitude of 1400 m above sea level at its center². To study the reconstruction performance for different array spacings we define various sub-arrays. The following arrays are investigated: 250 m, 500 m, 750 m, 1000 m, 1250 m and 1500 m. For each spacing (except 250 m) several unique sub-arrays can be defined, each of them corresponding to a different (relative) core position for a given simulation. Thus, for example, one single shower can be reconstructed on 36 unique sub-arrays with a spacing of 1500 m. In Fig. 7.1 an example shower measured with the full 250 m grid (top) and two different sub-arrays with a spacing of 1500 m (middle, bottom) is shown. In Tab. 7.1 the number of all unique sub-arrays for all 50 showers and the average number of antennas on these sub-arrays for each spacing are summarized.

For the simulations with the 1.5 km antenna array, the antenna multiplicity for the simulated showers is governed by the algorithm described in Sec. 4.1.2.1 and summarized in Tab. 7.2.

However, it should be stressed, that for (actual) measurements the antenna multiplicity is, in addition to the detector layout and shower size (energy, arrival direction), also governed by the data acquisition system of the experiment, in particular the trigger determining which radio antennas to read out. In Sec. 7.1.5 the effect of (external) triggering is discussed. The antenna multiplicity in this study is solely governed by the simulation settings. The

² Unlike for the simulation set with the 1.5 km detector layout, the detector plane with the dense 250 m grid does not follow the Earth's curvature

Table 7.2.: Average number of antennas simulated and maximum antenna-axis distance (measured perpendicular to the shower axis, i.e., in the shower plane) for the 1.5 km hexagonal grid as a function of the zenith angle in 2.5°-bins.

$\langle\theta\rangle/^\circ$	66.25	68.75	71.25	73.75	76.25	78.75	81.25	83.75
$\langle n_{\text{ant}} \rangle \pm \sigma_{\text{ant}}$	9 ± 1	10 ± 1	11 ± 1	16 ± 3	27 ± 6	47 ± 11	87 ± 21	173 ± 42
$r_{\text{ant}}^{\text{max}} / \text{m}$	1500	1500	1508	1822	2230	2785	3563	4707

average number of simulated antennas per shower and the maximum antenna-axis distance binned in zenith angle are listed in Tab. 7.2.

7.1.2. Interferometric reconstruction of the shower properties

In this section, we describe the reconstruction of the shower axis and the depth of the shower maximum X_{max} with RIT. The algorithms, developed in Ref. [150], make use of 3-dimensional interferometric maps providing information about the longitudinal development of air showers. From these maps the cosmic-ray properties, in particular the arrival direction and depth of the shower maximum X_{max} , can be inferred. The algorithms described below are adapted from [150], however, their actual implementation is independent and has, in parts, changed.

RIT exploits the coherence in the radio emission from air showers and one searches for an imaginary point source for which the coherent signal becomes maximal. The time-dependent coherent (beam-formed) signal $B_j(t)$ originating at an arbitrary location in the atmosphere \vec{j} is calculated by the sum over all time-shifted antenna signals $S_i(t - \Delta_{i,j})$ at positions \vec{i}

$$B_j(t) = \sum_i^{n_{\text{ant}}} S_i(t - \Delta_{i,j}). \quad (7.1)$$

The time shift between an antenna location \vec{i} and the source location \vec{j} is

$$\Delta_{i,j} = \frac{d_{i,j} \cdot \overline{n_{i,j}}}{c} \quad (7.2)$$

with the geometrical distance $d_{i,j}$ and effective (averaged) refractive index $\overline{n_{i,j}}$ between the positions \vec{i} and \vec{j} , and the vacuum speed of light c . That means, $\Delta_{i,j}$ corresponds to the light propagation time between positions \vec{i} and \vec{j} . In Fig. 7.2 (*bottom right*) the time-shifted signals $S_i(t - \Delta_{i,j})$ of 37 pulses are shown for one position \vec{j} on the shower axis of an example shower. To calculate the effective refractive indices between source locations \vec{j} and antenna positions \vec{i} we adopt the Gladstone-Dale law (Eq. (4.1)) together with a five-layer atmospheric density profile $\rho(h)$ as used also in CORSIKA/CoREAS. In Ref. [163] it is shown that this approximation is adequate for the frequency band of 30 MHz to 80 MHz, for higher frequencies the Global Data Assimilation System (GDAS) can be used to refine the refractivity model by then also including the influence of humidity. The practical calculation of the effective refractivity between two positions, $\overline{N_{i,j}}$, which cannot be calculated analytically in a curved atmosphere, is explained in appendix C.1. The

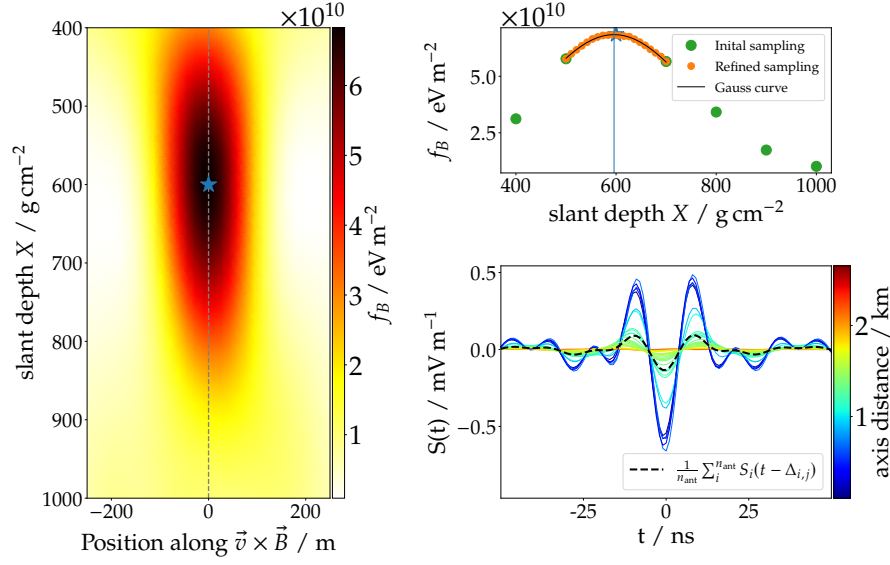


Figure 7.2.: Cross-section of the longitudinal (y-axis) and lateral (x-axis) profile of the coherent energy fluence f_{B_j} (color coded) of a 2.51 EeV, 77.5° proton shower sampled with 37 antennas on a 1500 m grid along the shower axis (vertical dashed line). Longitudinal profile $f_{B_j}(X)$ along the MC shower axis for the same shower (right top). Time shifted signals at ground $S_i(t - \Delta_{i,j})$ for a location \vec{j} at 600 g cm^{-2} on the shower axis (blue star).

calculation of the light propagation time (using the effective refractivity) along straight lines corresponds to the algorithm adopted in CoREAS. In nature, the emission between sources and observers propagates on slightly bent trajectories due to refraction in the atmospheric refractive index gradient. In Chap. 5 we found that the calculation on straight lines reproduces the relative propagation times between two different sources in the atmosphere better than within 0.1 ns, which is accurate enough to keep coherence properties in the frequency regime below a couple of hundred MHz.

To calculate $B_j(t)$, the electric field values of the time-shifted signals $S_i(t - \Delta_{i,j})$ are linearly interpolated to fit the finite time binning Δt of $B_j(t)$ ³. For each trace $B_j(t)$ we determine a time-independent signal, namely the sum over the squared amplitudes in a 100 ns signal window around the peak amplitude

$$f_{B_j} = \epsilon_0 c \Delta t \sum_{t_{\text{peak}}-50\text{ns}}^{t_{\text{peak}}+50\text{ns}} B_j^2(t) \quad (7.3)$$

where ϵ_0 is the vacuum permittivity and c the speed of light in vacuum. The peak amplitude and the peak time t_{peak} in $B_j(t)$ are determined from the maximum of the absolute Hilbert envelope of $B_j(t)$. The quantity f_{B_j} can be understood as the coherent energy fluence received by the array of observers i from a given location \vec{j} .

³ A linear interpolation is not strictly physically correct. Application of a phase gradient to the Fourier spectrum or adequate up-sampling of S_i would be more physically motivated. However, linear interpolation is computationally more efficient, and we validated that the reconstruction accuracy is independent of this procedure for $\Delta t = 1 \text{ ns}$ for frequencies up to 200 MHz and $\Delta t = 0.33 \text{ ns}$ for frequencies up to 350 MHz.

Eqs. (7.1), (7.2), and (7.3) allow us now to calculate the coherent energy fluence received from any position in the atmosphere. In Fig. 7.2 (left) a cross-section of the coherent energy fluence from an example shower sampled at 37 antenna locations is shown. The longitudinal profile along the shower axis (vertical line) is expressed in g cm^{-2} (y-axis) while the lateral profile is shown perpendicular to the shower axis along the $\vec{v} \times \vec{B}$ -direction (x-axis) in meters. It is apparent that the profile of the coherent energy fluence correlates with the particle cascade of the air shower, i.e., f_B is the strongest around the shower axis and exhibits a maximum. It has been shown that this maximum, defined as X_{RIT} , correlates linearly with the shower maximum of the particle cascade [150]. Thus, RIT allows to reconstruct the shower properties, e.g., the depth of the shower maximum and shower axis.

As in Ref. [150], only the signal in the $\vec{v} \times \vec{B}$ polarization, which is obtained by rotating the Electric field vector simulated in the North-South, West-East, Vertical polarizations using the true arrival direction, is used for reconstruction ($\equiv S_i(t)$). It seems natural to separate the radio emission based on its emission mechanisms, i.e., separate between geomagnetic and charge-excess emission, as any phase-shift in the signals between both mechanisms would reduce the signals' coherence. Such phase shifts correspond to a small degree of circular polarization observed both in simulations and data, see [49]. In inclined air showers the geomagnetic emission, which constitutes most of the signal in the $\vec{v} \times \vec{B}$ polarization, is dominant while the signal in the $\vec{v} \times \vec{v} \times \vec{B}$ polarization is completely comprised by the sub-dominant charge-excess emission. In fact, determining the longitudinal profiles $f_B(X)$ with signals in the $\vec{v} \times \vec{v} \times \vec{B}$ polarization yields no well-defined maxima which can be correlated to the depth of the showers.

7.1.2.1. Reconstruction of the shower axis

The shower axis, i.e., the extrapolated trajectory of the primary particle, is reconstructed with RIT by searching for an axis along which the longitudinal profile of the coherent energy fluence is maximal. For this purpose, the lateral profile of the coherent radio emission, i.e., the cross-section of $f_B(X = \text{const})$, is sampled at several depths along the shower's development. For each cross-section the location of its maximum is determined and interpreted as its intersection with the shower axis. Given these intersections, a straight line is fitted minimizing the distance between line and intersections, weighted by the signal strength of each maximum.

Each cross-section is sampled in a plane perpendicular to an initial (guessed) axis which is determined given the true arrival direction, but smeared in zenith and azimuth angle with a Gaussian resolution of 0.5° each, and an intersection point at ground given by the intersection of the true Monte-Carlo (MC) shower axis smeared in a perpendicular plane with a Gaussian resolution of 100 m. This accommodates for the imperfect knowledge of the shower axis from a traditional reconstruction as starting point for a RIT reconstruction under practical circumstances.

The following procedure is applied to find the maximum in each lateral cross-section at depths of 500, 600, 700, 800, 900, 1000 and 1100 g cm^{-2} : In a first iteration, the maximum is searched on a quadratic grid which is characterized by its overall size and grid spacing. Here, we chose a grid spacing of 60 m. The grid covers an area of 1 km^2 and is set such that

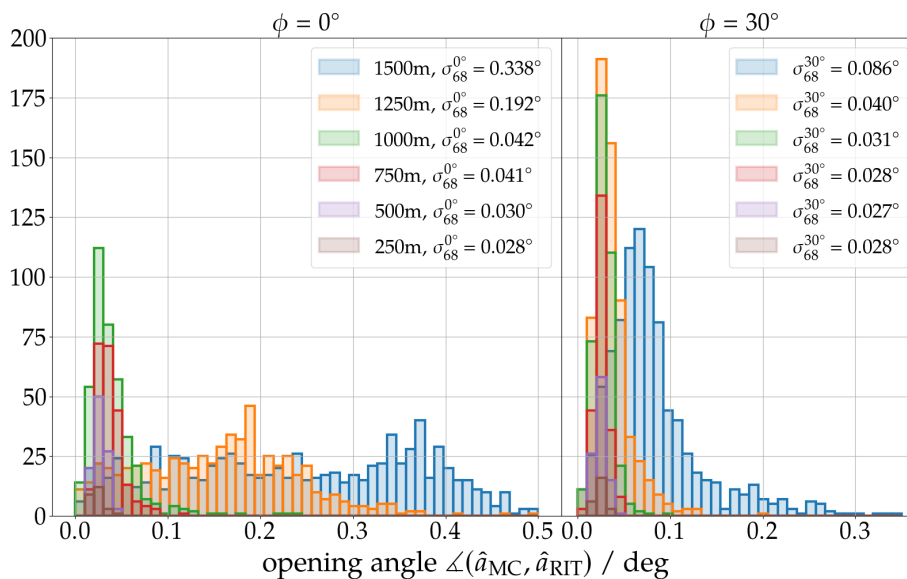


Figure 7.3.: Histograms of the opening angle distribution between true and reconstructed arrival direction for the different antenna spacings (colors) for showers with $\phi = 0^\circ$ resp. $\phi = 30^\circ$. The legend shows the resolution of the arrival direction reconstruction in terms of the 68%-quantile for all shower and all shower with $\phi = 0^\circ$ resp. $\phi = 30^\circ$.

the location of the MC shower axis is within the search grid. This is due to performance reasons; not all MC shower axes would be contained in a 1 km^2 -grid around the initial guessed axis under the starting conditions mentioned above. The 68% quantile of the distance between MC and guessed shower axis for an MC zenith angle of 77.5° at a depth of 700 g cm^{-2} is 675 m. However, the area is sufficiently dimensioned to realistically model interferometric maps containing grating lobes, i.e., local maxima. For experimental measurements one has to ensure to make the search region sufficiently scaled, of course at the expense of computational effort. In a second iteration, the cross-section is sampled on a refined quadratic grid around the previously found maximum, i.e., zoomed-in around the previously found maximum. This process is repeated until the grid spacing becomes smaller than 0.005° .

In Fig. 7.3 the opening angle distribution between true and reconstructed arrival direction for the dense simulations reconstructed on arrays with different antenna spacings with perfect time synchronization is shown. The histogram is separated between showers arriving with azimuth angles of $\phi = 0^\circ$ (left) and $\phi = 30^\circ$ (Right). The resolution in terms of the 68%-quantile is shown in the respective legend. The overall accuracy, especially for antenna spacings $\leq 1000 \text{ m}$, is very good with less than 0.1° for almost all configurations. For larger antenna spacings a bigger difference between showers from the two different incoming directions is evident. While the worsening of the resolution as a function of the antenna spacing for showers from $\phi = 30^\circ$ is moderate and just becomes significant for the 1500 m spacing, the degradation for showers from $\phi = 0^\circ$ is much more dramatic. For those showers a footprint where all high-signal antennas are aligned on a straight line parallel to the shower axis projected on the ground is likely as the antenna grid gets too

7. Interferometric reconstruction of the depth of the shower maximum

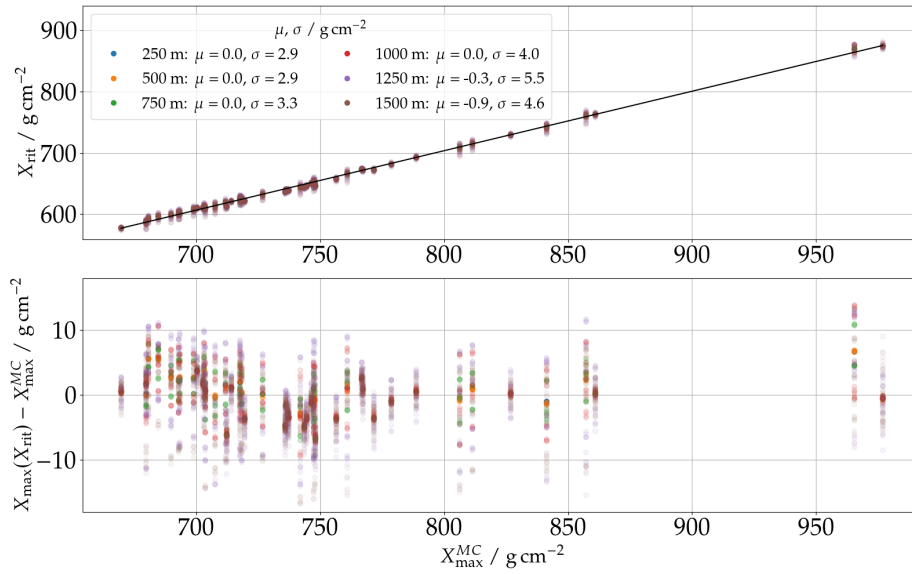


Figure 7.4.: *Top:* Reconstructed X_{RIT} as a function of $X_{\text{max}}^{\text{MC}}$ for the dense simulations. The black line indicates the calibration curve according to Eq. (7.4). Reconstruction along the MC shower axis with perfect time synchronization between the antennas. The different colors refer to reconstructions with (sub-)arrays of different spacings (transparency increases with number of reconstructions). The legend illustrates the bias and resolution for different array spacing. *Bottom:* Residuals between reconstructed and true depth of the shower maximum X_{max} .

coarse to sample the Cherenkov ring along the whole plane (cf. middle panel of Fig. 7.1). Inferring the correct arrival direction is more difficult for such geometries.

7.1.2.2. Reconstruction of the shower maximum

To reconstruct the depth of the shower maximum, we determine the maximum X_{RIT} of the longitudinal profile of the coherent signal $f_{B_j}(X)$ along the (Monte-Carlo or reconstructed) shower axis. A profile of $f_{B_j}(X)$ along the MC shower axis as a function of the slant depth X is shown in Fig. 7.2 (*top right*). To find X_{RIT} we employ the following algorithm: We sample the longitudinal profile $f_{B_j}(X)$ along the shower axis in steps of 100 g cm^{-2} between 500 and 1000 g cm^{-2} . If the maximum is found at an edge, the sampling range is dynamically extended. Once the maximum is well-confined, a 200 g cm^{-2} window around the found maximum is sampled with a refined step size of 10 g cm^{-2} . X_{RIT} is then determined by the maximum of a Gaussian curve fitted to this 200 g cm^{-2} window (cf. Fig. 7.2, *top right*).

In Fig. 7.4 (top) the reconstruction of X_{RIT} for all dense simulations with a zenith angle of $\theta = 77.5^\circ$ and the different aforementioned array spacings (color coded) as a function of the true shower depth $X_{\text{max}}^{\text{MC}}$ is shown. The reconstruction is performed with a perfect time synchronization between the different antennas, i.e., the signal arrival times are exactly known, and along the MC shower axis. A good, linear correlation is found between the reconstructed X_{RIT} and $X_{\text{max}}^{\text{MC}}$. Thus, with a linear equation the shower maximum can be reconstructed as a function of X_{RIT} :

$$X_{\text{max}}(X_{\text{RIT}}) = 1.03 \cdot X_{\text{RIT}} + 76.15 \text{ g cm}^{-2}. \quad (7.4)$$

The resulting residuals for the different spacings are shown on the bottom panel of the same figure (bias and resolutions of this residual in the legend of the top panel). It can be seen that regardless of the array spacing and thus the number of pulses used in the reconstruction (antenna multiplicity) an accurate reconstruction is achieved.

In Fig. 7.5 the reconstruction of X_{\max} for the simulations on the 1.5 km grid and showers with different zenith angles is shown. The application of a zenith-angle-independent calibration curve as in Eq. (7.4) is insufficient. Introducing a simple linear zenith-angle dependency to the intercept parameter of Eq. (7.4) is sufficient to accurately describe the relation between X_{\max} and X_{RIT} for the here considered zenith angles range. A fit to showers with $\theta \geq 75^\circ$ yields the following calibration function:

$$X_{\max}(X_{\text{RIT}}, \theta) = 1.04 \cdot X_{\text{RIT}} + \left(68.31 - \frac{\theta - 77.5^\circ}{0.35^\circ} \right) \text{g cm}^{-2}. \quad (7.5)$$

In Fig. 7.5 (*left*) the reconstructed X_{\max} as a function of the true X_{\max}^{MC} is shown. The comparison exhibits a significant scatter, only for showers with higher zenith angles (color coded) is a good correlation achieved. The residual of the reconstructed X_{\max} as a function of the zenith angle and its profile (mean and standard deviation binned in 2.5° zenith-angle bins) is also shown (*right*). It is apparent that the reconstruction accuracy strongly depends on the zenith angle. The dominant effect here is the insufficient antenna multiplicity for lower zenith angles (cf. Tab. 7.2). The dependence of the reconstruction accuracy on the antenna multiplicity is investigated in more detail in Sec. 7.1.3.

Comparing Eqs. (7.4) and (7.5), evaluated for $\theta = 77.5^\circ$, reveals no significant deviation between each other. Furthermore, no significant bias between the X_{\max} reconstructions with different antenna spacings is evident (cf. legend in Fig. 7.4). Hence, it seems that the calibration between X_{\max} and X_{RIT} is independent of the antenna spacing and the different detector layouts covered in this work. The calibration found here is also in good agreement with [150] which found an average depth $X_{\text{RIT}} \sim 615 \text{ g cm}^{-2}$ for a true depth of the shower maximum of $X_{\max} \sim 700 \text{ g cm}^{-2}$ for showers with $\theta = 75^\circ$.

7.1.2.3. Uncertainty due to atmospheric refractive index and density profiles

In this section, we evaluate the impact of an inaccurately known atmospheric refractive index profile on the reconstruction. To that end, we reconstruct the showers with different atmospheric refractivity profiles than used in the CoREAS simulations. We use the refractivity profiles (\equiv refractivity at sea level & atmospheric density profile) as adequate for the site of the Pierre Auger Observatory for the months of February and June for reconstruction, while the October profile was used for the CoREAS simulations. These two months represent the extreme in the yearly fluctuation of the refractivity at ground at the location of the Pierre Auger Observatory (for which the simulated October atmosphere resembles a good yearly average) [66, Fig. 3.21]. The yearly fluctuation is on the order of 7% and thus larger than for the locations of other radio air-shower experiments such as LOFAR or Tunka-Rex with a yearly fluctuation of 4% and 3% [66, p. 51], respectively. Thus using the refractivity profiles for February and June implies minimal knowledge of the true refractivity in the atmosphere.

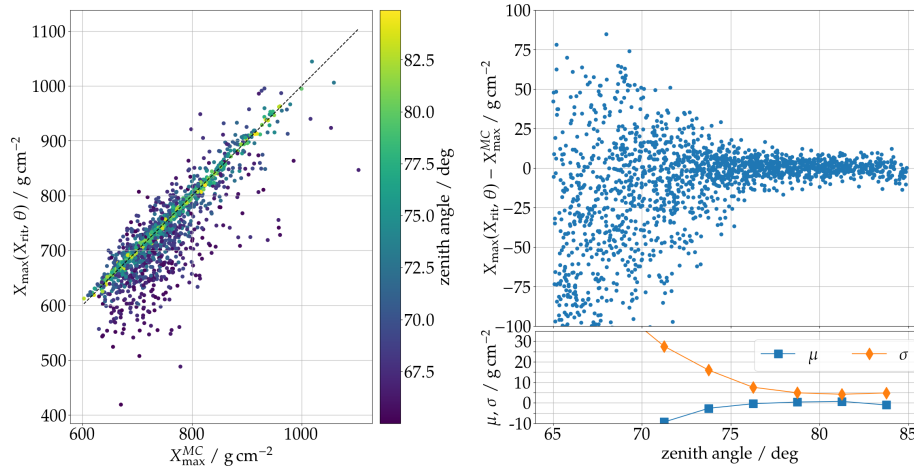


Figure 7.5.: *Left:* Reconstructed X_{\max} as a function of X_{\max}^{MC} for the simulations on the 1.5 km grid along the MC shower axis with perfect time synchronization between the antennas. The reconstruction of X_{\max} is a function of X_{RIT} and the zenith angle θ according to Eq. (7.5). The black dashed line indicates the identity, the color code shows the zenith angle. *Right:* Residuals between reconstructed and true depth of the shower maximum X_{\max} as a function of the zenith angle. Bottom panel shows the profile, i.e., mean μ and standard deviation σ of the above residual.

Using a mismatching atmospheric density profile for reconstruction will yield a wrong atmospheric depth even if the point of origin of the maximally coherent emission is correctly determined. Thus, the atmospheric depth of a maximum, reconstructed with an inaccurate refractive index profile, is determined using the correct atmospheric density profile. The deviation in X_{RIT} between the reconstruction with different refractive index profiles shown in Fig. 7.6 is $\lesssim 3 \text{ g cm}^{-2}$.

The uncertainty due to an inaccurate knowledge of the atmospheric density profile is identical to the corresponding uncertainty of X_{\max} measurements with the fluorescence technique which is on the order of 2 g cm^{-2} to 4 g cm^{-2} [164] for higher energies at the Pierre Auger Observatory.

For the following investigation the (correct) simulated atmosphere density profile and refractive index at sea level is used for the reconstruction.

7.1.3. Interferometric reconstruction of the depth of the shower maximum under realistic conditions

Having evaluated the achievable performance under idealized conditions, largely confirming the results reported in Ref. [150], in the following sections we will evaluate the X_{\max} reconstruction with RIT for a more practical scenario, i.e., with imperfect time synchronization and along the reconstructed shower axis.

7.1.3.1. Reconstruction for a detector with a 1.5 km grid spacing

Before we examine the interferometric reconstruction for simulations with varying detector layouts we evaluate the technique on simulations with the finite 1.5 km antenna array

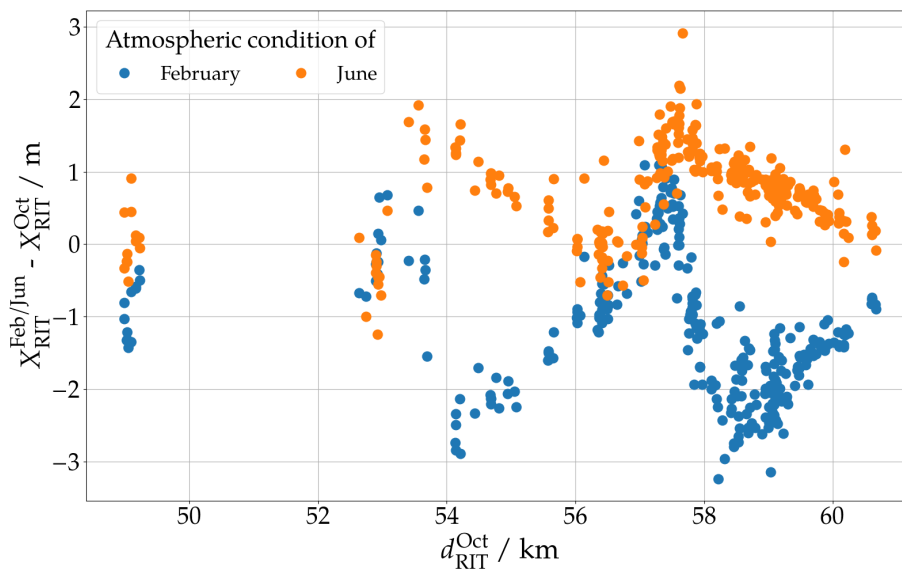


Figure 7.6.: Deviation in X_{RIT} reconstructed with different refractive index profiles along the MC shower axis. A deviation of $\lesssim 3 \text{ g cm}^{-2}$ which corresponds to $\lesssim 150 \text{ m}$ is small compared to the absolute distance $\sim 55 \text{ km}$. Here, all 50 dense showers are reconstructed once for each array spacing.

and showers with varying zenith angles. In order to study the effect of imperfect time synchronization between antennas we repeat the interferometric reconstruction several times after introducing random Gaussian time jitters. To gain quantitative insights, we evaluate the reconstruction quality in terms of the resolution (standard deviation) in X_{max} .

In Fig. 7.7 the resolution of the X_{max} reconstruction via Eq. (7.5) binned as a function of the antenna multiplicity is shown. The reconstructions along the MC and reconstructed shower axes are shown with solid and dashed lines, respectively. Different Gaussian time jitters are shown in different colors and markers. The horizontal error bars indicate the bin size, the vertical bars correspond to the statistical fluctuation of the resolution determined via a bootstrapping procedure. The reconstruction quality depends on both the antenna multiplicity and the accuracy of the time synchronization. Even with a perfect time synchronization, a minimum number of antennas $\gtrsim 12$ is required to keep the resolution below 40 g cm^{-2} . An imperfect time synchronization limits the achievable accuracy. Very accurate results ($\sigma_{X_{\text{max}}} < 20 \text{ g cm}^{-2}$) are only achieved for a time jitter of 1 ns or less and $\gtrsim 50$ antennas. It is visible that the effect of an increasing time jitter is more drastic for lower antenna multiplicities. This correlation is studied in more detail in the following section.

The reconstruction along the reconstructed axis exhibits a significant scatter, also for higher antenna multiplicities. This is due to a few but significant outliers which are result of misreconstructed axes (For example: For $\sigma_t = 2 \text{ ns}$, there is one outlier in the bin centered around $\langle n_{\text{ant}} \rangle \sim 100$ and 3 in the last bin).

In Sec. 7.1.5 the results obtained here are discussed and compared to other measurements of the depth of the shower maximum.

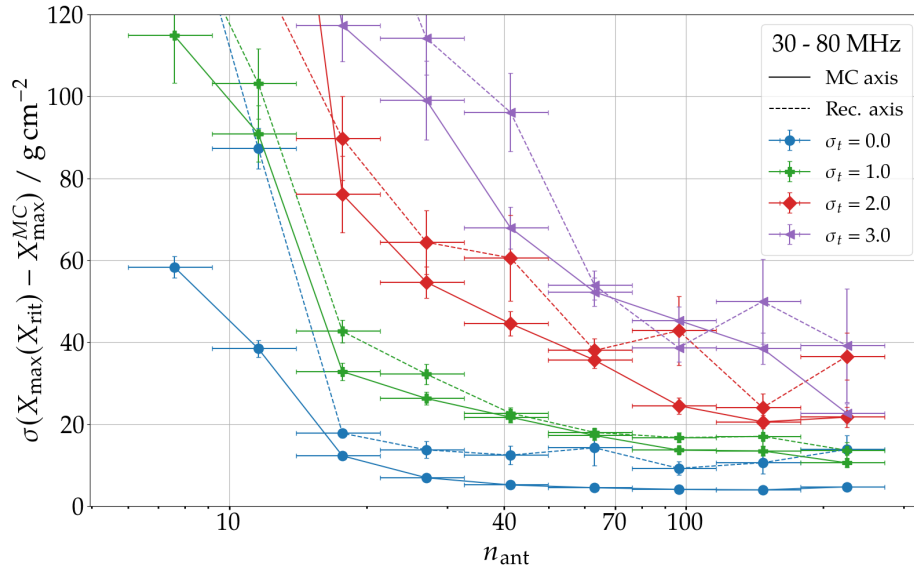


Figure 7.7.: Resolution of the X_{\max} reconstruction for the simulations on the 1.5 km grid along the true and reconstructed shower axes (solid and dashed lines, respectively), and for different Gaussian time jitters. The resolution is binned as a function of the antenna multiplicity, the horizontal error bars indicate the bin size, the vertical bars correspond to the statistical fluctuation of the resolution. The X_{\max} reconstruction along the reconstructed axes can contain a few outliers where the axis reconstruction was inaccurate, causing the visible fluctuations in the X_{\max} resolution.

7.1.3.2. Reconstruction for varying-density antenna arrays

Now we study the effect of imperfect time synchronization between antennas on the reconstruction of showers measured with different array spacings / antenna multiplicities. To that end, we repeat the reconstruction of the 50 simulated showers several times on various different sub-arrays after introducing random Gaussian time jitters mimicking an inaccurate time synchronization between the antennas. Figure 7.8 shows the resolution in X_{\max} as a function of the antenna spacing and for different time jitters. The average number of antennas $\langle n_{\text{ant}} \rangle$ per event and spacing is shown on the top x-axis. The figure demonstrates that again the resolution worsens in the presence of a time jitter. This deterioration is amplified for showers reconstructed with a low antenna multiplicity. With a time jitter of 3 ns the reconstruction on a very dense array with > 1000 antennas is still very accurate with a resolution of $\lesssim 10 \text{ g cm}^{-2}$. However, when the antenna multiplicity is $\lesssim 100$, i.e., the showers measured with the 1000 m grid or larger, the resolution deteriorates significantly to $\gtrsim 40 \text{ g cm}^{-2}$. Reconstructing X_{\max} along an imperfectly reconstructed axis seems to have no significant implications for data taken with a Gaussian time jitter of 0 ns to 2 ns and only a little effect for the 3 ns time jitter. In contrast to the simulations with the 1.5 km-spaced array for which showers can be simulated at the edge of the finite 3000 km^2 array and thus their footprints are eventually not evenly sampled, the showers with the dense 250 m-spaced array are always evenly sampled.

Incorrect time synchronization between antennas also affects the arrival direction reconstruction. In case of a 3 ns Gaussian time jitter the resolution in the direction

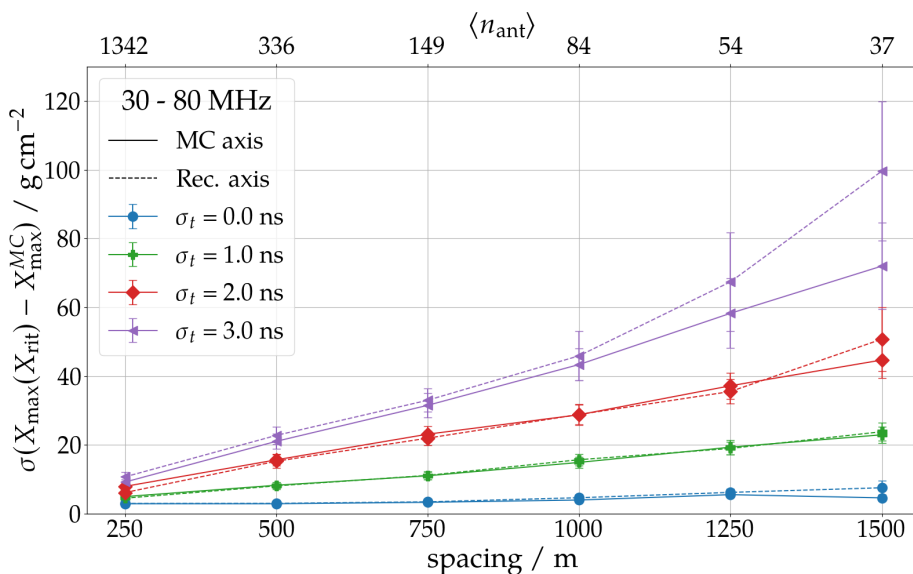


Figure 7.8.: Reconstruction resolution in X_{\max} of the 50 densely sampled showers with a zenith angle of 77.5° . Resolution is shown for different time jitter scenarios (different colors & markers) and along the MC shower axis (solid line) or reconstructed axis (dashed line) as a function of the antenna spacing. The average number of antennas per spacing is given on the top x-axis as reference.

reconstruction worsens by a factor of $\sim 1.5 - 3$ for all spacings. The difference in resolution between showers with $\phi = 0^\circ$ and 30° (cf. Fig. 7.3) decreases.

It is important to stress that the primary factor governing the X_{\max} resolution, in case of imperfect time synchronization between antennas, is the antenna multiplicity. The average number of antennas for each array spacing as listed in table 7.1 refers to an instrumented area of 72.5 km^2 (cf. Fig. 7.1). Smaller but denser arrays still need to accommodate a sufficiently high number of antennas and/or very good time synchronization to allow accurate reconstructions. In addition, our tests have shown that a complete and symmetric sampling of the radio-emission footprint, i.e., inside, on top, and outside the Cherenkov ring, is needed to ensure accurate reconstruction.

In Sec. 7.1.5 we use an analytic description of the radio-emission induced area as a function of the zenith angle to generalize the results acquire here with showers with $\theta = 77.5^\circ$ and an instrumented area of 72.5 km^2 to lower zenith angles and smaller and denser arrays.

7.1.4. Interferometric reconstruction for higher frequency bands

Many next-generation radio-detection experiments aim to observe extensive air showers with broader frequency bands and at higher frequencies. Here, we test the interferometric reconstruction of X_{\max} for two additional frequency bands: 50 MHz to 200 MHz and 150 MHz to 350 MHz. Applying the interferometric algorithm to data recorded at higher frequencies requires more stringent coherence criteria and thus a more accurate time synchronization between antennas. The considered time jitter scenarios do not reflect

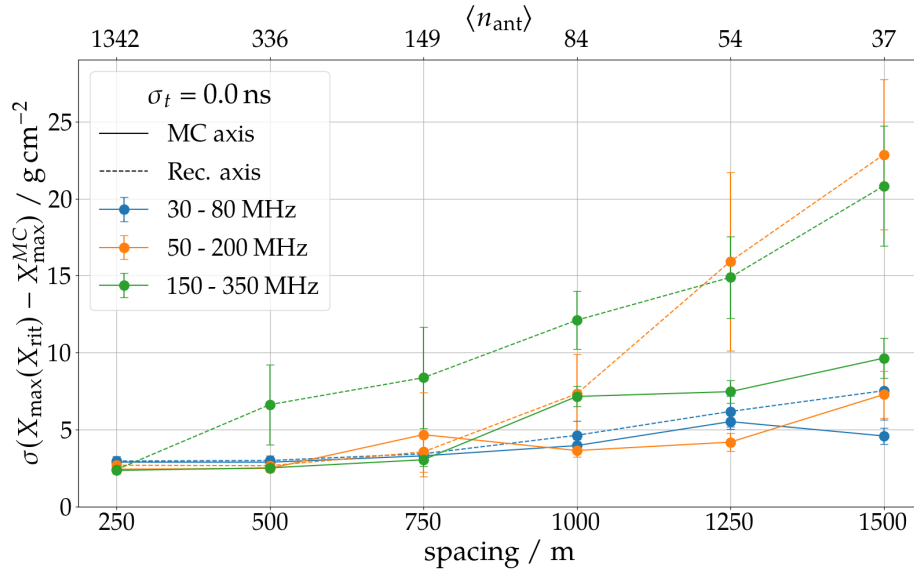


Figure 7.9.: Reconstruction resolution in X_{max} for the 30 MHz to 80 MHz, 50 MHz to 200 MHz, and 150 MHz to 350 MHz frequency bands (different colors) along the MC or reconstructed shower axis (solid or dashed line) for perfect time synchronization as a function of the antenna spacing.

equivalent phase-accuracy across the frequency bands but were chosen from a practical point of view, i.e., what time synchronization accuracy an experiment has to achieve to employ RIT for higher frequencies. Furthermore, we found that the 3-dimensional profile of the coherent signal f_{B_j} around the shower axis is increasingly narrow for higher frequencies. Hence, the resolution with which the lateral cross-sections are sampled to infer the shower axis needs to be refined. For the axis reconstruction of showers recorded in the frequency band from 150 MHz to 350 MHz an overall size of 0.16 km^2 and a search grid spacing of 20 m was used.

In Fig. 7.9 the X_{max} resolution with perfect time synchronization and along the MC and reconstructed shower axes for the different frequency bands (color coded) are compared. For the higher frequencies the reconstruction accuracy (along the MC shower axis) slightly decreases for sparser antenna arrays (150 MHz to 350 MHz). This is even more prominent for the reconstruction along the reconstructed axis (50 MHz to 200 MHz and 150 MHz to 350 MHz). One reason for this could be an insufficient sampling of the Cherenkov ring with these sparse arrays. As the Cherenkov ring itself is more dominating but also more narrow for showers measured with higher frequencies, the reconstruction accuracy depends more strongly on the antenna spacing. Furthermore, an offset in X_{RIT} between the different frequency bands is found, e.g., the X_{RIT} reconstructed for 150 MHz to 350 MHz is $\sim 16.5 \text{ g cm}^{-2}$ smaller than for 30 MHz to 80 MHz. This offset has been taken into account when determining X_{max} . For this purpose we repeated the parameterization of Eq. (7.4) for the different frequency band, see Table 7.3.

Figure 7.10 shows the achieved X_{max} resolution for the two higher frequency bands (left: 50 MHz to 200 MHz, right: 150 MHz to 350 MHz) and different Gaussian time jitter scenarios. As expected, for the higher frequency bands already more modest time jitters, e.g., 2 ns for 50 MHz to 200 MHz and 1 ns for 150 MHz to 350 MHz, worsen the results

Table 7.3.: Parameters of Eq. (7.4), i.e., $X_{\max} = a \cdot X_{\text{RIT}} + b$ for the different frequency bands.

	a	b
30 to 80 MHz	1.029	76.15 g cm ⁻²
50 to 200 MHz	1.027	76.97 g cm ⁻²
150 to 350 MHz	1.024	92.91 g cm ⁻²

significantly. The antenna multiplicity has to be higher than ~ 70 (100) and the time synchronization better than $\sigma_t = 1$ ns (0.5 ns) for 50 MHz to 200 MHz (150 MHz to 350 MHz) to achieve a resolution of $\sigma_{X_{\max}} < 40$ g cm⁻².

As mentioned before, the axis reconstruction for 150 MHz to 350 MHz requires a finer sampling of the lateral cross-sections. With the refined search-grid spacing of 20 m a similar resolution of X_{\max} , reconstructed along the reconstructed axis, compared to the lower frequency bands with a search-grid spacing of 60 m is observed. However, the overall grid size used to reconstruct the shower maximum for data recorded with 150 MHz to 350 MHz does not reflect the reconstruction under practical circumstances as the searched area is too small to reliably contain the true maximum for an axis (starting point) which is known with an accuracy of 0.5° in zenith and azimuth each.

A, more sophisticated, gradient-descent based algorithm could reduce the computing time significantly and would allow the shower axis reconstruction under practical circumstances also for higher frequency bands. Such an algorithm has to be robust against grating lobes, i.e., local maxima in the interferometric maps.

In Ref. [150], in addition to an algorithm similar to the one described above, the shower axis is refined by maximizing the integrated longitudinal profile along the axis. Also in LOPES the arrival direction is inferred by a two-folded approach, first applying a raster-search algorithm and upon this a gradient-descent algorithm.

7.1.5. Discussion

Here, we discuss our results and also mention a few aspects which could not be studied in detail within the scope of this work.

The study presented here for different detector layouts, especially those with an antenna spacing of < 1.5 km, is limited to simulations with a zenith angle of $\theta = 77.5^\circ$. In Ref. [150], a modest improvement of the reconstruction accuracy with increasing zenith angle, i.e., with increasing distance between observer and source region, is found for simulations with a constant antenna multiplicity. The drastic improvement in resolution with increasing zenith angle found in this work (cf. Fig. 7.5) cannot be exclusively explained by this. In fact, the antenna multiplicity is identified as the crucial factor for an accurate reconstruction. Showers with a lower zenith angle illuminate smaller areas at ground and thus the antenna multiplicity decreases for showers measured with a constantly-spaced array. Assuming that the size A of the radio-emission footprint at ground scales with the radius of the Cherenkov ring r_0 (cf. Eq. (4.4)) yields the following relation:

$$A \sim \frac{\pi r_{\text{Che}}^2}{\cos \theta}. \quad (7.6)$$

7. Interferometric reconstruction of the depth of the shower maximum

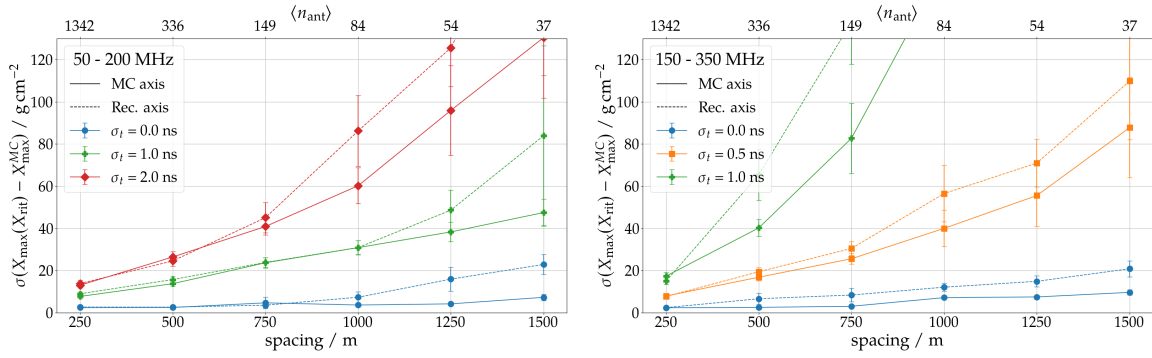


Figure 7.10.: Reconstruction resolution in X_{\max} for the 50 MHz to 200 MHz (*left*) and 150 MHz to 350 MHz (*right*) frequency bands and different time jitters (different colors and markers) along the MC or reconstructed shower axis (solid or dashed line) as a function of the antenna spacing.

The antenna multiplicity is proportional to the footprint area A . To instrument a given area with a certain number of antennas the antenna spacing Δ_{ant} has to satisfy the relation: $\sqrt{\Delta_{\text{ant}}} \sim \sqrt{A}$. Figure 7.11 shows the antenna spacing as a function of the zenith angle necessary to satisfy the antenna multiplicity $\langle n_{\text{ant}} \rangle = 84$, i.e., the antenna multiplicity of the reference point at $\theta = 77.5^\circ$ (black marker) for showers measured with a 1000 m hexagonal grid (cf. Tab. 7.1). Ignoring any additional zenith-angle related effects, this curve indicates the necessary antenna spacing to achieve a reconstruction as accurate as for the reference, i.e., $\sigma_{X_{\max}}(\sigma_t = 1 \text{ ns}) = 16 \text{ g cm}^{-2}$ or $\sigma_{X_{\max}}(\sigma_t = 2 \text{ ns}) = 29 \text{ g cm}^{-2}$ (cf. Figs. 7.7, 7.8). The different colors refer to different observation heights and the shaded areas correspond to X_{\max} values ranging from 550 g cm^{-2} to 950 g cm^{-2} with a nominal value of 750 g cm^{-2} (solid lines). These values resemble the mean and range of X_{\max} values for a cosmic ray composition of half proton and half iron primaries with energies around 10 EeV. It is apparent that an accurate reconstruction for more vertical showers with $\theta < 40^\circ$ is only achievable with antenna spacings below 100 m. For showers with zenith angles below 25° the antenna spacing cannot be larger than \sim tens of meters. Those showers, when measured at an altitude of 1000 m a.s.l., can reach ground before developing the full maximum (this happens with a depth of the maximum of $> 850 \text{ g cm}^{-2}$) and thus no lower limit can be calculated. This emphasizes that for vertical air showers the observation altitude matters. This is further underlined by the finding in Ref. [150] that the accuracy in X_{\max} deteriorates when the distance between observer and source becomes smaller. The area associated to a given antenna spacing and $\langle n_{\text{ant}} \rangle = 84$ is shown on the second (right) y-axis.

Furthermore, in this study the issue of triggering the readout of the radio signals, be it based on radio signals or measured particles, has not been considered. The interferometric reconstruction profits also from low signals and thus a readout of all antennas for a given event is optimal (as simulated in this study), even if no measurable radio pulse or particles are present. However, most cosmic-ray experiments employ a trigger based on the signal strength per detector station to reduce the amount of data recorded. This might lead to a reduction of recorded radio pulses and thus limit the accuracy of interferometric measurements. Experiments with an accompanying particle detector can profit from a lower trigger threshold and thus recorded more radio pulses for vertical showers. For

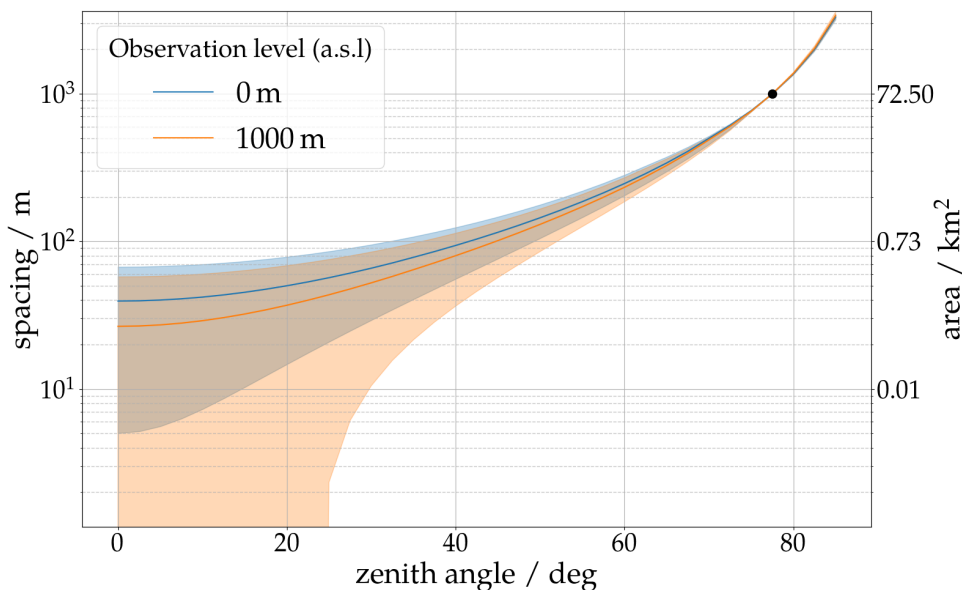


Figure 7.11.: Antenna spacing required to achieve an antenna multiplicity of ~ 84 . This is the mean antenna multiplicity for showers with $\theta = 77.5^\circ$ measured with a 1000 m hexagonal grid (black dot) over an instrumented area of 72.5 km^2 . The second y-axis shows the area associated to a given antenna spacing and the aforementioned antenna multiplicity. For these showers an X_{max} resolution below 20 g cm^{-2} when measured with a 1 ns Gaussian time jitter in the 30 MHz to 80 MHz band is achieved (cf. Fig. 7.8). The different colors refer to different observation heights and the shaded areas correspond to X_{max} values ranging from 550 g cm^{-2} to 950 g cm^{-2} with a nominal value of 750 g cm^{-2} (solid lines). The curves are calculated using Eqs. (7.6) and (4.4). For the calculation of the radius of the Cherenkov ring the US standard model of the atmospheric density profile and a refractivity at ground of $N_0 = 292 \cdot 10^{-6}$ are used. For showers with a zenith angles below 25° measured at an observation altitude of 1000 m the shower maximum can lie underground, thus no lower limit can be calculated.

air showers with zenith angles beyond 75° to 80° , however, the size of the radio-emission footprint eventually exceeds the size of the particle footprint [71], and a trigger relying on information of particle detectors alone will limit the amount of radio pulses recorded. For instance, the AugerPrime Radio Detector will only record radio pulses of antennas for which the water-Cherenkov detector (WCD) beneath has triggered. Thus, the number of pulses recorded is governed by the particle footprint, i.e., the footprint for which the water-Cherenkov detectors will trigger, and as such is a function of the primary energy and the zenith angle. To trigger more than 12 WCD, a minimum zenith angle of $\gtrsim 75^\circ$ or energy of $\gtrsim 10 \text{ EeV}$ has to be reached [84]. More than 50 stations are almost never triggered. Given these limitations in the triggering for the AugerPrime Radio Detector, the application of a RIT reconstruction unfortunately does not seem very promising even if the time synchronization can be improved to $\sigma_t \sim 1 \text{ ns}$ (cf. Fig. 7.7).

We point out that a description of the directional sensitivity of an appropriate radio antenna was not taken into account in this study. Moreover, we assume that the full 3-dimensional electric field vector, in particular the electric field in the $\vec{v} \times \vec{B}$ polarization, is accessible from the experimental measurements.

Besides detector effects, ambient noise is a crucial aspect for the detection of air showers with radio antennas. However, the ambient noise conditions can change dramatically between different locations around the Earth, their significance depends on the observed range of cosmic-ray energies and the frequency-band of choice, and their modeling taking into account different contributions, e.g., narrow- and broadband radio-frequency-interference, is not straightforward. Furthermore, it is anticipated that the effect of ambient noise is attenuated for interferometric measurements scaling with the square root of the number of antennas [150]. Dedicated studies for specific experiments are needed to determine the impact of noise at their specific location. Such a study can also determine if the interferometric detection threshold can be lowered when measuring in a higher frequency band [165].

Judging the required X_{\max} resolution to be achieved with a large sparse antenna arrays is a complex question as it depends on several factors such as the scientific objective, e.g., measuring the average mass composition or aiming for a light-heavy particle discrimination, the available statistics, and the astrophysical scenario, i.e., the actual mass composition of cosmic rays. To simplify, we compare the achievable X_{\max} resolution with RIT to different experimental results. Recently, the Pierre Auger Collaboration has demonstrated that an accurate X_{\max} reconstruction with the 1.5 km-grid of water-Cherenkov (particle) detectors is possible using deep-learning techniques [166]. The resolution with this method for vertical showers with energies of around 3 EeV is 40 g cm^{-2} and improves to 25 g cm^{-2} for energies above 20 EeV. The resolution achieved by the Auger Fluorescence Detector is 25 g cm^{-2} (15 g cm^{-2}) for energies above 1 EeV (10 EeV) [164]. LOFAR, a radio air shower experiment, measures vertical showers with hundreds of antennas in the energy range from 10^{17} to 10^{18} eV with a typical accuracy of 17 g cm^{-2} [167]. Tunka-Rex, another radio air shower experiment, measures X_{\max} with a low, typical multiplicity of 7 antennas with an accuracy of 25 g cm^{-2} [168]. However, both results achieved with these radio experiments rely on the extensive use of very time-consuming and computing-intensive Monte-Carlo simulations and are not applicable for larger antenna arrays (with higher event statistics). Furthermore, have those methods never been applied to inclined air showers and the resolution seems questionable because of the large distance between the shower maximum and detector.

The results obtained in this work show that the application of RIT with large, sparse antenna arrays relying on wireless communication is very challenging. Even with specialized hardware which improves the time synchronization to $\sim 1 \text{ ns}$ (or better for higher frequencies), an antenna multiplicity of $\gtrsim 20$ (50) has to be achieved to obtain competitive results of $\sigma_{X_{\max}} \approx 35 \text{ g cm}^{-2}$ (20 g cm^{-2}). These requirements will likely not be met by existing or currently planned experiments such as the Pierre Auger Observatory or GRAND.

More suitable for the application of RIT seem smaller ultra-dense antenna arrays with cabled communication such as the Square Kilometer Array SKA-Low [161], which in fact is designed as an interferometer and thus will meet the required timing accuracy for interferometric analyses.

After this analysis had been concluded and published, the authors of [150] published their reviewed and revised work in Ref. [169]. In their revised work, they also study the effect of a Gaussian time jitter on the achievable X_{\max} resolutions. They found a

less dramatic degradation of the resolution with the magnitude of timing uncertainty, with $\sigma_t = 3$ ns a resolution of $\sigma_{X_{\max}} \sim 30 \text{ g cm}^{-2}$ with minor differences between different zenith angle bins. The antenna multiplicity does not scale with the zenith angle as their detector layout and thus their antenna density scales with the zenith angle to keep the multiplicity constant. Those results are claimed to be achieved with only 25 - 40 antennas. The fact the quoted antenna multiplicities still change suggests that a selection criterion (based on the signal strength) to count antennas and/or use them in the reconstruction is used, however details are missing. The simulated antenna densities for the zenith-angle dependent antenna grids suggest very compact arrays, e.g., an antenna density of 400 km^{-2} for 0° -showers with a maximum antenna multiplicity of 40 yield a radius of the radio footprint of ~ 180 m.

7.1.6. Conclusion

This study explores the potential for interferometric measurements of the depth of maximum of extensive air showers X_{\max} with large, sparse arrays of radio antennas under realistic conditions. It has been shown that for measurements in the frequency band of 30 MHz to 80 MHz, in addition to a very good time synchronization of 1 ns also a sufficiently large number of antennas per shower ($\gtrsim 100$) is needed for an accurate determination of X_{\max} with a competitive X_{\max} resolution of below 20 g cm^{-2} . For a decent reconstruction with a resolution $\lesssim 35 \text{ g cm}^{-2}$, a signal multiplicity of at least $\gtrsim 20$ is imperative. Given the size of the radio-emission footprint scales with the zenith angle, this constrains the maximal suitable array spacing to < 100 m for vertical showers with zenith angles $\theta < 40^\circ$ and to a few hundred meters for showers with zenith angles $\theta \lesssim 75^\circ$. Only for higher zenith angles, arrays with an antenna spacing of 1000 m or larger accommodate a sufficient antenna multiplicity. However, any kind of trigger based on the signal strength per detector station will reduce the amount of recorded radio pulses, cf. Sec. 7.2. Thus, it seems very challenging to accommodate such requirements for (existing) air shower arrays with spacings $\gtrsim 1000$ m which were designed and constructed without specific considerations for interferometric measurements, and in particular do not meet the requirements on the accuracy of time synchronization.

The interferometric reconstruction of data recorded with higher frequencies showed no improvement in the achievable accuracy. Moreover, we found that, in addition to more stringent requirements to the time synchronization between antennas, no improvement in accuracy of the X_{\max} reconstruction is achieved when the geometry and signals' arrival times are exactly known. Thus, no advantage is found when applying the interferometric reconstruction to data recorded with higher frequencies.

Experiments which facilitate a large number of antennas combined with a very accurate time synchronization such as the Square Kilometer Array have great potential to exploit interferometric measurements of X_{\max} . If combined with a muon detector, this approach could yield very valuable information to study the physics of extensive air showers and their hadronic interactions, as well as the mass composition of cosmic rays, with unprecedented detail.

7.2. Interferometric reconstruction of the depth of the shower maximum with the Auger radio detectors

With the evaluation of the performance of interferometric X_{\max} reconstruction specifically for the RD and AERA, we address a few shortcomings of the previous section. For the RD we use Offline-simulated triggers of the WCD to select radio pulses for the reconstruction. For AERA we use dedicated simulations with the AERA detector layout and add generated noise to the simulated signals. This analysis preceded the analysis presented in the previous sections. Hence, for this analysis fewer simulations with the detector layout of the RD were available. Furthermore, we use a slightly different function to reconstruct X_{\max} from X_{RIT} , namely,

$$X_{\max}(X_{\text{RIT}}, \theta) = \frac{X_{\text{RIT}} - (a_2 \cdot \theta + b_2)}{a_1 \cdot \theta + b_1}. \quad (7.7)$$

with the parameters a_1 , a_2 , b_1 , and b_2 determined for each detector independently.

7.2.1. Simulations

To evaluate the potential for RD, we use a set of 207 proton-induced air showers with pulses simulated for observers on a 1.5 km hexagonal grid with random core positions⁴. The showers have an energy of 10 EeV and binned arrival directions⁵. For showers below $\sim 75^\circ$ to 77.5° the antenna multiplicity is likely limited by the number of simulated pulses, i.e., the size of the radio-emission footprint at the ground. For showers with higher zenith angles, the radio footprint exceeds the size of the particle footprint which limits the station multiplicity since the RD relies on triggers from the WCDs, see appendix C.3. For this analysis, only radio pulses are considered for which the underlying WCD triggered as simulated with Offline. Given the muon deficit in simulations, the multiplicity of triggered stations for measured events will be slightly higher.

To evaluate the potential for AERA, we use a set of 874 proton- and iron-induced air showers with parameters (arrival direction, primary energy, core position) matching those of 530 inclined AERA-reconstructed events. The air showers were simulated with CORSIKA/CoREAS v7.56 and with the October Malargüe atmosphere. In contrast to other simulations with the October Malargüe atmosphere, a refractive index at sea level of $n_0 = 1 + 3.03 \times 10^{-4}$ is used. The set has a mean energy of 3.25 EeV and zenith angles from $\sim 60^\circ$ to 84° .

The antennas are situated on an average altitude of ~ 1570 m on a, comparably, dense but irregular grid with station spacings varying between 144 and 750 m. Unlike other simulations used in this work, for AERA, showers are not necessarily contained in the area enclosed by the antenna array. Each simulation contains pulses for all AERA stations⁶.

⁴ The selection of the observers for each shower is similar to the one described in Sec. 4.1.2.1 but with a different maximum distance.

⁵ The arrival direction bins are the same as for the star-shaped simulations.

⁶ Which comprises stations equipped with 2 different electronics and trigger concepts that would be particularly difficult to combine in an interferometric reconstruction in which timing is crucial.

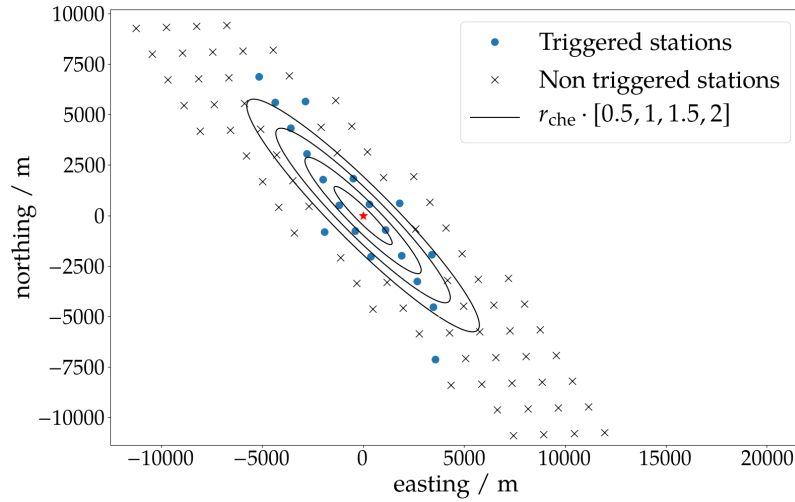


Figure 7.12.: Example for an 80° air shower detected by the RD with triggered (blue circles) and non triggered (black crosses) stations. Only stations for which a radio pulse was simulated are shown. The ellipses indicate the edges of the 4 annuli which correspond to circles in the shower plane with radii $r = x \cdot r_{\text{Che}}^{\text{param}}$ for $x \in [0.5, 1, 1.5, 2]$.

7.2.2. Shower selection

For an accurate reconstruction with an irregular array (AERA) or sparse array (RD), it is beneficial to determine criteria to ensure adequate sampling of the radio-emission footprint and thus a good resolution. Given that the coherence properties of the emission shape the characteristic lateral distribution at the ground (e.g., the Cherenkov ring) it is evident to sample the showers' signal distributions within, on, and outside the Cherenkov ring. We determine the radius of the Cherenkov ring for each shower according Eq. (4.4) but with a parameterized correcting factor $A(d_{\text{max}})$ for the Cherenkov angle δ_{Che} . The correction is necessary to describe the radius of a ring which is defined by the maximum (geomagnetic) energy fluence.

$$r_{\text{Che}}^{\text{param}} = \tan(\delta_{\text{Che}}(h_{\text{max}}, n_0) \cdot A(d_{\text{max}})) \cdot d_{\text{max}}. \quad (7.8)$$

Details are given in Sec. C.2. This correction has only been used in this section.

With this, we subdivide the radio footprints into different annuli, whose edges are defined in units of the Cherenkov radius, and count the stations in each of them. We tested several configurations for the number and size of the annuli and the minimum number of stations per annulus for each detector to obtain a very accurate reconstruction resolution while retaining a high selection efficiency. Finally, we define 4 annuli with equidistant width between an axis distance of 0 and 2 Cherenkov radii and require at least 2 stations (i.e., simulated pulses) in 3 of the 4 annuli for RD and at least 3 stations in each of the 4 annuli for AERA. In Fig. 7.12 the footprint of a simulated shower with a 80° zenith angle measured by RD is shown. The number of (triggered) stations within the 4 annuli (drawn as black ellipses) is sufficient to meet the aforementioned criteria.

7. Interferometric reconstruction of the depth of the shower maximum

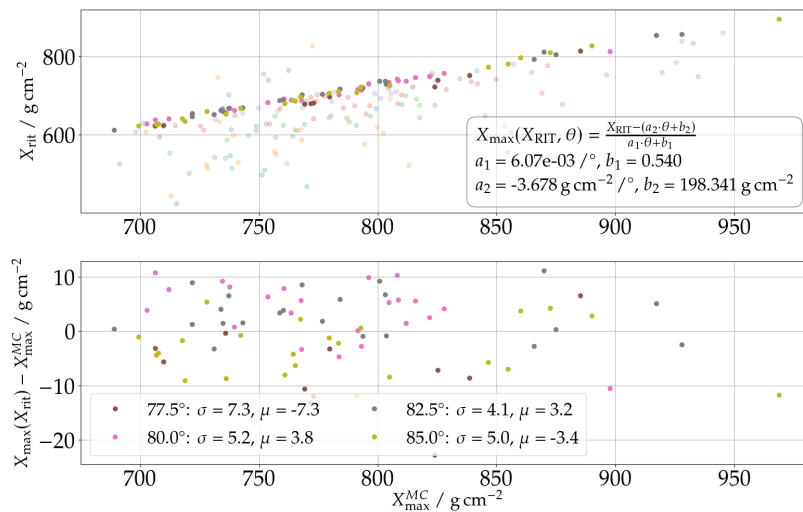


Figure 7.13.: Reconstruction of the depth of the shower maximum X_{\max} with the RD assuming a perfect time synchronization and considering only stations with a triggered WCD. Only the selected (full markers) showers were used to determine the parameters from Eq. (7.7) (parameters are shown in legend). Deselected showers are indicated by transparent markers in the top panel.

7.2.3. Expected reconstruction performance for the RD

For the RD, 79 of 207 showers passed the footprint-sampling selection outline in the previous section 7.2.1. Only showers with a zenith angle of 77.5° or larger fulfill the criterion (for more details also see Sec. C.3). In Fig. 7.13, the X_{RIT} reconstruction for the showers passing the selection (full markers) and the remaining showers (transparent markers) is shown in the top panel. To the selected showers, the Eq. (7.7) is fitted to reconstruct X_{\max} (see parameters a and b in the figure legend). The residuum for the reconstructed $X_{\max}(X_{\text{RIT}}, \theta)$ is shown for selected showers in the bottom panel (resolution and bias per zenith angle bin are shown in the legend). Despite low statistics, a high resolution is achieved for the selected showers, the overall resolution is found to be 6.7 g cm^{-2} .

Tests of the Auger upgraded unified boards indicate a GPS-based time synchronization between SD stations to within $\sim 5 \text{ ns}$ [170]. Unfortunately, such a time synchronization is insufficient for any interferometric analysis given the coherence criteria mentioned in Chap. 7. A significant improvement of that temporal resolution seems very challenging without different electronics⁷. A beacon system as employed for AERA (cf. Sec. 7.2.4) can hardly be extended to an array of 3000 km^2 . Hence, a resolution of $< 1 \text{ ns}$ to 3 ns seems extremely challenging to achieve. Nonetheless, to optimistically estimate the potential of the technique applied to the RD, we repeat the reconstruction of X_{\max} adding Gaussian time jitters to the signals' start times of 1, 2, and 3 ns. In Fig. 7.14 the reconstruction of X_{RIT} as well as the resolution of X_{\max} with a 3 ns time jitter are shown. To decrease statistical fluctuations each shower is reconstructed 6 times changing the random time jitters. The accuracy of the reconstruction decreased significantly to 124.2 g cm^{-2} for

⁷ Private Communication Corbin Covault.

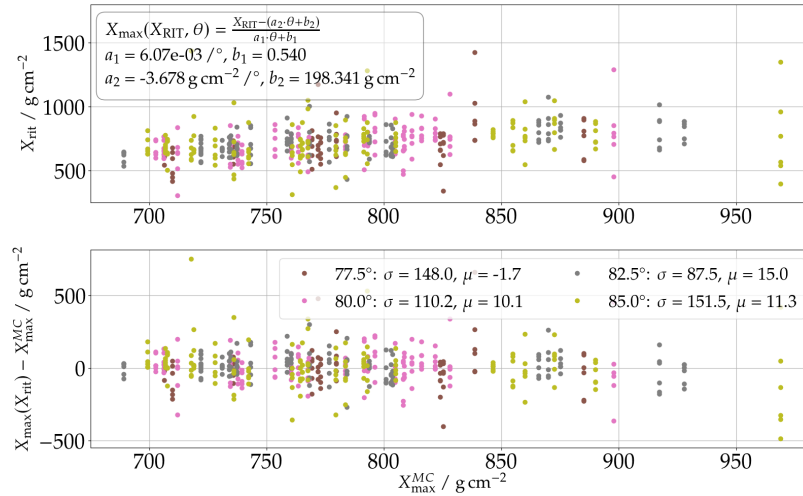


Figure 7.14.: Reconstruction of the depth of the shower maximum X_{max} with the RD and a 3 ns Gaussian time jitter. Each shower is reconstructed 6 times with different time jitters to reduce the statistical fluctuation.

3 ns. All resolutions are summarized in Tab. 7.4. The uncertainties are determined using bootstrapping with sub-sets of the size of the total number of unique showers.

Thus, it seems clear that a time resolution of 3 ns is too inaccurate to apply RIT to RD-measured showers. In Ref. [150] no such significant degradation for a 3 ns time jitter was reported. The resolution improves when including non-WCD-triggered stations (at larger axis distances) in the reconstruction. This agrees with the results from the previous section where a strong correlation between reconstruction accuracy and antenna multiplicity is found when introducing a time jitter. Also, the results for AERA (next section), which has typically a much higher antenna multiplicity, indicate the same.

7.2.4. Expected reconstruction performance for AERA

For AERA, 233 out of the 874 showers are passing the sampling selection. The zenith angle distribution of all simulated showers and the selected showers is shown in the appendix, Fig. C.3 (right). In Fig. 7.15, the reconstruction performance for X_{max} is shown assuming a perfect time measurement. The resolution is found to be 10.1 g cm^{-2} . While in the top panel the X_{RIT} reconstruction is shown also for showers that did not pass the footprint-sampling selection (transparent markers), the X_{max} reconstruction (calibration and residuum) only refers to the selected 233 showers (full markers).

As a next step, we evaluate the reconstruction performance under more realistic conditions, adding a time jitter and generated, ambient noise to the simulated signals. To minimize statistical effects in the reconstruction when adding random time jitter or generated ambient noise we repeat the reconstruction of each selected shower 6 times.

The time resolution achievable with AERA is significantly better than for the RD since at the AERA site a beacon system is installed [160]. This device transmits a reference signal which is recorded by the antennas along with the air shower signal and can be used to improve the timing given by GPS. This results in a resolution estimated to be

7. Interferometric reconstruction of the depth of the shower maximum

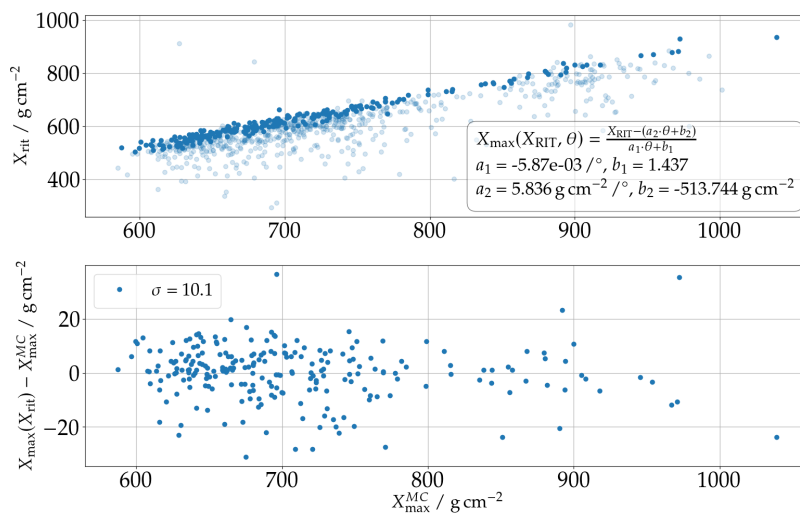


Figure 7.15.: Reconstruction of the depth of the shower maximum X_{\max} with AERA assuming a perfect time synchronisation. The subset of 233 showers which passed the sampling selection (full marker) were used to determine the parameters of Eq. (7.7). Deselected showers are indicated by transparent markers in the top panel.

better than 2 ns [93]. The beacon system was installed with the specific goal of enabling interferometric analyses with AERA, which had, however, so far not been successful [154].

The noise traces are generated in the following way: For a given frequency-independent noise temperature, an amplitude spectrum in the frequency domain is drawn randomly according to a Rayleigh distribution⁸. To the amplitude spectrum, uniformly drawn random phases are applied. The generated, band-pass-filtered frequency spectra are finally Fourier-transformed to real-time series data. The noise temperature is chosen such that the resulting noise traces on average have a maximum peak amplitude of the Hilbert envelope of $\sim 50 \mu\text{V}/\text{m}$. This matches the mean found for the ambient noise recorded with inclined air showers with AERA.

To estimate the influence of a realistic geometrical reconstruction, we first reconstruct the shower axis adding the generated noise and a 2 ns time jitter, and given that axis, reconstruct X_{RIT} . The result for the shower axis reconstruction, i.e., the opening angle distribution between true and reconstructed shower axis, is shown in Fig. 7.16 (left). The resolution achieved with the subset of 233 optimally sampled events is 0.4° . The X_{\max} reconstruction using the reconstructed axis in the presence of generated ambient noise and a time jitter of 2 ns is shown in Fig. 7.16 (right). The resolution of X_{\max} decreased to 52.8 g cm^{-2} . Repeating this reconstruction by adding neither noise nor time jitter yields a similar resolution of the shower axis of 0.4° and an X_{\max} resolution of 24.1 g cm^{-2} . However, there remain some doubts if the axis reconstruction could not be refined given the fact that it does not deteriorate when adding noise and the time jitter. To evaluate the most

⁸ The Rayleigh distribution is normalized such that the resulting amplitudes are distributed as if the real and imaginary parts of the complex amplitude had been drawn as uncorrelated from a Gaussian distribution each with the same initial noise temperature.

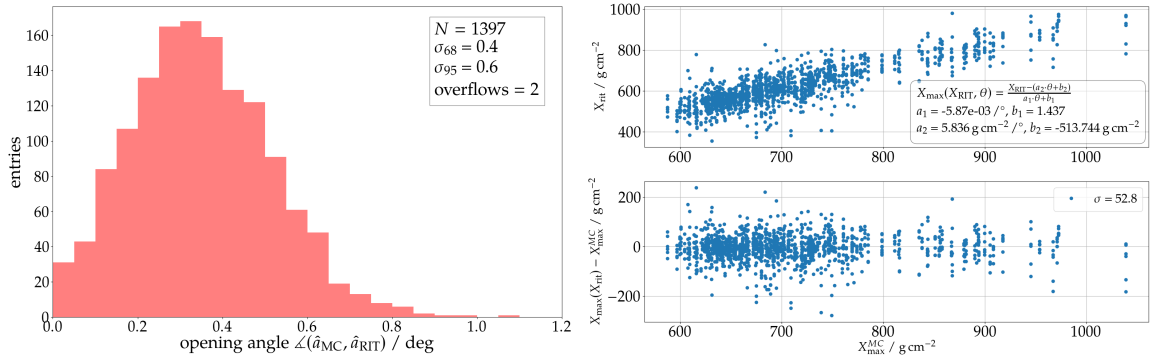


Figure 7.16.: *Left:* Distribution of the opening angle between true and reconstructed shower axis for the reconstruction of 233 air showers with AERA assuming a 2 ns Gaussian time jitter and ambient noise. The reconstruction of each shower was repeated six times to decrease statistical uncertainties. *Right:* Reconstruction of the depth of the shower maximum X_{\max} of the same showers. The reconstruction was repeated three times per shower.

promising potential for AERA measured events we also estimated the expected resolution with the true MC shower axis. The reconstruction of X_{\max} with a 2 ns Gaussian time jitter and true shower axis yields a resolution of 25.6 g cm^{-2} (cf. Tab. 7.4). When adding both a 2 ns time jitter and generated noise, the resolution decreases to 31.5 g cm^{-2} . These results are achieved without any further selection but the sampling cut. If a method is found to reconstruct the shower axis significantly better than within the here-achieved 0.4° , some potential to reconstruct X_{\max} with AERA data thus remains. All achieved X_{\max} resolutions are summarized in table 7.5.

7.2.5. Conclusion

To evaluate the potential of the interferometric technique for the reconstruction of showers measured with the Auger radio detectors we applied this technique to tailored simulations with the detector layout of the RD and AERA. Moreover, we considered the effect of the (particle) trigger-threshold of the WCD on the signal multiplicity available for the interferometric reconstruction for the RD and investigated the effect of noise for AERA.

For RD it can be concluded that with the limited timing accuracy of the currently envisioned electronics, no accurate reconstruction with the radio-interferometric technique will be possible. For the radio-interferometric technique to apply to the RD, a method would need to be found to achieve a timing accuracy of approximately 1 ns or better over the complete array. Then, for zenith angles of 77.5° or more, measurements of the muon content, the electromagnetic energy content, and X_{\max} could be performed, which would be a powerful tool to study hadronic interactions. For lower zenith angles the antenna multiplicity will be too low. Moreover, at higher zenith angles the signal multiplicity is limited by the trigger-threshold of the WCD. That said, the aperture for which an accurate X_{\max} reconstruction would be possible is very small. For the SD-infill, the technique would be applicable for lower zenith angles (cf. Sec. C.3, e.g., Fig. C.3 right).

For AERA, due to the denser station spacing and better time resolution, the technique seems more promising. In this analysis, it was found that the shower axis was reconstructed

7. Interferometric reconstruction of the depth of the shower maximum

Table 7.4.: Resolution $\sigma_{X_{\max}}$ / g cm^{-2} for different Gaussian time jitters.

σ_t / ns	RD	AERA
0	6.7 ± 0.6	10.1 ± 0.7
1	32.0 ± 2.9	15.2 ± 0.3
2	63.5 ± 6.0	25.6 ± 1.4
3	124.2 ± 18.9	–

Table 7.5.: Resolution $\sigma_{X_{\max}}$ / g cm^{-2} for different scenarios.

	RD	AERA
ideal	6.7 ± 0.6	10.1 ± 0.6
rec. axis	–	24.1 ± 2.1
$\sigma_t = 2$ ns	63.5 ± 6.0	25.6 ± 1.4
$\sigma_t = 2$ ns; noise	–	31.5 ± 2.5
$\sigma_t = 2$ ns; noise; rec. axis	–	52.8 ± 3.8

too inaccurately to obtain a good X_{\max} resolution. Also, for AERA, inaccuracies in the timing synchronization and the influence of ambient noise already cause significant degradation in X_{\max} resolution. If a very accurate reconstruction of the air-shower axis were achieved, an X_{\max} resolution of order 30 g cm^{-2} could potentially be achieved. Given that the set of simulations used in this study is representative of events recorded with AERA, the expected statistics for the reconstruction of showers with RIT are expected to be of the order of a few hundred over the full life span of AERA.

Part III.

Measuring inclined extensive air showers with the Radio Detector of the AugerPrime Observatory

8. Detecting and reconstructing inclined air showers with the AugerPrime Radio Detector

Parts of this chapter have been published in:

F. Schlüter for the Pierre Auger Collaboration

"Expected performance of the AugerPrime Radio Detector"

PoS (ICRC21) 262

The potential of the AugerPrime Radio Detector to enhance the capabilities of the Pierre Auger Observatory in determining the mass composition of UHECRs at the highest energies, e.g., above about 4×10^{19} eV, will depend on its performance in detecting and reconstructing extensive air showers. Two aspects are of particular interest for us: How many air showers at the highest energies will the RD detect, and with which accuracy are their energies reconstructed.

To study the performance of the RD, we conduct an end-to-end simulation study of the AugerPrime Radio Detector. This study entails air showers simulated with CORSIKA/CoREAS, a complete simulation of the RD instrumental response, and a full event reconstruction using Offline. For the latter, we implemented the LDF model developed in Chap. 6 in Offline. The simulation and reconstruction of RD events relies in several aspects on the SD. Most notably, the radio antennas are triggered by the WCDs; however, the SD-reconstructed shower geometry is also used in the radio reconstruction. Hence, before we simulate and reconstruct RD events, we perform a complete detector simulation and event reconstructions for the WCDs with Offline. An analysis of hybrid measurements of air showers with the SD and RD, based on the event reconstruction presented here, is performed in Chap. 9.

Although the detector simulation and event reconstruction for the SD and RD are performed with Offline, we try to keep the following description generic for readers who are not familiar with the framework. Explicit references and details to applications, *ModuleSequences*, and modules are given in the appendix D.8.

To account for the fact that the radio antennas are a part of the upgraded Surface Detector, in the following, we will use the abbreviation WCD to refer to the array of water Cherenkov detectors as a whole (a manifold of water Cherenkov detectors might still be called WCDs).

8.1. Simulations of AugerPrime events

To study the performance of the RD, we use the simulations with the ideal layout of the WCD array as presented in Sec. 4.1. In particular, we will show results obtained with the 7972 air showers generated with the hadronic interaction model QGSJetII-04 and the October atmosphere. An example for a simulated RD event is given in Fig. 4.4 (*right*). The effect of particle-thinning in simulations on the prediction of the radio emission has already been discussed in Chap. 6. For the following analyses, thinning only constitutes a problem if the artificial power introduced by thinning exceeds the (measured) noise power. As the thinning energy threshold and maximum weight (cf. Sec. 4.1), and thus the artificial power, scale with shower energy, we expect thinning to only affect signals of higher energy showers and at larger distances from the shower axis, where the coherent signal is weak. The solutions applied in Chap. 6 are not applicable here, as we do not have detailed knowledge of the lateral signal distribution, prior to the reconstruction (with non-star-shaped simulations). However, we will discuss the results for showers simulated with Sibyll-2.3d and a refined thinning (and different atmospheric conditions) in Secs. 8.3.4 and 8.4.4.

For each shower, we conduct a full detector simulation for the WCD (including the small photon multiplier tube SPMT), SSD, and UUB. The core position of the simulated shower is set to the one specified by the CoREAS simulation¹. Furthermore, we count and store the number of muons at ground² and reconstruct the air shower with the WCD.

8.1.1. Detector simulation

In the following, we describe the simulation of the RD instrumental response to radio signals from inclined air showers performed with Offline. Thereby, we will highlight and motivate changes made in the context of this work. The detector simulation “translates” the electric fields from air showers which induce an analog signal in the antennas, to the amplified and digitized signals which are sent to the data acquisition. From each antenna station, the digitized traces from the two orthogonally-aligned antennas are recorded. We conduct the detector simulation only for antenna stations with a triggered WCD (any trigger), as data will be recorded only for those antennas. Simulated radio pulses associated with RD stations with non-triggered WCDs are omitted. For RD stations with a triggered WCD for which no radio signal was simulated, traces without any signal are initialized.

Before simulating the detector response, the electric field traces in the three polarizations EW, NS, and V, are zero-padded. This serves several purposes: 1) It increases the frequency resolution of their Fourier-transform, 2) It allows simulating detector traces with the required length of 8192 ns, and 3) The signal position within the padded trace can be set freely, i.e., to a position as expected in data. In this work, we set the start of CoREAS-simulated traces to 3520 ns within the padded traces and adopt the absolute time of each CoREAS trace for the Offline trace. Already in CoREAS, the air shower signals are roughly

¹ The `SIMnnnnn.reas` file contains metadata which is read-in into Offline like the shower core position, magnetic field declination, etc. .

² As mentioned before, the muon count stored in the CORSIKA binary particle file is not reliable for MPI-generated simulations.

at the same position within the simulated traces which resembles data-taking with a trigger from the WCD beneath. However, the variations in the signal position from CoREAS (cf. Fig. 8.2) might not fully reflect variation of the signal position in data. Also, the absolute arrival times of the radio pulses are offset from those simulated for the WCD [171]. However, this mismatch does not affect this analysis and can be improved in the future when developing a hybrid reconstruction or hybrid trigger.

First, to simulate the detector response, the directional response pattern of the SALLA is used to predict the voltage traces registered at the outputs of both antennas for a given electric field, before amplification. The response pattern is described by the complex vector effective length $\vec{\mathcal{H}}(\nu, \theta, \phi)$. As indicated, the antenna response depends on the electric field's arrival direction and frequency. In the Fourier-space, $\vec{\mathcal{H}}$ describes the linear relationship ([96])

$$\mathcal{U}(\nu) = \vec{\mathcal{H}}(\nu, \theta, \phi) \cdot \vec{\mathcal{E}}(\nu) \quad (8.1)$$

where $\vec{\mathcal{E}}(\nu)$ is the incoming electric field vector and $\mathcal{U}(\nu)$ is the voltage at the antenna output. As mentioned in Sec. 3.4.3, for this work, the SALLA response pattern $\vec{\mathcal{H}}$ is simulated using the NEC-2 code³. We did not indicate a specific arrival direction for $\vec{\mathcal{E}}(\nu)$, as in general, it is not known in data and neither in simulations⁴. To describe the antennas' directional sensitivity, the signal arrival direction at each antenna is approximated with the direction of the line-of-sight between the antenna and a point(-source) at the true shower maximum. This ansatz of differential signal arrival directions, effectively describing the arrival directions with a spherical shower front, has been implemented in `Offline` in the context of this work. Previously the direction of the MC shower axis has been used for each antenna, effectively describing a plane shower front. As it turns out both approximations result in considerably different antenna sensitivity for very inclined air showers and distant antennas. The matter is discussed in more detail in appendix D.1. From simulations only, one can not judge which approximation describes reality best. We choose the spherical-shower-front approximation because it has been found to adequately describe the signal arrival times from inclined air showers [172]. With Eq. (8.1), we only predict the antenna signals $\mathcal{U}(\nu)$ for the two horizontal polarizations EW and NS and thus lose information regarding the third dimension of the electric field⁵. In Fig. 8.1 (left), the analog antenna signal after describing the directional response is shown.

Second, the amplification and attenuation of the different components in the signal-processing chain between antenna and digitizer are described. This comprises the LNA, an impedance matching, the signal transmission through a cable, and amplification in the filter amplifier. The response of the entire chain is the product of the responses of each component described by a complex, frequency-dependent function. The frequency

³ We use the patterns with the `Offline` ID: `SALLA_RD_NEC2_with-WCD-SSD_{EW,NS}_GND-6-Very_Poor`.

⁴ This information is not given by CoREAS. As the signal from each particle arrives under a different angle at an observer, being strictly correct, a response pattern would need to be taken into account during the superposition of the microscopic signals within the air shower simulation.

⁵ As part of this procedure, a non-physical rectangular band pass filter is applied. The reason is of technical nature, the directional response pattern currently in `Offline` is only described within 30 MHz to 80 MHz. As the response of the analog signal chain, described in the following paragraph, strongly attenuates signals outside this bandwidth anyway, the effect of applying the rectangular band pass filter is negligible.

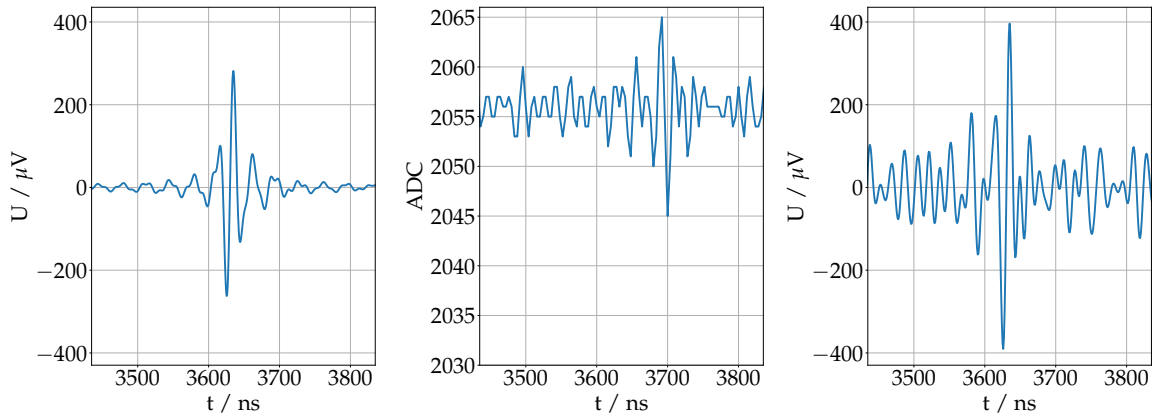


Figure 8.1.: Signal trace in one antenna (-polarization) at different stages of the detector simulation and signal reconstruction. On the left is the voltage trace at the antenna output, i.e., after applying the directional response but before applying the antenna amplification. In the middle is the signal in ADC counts after all simulations steps were performed including the injection of measured noise. This trace is representative of data received by CDAS. On the right is the reconstructed voltage trace after removing the response of the signal-processing chain but before unfolding the directional antenna response.

spectrum of the recorded voltage traces $\mathcal{U}(v)$ and the response of the signal chain are then multiplied. The attenuation or amplification of the different components in the signal-processing chain from the antenna output to the digitizer were shown in Fig. 3.6 (right) and are listed in Tab. 8.1. In addition to the response of the signal-processing chain, frequency-independent amplitude correction factors from the absolute galactic calibration of -0.4 dB and 0.23 dB are applied for the NS and EW aligned antennas respectively [102]. This corresponds to a change of about -4% and $+3\%$ respectively.

So far, we have described each antenna station as being identical and assumed perfect knowledge of their response. However, in reality, each antenna station will have a different response which is only known with a certain precision. Differences between antenna stations in their response, are, if known, uncritical and can be calibrated out. However, discrepancies in the actual response from the described one, i.e., uncertainties in the description, are problematic as they introduce antenna-to-antenna variations in the reconstructed signal and contribute to the uncertainty of the reconstructed air shower properties.

To mimic uncertainties in the response of antennas that persist after a calibration, we have implemented an amplitude smearing of the analog detector signals. Here, an uncertainty of 5% in amplitude between antennas is simulated by multiplying their signals with a Gaussian-distributed variable with a mean of $\mu = 1$ and a standard deviation of $\sigma_A = 0.05$. An uncertainty of 5% is motivated by an analysis of periodically recorded data of the ambient background radiation with AERA Butterfly antennas. The 5% variation in the amplitudes at all frequencies between 30 MHz to 80 MHz between antenna stations was found after applying a relative galactic calibration [91, Fig. 4.8]. This measurement, as well as galactic calibrations in general, is insensitive to directionally dependent variations on small angular scales in the antenna response and thus those could be larger than

Table 8.1.: Components of the RD signal-processing chain. The components are described by their average gain in decibel.

Component	ResponseId	average gain / dB
impedance matching	<i>RD_Impedance_match_GND-6-Very_Poor_{NS,EW}</i>	-6.04
low-noise amplifier (LNA)	<i>RD_LNA_gain</i>	+12.73
cable	<i>Cable_RG58_1m</i> (multiplied by a factor of 6)	-0.72
amplifier	<i>RD_Digitizer_gain_V1</i>	+17.61
total		= 23.39
calibration [102]	<i>AbsoluteGalacticCalibrationConstant_{NS,EW}_V0.1</i>	-0.4 / +0.23
total /w calibration		= 23.8 / 23.19

5%. However, for the measurement of air showers, variations in the directional antenna response on small angular scale matter as their signals arrive from particular directions. In Sec. 8.4.4.3, we estimate an additional contribution to the uncertainty from variations on small angular scales and the effect on the reconstruction of the air showers.

Third, the amplified voltage traces are resampled and truncated to match the appearance of data recorded by the RD with a sampling frequency of 250 MHz and trace length of 8192 ns (2048 samples). Then, the traces are digitized from a voltage range of ± 1 V to ADC counts ranging from 0 to $2^{12} - 1 = 4095$ with a perfect pedestal (baseline).

Fourth, traces of the ambient background recorded by 5 RD-EA antenna stations are added to the digitized traces, including those without any signal. This “noise” contains the diffuse galactic emission, electronic and thermal noise as well as anthropogenic radio-frequency interference (RFI). The data were recorded during a special data-taking campaign and described in more detail in appendix D.2. The more than 17000 traces per antenna polarization have a length of 8192 ns and cover the ADC count range from -2048 to 2047 with a non-perfect pedestal⁶. Every recorded noise trace is used several times but shifted in time (rolled) w.r.t. the signal position. Hence, every time, the signal (peak) is superposed with different noise. The noise power from the galaxy is correlated with the local sidereal time. However, due to the limited statistics, we do not constrain the time, at which the noise traces were measured, to be the same or similar for the traces added to one event.

Lastly, to simulate inaccuracies in the time synchronization between different detector stations, a 5 ns Gaussian time jitter, the same as used for the WCD, is applied. The uncertainty of 5 ns is mainly driven by the GPS clock and corresponds to the latest estimate of the timing uncertainty with the UUB [170].

The result of the detector simulation can be inspected in the two left panels of Fig. 8.1, which shows the signal trace in one antenna just after simulating the directional antenna response (*left*) and at the end of the detector simulation after digitization and superposed with measured noise (*middle*).

⁶ Hence, the simulated signals and measured noise traces can be directly summed together, and the obtained traces have a realistic pedestal.

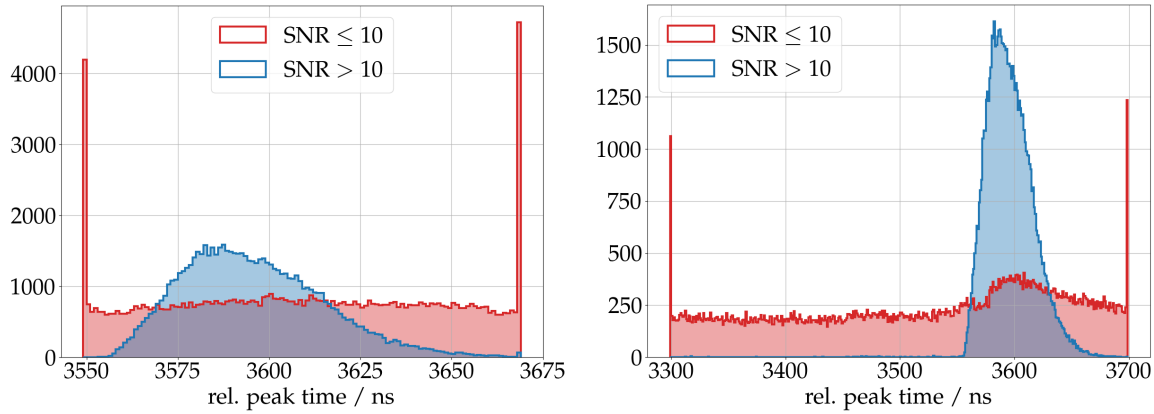


Figure 8.2.: Histograms of the pulse arrival times t_{signal} relative to the traces start time for noise pulses (with a $\text{SNR} \leq 10$, in red) and signal pulses (with a $\text{SNR} > 10$, in blue). The left histogram shows the relative pulse positions when searching for signals in a small 120 ns window (used in this work) and the right histogram for a larger 400 ns window (shown for comparison).

8.2. Signal reconstruction with the Radio Detector

Now, that the traces resemble data recorded with the RD-SALLAs and sent to data acquisition, a reconstruction procedure is performed. First, the digital signals are converted back to analog, bipolar voltage traces and up-sampled with a factor of 4 yielding a sample size of 1 ns. Then, the pedestal, which was introduced from the measured noise, is removed for each antenna.

Second, the response of the signal-processing chain is inversely applied to remove any amplification from the recorded data. Afterwards, the traces are smoothed at both ends with a *Hann*-window before unfolding the directional antenna response pattern.

Lastly, to unfold the antenna response, again, the direction of the line of sight between the antenna and a point source at an estimated shower maximum is used. To estimate the position of the shower maximum, we use the WCD-reconstructed shower axis and estimate X_{max} from a parameterized function [173] with WCD-reconstructed energy and by averaging between proton and iron. For a given arrival direction, the full 3-dimensional electric field vector can be reconstructed from signals in the horizontal plane under the assumption, that the electric field is completely transversely polarized (w.r.t. the assumed arrival direction). From the unfolding, we obtain time traces of the recorded electric field pulses in three orthogonal polarizations, e.g., EW, NS, and V. During this procedure, a rectangular band pass filter from 30 MHz to 80 MHz is applied. Now, the reconstructed electric field traces carry no dependency on the detector characteristics other than the bandwidth.

If necessary, noise cleansing algorithms like band stop filtering or sine wave suppression, which were developed for AERA, can be applied to remove narrowband transmitters and improve the signal over noise ratio, before unfolding the directional antenna response. For this analysis, no such procedures have been employed.

Next, we use the unfolded traces to derive several signal quantities for each radio station. The two most important quantities are the *signal-to-noise ratio* SNR and the *energy fluence*

f with uncertainty σ_f . To determine them, we first need to “define” a signal. To this end, we determine the maximum amplitude $|A_{\text{tot}}^{\text{hilb}}|_{\text{max}}$ from the Hilbert-envelope of the electric field traces of all three polarizations quadratically summed together within a signal-search window. For AERA and vertical air showers, usually, only the quadratic sum over the horizontal plane, i.e., the polarizations EW and NS, is used as not much signal is contained in the vertical polarization. This changes for inclined air showers and we obtained better results using all 3 polarizations. The signal-search window is set to be 3550 ns to 3670 ns within the trace and thus more narrow than what is typically used for AERA. This is because the signal position is much more constrained for the RD by the station trigger from the WCDs than it is for AERA with the T3 triggers. Once $|A_{\text{tot}}^{\text{hilb}}|_{\text{max}}$ is determined, we can calculate the SNR which is defined as

$$\text{SNR} = \left(\frac{|A_{\text{tot}}^{\text{hilb}}|_{\text{max}}}{V_{\text{RMS}}^{\text{noise}}} \right)^2. \quad (8.2)$$

$V_{\text{RMS}}^{\text{noise}}$ is the root-mean-square calculated in a noise window from the same trace, i.e., using the Hilbert-envelop of the 3 polarizations. The noise window is set between $t_3 = 6000$ ns and $t_4 = 8000$ ns relative to the trace start. In the following, we interpret pulses, i.e., recorded traces, with a $\text{SNR} > 10$ as air shower signals and pulses with $\text{SNR} \leq 10$ as noise. The position of $|A_{\text{tot}}^{\text{hilb}}|_{\text{max}}$ for signal (blue) and noise (red) pulses is shown in Fig. 8.2 for two differently sized signal-search windows. The histogram on the left shows the signal positions within the window used in this work, the histogram on the right, for comparison, uses a larger window size. The dominant peaks at the edges of the signal-search windows are due to a pile-up of pulses that have their peak outside the windows but whose tails are identified as a peak within the windows. For the larger window, most signals are found in a window of ~ 100 ns after 3520 ns as expected. The rate of “false-positives”, i.e., signals which are found apart from the dominant peak, is very low $< 1\%$. A deviation from uniformity in the red histogram, i.e., a hump, coinciding with the peak of the blue histogram indicates that pulses from air showers were not identified as such, i.e., “false-negatives”⁷. We do not observe a significant pile-up of signals at the edges of the smaller signal-search window. Hence, it can be concluded that the signal-search window used in this work is adequate.

The energy fluence f is the time integral over the absolute value of the Poynting vector and quantifies the energy deposit per unit area [88]. To derived it from the reconstructed electric field traces, a 100 ns signal-integration window $[t_1, t_2]$ centered around the position of the $|A_{\text{tot}}^{\text{hilb}}|_{\text{max}}$, i.e., the signal time t_{signal} , is defined for each station: $t_1 = t_{\text{signal}} - 50$ ns and $t_2 = t_{\text{signal}} + 50$ ns. Within this signal-integration window, the sum of the squared electric field amplitudes is computed. To mitigate the effect of noise recorded alongside the air shower signals, the same sum from the noise window is subtracted taking into account the different window sizes. Thus the energy fluence f is given by

$$f = \epsilon_0 c \Delta t \left(\sum_{t_i=t_1}^{t_2} A(t_i)^2 - \frac{t_2 - t_1}{t_4 - t_3} \sum_{t_i=t_3}^{t_4} A(t_i)^2 \right), \quad (8.3)$$

⁷ The hump is present in both histograms but barely visible in the left one.

where ϵ_0 is the vacuum permittivity, c the speed of light, and Δt the sample size. Typically, we express the energy fluence in units of electron volt per area. The energy fluence is computed from the electric field trace of each polarization independently. To obtain the energy fluence of the entire electric field, the fluences of each polarization are summed linearly. Instead of calculating the energy fluence for the EW, NS, and V-polarizations, it is useful to rotate the electric field traces and calculate the energy fluence for the $\vec{v} \times \vec{B}$, $\vec{v} \times (\vec{v} \times \vec{B})$, and \vec{v} polarizations. For the rotation of the electric field traces, the WCD-reconstructed arrival direction $\vec{v} = -\vec{a}_{\text{WCD}}$ is used, and the magnetic field orientation is taken from the simulations⁸.

Critical for the reconstruction of the shower energy is the uncertainty of the energy fluence. The uncertainty model used in Offline can be divided into 3 components. First, the influence of noise when using Eq. (8.3) is estimated directly from the measured electric field traces with the following formula:

$$\sigma_{f_{\text{Gauss}}}^2 = 4|f|\epsilon_0 c \Delta t V_{\text{RMS}}^{\text{noise}^2} + 2(t_2 - t_1) (\epsilon_0 c)^2 \Delta t V_{\text{RMS}}^{\text{noise}^4}. \quad (8.4)$$

It assumes, that recorded amplitudes $A(t) = S(t) + e(t)$ are a superposition of the air shower signal $S(t)$ and white noise $e(t)$. The latter is assumed to be Gaussian-distributed with a mean of $\mu_{\text{noise}} = 0$ and a standard deviation of $\sigma_{\text{noise}}^2 = V_{\text{RMS}}^{\text{noise}}$. The equation is derived and explained in more detail in Ref. [66, Sec. 5.5.2]. The second term describes the uncertainties in the description of the detector sensitivity $\sigma_A \cdot 2 \cdot f$. Those uncertainties, were simulated with $\sigma_A = 5\%$, consequently, we adopt this value. The factor 2 is due to the quadratic relationship between energy fluence and electric field amplitude $f \sim A^2$. The third term is inherited from previous analyses: The noise energy fluence f_{noise} is used to minimize the impact of signals close to the noise floor in the reconstruction. This last term is not well motivated as the impact of noise is already (but maybe insufficiently) described by the first term. Adding all 3 terms in quadrature yields

$$\sigma_f^2 = \sigma_{f_{\text{Gauss}}}^2 + (\sigma_A \cdot 2 \cdot f)^2 + f_{\text{noise}}^2. \quad (8.5)$$

The signal times t_{signal} are used to fit a shower front and reconstruct the shower arrival direction. The uncertainty on the signal time for a single antenna station is composed of components:

$$\sigma_{t_{\text{signal}}}^2 = \sigma_{\text{sync}}^2 + \sigma_{\text{noise}}^2 + \left(\frac{\Delta t}{12}\right)^2 \quad (8.6)$$

The first and largest component reflects the precision of the GPS clock (and other electronic components). We have simulated the time synchronization between different stations with $\sigma_{\text{sync}} = 5$ ns. Hence, the same value is used here. The second component describes the uncertainty in determining the true position of a signal peak in the presence of noise and is given by a parameterization as a function of the SNR ([66, Fig. 5.18]):

$$\sigma_{\text{noise}}(\text{SNR}) = \frac{11.7 \text{ ns}}{\text{SNR}^{0.71}}. \quad (8.7)$$

⁸ Offline provides a time- and location-dependent model for the geomagnetic field which is used to define the magnetic field simulated by CORSIKA/CoREAS.

The maximum uncertainty for a signal pulse is $\sigma_{\text{noise}}(\text{SNR} = 10) = 2.28 \text{ ns}$. The last component, the uncertainty due to the limited binning-resolution, is small with an up-sampled sample size of $\Delta t = 1 \text{ ns}$, i.e., $1 \text{ ns}/\sqrt{12} = 0.29 \text{ ns}$.

8.3. Collectable number of events

Based on the reconstructed antenna signals, we can estimate the number of air showers the RD will detect in a 10-years operation period. To this end, the detection efficiency of the RD as a function of the arrival direction and energy is estimated, and based on this, the aperture is determined.

As a condition to detect an air shower, we require at least three antenna stations with a reconstructed pulse surpassing $\text{SNR} > 10$. Three “signal” stations allow inferring basic information from an air shower solely relying on radio data. An accurate reconstruction is often not possible and requires stronger conditions such as a higher signal multiplicity which will naturally result in a lower efficiency. However, when combining data from radio antennas and WCDs, it might be possible to extract valuable information about air showers detected with only one or two antenna stations, hence improving the efficiency.

We have checked carefully, that the number of simulated pulses is sufficient to not affect the efficiency estimation. We reject 7 showers (out of 7972) that had only 1 or 2 pulses simulated, cf. Sec. 4.1.2.1.

8.3.1. Detection efficiency

The detection efficiency derived from simulations is typically calculated by the probability of detecting air showers fulfilling certain conditions. In this study, the efficiency is determined using only WCD-reconstructed air showers and not all simulated air showers. The reason for this is the following: As the radio antennas are triggered by the WCDs, their trigger efficiency is implicitly introduced into the estimated efficiency for the RD. But the simulated (trigger-) efficiency of the WCD is underestimating the true efficiency due to the muon deficit in simulations [14]. Furthermore, the performed WCD simulations with the UUB are not yet completely validated and exhibit differences w.r.t. to the UB simulation. Estimated from data, the WCD reconstruction is fully efficient for energies above $4 \text{ EeV} \sim 10^{18.6} \text{ eV}$ and zenith angles above $\theta > 62^\circ$ [14]⁹. Hence, the RD efficiency estimated in this phase-space from all WCD-reconstructed air showers, even though the WCD is not fully efficient in simulations, should translate well to data¹⁰. We adopted a binned analysis and estimate the efficiency in discrete bins in energy and zenith angle:

$$\epsilon(\theta_1, \theta_2, E_1, E_2) = \frac{n(\theta_1, \theta_2, E_1, E_2, n_{\text{ant}}(\text{SNR} > 10) \geq 3)}{n(\theta_1, \theta_2, E_1, E_2, \text{WCD-reconstructed})} \quad (8.8)$$

⁹ In our simulations we found that the WCD is very efficient $> 96\%$ up to zenith angles of 85° for showers above 10^{19} eV , the energy range relevant for mass-compositions studies. We expect the efficiency in data to be even higher.

¹⁰ This is only accurate when the WCD and RD efficiencies are not correlated by means of shower-to-shower fluctuations

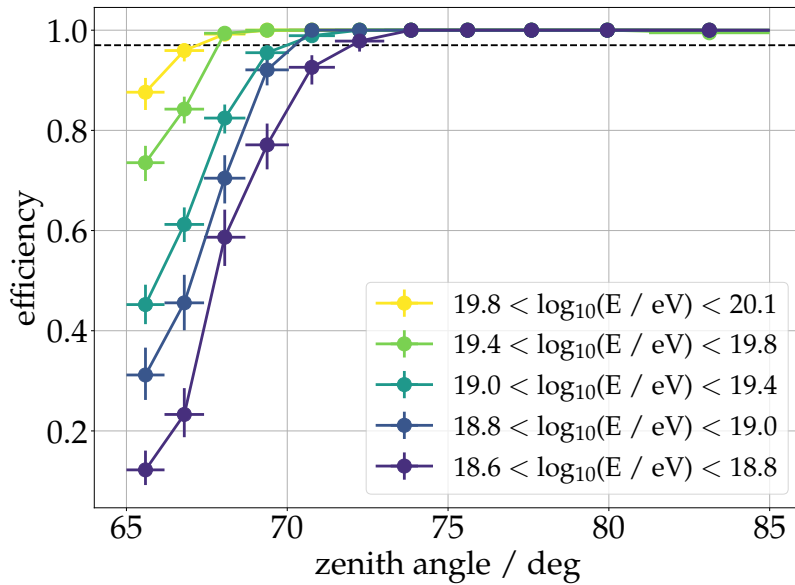


Figure 8.3.: Detection efficiency for the RD as a function of the zenith angle (in bins of $\sin^2 \theta$) for different energy bins (color-coded in non-equidistant logarithmic bins). The horizontal black dashed line indicates an efficiency of 97%.

The efficiency as a function of the true zenith angle binned in $\sin^2 \theta$ (x -axis) and energy binned in $\log_{10}(E/\text{eV})$ (color-code) is presented in Fig. 8.3. The error bars indicate the statistical uncertainty with the 1-sigma confidence intervals assuming binomial statistics. The estimated efficiency has its strongest dependency on the zenith angle. Between 65° and 70° , the RD shows a rapid increase in efficiency with the zenith angle and energy, while beyond that, the RD is fully efficient for energies above $10^{18.8}$ eV. This is different to the WCD or other particle detectors whose efficiency more strongly depends on the energy and might even decrease at higher zenith angles. However, radio emission is barely attenuated in the atmosphere, hence the efficiency of radio experiments increases with the zenith angle because the strongly forward beamed emission is projected onto larger areas and thus more antennas register a sufficiently strong signal. At the very highest energies, the RD is almost fully efficient down to 65° .

Typically, the efficiency of radio-antenna arrays also depends on the azimuth angle of the air showers or, to be more specific, on the angle between the air shower arrival direction and the geomagnetic field α . This is because the strength of the dominant geomagnetic emission increases with $\sim \sin \alpha$. However, we found only a second-order correlation with the azimuth angle at lower zenith angles (similar to the energy). This is in agreement with the fact that the geomagnetic field vector at Auger points upwards with a zenith angle of $\theta_{\vec{B}} \approx 54^\circ$, and hence is not within the zenith angle range of inclined air showers. More details on this can be found in appendix D.3.

The efficiency presented in Fig. 8.3 is calculated using only the QGSJetII-04-generated air showers. For Sibyll-2.3d-generated air showers, the efficiency is, although slightly lower, found to be comparable. In particular, full-efficiency is also reached at $\sim 70^\circ$ for showers with an energy above 10^{19} eV.

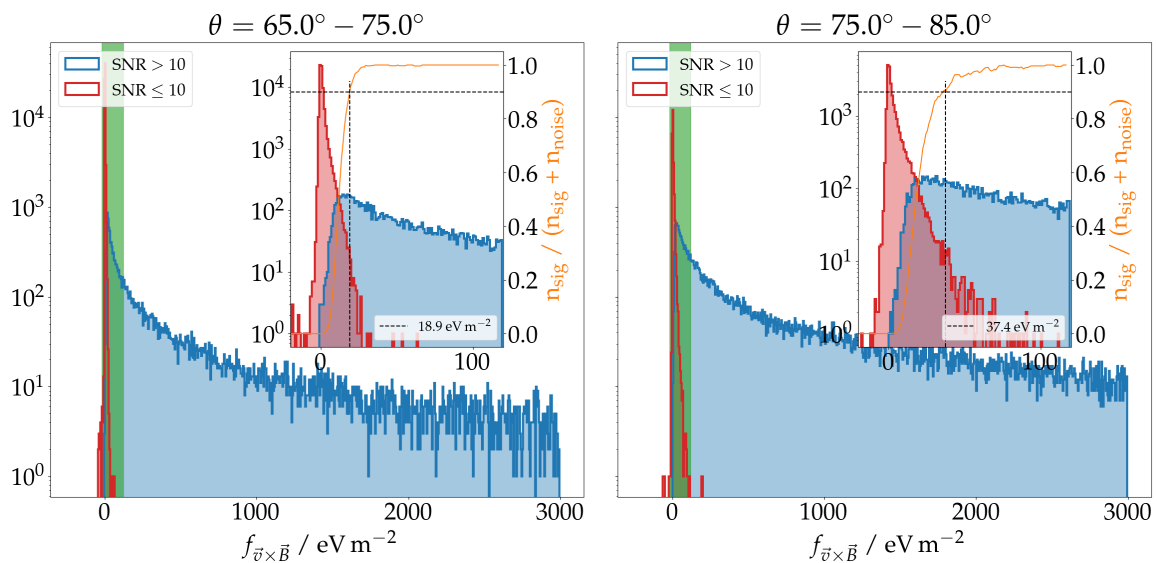


Figure 8.4.: Histograms of the energy fluence $f_{\vec{v} \times \vec{B}}$ for pulses with a SNR > 10 (blue) and a SNR ≤ 10 (red) for air showers with zenith angles below (*left*) and above (*right*) 75° , respectively. In each panel the inset shows a zoom to the region highlighted in green. The fraction of signals having a SNR > 10 (orange line, second y -axis) and the energy fluence at which this fraction is 90% (dashed black lines, legend) are shown.

We also studied the differences in the efficiency of air showers initiated by different cosmic ray primaries. Although the efficiency for iron-induced air showers was found to be slightly larger than for proton-induced air showers for most energies and zenith angles (below 70°), the differences are within the statistical uncertainties. The indication that iron-induced air showers might have a slightly higher efficiency at lower zenith angles could be explained by larger footprints and strong electromagnetic radiation from more shallow air showers (the latter is due to the known anti-correlation with the density at the shower maximum, cf. Sec. 8.4). For the lowest zenith angles, i.e., at zenith angles where the RD is not fully efficient, the efficiency will depend on the core position of the air shower. A shower that falls in the array relatively close to a station is unlikely to produce detectable signals in more than this one station. However, the exact effect of the core position needs to be investigated in the future.

Finally, we also investigated the probability of a pulse to have a SNR > 10 , as a function of the energy fluence in the $\vec{v} \times \vec{B}$ polarization. The histogram of $f_{\vec{v} \times \vec{B}}$ for all pulses with a SNR > 10 (blue) and a SNR ≤ 10 (red) for air showers with zenith angles below (*left*) and above (*right*) 75° is shown in Fig. 8.4¹¹. In each figure, the inset shows a zoom to the region highlighted in green. The yellow curve shows the fraction of pulses with a SNR > 10 for the given energy fluence as a rolling average over 5 bins (right y -axis). The dashed black lines indicate the energy fluence at which a fraction of 90% is reached. This energy fluence increases with the zenith angle from 18.9eV m^{-2} to 37.4eV m^{-2} for showers below and above 75° , respectively. The reason for this change with the zenith angle is assumed to

¹¹ We choose to split the showers at 75° , because above that, the energy fluence at which 90% of pulses have a SNR > 10 increases with the zenith angle while below that, it remains rather constant.

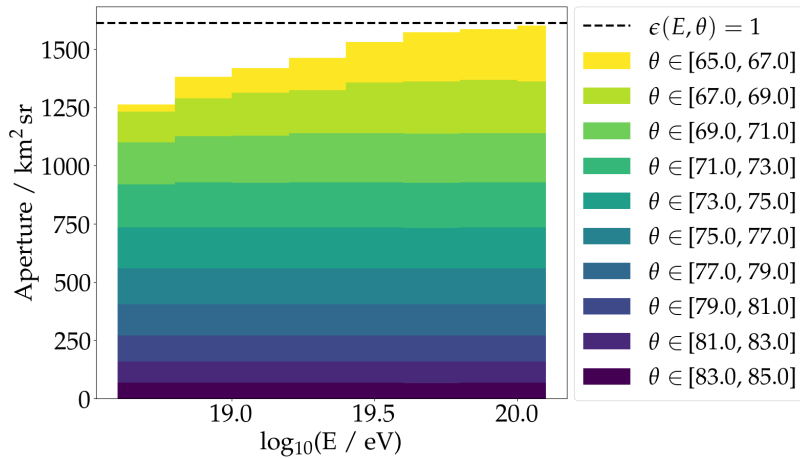


Figure 8.5.: Stacked histogram of the aperture. Each layer shows the contribution of the corresponding zenith angle bin to the overall aperture as a function of the energy. The equidistant zenith angle binning is only used in this figure for illustration purposes as it highlights the decline of the aperture at higher zenith angles.

be two folded. On the one hand, the SALLA directional sensitivity decreases towards the horizon causing a degradation of the SNR. And on the other hand, the pulse shapes from air showers flatten with the zenith angle, i.e., become wider in time. Hence, for the same SNR (maximum amplitude), the energy fluence has to increase. A consequence of this is, that the signal definition with the currently defined SNR is zenith angle-dependent. In particular, for the RD, for which the signal position is well constrained by the WCD trigger, an alternative definition for the SNR based on the contained power in a signal window might be more adequate.

In Ref. [94, cf. Sec. 8], the correlation between the total energy fluence and the SNR was estimated using data from AERA-SALLA prototype antennas. An energy fluence threshold of 5 eV m^{-2} was determined using a different definition than the one employ here. Hence, both results can not directly be compared.

8.3.2. Aperture

With the efficiency determined in the previous section, we can now calculate the aperture, i.e., effective area, of the RD. Assuming a flat array with an area of 3000 km^2 , the aperture is

$$\mathcal{A}(\theta_1, \theta_2, E_1, E_2) = 3000 \text{ km}^2 \pi [\cos^2 \theta_1 - \cos^2 \theta_2] \epsilon(\theta_1, \theta_2, E_1, E_2). \quad (8.9)$$

The term $[\cos^2 \theta_1 - \cos^2 \theta_2]$, which reduces the aperture at higher zenith angles, is owed to the fact that the size of the array projected into the shower plane, decreases with the zenith angle. That means it becomes less likely that an air shower falls with its core inside the array, which is a necessary condition for an accurate reconstruction. Considering only “contained” events, the (ideal) aperture does not increase, although the radio-emission footprint gets larger with the zenith angle. If we were to include non-contained showers, the area of the array would effectively increase depending on the shower zenith angle and the aperture would increase especially at larger zenith angles.

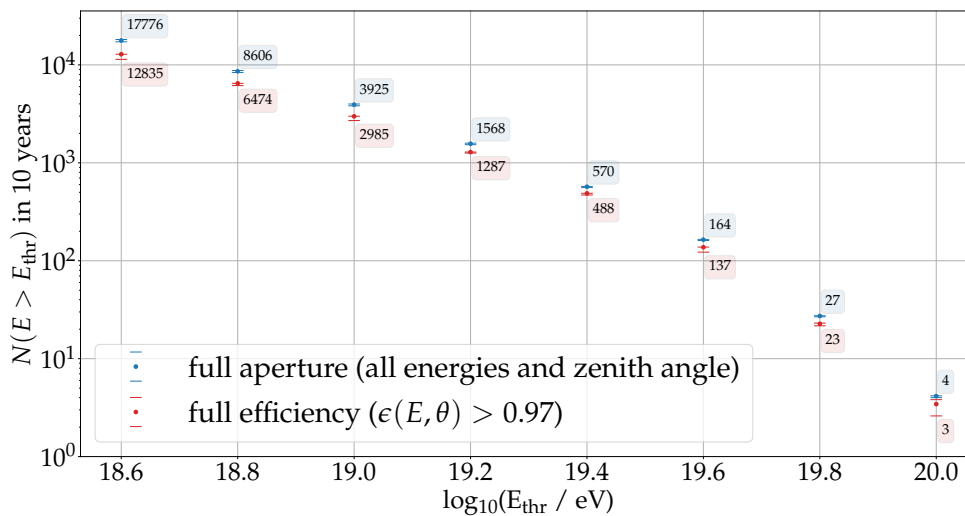


Figure 8.6.: Integrated number of events for a 10-year period as a function of the lower threshold energy E_{thr} , above which the number of events is integrated. We calculate the number of events once for the full aperture (blue), i.e., over all zenith angles, and once only for all zenith angle and energy bins in which the estimated efficiency is above 97 % (red). The error bars indicate the uncertainty due to the (binomial) statistical uncertainty estimated for the efficiency. They neither describe a systematic uncertainty nor the Poisson uncertainty an actual measurement of the energy spectrum will be affected by.

The aperture stacked for different zenith angle bins as a function of the energy is shown in Fig. 8.5. Equidistant zenith angle bins are used to highlight the effect of a decreasing aperture. At the highest energies, the ideal aperture of $1612 \text{ km}^2 \text{ sr}$ assuming a perfect efficiency $\epsilon(\theta, E) = 1$ is approached. At lower energies and lower zenith angles the aperture decreases with the efficiency illustrated by the steps in the histogram. Flat contours in the histogram indicate that the array is fully efficient for this zenith angle range. With an ideal aperture of $1612 \text{ km}^2 \text{ sr}$, the RD will increase the aperture of AugerPrime Surface Detector for mass-sensitive measurements by about 23% (w.r.t. the ideal aperture for detection with the WCDs and SSD up to a zenith angle of 60°).

For the exposure- and event statistics calculation, we use the aperture binned in $\sin^2 \theta$ to ensure similar statistical uncertainties for all bins.

8.3.3. Number of events

For a 10-year operation period, the collectable number of events can be calculated by multiplying the Auger-measured flux of ultra-high-energy cosmic rays [19] with the expected exposure $\mathcal{A} \cdot 10 \text{ y}$. The integrated number of events above a given energy E_{thr} is shown once for the full aperture including all zenith angles and energies, and once only for the phase-space with $\epsilon(\theta, E) > 0.97$ in Fig. 8.6. We find that the RD will detect 3925^{+62}_{-102} (8606^{+152}_{-236}) air showers for energies above 10^{19} eV ($10^{18.8} \text{ eV}$) in 10-years of operation with the full aperture. The uncertainties are obtained by systematically shifting the efficiency by its statistical 1-sigma uncertainty and re-evaluating the event statistics. No Poisson

uncertainty, as appropriate when measuring the flux of UHECRs, is folded in. Also, no systematic effects are considered yet but will be discussed in the following section.

8.3.4. Discussion

The presented results are based on the QGSJetII-04 generated air showers. When using Sibyll-2.3d generated showers, we obtain very compatible results for the number of events within 10-years, i.e., within the statistical uncertainty: 3908_{-100}^{+59} (8811_{-229}^{+140}) for $E \geq 10^{18.8}$ eV (10^{19} eV). Using the set of 8000 Sibyll-2.3d generated air showers with different atmospheric conditions and the refined particle thinning (cf. Sec. 4.1), we obtained, again, very compatible results within the statistical uncertainty for the expected number of events. We find changes of $\lesssim 10\% - 15\%$ in the efficiency at lower energies and zenith angles for different atmospheric conditions: For February, the efficiency is found to be higher while for June it is lower. However, the full efficiency is in any case achieved for showers with zenith angles above 70° and energies above $10^{18.8}$ eV. The effect of atmospheric conditions is further discussed in Sec. 8.4.4.2. The fact that we do not find noteworthy differences in the estimated number of events for simulations with a particle thinning of $\epsilon_{\text{th}} = 1 \times 10^{-6}$ or $\epsilon_{\text{th}} = 1 \times 10^{-7}$ respectively, suggests that thinning has no significant (systematic) effect on the results.

Two additional effects may systematically affect the estimated efficiency and thus number of events. If the detector simulation described the antennas with a higher sensitivity than they actually have, and if the utilized measured noise did not represent the typical noise conditions for the entire array during longer periods, the efficiency would decrease. In this work, the description of the antenna sensitivity includes a (preliminary) absolute galactic calibration, which is assigned an uncertainty of $\sim 10\%$ on the voltage [102]. To test whether the antenna sensitivity has a systematic effect on the estimated number of events, we described the antenna sensitivity with a -0.915 dB reduced gain independent of the frequency which corresponds to a 10% shift on the voltage amplitude and repeat the reconstruction and efficiency calculation. We found a minimal decrease in efficiency at lower zenith angles and energies of $< 5\%$. The expected integrated 10-years event statistic decreased only within the statistical uncertainty: 3867_{-104}^{+65} (8482_{-248}^{+166}). The latter would affect the efficiency only if local anthropogenic noise sources produced broadband pulses at a frequency that affects the reconstruction of air shower signals. That might be the case for some locations with nearby human activity and would decrease the exposure.

A study utilizing an analytic model of the radio emission to estimate the number of events without conducting a detector simulation or adding ambient noise obtained similar results [6].

It is worth highlighting that the number of events predicted to be detected by the RD is several magnitudes higher than what is measured with fluorescence telescopes at the highest energies. In 15 years, the Auger FD measured 289 high quality inclined air showers with a zenith angle larger 62° and energy above $10^{18.6}$ eV [14], the RD will detect over 10000 events with full efficiency and energies above $10^{18.6}$ eV in 10 years (cf. Fig. 8.6). Even with more stringent criteria for an accurate reconstruction of the shower energy with the RD, which are introduced in the following section, the number of events expected to be collected by the RD improve on this by at least one order of magnitude. For energies above

Table 8.2.: WCD selection for inclined air showers. n_{cand} is the number of triggered stations after removing “accidental” triggered stations.

WCD	N / 7972
Suc. LDF fit	7497 (94.0%)
T4 & T5	7460 (99.5%)
$n_{\text{cand}} \geq 4$	7456 (99.9%)
$\lg E_{\text{WCD}} > 18.6$	6125 (82.1%)
Total	6125 (76.8%)

Table 8.3.: Minimal RD selection for arrival direction reconstruction.

RD	N / 7972
min. 4 signal stations	5615 (70.4%)
Suc. shower front fit	5452 (97.1%)
Total	5452 (68.4%)

Table 8.4.: Parameters of Eqs. (6.16) and (6.17) in Offline.

S_{19}/GeV	γ	$\langle \rho \rangle / \text{kg m}^{-3}$	p_0	$p_1 \text{ kg/m}^3$
3.095	2.0046	0.3	0.497	-2.737

4×10^{19} eV, the combined statistics of high-quality reconstructed air showers measured with the fluorescence telescopes of several experiments is below 100 [4]. The RD will provide more statistics with an expectation of 570_{11}^{+5} detected air showers within 10 years.

8.4. Reconstruction of inclined air showers with the Radio Detector

In the following, we present the reconstruction of air shower properties with the RD based on the reconstructed radio signals. First, the arrival direction of the air showers is reconstructed by fitting a spherical shower front model to the signal arrival times of each antenna station. Second, the electromagnetic shower energy and core position are reconstructed with a fit of the LDF model described in Chap. 6 to the reconstructed energy fluences.

To reconstruct the air showers, no specific algorithm to select or reject certain station signals, such as a top-down selection or cluster-finder, was used to associate signals to an air shower, on top of the $\text{SNR} > 10$ condition. However, such modules exist for AERA and the WCD and can be adapted for RD in the future when needed.

8.4.1. Arrival direction reconstruction

To reconstruct the air shower arrival direction, the signal times t_{signal} at each antenna station are compared to a description of a spherical shower front. For a point source at the location \vec{R}^{12} , the signal time at each antenna station with the position \vec{x}_i , is described by

$$t_{\text{exp},i} = \frac{|\vec{x}_i - \vec{R}|}{c} + t_0 \quad (8.10)$$

¹² \vec{R} describes the position of the point source relative to the impact point on the ground reconstructed by the WCD.

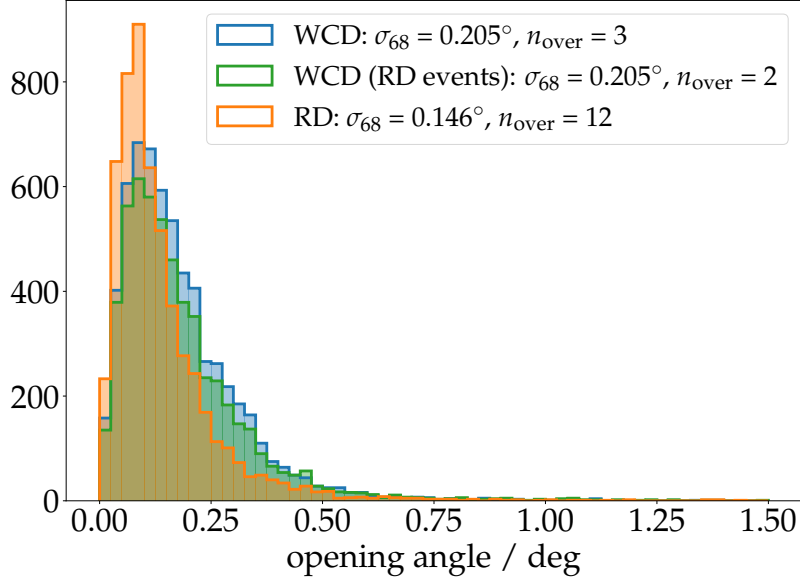


Figure 8.7.: Opening-angle distributions for the RD- and WCD-reconstructed shower axes w.r.t. the MC shower axis. For the WCD, the distribution is shown for two event sets.

with the speed of light c and a constant t_0 . The source location \vec{R} is described in spherical coordinates by three fit parameters, the zenith angle θ , the azimuth angle ϕ , and length R . The constant time offset t_0 is not fitted as it cancels out with the following loss function

$$\chi^2 = \sum_{i=1}^N \left(\frac{(t_{\text{signal},i} - \langle t_{\text{signal}} \rangle) - (t_{\text{exp},i} - \langle t_{\text{exp}} \rangle)}{\sigma_{t_{\text{signal},i}}} \right)^2. \quad (8.11)$$

We attempt a fit of the shower front for all showers with at least 4 signal antenna stations, i.e., $n_{\text{ant}}(\text{SNR} > 10) \geq 4$. For 5452 out of 5615 showers fulfilling this condition, the fit is successful, cf. Tab. 8.3. Figure 8.7 shows the opening angle between the RD-reconstructed and the MC shower axis (orange histogram). The angular resolution, defined as the 68%-quantile of this distribution, is $\sigma_{68\%}^{\text{RD}} = 0.146^\circ$.

We compare the RD reconstruction with that of the WCD for two different shower sets: one set containing 6125 showers passing a WCD selection (blue histogram), and the other set contains all RD-selected showers (green histogram). The WCD selection is detailed in Tab. 8.2. The WCD resolution is $\sigma_{68\%}^{\text{WCD}} = 0.205^\circ$ for both shower sets.

The angular resolution can also be estimated from the fit uncertainties σ_θ and σ_ϕ with

$$\text{AR} = \sqrt{\frac{-2 \ln(1 - 0.68)}{2} \left(\sigma_\theta^2 + \sin^2 \theta \sigma_\phi^2 \right)} \quad (8.12)$$

for each shower [174]. The 68%-quantile of this distribution is 0.124° for the RD and 0.2° for the WCD, which agrees well with the MC-derived resolution.

For the RD, the resolution improves with both the energy and zenith angle from $\sim 0.2^\circ$ to $\sim 0.1^\circ$. It should be noted that the RD-selection is not fully efficient for all zenith angles (and energies) and that only very few showers are reconstructed with zenith angles below 68° .

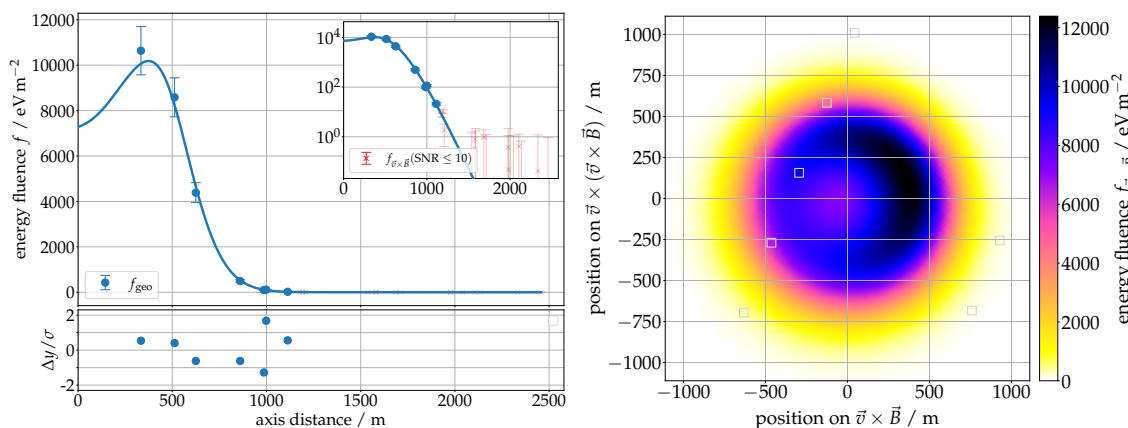


Figure 8.8.: Example LDF fit of a $10^{19.4}$ eV proton-induced air shower arriving with a zenith angle of 72.3° . The LDF is shown in two representations: On the left side, the symmetric geomagnetic emission is shown in 1 dimension. On the right side, the asymmetric $\vec{v} \times \vec{B}$ emission is shown in 2 dimensions. *Left:* The blue markers and curve show the measured and fitted geomagnetic energy fluence. The bottom panel shows the residual normalized to the uncertainty. The inset shows the same data on a logarithmic scale including the energy fluence $f_{\vec{v} \times \vec{B}}$ of “non-signal” antenna stations with a $\text{SNR} \leq 10$. *Right:* 2-dimension LDF showing the predicted asymmetric energy fluence in the $\vec{v} \times \vec{B}$ polarization. The measured energy fluences $f_{\vec{v} \times \vec{B}}$ are indicated by squared colored markers.

The angular resolution for the WCD derived from data [85] and from simulations [84] is $\sim 0.3^\circ$ to 0.5° for zenith angles $\theta \gtrsim 65^\circ$, and thus worse than what is found here. However, we have simulated UUBs which have a higher sampling rate, 120 MHz, as opposed to 40 MHz for the UBs and a better (GPS-) timing uncertainty of 5 ns [170] as opposed to 10 ns. Simulating UUBs, the resolution for the WCD decreases to $\sim 0.273^\circ$ which is more comparable to the aforementioned results. Furthermore, differences in energy and zenith angle distributions of the showers also could cause some of the remaining discrepancies.

The distribution for the RD exhibits more outliers (12 as opposed to 2 for the WCD), indicating that for a few showers the shower axis could not be reconstructed with the typical accuracy. With a constraint on the maximum zenith angle uncertainty of $\sigma_{\theta_{\text{RD}}} < 0.3^\circ$, the number of outliers reduced to 3 while the event statistic decreases by 1.5% to 5369¹³. Applying all quality cuts, as applied to evaluate the reconstructed energy (cf. following section and Tab. 8.5), removes all outliers.

The length of the vector describing the source location R is in principle an observable of interest. It could be used as an estimator for d_{max} or to determine X_{max} . However, as it turns out, the reconstructed value of R is not accurate enough to be of any use.

8.4.2. Reconstruction of the electromagnetic shower energy

Now, we fit an LDF to the reconstructed energy fluences. We employ the newly developed LDF-model presented in Chap. 6, which we implemented in `Offline`. The LDF model

¹³ Also, the constraint on the sampling of the footprint, as introduced in the following section, reduces the number of outliers to 1. However, to apply this cut a successful LDF fit which is only attempted for showers with 5 signal stations is required and hence the event statistics decrease by more than 10%.

Table 8.5.: Event and quality selection for the reconstruction of the electromagnetic shower energy.

Primaries	p	He	N	Fe	All
N_0	1996	1997	2000	1979	7972
min. 5 signal stations	1143 (57.3%)	1171 (58.6%)	1213 (60.7%)	1267 (64.0%)	4794 (60.1%)
Has spherical fit	1133 (99.1%)	1161 (99.1%)	1204 (99.3%)	1254 (99.0%)	4752 (99.1%)
$\alpha_{\text{RD}} > 20.0^\circ$	1120 (98.9%)	1148 (98.9%)	1191 (98.9%)	1242 (99.0%)	4701 (98.9%)
$\theta_{\text{RD}} \geq 68.0^\circ$	1099 (98.1%)	1119 (97.5%)	1163 (97.6%)	1204 (96.9%)	4585 (97.5%)
$\sigma_{\theta_{\text{RD}}} < 0.3^\circ$	1096 (99.7%)	1114 (99.6%)	1160 (99.7%)	1200 (99.7%)	4570 (99.7%)
Has rec. LDF	1085 (99.0%)	1106 (99.3%)	1158 (99.8%)	1199 (99.9%)	4548 (99.5%)
$n_{\text{stat}}(r < 1.5r_0) \geq 0$	1067 (98.3%)	1085 (98.1%)	1139 (98.4%)	1180 (98.4%)	4471 (98.3%)
$\sigma_{E_{\text{em}}} < 30.0\%$	1046 (98.0%)	1064 (98.1%)	1120 (98.3%)	1159 (98.2%)	4389 (98.2%)
$\chi^2 / \text{ndf} < 10.0$	1037 (99.1%)	1049 (98.6%)	1113 (99.4%)	1143 (98.6%)	4342 (98.9%)
$ \vec{x}_{\text{core}}^{\text{RD}} < 1 \text{ km}$	1036 (99.9%)	1049 (100.0%)	1113 (100.0%)	1143 (100.0%)	4341 (100.0%)
$\angle(\hat{a}_{\text{RD}}, \hat{a}_{\text{WCD}}) < 1.50^\circ$	1036 (100.0%)	1047 (99.8%)	1113 (100.0%)	1143 (100.0%)	4339 (100.0%)
Total	1036 (51.9%)	1047 (52.4%)	1113 (55.6%)	1143 (57.8%)	4339 (54.4%)

describes the highly asymmetric signal distribution of the radio emission in the $\vec{v} \times \vec{B}$ -polarization for a position of the shower core¹⁴ \vec{x}_{core} with only two parameters: the geomagnetic radiation energy E_{geo} and the distance between the shower core and the shower maximum d_{max} . In addition, the LDF-model requires the shower arrival direction and profiles for the atmospheric density and refractive index gradients as input. The arrival direction is taken from the aforementioned spherical fit to the RD data. The atmospheric profiles are provided by Offline, which has a flexible interface to import atmospheric profiles from all kinds of sources. In this work, the CORSIKA/CoREAS simulated profiles are imported unless stated otherwise.

To obtain optimal start values for the fit-parameters E_{geo} , d_{max} , and \vec{x}_{core} , we use the WCD-reconstructed shower energy E_{WCD} and core position in combination with the RD-reconstructed arrival direction. Details about this can be found in the appendix D.7. We optimize E_{geo} , d_{max} , and \vec{x}_{core} with a standard χ^2 -minimization using TMinuit¹⁵ [175]. The prediction of $f_{\vec{v} \times \vec{B}}$ and the loss function are given by Eqs. (6.18) and (6.19). Only antenna stations with a SNR > 10 are used in the minimization. Saturated antennas are also not considered, however, their occurrence is very rare and limited to showers which are unlikely to illuminate more than 3 stations.

All parameters are assigned weak limits. The fitting procedure features several steps, in each step we perform a minimization with a different set of free parameters while the other parameters are fixed. First, only E_{geo} is fitted while the core position and d_{max} are fixed. Then, the core position is optimized together with E_{geo} and d_{max} is kept fixed. In a third step, E_{geo} and d_{max} are optimized together while the core is being fixed. Finally, all parameters are optimized together. Here, we focus on the reconstruction of air showers that were detected with signals in at least 5 antenna stations to allow a fit of all parameters

¹⁴ As the position of the shower core is also determined with the LDF fit, it introduces two additional free parameters.

¹⁵ With the easy-to-use Offline-wrapper *Minou*.

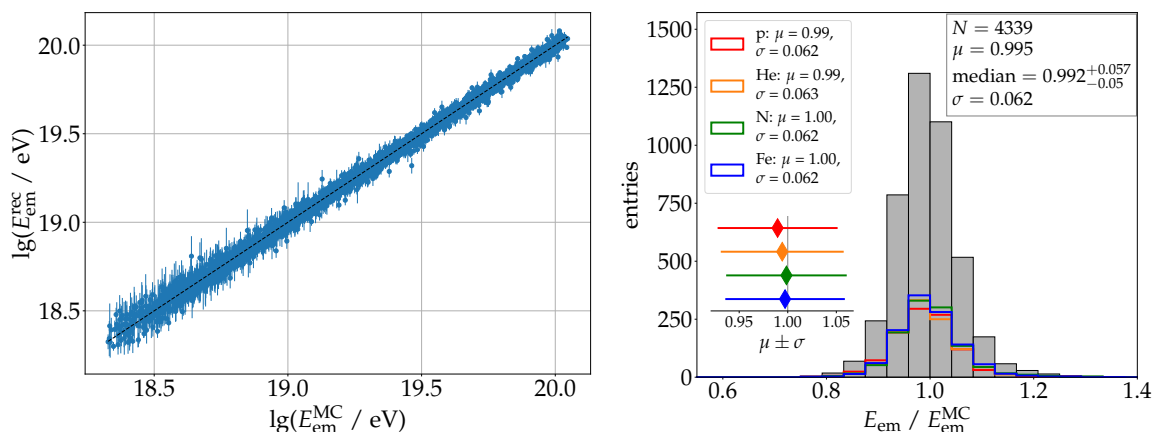


Figure 8.9.: *Left:* The reconstructed electromagnetic energy E_{em} as a function of the true electromagnetic energy $E_{\text{em}}^{\text{MC}}$ in double logarithmic scale, for all selected showers (cf. Tab. 8.5). The dashed black line indicates the diagonal. *Right:* Histogram of $E_{\text{em}}/E_{\text{em}}^{\text{MC}}$ for all selected showers and for showers initiated by four different primaries (colored histogram). The legend on the right-hand side, gives the statistics for the full distribution. On the left side, the means and standard deviations for the different primaries are shown. Those values are also illustrated in the inset below the legend.

with a *number of degrees of freedom* $\text{ndf} \geq 1$. The fit efficiency for those showers, not applying any quality criteria, is $\sim 98\%$. An example of the fit is shown in Fig. 8.8 in two different representations. The symmetrized, geomagnetic emission allows the display of the LDF in one dimension, i.e., as a function of the axis distance (*left*). The integral over the fitted LDF yields E_{geo} . However, the minimization is performed with $f_{\vec{v} \times \vec{B}}$, which cannot be represented with one line alone, hence a more appropriate representation is in two dimensions (*right*). The predicted energy fluence $f_{\vec{v} \times \vec{B}}$ is color-coded. The measured signals are indicated by colored squares in the same color scale. Hence, if the LDF describes the signals accurately, their colors match the background.

The fitted geomagnetic radiation energy E_{geo} is used to estimate the electromagnetic shower energy E_{em} . The procedure has already been described in Sec. 6.3: First, we compensate for the scaling of the geomagnetic radiation energy with the geomagnetic angle α and air density at the shower maximum ρ_{max} and obtain the corrected geomagnetic radiation energy S_{geo} , see Eq. (6.16). Then, we calculate E_{em} from S_{geo} using Eq. (6.17). The necessary parameters S_{19} , γ , p_0 , and p_1 as implemented in Offline are given in Tab. 8.4. It should be noted that the parameters in Tab. 8.4 vary w.r.t. the ones given in Chap. 6, which represent a minute update to the values given here.

In the following, we evaluate the reconstruction of E_{em} with the set of 7972 simulated air showers. However, to achieve an accurate reconstruction we have to apply a shower selection and quality conditions. We select showers with at least 5 signal stations, an RD-reconstructed geomagnetic angle $\alpha_{\text{RD}} > 20^\circ$, and a zenith angle $\theta_{\text{RD}} > 68^\circ$ with an uncertainty of $\sigma_{\theta_{\text{RD}}} < 0.3^\circ$. This implies that the shower front could be successfully fitted. The selection yields 4570 air showers out of 7972, cf. Tab. 8.5. Of those, an LDF is fitted successfully for 4548 showers. Additionally, we apply quality criteria which are detailed in Tab. 8.5. All quality criteria have a high efficiency of $> 98\%$. The selection comprises a

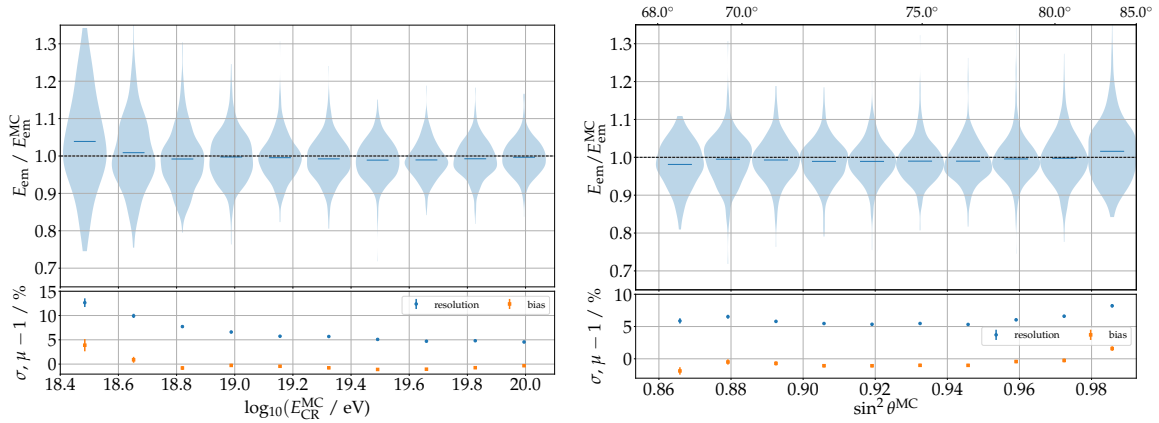


Figure 8.10.: Binned distributions (top) and profiles (bottom) of $E_{\text{em}}/E_{\text{em}}^{\text{MC}}$ as a function of the total shower energy (\equiv cosmic-ray energy) $E_{\text{CR}}^{\text{MC}}$ (left) and $\sin^2 \theta^{\text{MC}}$. The profiles are expressed by the resolution, i.e., the standard deviation of the above distributions σ , and the bias, i.e., the mean of the above distributions $\mu - 1$, in percentage. A significant improvement of the reconstruction resolution with the energy is found, while it is rather constant as a function of the zenith angle with only a minor degradation at the highest zenith angle.

minimal condition for adequate sampling of the lateral signal distribution which is crucial to reject wrongly reconstructed air showers: at least one signal station is required to be within 1.5 times the fitted Cherenkov radius r_0 . The fit must yield a $\chi^2/\text{ndf} < 10$, which rejects around 1% of the reconstructed events. An inspection of the distribution of the fitted χ^2 reveals that it does not follow the expectation of an χ^2 -distribution, which is also reflected by the high cut value of 10. The matter is discussed in more detail in the appendix D.4.

The entire selection passed 4339 out of the 7972 showers, which equates to an efficiency of 54.4%. However, if we consider only the selected 4570 showers, the reconstruction efficiency is almost 95%. It is also noteworthy, that the selection summarized in Tab. 8.5 is not equally efficient for the entire zenith angle and energy range or between the different primaries. The heavier elements, nitrogen and iron, exhibit a higher efficiency than the lighter elements proton and helium with a difference between protons and iron nuclei of $\sim 6\%$. The interpretation of this difference is the same as in Sec. 8.3.1. This poses a potential problem for mass-composition studies as any larger differences in the efficiency (of several %) will introduce biases in the determination of, e.g., the mass composition of UHECRs. Applying a cut on the reconstructed electromagnetic energy of 10^{19} eV will bring down this difference to $\sim 2.5\%$. Increasing the zenith angle cut will decrease the discrepancy further. More details on this are given in Chap. 9.

With the selected showers, the reconstruction of the electromagnetic energy is evaluated. The correlation between the reconstructed and true E_{em} is shown in Fig. 8.9 (left). An overall good correlation is demonstrated as indicated by the small scatter around the diagonal (black dashed line). A histogram of the ratio $E_{\text{em}}/E_{\text{em}}^{\text{MC}}$ is shown in the same figure on the right. The reconstruction resolution, directly determined from this distribution, is $\sigma_{E_{\text{em}}} \equiv \sigma(E_{\text{em}}/E_{\text{em}}^{\text{MC}}) = 6.2\%$, the bias $\equiv \mu(E_{\text{em}}/E_{\text{em}}^{\text{MC}}) - 1$ is consistent with 0. The reconstruction for showers induced by each of the 4 different primaries are shown in

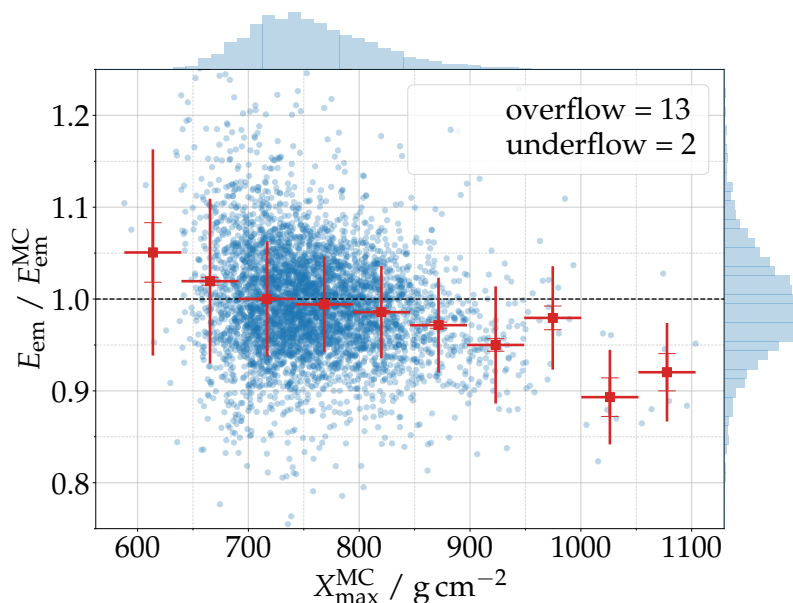


Figure 8.11.: Reconstruction accuracy expressed by $E_{\text{em}}/E_{\text{em}}^{\text{MC}}$ as a function of the MC X_{max} . The red markers show the binned mean and standard deviation (the error bar caps represent the uncertainties on the mean). An energy reconstruction bias as a function of X_{max} is apparent. The distributions of $E_{\text{em}}/E_{\text{em}}^{\text{MC}}$ and X_{max} are indicated on the top, respectively right axis. The bias is moderate $\lesssim 5\%$ for most showers, i.e., $X_{\text{max}} < 900 \text{ g cm}^{-2}$.

colors. Their resolution σ and mean μ are given by the right-hand-side legend and are illustrated in the inset beneath it. No noteworthy primary-dependent reconstruction bias is found, which is advantageous for mass-composition studies.

The ratio $E_{\text{em}}/E_{\text{em}}^{\text{MC}}$ binned as a function of the shower energy $E_{\text{CR}}^{\text{MC}}$ (left) and as a function of the zenith angle in bins of $\sin^2 \theta^{\text{MC}}$ (right) are shown in Fig. 8.10. The top panels show the full distributions of the ratio in each bin while the bottom panels show the bias and resolution determined for each bin. In the left figure, it is visible that both, bias and resolution improve with energy. This is expected and can be attributed to the effect of ambient and electronic noise, which decreases with energy. The profile in the right figure indicates no significant correlation with the zenith angle and only a minor degradation of the resolution at the highest zenith angles, which can be mostly attributed to low energy showers. We found, that the resolution improves with the signal multiplicity from, on average, $\approx 7\% - 8\%$ with 5 signal stations, to 5% with around 20 signal stations or more.

The ratio $E_{\text{em}}/E_{\text{em}}^{\text{MC}}$ for all individual showers as a function of the true X_{max} is shown in Fig. 8.11. The red markers refer to the binned mean and standard deviation (error bars). The statistical uncertainty of the means are indicated by the error caps. A reconstruction bias in E_{em} that depends on X_{max} is visible. At first glance, this seems to be in tension with the above statement that no primary-dependent bias in the reconstruction of E_{em} is observed. However, it should be noted that the majority of showers have an $X_{\text{max}} \in [650 \text{ g cm}^{-2}, 900 \text{ g cm}^{-2}]$ for which the reconstruction bias is small $\lesssim \pm 3\%$. The distribution of X_{max} and also $E_{\text{em}}/E_{\text{em}}^{\text{MC}}$ are indicated by histograms at the top and on the right of the plot respectively.

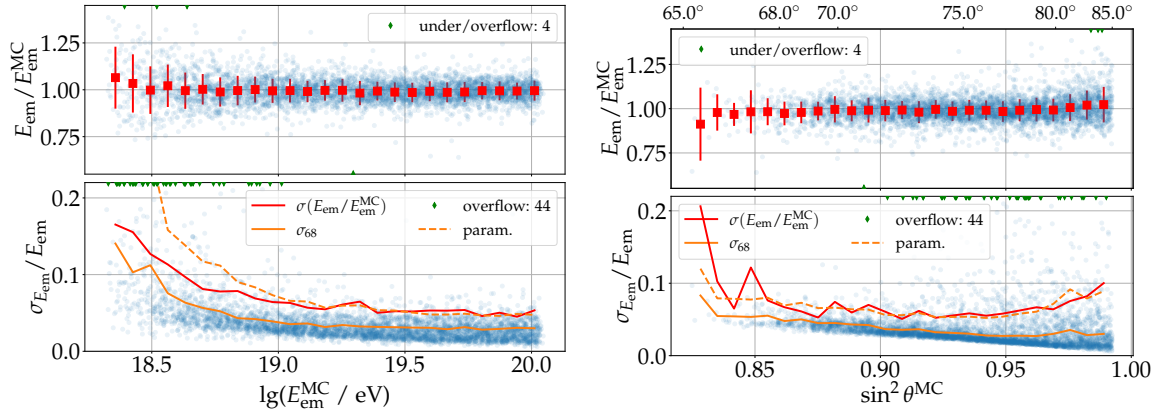


Figure 8.12.: The top panels show $E_{\text{em}}/E_{\text{em}}^{\text{MC}}$ as a function of $E_{\text{em}}^{\text{MC}}$ (left) and $\sin^2 \theta^{\text{MC}}$ (right). The red markers show the mean and standard deviation. The standard deviation yields the MC-derived energy resolution. The bottom panels show the fit-estimated resolution $\sigma_{E_{\text{em}}}/E_{\text{em}}$. The orange lines indicate the 68%-quantiles of the underlying distribution. The MC-derived resolution is illustrated by the red line (shows the one-sided size of the error bars in the top panels). The disagreement between red and orange lines is a clear indication that the uncertainties are underestimated by the fit. The dashed orange lines show the 68%-quantile of the corrected distributions (not shown) according to Eq. (8.13). The green markers indicate the position of over- and/or underflow data.

8.4.2.1. Correction of the energy resolution

The resolution for the reconstruction of E_{em} can not only be estimated by comparisons with the MC truth but also derived from the fit-estimated uncertainties in E_{geo} and d_{max} . The necessary equations (D.1) - (D.4) to determine the uncertainty $\sigma_{E_{\text{em}}}$ from the fit are explained in the appendix D.5. The fit-derived resolution $\sigma_{E_{\text{em}}}/E_{\text{em}}$ is compared with the MC-derived resolution, i.e., $\sigma(E_{\text{em}}/E_{\text{em}}^{\text{MC}})$, in Fig. 8.12 as a function of $E_{\text{em}}^{\text{MC}}$ (left) and $\sin^2 \theta^{\text{MC}}$ (right). In the top panels, showing $E_{\text{em}}/E_{\text{em}}^{\text{MC}}$, the MC-derived resolution is indicated by the error bars. The bottom panels show the distributions of $\sigma_{E_{\text{em}}}/E_{\text{em}}$. Their 68%-quantile as a function of the energy and zenith angle is given by the solid orange lines, respectively. For comparison, the MC-derived resolution $\sigma(E_{\text{em}}/E_{\text{em}}^{\text{MC}})$ is indicated in the same panels by the red lines. A disagreement between the fit-estimated and MC-derived resolution is visible indicating that the fit-derived uncertainties are underestimated. The mismatch is rather independent of the energy but changes with the zenith angle. Another indication of the underestimation of the fit-derived uncertainties is found by analyzing the χ^2 distribution in appendix D.4. The origin of the underestimation has been investigated in some detail. For example, we verified, that the fit-estimated uncertainties $\sigma_{E_{\text{geo}}}$ and $\sigma_{d_{\text{max}}}$ are correctly describing the contour defined by $\chi^2 = \chi_{\text{min}}^2 + 1$ when varying the core position. Another possible explanation is that the signal uncertainty model of the energy fluence according to Eqs. (8.4) and (8.5), is incorrectly describing the uncertainties in the reconstructed signals and thus cause the underestimation in the uncertainty of the reconstructed shower energy. Similar to what is reported here, an underestimation of the uncertainty of the shower energy reconstructed with AERA, utilizing a different LDF model but the same signal uncertainty model, has been reported [122].

An accurate estimation of the uncertainty of the reconstructed energy is important for two central reasons: First, it allows an efficient selection of high-quality events. Second, it enables the precise estimation of the physical fluctuations of the number of muons from inclined air showers, cf. Chap. 9. To obtain a better estimation of the resolution, we introduce a correction factor $c_{\sigma_{E_{\text{em}}}}(\theta)$ as a function of the zenith angle to correct the fit-estimated uncertainty

$$c_{\sigma_{E_{\text{em}}}}(\theta) = 1.986 \times 10^3 (\sin(\theta)^2 - \sin(65^\circ)^2)^4 + 1.446. \quad (8.13)$$

Details on this parameterization are given in appendix D.6. The 68%-quantile of the corrected resolution, i.e., of $c_{\sigma_{E_{\text{em}}}}(\theta) \cdot \sigma_{E_{\text{em}}}/E_{\text{em}}$, is also shown in Fig. 8.12 with the dashed orange lines. It is shown, that the corrected resolution slightly overestimates the MC-derived resolution for lower energies. However, for the energy region most relevant for mass-composition studies $E \gtrsim 10^{19}$ eV, the resolution is well described by the corrected estimation. The corrected fit-estimated uncertainty $\sigma_{E_{\text{em}}}$ has already been used in the previously introduced shower selection, i.e., Tab. 8.5.

8.4.2.2. Reconstruction of the shower core position

The shower core position is fitted in a plane perpendicular to the RD-reconstructed air shower direction which is defined by $\vec{v} \times \vec{B}$ and $\vec{v} \times (\vec{v} \times \vec{B})$ with the origin set to the WCD-reconstructed core (start value). We evaluate the RD- and WCD-reconstructed core position w.r.t. the MC core in a plane perpendicular to the MC arrival direction in a coordinate system where the y -axis is in parallel with the air shower arrival direction (the positive y -axis points towards the incoming direction of the air shower) and the x -axis is perpendicular to that. Figure 8.13 shows the two-dimensional histogram of the core positions reconstruct with the RD (*left*) and WCD (*right*). The legend in both histograms shows the mean and standard deviation of the reconstructed core positions along the x - and y -axis: $\langle x \rangle$ and $\langle y \rangle$, respectively. An inspection of the histograms reveals that the resolution of the RD is better than the WCD. However, the RD-reconstructed core positions exhibit a significant bias towards the arrival direction of the air showers which is not seen for the WCD. This bias is even more pronounced for more inclined air showers with zenith angles between 81.9° and 85° .

An illustration of the reconstruction bias and resolution binned in $\sin^2 \theta$ for both detectors is shown in Fig. 8.14. The bias is expressed with $\sqrt{\langle x \rangle^2 + \langle y \rangle^2}$ and shown (solid lines, “o”-markers) for the RD (orange), WCD (blue), and WCD using only the RD-selected events (green). The WCD reconstruction bias remains constant and comparable with zero. However, the RD exhibits a significant bias which is correlated with the zenith angle. Such a bias is expected due to the refractive displacement of the radio-emission footprint from the MC axis, as explained in Chap. 5. The predicted displacement according to the model introduced in Chap. 5 for an air shower with its shower maximum at $X_{\text{max}} = 750 \text{ g cm}^{-2}$ is shown with the thick red line. The markers represent the predicted displacement for the central value of each zenith angle bin while the error bars represent the displacement at the edges of each bin. The agreement between the reconstruction bias and the expected displacement is good for the higher zenith angles $\gtrsim 75^\circ$ while for lower zenith angles, the predicted displacement can not describe the reconstruction bias. However, in

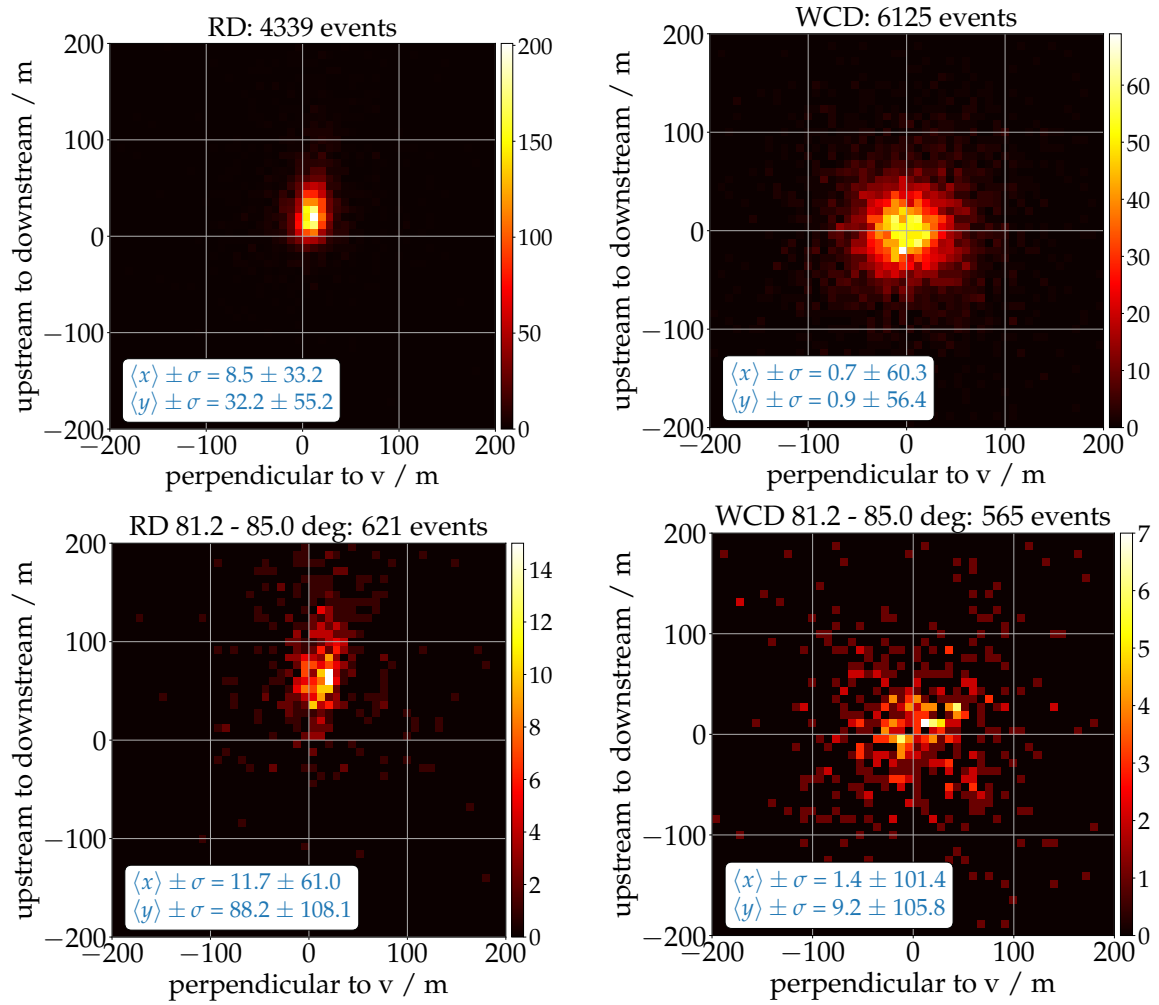


Figure 8.13.: Reconstructed shower core positions in shower-plane coordinates and with the corresponding MC core in the origin for the RD (*left*) and WCD (*right*), and for all showers (*top*) and the most inclined air showers (*bottom*). The positive y -axis points into the incoming direction of the air showers, while the x -axis is perpendicular to this.

Chap. 5 a deviation between the displacement derived from the CoREAS simulations and the displacement predicted from the refraction model was already found at lower zenith angles. In that chapter, the displacement was derived from CoREAS simulation without assuming a particular shape of the lateral signal distribution, i.e., without using any LDF. Hence, it is likely that the deviation from the model prediction found in Chap. 5 and here has an actual (unknown) physical causation rather than being a reconstruction bias. The resolution, for the WCD, is expressed in terms of the 68%-quantile of the distance between MC and WCD core: $\sigma_{68}(\sqrt{x^2 + y^2})$ (dashed lines, “x”-markers). This estimation overestimates the resolution in case of a biased core reconstruction. Hence, the RD resolution is estimated by subtracting the mean x - and y -coordinate before calculating the distance: $\sigma_{68}(\sqrt{(x - \langle x \rangle)^2 + (y - \langle y \rangle)^2})$ (dotted line, “+”-markers). The WCD-reconstructed core resolution reported in Ref. [84], is 80 m to 160 m for zenith angle between 60° and 80°

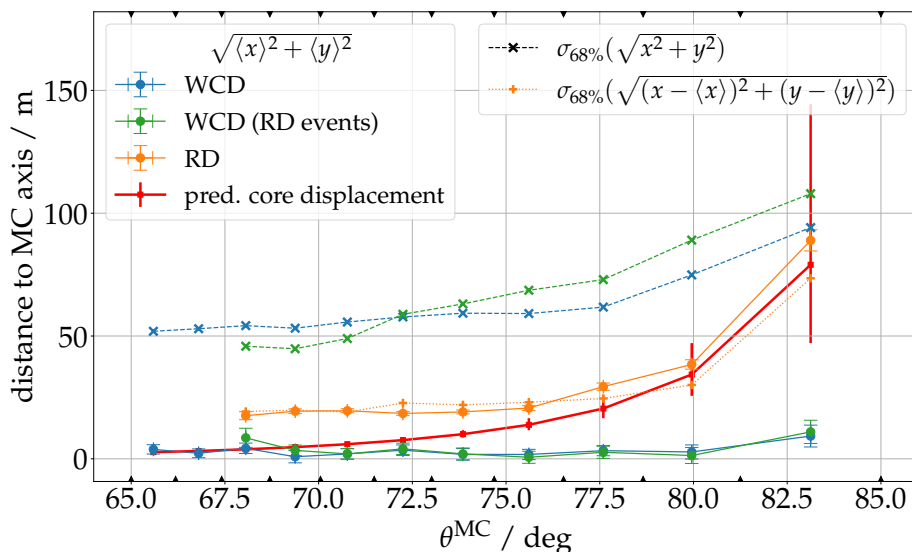


Figure 8.14.: Reconstruction bias (solid lines, “o”-markers) and resolution (dashed and dotted lines, “x”- and “+”-markers, see details in text) of the shower core position in bins of $\sin^2 \theta^{\text{MC}}$ for the RD (orange), WCD (blue, WCD selection), and WCD (green, RD selection). The bin edges are indicated by triangles on the bottom and top x-axis. The RD bias is compared to a prediction for the refractive displacement introduced in Chap. 5 (red line and markers).

and thus the values reported here are significantly better. This discrepancy can not be attributed to the use of the UUB in simulation and reconstruction and needs further investigation.

8.4.2.3. Reconstruction of the geometrical distance to the shower maximum

The distance to the shower maximum d_{max} , which is reconstructed together with E_{geo} and used to determine E_{em} (by translating into ρ_{max}), is in principle of high interest on its own. From it, one can determine X_{max} which can be used to constrain the mass of the primary cosmic ray. However, as already pointed out in Sec. 6.4, the resolution in d_{max} has to be better than 1% to be of any use, i.e., to enable a reconstruction of X_{max} with a resolution of $\sigma_{X_{\text{max}}} < 20 \text{ g cm}^{-2}$ to 50 g cm^{-2} depending on the zenith angle. This is not achieved with this reconstruction, which yields a resolution of 7% and an on average +3% reconstruction bias. The fact that the resolution in X_{max} decreases significantly with the zenith angle for a constant resolution in d_{max} reinforced the assumption that the lateral amplitude profiles of the radio emission from air showers lose sensitivity to X_{max} with increasing distance to the source, i.e., X_{max} , with increasing zenith angle.

8.4.3. Reconstruction of the cosmic-ray energy

So far we have reconstructed the electromagnetic shower energy E_{em} . The fact that it can be reconstructed from radio data with no significant primary-dependent bias makes it a very suitable energy estimator for use in the discrimination of air showers induced by cosmic rays of different primaries. Mass-sensitive observables, such as the number of muons,

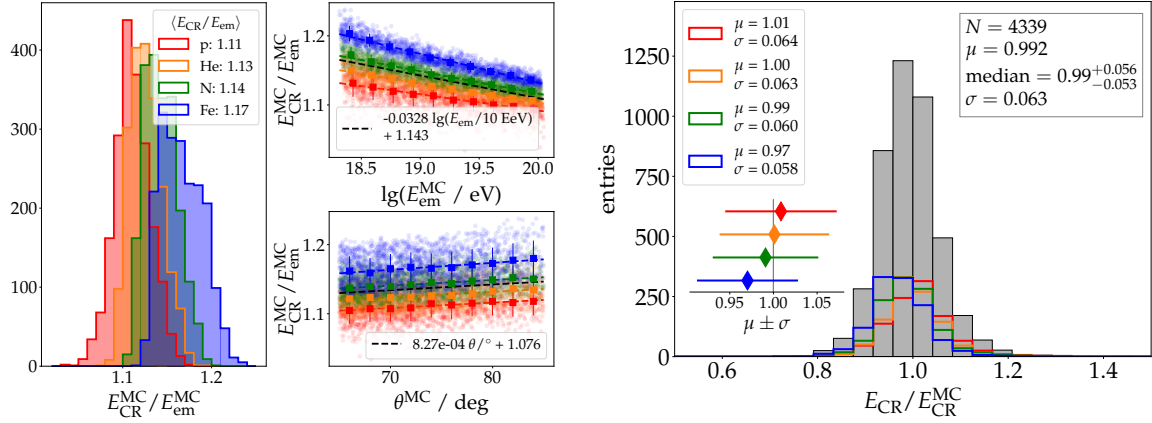


Figure 8.15.: *Left:* The relative difference between the true electromagnetic and cosmic-ray energy for the QGSJetII-generated showers. The different colors donate the different primary particles. *Middle:* The ratio E_{CR}/E_{em} as a function of the electromagnetic shower energy (*top*) and zenith angle (*bottom*). The black line indicates a primary-independent linear model. *Right:* Reconstructed over true cosmic-ray energy.

often have a large ambiguity between the cosmic-ray mass and energy; therefore, a precise and bias-free energy reconstruction is pivotal. However, of astrophysical importance is the primary cosmic-ray energy E_{CR} (\equiv total shower energy) as it governs the acceleration, interaction, and the magnetic deflection of cosmic rays. A calibration function to obtain E_{CR} from E_{em} is needed and can be derived from simulations. Figure 8.15 shows the ratio E_{CR}^{MC}/E_{em}^{MC} as a histogram (*left*), a function of the electromagnetic energy (*top-middle*), and a function of the zenith angle (*bottom-middle*) for the 4 different primaries (color-coded). As expected, a strong dependency on the primary particle mass is found. The difference between E_{em} and E_{CR} is largest for iron-induced showers as in those showers more muons are produced, which do not contribute to electromagnetic energy, than for other primaries. Also, a considerable dependency on the energy and a minor dependency with the zenith angle is found. The correlation with the energy is expected and hence described to calibrate E_{em} and E_{CR} . To determine a calibration depending on the E_{em} , a linear fit is made to the data shown in the top-middle panel. The black line indicates a primary-independent description of the calibration which is needed as typically in measurements the primary particle type is unknown. This yields the following calibration function

$$E_{CR} = E_{em} \cdot \left[1.1426 - 0.0328 \log_{10}(E_{em}/10 \text{ EeV}) \right] \quad (8.14)$$

Relying on a calibration that does not take into account the primary particle type yields a mass-dependent bias in the reconstructed cosmic-ray energy. This can be seen in Fig. 8.15 (*right*) which shows the ratio of the reconstructed cosmic-ray energy over true cosmic-ray energy. The resolution is slightly affected w.r.t. the reconstruction of E_{em} . We found no significant difference in this calibration between QGSJetII- and Sibyll-generated showers.

8.4.4. Investigation of systematic effects in the energy reconstruction

We also studied systematic effects originating from the employed detector and air shower simulations. This comprises an evaluation of the different high-energy hadronic interaction models, atmospheric conditions used in the CORSIKA/CoREAS simulations as well as assumptions made in the simulation of the instrumental response that are discussed in the following sections.

8.4.4.1. Different high-energy hadronic interaction models

In reconstructing air showers generated with Sibyll-2.3d, we did not observe any significant changes to what has been found for QGSJetII-04 showers. In particular, the energy resolution is unchanged. Nonetheless, two minor aspects are noteworthy: First, a constant -2% reconstruction bias in the electromagnetic energy was found. A similar bias has already been reported in Chap. 6. Second, the efficiency of the selection detailed in Tab. 8.5 decreased by 2%. The decrease in efficiency is mainly due to a $\approx 3\%$ lower efficiency of the signal multiplicity cut $n_{\text{ant}}(\text{SNR} > 10) \geq 5$. A slightly lower efficiency at lower energies and zenith angles was already discussed in Sec. 8.3.4. This underlines, that the simulation of the radio emission is relatively unaffected by the hadronic interactions.

8.4.4.2. Varying atmospheric conditions

in studying the effect of the atmospheric conditions on the reconstruction of air showers, two aspects need to be considered: “What consequences does varying the atmospheric conditions has for the application of the utilized LDF model, which has been parameterized with the October atmosphere?”, and, “What effect does an inaccurate description of the atmospheric conditions has during the reconstruction?”.

To address the first question, we reconstructed the 8000 (Sibyll-2.3d) showers generated with the atmospheric conditions of the observatory in February and June. For their reconstruction with Offline, we used the same atmosphere with which they were simulated. For the February atmosphere we found a $+2\%$ reconstruction bias w.r.t. the October atmosphere. Showers simulated and reconstructed with the June atmosphere exhibit a $\sim -2\%$ bias. We also found that the selection efficiency varied within $\pm 1\%$ to 2% following the direction of the energy bias, again mostly due to a changed efficiency in the signal multiplicity cut.

To address the second question, we reconstructed the 7972 QGSJetII showers, simulated with the October atmosphere, for varying atmospheric conditions described by monthly average profiles provided by Offline [113]. This implies minimal knowledge of atmospheric conditions. We found only a minor degradation of the resolution by 1%. However, using the Offline profiles we found a significant bias in the reconstructed energy of -6% to -7% which does not vary much for the different months (atmospheric profiles) and only slightly with the zenith angle. In particular also for the October atmosphere described with Offline, the bias remains. This indicates a disparity between the profiles used in Offline and CORSIKA/CoREAS. We found that the wavelength-independent description of the refractive index as a function of the height above sea level varies between Offline and CORSIKA/CoREAS. This discrepancy has to be understood and resolved in the future.

8.4.4.3. Discrepancies in the simulation of the detector sensitivity with respect to a real detector

Potential discrepancies in the detector simulation w.r.t. the real detector influence the reconstruction of air showers in different aspects. In Sec. 8.3.4 we already discussed a change in the absolute antenna sensitivity for all antenna stations. We did not find any difference in the reconstruction accuracy of air showers simulated with the lower instrumental antenna response when correctly describing the antennas with the lower sensitivity in reconstruction. Only the selection efficiency of air showers (cf. Tab. 8.5) decreased by 1%. Of course, this does not reflect the systematic uncertainty (i.e., reconstruction bias) when describing the detector sensitivity incorrectly during reconstruction. A 10% shift in amplitude, i.e., a 10% systematic uncertainty in the description of the instrumental response, propagates into a 10% shift of the shower energy.

More problematic for the reconstruction of air showers are uncertainties in the description of the instrumental response of individual antennas, which introduce antenna-to-antenna variations to the reconstructed signals which propagate into uncertainties in the reconstructed air shower properties. In Sec. 8.1.1 we described this variation with a frequency- and direction-independent amplitude uncertainty (smearing) of 5%. Now, we repeated the analysis with a more conservative estimation for the variation between stations of 10% (translate to 20% in energy fluence). The thereby obtained energy reconstruction, i.e., $E_{\text{em}}/E_{\text{em}}^{\text{MC}}$ as a function of the zenith angle is presented in Fig. 8.16 (left). In comparison to the reconstruction with a simulated uncertainty of 5%, the overall resolution worsened by $\sim 50\%$ to about 9% and is still below 10% for air showers with energies above 10^{19} eV. It can be seen that especially the reconstruction at lower zenith angles, i.e., with lower station multiplicity, worsens. In addition, at higher energies a constant bias of -2% is found. The origin of this bias is not obvious at the moment and needs further investigation. It should be noted that for the here-presented studies, the simulated uncertainty in the instrumental response of individual antennas was always perfectly known for reconstruction, i.e., for the energy-fluence uncertainty model Eq. (8.5). In reality, the inaccuracy in the detector description will not be known perfectly. Although we do not expect this to have a large influence on our results, a dedicated investigation is needed to verify this claim. It should also be mentioned the the results for $\sigma_A = 10\%$ are obtained without correcting the fit-estimated uncertainty on the electromagnetic energy as it would require a re-parameterizations of the correction Eq. (8.13). If one would do so, the applied selection would be more rigorous and the achieved resolution improve.

Lastly, potential variations in the antenna response on small angular scales that might arise from mechanical differences in the detector stations such as a misalignment of the SALLA antennas are examined. Measurements of those variations are not easy as they require a mobile, point-like reference source. A reference source carried by an octocopter could be adequate and measurements with one are planned for the near future [104]. However, measuring the direction-dependent response pattern for a great number of different antenna stations will not be possible for logistical reasons. Here, we employ a straight forward approach to estimate the magnitude of possible variations and simulate their effect on the energy reconstruction. During the detector simulation, we vary the signal arrival direction for which the antenna sensitivity is described at each antenna

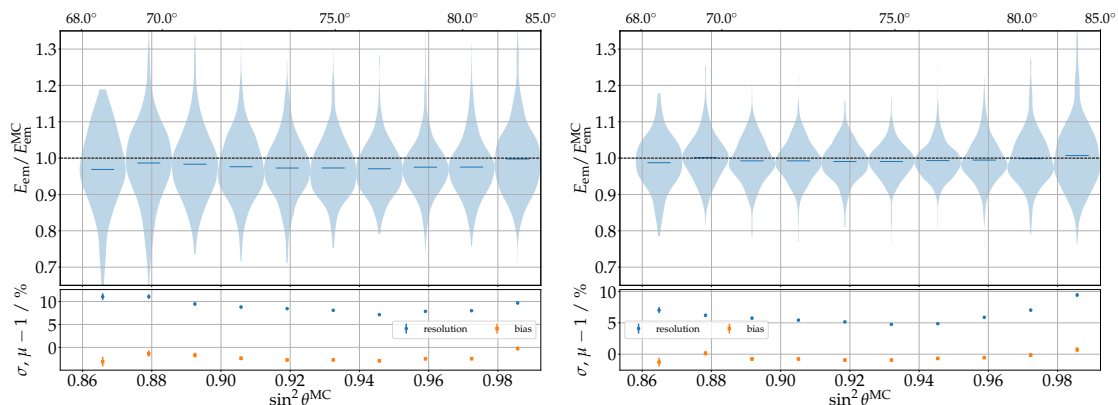


Figure 8.16.: *Left:* Reconstruction of the electromagnetic energy with an amplitude uncertainty (smearing) in the description of the instrumental response of individual stations of $\sigma_A = 10\%$. *Right:* Reconstruction of the electromagnetic energy with misaligned SALLA antennas, described by a $\pm 1^\circ$ smearing of the signal arrival direction at each antenna with a uniform distribution in zenith and azimuth, which causes variations in the directional response of the antenna stations. See details in text.

station independently. This describes a tilting and rotation of the entire antenna station (including WCD, SSD, and even the ground) w.r.t. the air shower. For obvious reasons, this is not entirely realistic, as it does not change the orientation and position of the antenna w.r.t. the ground or WCD. The antenna will be aligned w.r.t. to the horizon and thus a misaligned w.r.t. the ground is intentionally accepted if the area in which the WCD is deployed is not flat.

The thereby introduced antenna-to-antenna variations depend on the air shower arrival direction, i.e., the gradient of the antenna response, which is a realistic assumption. Studying the variation introduced in the vector-effective length \vec{H} by varying the zenith angle uniformly within $\pm 1^\circ$ around a nominal value, we found a mean relative deviation in \vec{H} of $\lesssim 10\%$ at a zenith angle of 85° for both antenna polarizations and all azimuthal directions. These deviations decrease with the zenith angle and are about 2% to 3% at 75° . We found that rotations in azimuth have a negligible effect. Varying the zenith angle of the signal arrival direction implies a tilting of the antenna aligned with the incoming direction of an air shower and hence represents an upper limit for an arbitrary tilted antenna. For a variation of the zenith angle within $\pm 2^\circ$ or $\pm 3^\circ$, we found the mean deviation to increase linearly with this angle. Using a Gaussian¹⁶ to randomly vary the zenith angle, the average deviation increased by around 50% w.r.t. using a uniform distribution.

To evaluate the effect on the reconstruction of air showers, we repeat the detector simulation and vary the signal arrival directions. For a uniform smearing of the zenith and azimuth angle of 1° , the achieved energy reconstruction as a function of the zenith angle is shown in Fig. 8.16 (*right*). Only at higher zenith angles, a mild degradation of the resolution is observed. Using a Gaussian distribution, this degradation is accentuated. For larger deviations, the resolution of showers above $\gtrsim 80^\circ$ is significantly affected, and also the reconstruction efficiency (applying the above-introduced quality criteria) of those

¹⁶ In this case, the width of the Gauss is set to 1° , 2° , or 3° .

showers decreases. Hence, to maintain an efficient and accurate reconstruction of very inclined air showers with zenith angles beyond 80° , the alignment of the antennas should have an accuracy of within 1° .

8.4.5. Discussion

The here-performed detector simulation of the RD makes assumptions about expected inaccuracies in the description of the detector sensitivity. In particular, the amplitudes are smeared with an uncertainty of 5%. This introduces antenna-to-antenna variations in the reconstructed signals. With that, the reconstruction of the shower energy with the RD is found to be very accurate with an overall resolution of $\sim 6.3\%$, which improves for energies beyond 10^{19} eV. In particular, this energy reconstruction will allow for a precise estimation of the mass composition of UHECRs, cf. Chap. 9. Better estimation of the variations introduced to the reconstructed signals by the detector will only be possible with the full detector deployed and operating. However, we also examined the energy reconstruction under more conservative assumptions, namely an amplitude smearing of 10% and a variation of the directional response of the SALLAs of up to 10% at 85° zenith angle. Although the resolution decreases, an accurate reconstruction with below 10% resolution can be maintained for most energies and zenith angles. Other systematic uncertainties, due to hadronic interaction models or atmospheric conditions, only introduce biases on the percentage level.

The shower geometry, i.e., the arrival direction and core position, are reconstructed by the RD with high precision. In the future, the WCD reconstruction can profit from a better-constrained geometry provided by the RD to improve the resolution of the reconstructed shower size N_{19} . This also carries the potential to extend the WCD reconstruction to showers beyond 82° .

9. Evaluating the sensitivity of the AugerPrime Radio Detector to the masses of ultra-high-energy cosmic rays using inclined air showers

Parts of this chapter have been published in:

F. Schlüter for the Pierre Auger Collaboration

"Expected performance of the AugerPrime Radio Detector"

[PoS \(ICRC21\) 262](#)

The primary scientific goal of the AugerPrime Radio Detector is enhancing the capabilities of the Pierre Auger Observatory to study the mass(-composition) of ultra-high-energy cosmic rays. It achieves that by measuring inclined air showers in coincidence with the water-Cherenkov detectors. The RD enables a reconstruction of the shower energy with a resolution better than 10% and minimal dependency on the cosmic ray mass, cf. Chap. 8. The WCDs measure the size of the muonic component which, for a given energy, is strongly correlated with the cosmic ray mass, cf. Chap. 2.1, 2.2, and 4.

In this chapter, we investigate the potential to combine this highly complementary information from hybrid detections of inclined air showers to infer the mass(-composition) of UHECRs. Thereby, we focus on two different objectives: I) Is it possible to determine the cosmic-ray mass for individual air shower events, i.e., can we differentiate proton- from iron-induced air showers, and, II) With which accuracy can we determine the average mass composition of UHECRs, i.e., is it possible to distinguish between different mass-composition scenarios and thus draw conclusions about the origin of UHECRs.

9.1. Reconstructing the number of muons from inclined air showers

For inclined air showers, the WCD directly reconstructs the relative number of muons at ground N_{19} , cf. Sec. 3.2.3. However, for an accurate determination of the cosmic ray mass, systematic uncertainties of the reconstruction need to be taken into account. Hence, a bias correction with the MC-derived R_{μ}^{MC} (cf. Sec. 4.1) is necessary. In Ref. [24] "PRD15", a

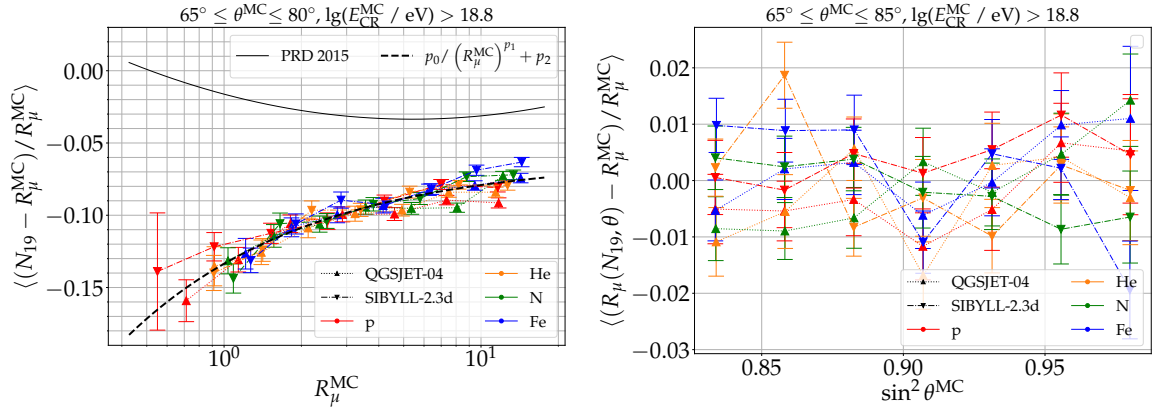


Figure 9.1.: *Left:* Bias of the reconstructed relative muon number N_{19} w.r.t. R_{μ}^{MC} for different primaries and hadronic interaction models as a function of R_{μ}^{MC} . *Right:* Deviation between bias-corrected relative muon number $R_{\mu}(N_{19}, \theta)$ and R_{μ}^{MC} as a function of the zenith angle.

$< 5\%$ bias between N_{19} and R_{μ}^{MC} depending on R_{μ}^{MC} (\sim energy) for showers with different primaries (protons and iron nuclei), hadronic interaction models, and zenith angles from 60° to 80° was found. Investigating the bias between N_{19} and R_{μ}^{MC} for our reconstructed showers with energies above $10^{18.8}$ eV and zenith angles from 65° to 80° , to ensure a fully efficient reconstruction for all primaries and zenith angles, we found a significantly increased bias of $\sim -10\%$, cf. Fig. 9.1 (*left*). In the meantime, this increase in the bias between N_{19} and R_{μ}^{MC} , has been confirmed by other collaborators. Preliminary investigations into the causation of the change point towards the simulation of the instrumental response of the WCDs rather than a change in the reconstruction procedure [176]. To ensure an accurate reconstruction of N_{19} , a selection similar¹ to the one detailed in Tab. 8.2 is applied. The bias, which decreases with the number of muons, can be described by the following empirical model:

$$\frac{N_{19} - R_{\mu}^{\text{MC}}}{R_{\mu}^{\text{MC}}} \equiv f_{\mu}(R_{\mu}^{\text{MC}}) = \frac{p_0}{(R_{\mu}^{\text{MC}})^{p_1}} - p_2 \quad (9.1)$$

We found, that with this correction applied to showers with zenith angles from 80° to 85° , a $\sim -5\%$ bias remains. Including showers from 80° to 85° in the determination of the parameterization of the bias correction according to Eq. (9.1) would shift the parameterization by $\sim -1\%$ but not resolve the bias for those showers. To resolve this bias, an explicit zenith-angle dependence into the bias corrections has to be introduced. We found the following empirical model to yield good results

$$f_{\mu}(R_{\mu}^{\text{MC}}, \theta) = \frac{p_0}{(R_{\mu}^{\text{MC}})^{p_1}} - p_2 + p_3 \left(\frac{\theta - 60^\circ}{\text{rad}} \right)^4. \quad (9.2)$$

With the above equation, a bias-corrected muon number R_{μ} is obtained from N_{19} for θ by solving the following equation numerically

$$(1 + f_{\mu}(R_{\mu}, \theta)) \cdot R_{\mu} - N_{19} = 0, \quad (9.3)$$

¹ In addition, we also required $\sigma_{N_{19}}/N_{19} < 0.5$ which only rejected 1 more shower.

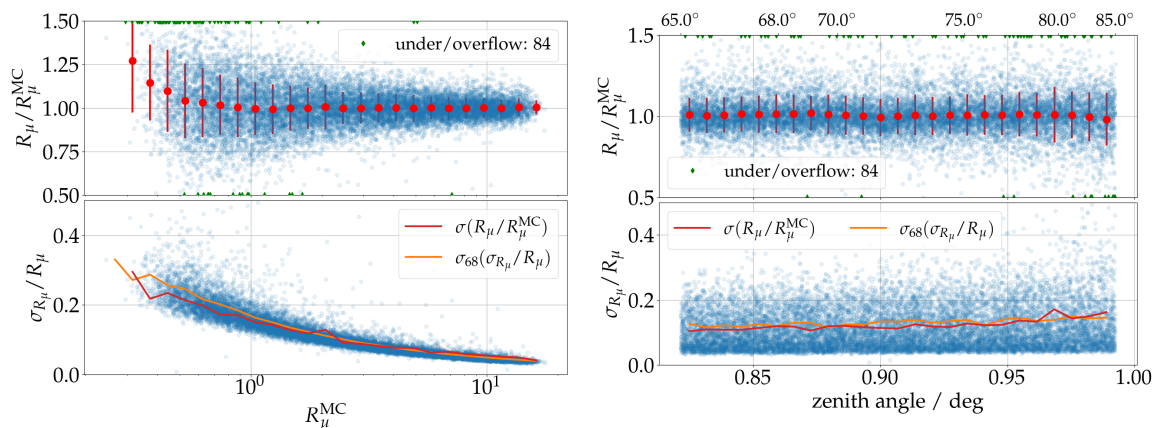


Figure 9.2.: Evaluation of the bias-corrected muon number R_μ with the ratio R_μ/R_μ^{MC} (top) and σ_{R_μ}/R_μ as a function of R_μ^{MC} (left) and the zenith angle (right).

i.e., by finding the R_μ for which the left side of the equation is 0. A comparison between the bias-corrected muon number R_μ and the true muon number R_μ^{MC} is shown in Fig. 9.1 (right). No significant bias remains, the variation across all primaries and interaction models is within $\pm 2\%$.

The bias-corrected muon number R_μ is evaluated in Fig. 9.2 as a function of the true muon number (\sim energy, left) and zenith angle (right) for showers simulated with both high-energy hadronic interaction models: Sibyll-2.3d and QGSJetII-04. The reconstruction is found to work reliably for all zenith angles and showers with a $R_\mu^{\text{MC}} \gtrsim 0.5$. Furthermore, the R_μ resolution is described accurately by the fit uncertainties and improves with energy.

9.2. Generation of realistic event sets for different astrophysical scenarios

To accurately estimate the capability of combined measurements of the RD and WCD to determine the cosmic-ray mass for individual showers or to determine the mass composition of UHECRs, the set of events upon which the analysis is based needs to be representative of what will be measured by the RD. The arrival direction distribution of our simulations is already representative for an isotropic injection of cosmic rays measured with a flat detector. However, the simulated energy spectrum is much harder than what has been measured with, e.g., Auger, i.e., our simulations have disproportionately many high-energy showers. Furthermore, the (relative) abundance of the four simulated primaries, protons (p), helium (He), nitrogen (N), and iron (Fe), each of them representing a different mass group, are equally frequent in our simulations, which does not reflect nature. As the exact mass composition of UHECRs is unknown, we utilize the two different mass-composition scenarios from Ref. [5] and introduced in Sec. 2.1.4, the *maximum-rigidity* and *photo-disintegration* scenarios, as references. Each scenario predicts the energy-dependent relative abundance for each of the four primaries $f_{p_i}(E)$ with $\sum_i f_{p_i}(E) = 1$.

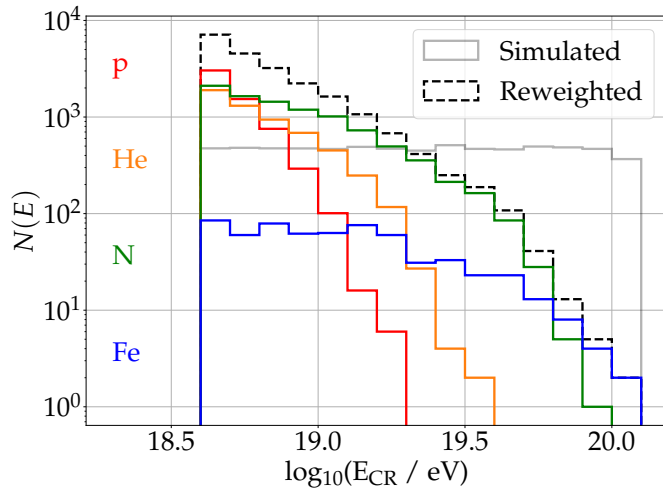


Figure 9.3.: Example for a randomly drawn energy spectrum with 4 primaries. The light gray histogram shows the simulations with a very hard energy spectrum ($\sim E^{-1} \sim \log E$). The dashed histograms show the reweighted spectrum for a 10 year measurement with the Auger-measured flux, the ideal RD exposure, and the *maximum-rigidity* scenario. The black line corresponds to the total reweight spectrum while the colored histograms indicate the event numbers for each primary.

To obtain a realistic set of events, we have to reweight our simulations, i.e., select showers which reproduce the expected energy spectrum and reference mass composition. The following procedure is applied: First, with the ideal aperture $\mathcal{A}_{\text{ideal}}(\theta_1 = 65^\circ, \theta_2 = 85^\circ, \epsilon = 1)$, cf. Eq. (8.9), the 10-year exposure for the RD is calculated to be $\sim 16\,120 \text{ km}^2 \text{ sr}$. For this exposure and the Auger-measured flux $J(E)$ [19, Fig. 2.10], the expected number of air showers is determined by numerically integrating over discrete logarithmic energy bins with $\log(\Delta E/\text{eV}) = 0.1$ individually from $10^{18.6} \text{ eV}$ to $10^{20.1} \text{ eV}$ ². For each energy bin $[E_1, E_2)$ we estimate the number of showers per primary taking into account their relative abundance

$$n_{\text{exp}}(p_i, E_1, E_2) = 16\,120 \text{ km}^2 \text{ sr} \cdot f_{p_i}(E_1, E_2) \cdot \int_{E_1}^{E_2} J(E^\dagger) dE^\dagger. \quad (9.4)$$

Given this expectation, for each energy bin and primary, we draw a value $k \in \mathbb{N}_0$ from the Poisson-distribution, i.e., following the probability density function $f(k; n_{\text{exp}})$

$$f(k; n_{\text{exp}}) = \frac{n_{\text{exp}}^k}{k!} e^{-n_{\text{exp}}}, \quad (9.5)$$

to reweight our simulations and to account for statistical fluctuations. For lower energies, $E \lesssim 10^{19.1} \text{ eV} - 10^{19.4} \text{ eV}$, we have simulated fewer events than required. In this case, events are selected multiple times (it is not ensured that each event is selected at least once). If enough events are simulated, no event is used twice. An example for the reweighting of our simulations for the maximum-rigidity scenario is shown in Fig. 9.3. It is important to stress that the generated event set is representative for what “reaches” the detector, not what is actually detected and reconstructed. For the latter, a detection and reconstruction selection needs to be applied. By doing so, the RD efficiency is incorporated in the selected events without the need of discretizing the efficiency as done in Sec. 8.3.1.

² The last bin is integrated until $\log(E/\text{eV}) = 21$.

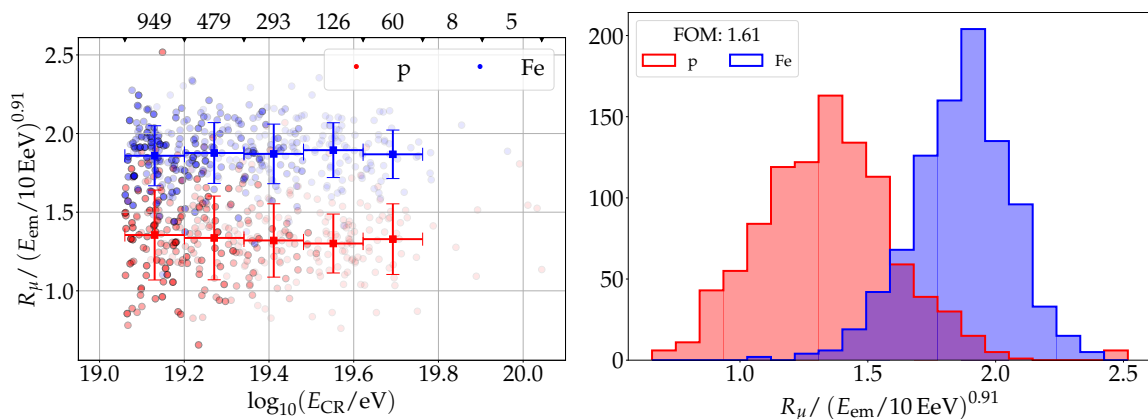


Figure 9.4.: *Left:* Proton-iron separation via $r(R_\mu, E_{em})$ as a function of E_{CR} . The transparency of the markers reflects their frequency due to reweighting. The energy-bin edges and the event number in each bin are indicated at the top x-axis. The squared markers and error bars in each bin indicate the mean and standard deviation of $r(R_\mu, E_{em})$, respectively. *Right:* The histograms of the ratio $r(R_\mu, E_{em})$ for proton- and iron-induced air showers over all energies. The FOM, quantifying the separation of both distributions, is given in the legend.

9.3. Separation of proton- and iron-induced inclined air showers

First, we investigate whether it is possible to separate proton- from iron-induced air showers reconstructed with the RD and WCD. We have already seen that R_μ scales with the energy and the primary-particle mass, cf. Sec. 4.1. Hence, normalizing the WCD-reconstructed R_μ with the RD-reconstructed (electromagnetic) shower energy E_{em} yields a mass sensitive variable $r(R_\mu, E_{em}) = R_\mu / (E_{em}/10 \text{ EeV})^b$. We use E_{em} as it can be reconstructed with no primary-dependent bias. The exponent b accounts for the fact that R_μ does not scale linearly with the energy, i.e., $R_\mu \sim E^b$ with $b \approx 0.9$. To obtain a suitable value for b for every event set, we employ a Fisher-linear-discriminant analysis to separate proton and iron nuclei using R_μ and $(E_{em}/10 \text{ EeV})$ and determine the slope of the discriminant. We quantify the separation in terms of the *figure of merit* FOM for Gaussian distributions which is given for a separation of proton and iron showers with $r(R_\mu, E_{em})$ by

$$\text{FOM} = \frac{|\langle r_p \rangle - \langle r_{Fe} \rangle|}{\sqrt{\sigma_{r_p}^2 + \sigma_{r_{Fe}}^2}}. \quad (9.6)$$

To evaluate the separation between proton- and iron-induced air showers, we use the reweighted event sets following the expected 10-year energy spectrum but with an unrealistic 50%-50% proton-iron mix³. After selecting showers with a reconstructed electromagnetic energy above 10^{19} eV, a RD-reconstructed zenith angle above 70° , and fulfill additional quality criteria for WCD and RD, see appendix E.1, the discrimination between both primaries in terms of $r(R_\mu, E_{em})$ is shown in Fig. 9.4 as a function of the

³ Modulo Poisson fluctuations.

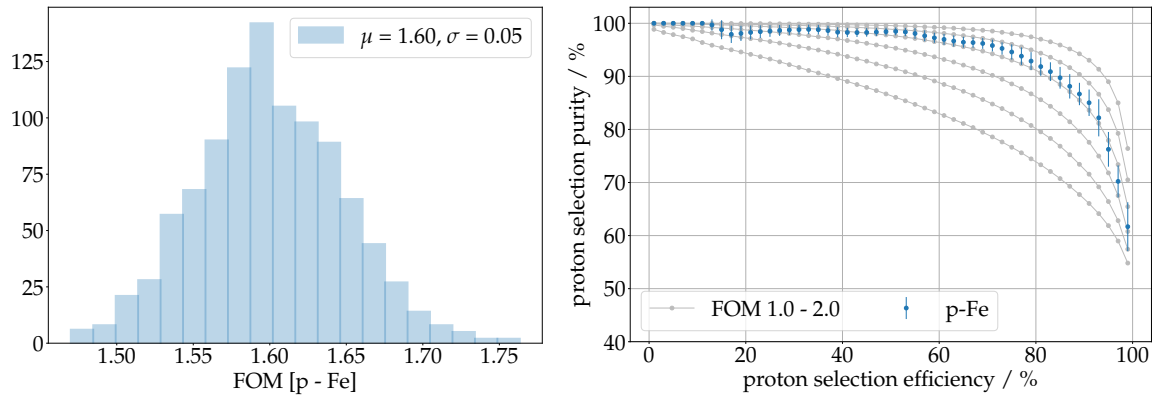


Figure 9.5.: *Left:* Distribution of the FOM for the separation of proton- and iron-induced air showers with $r(R_\mu, E_{\text{em}})$ for 1000 random event sets. *Right:* Proton selection purity as a function of the efficiency for the selection with $r(R_\mu, E_{\text{em}})$ averaged over 50 random event sets. The mean is given by the marker, the standard deviation by the error bars. The gray lines show the expectation from Gaussian distributed (toy) data for a FOM of 1 to 2.

RD-reconstructed (total) shower energy E_{CR} (*left*) and as histogram over all energies (*right*). Although we use E_{em} for the normalization of R_μ and hence for the separation between proton and iron-induced air showers, for a better interpretation of the separation within an astrophysical context and comparison with other techniques we use E_{CR} . The transparency of each marker represent the frequency of this shower in the event set. The binned mean and standard deviation of $r(R_\mu, E_{\text{em}})$, for both primaries and 5 equidistant logarithmic bins with more than 10 entries, are indicated by the thick squares and error bars. The event number in each bin is given on the top axis. The separation first improves with energy, while at higher energies the statistics are too small to draw robust conclusions about any correlation or anti-correlation with energy. The overall separation is quantified with a FOM = 1.60. To investigate the effect of statistical fluctuations onto the separation, we repeated the estimation of the FOM for 1000 random event sets. The result is shown in the histogram on the left in Fig. 9.5. A $\langle \text{FOM} \rangle \pm \sigma_{\text{FOM}} = 1.60 \pm 0.05$ is found. The distribution of the slope b , which is determined for each event set individually, has a mean of 0.90 and standard deviation of 0.01. In data, we can not determine b with a Fisher analysis as the primary-particle type is unknown. Therefore, we repeated the above procedure with a fixed slope of 0.90. The results, e.g., the separation for the presented event set and FOM distribution for 1000 random event sets remain unchanged. We found that the applied selection has a slightly higher efficiency for proton- than for iron-induced air showers. More details on this can be found in appendix E.1.

For Sibyll-generated showers we obtained a slightly better separation: The FOM distribution for 1000 random event sets is quantified with $\langle \text{FOM} \rangle \pm \sigma_{\text{FOM}} = 1.61 \pm 0.04$. The slope is found with $\langle b \rangle \pm \sigma_b = 0.9 \pm 0.01$. Fixing the slope to the mean value also does not change the separation. Interestingly, with Sibyll the selection efficiency is comparable for proton- and iron- induced showers. We also found that the separation improved when using only showers until 80° to $\langle \text{FOM} \rangle = 1.65$. For the QGSJetII-generated showers we

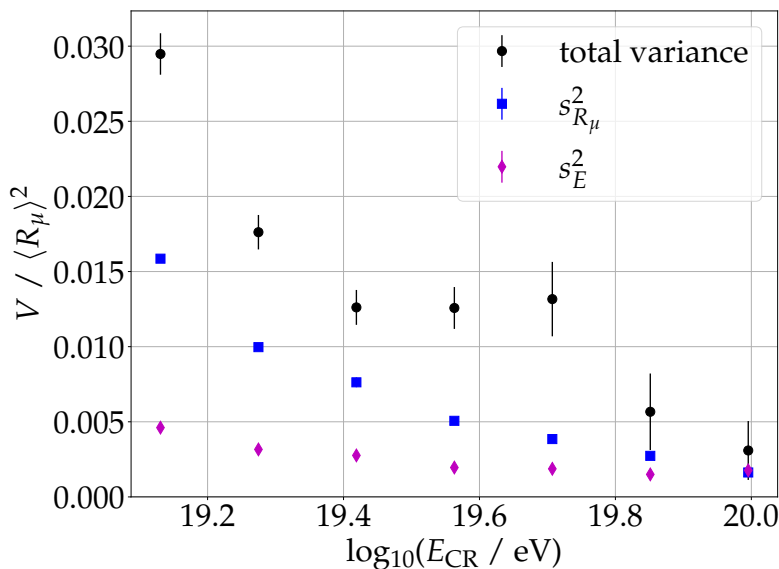


Figure 9.6.: Total relative variance of the reconstructed muon number as a function of the energy. The fit-estimated variances of R_μ (cf. Fig. 9.2) and E_{CR} (cf. Fig. 8.12) are shown as well. The error bars represent the statistical uncertainties only. The uncertainty estimation uses the uncertainty on the standard deviation from [177].

found a smaller improvement to $\langle FOM \rangle = 1.62$. However, we want to note, that those comparisons are limited by the statistics of showers we have simulated.

To bring the achieved resolution into perspective, we evaluated the separation of air showers in X_{max} using the parameterizations from Ref. [173], cf. appendix E.2. Depending on the energy and the hadronic interaction model, a separation of $FOM = 1.6$ is obtained for Sibyll-2.3d only with a detector resolution of 10 g cm^{-2} which is better than what state-of-the-art fluorescence telescopes achieve, cf. Sec. 2.1.2. This does not mean that a measurement of X_{max} with a resolution of $\sim 20 \text{ g cm}^{-2}$ to 30 g cm^{-2} in combination with $r(R_\mu, E_{\text{cm}})$ would not improve the separation. The fact that both observables are anti-correlated w.r.t. their dependency with the cosmic-ray mass, should improve the separation considerably. However, coincidence events at the highest energies and with very high inclinations $\theta > 68^\circ - 70^\circ$ with the WCDs, RD, and FD will be very rare. An interferometric reconstruct of X_{max} with radio antennas as recently proposed [150], is, unfortunately, not promising for the application with the RD, cf. Chap. 7.

The separation between protons and iron nuclei can also be evaluated in terms of the proton selection purity as a function of the selection efficiency. This is of particular relevance because a clean and efficient selection of protons would, if they are abundant at the highest energies, enable cosmic ray astronomy. The proton selection purity as a function of the selection efficiency, averaged over 50 random event sets, is shown in Fig. 9.5 (right).

It should be mentioned, that the here-studied scenario of a nearly 50%-50% proton-iron mix is far from being likely. More realistic scenarios as discussed in the following section include intermediate mass elements such as helium and nitrogen. Separating those from protons is much more difficult. The separation of light (protons and helium nuclei) from heavy (nitrogen and iron nuclei) elements is determined with a $FOM \approx 1$ for events where all elements are equally abundant.

9.4. Measuring the number of muons in inclined air showers

The mean number of muons $\langle R_\mu \rangle(E)$ as a function of the energy as well as their physical fluctuations $\sigma_{R_\mu}/\langle R_\mu \rangle$ are composition sensitive observables and can be used to study the mass composition of UHECRs. For both observables, we have derived parameterizations as functions of the energy, hadronic interaction model, and primary particle from predictions based on our CORSIKA simulations which can be used here to interpret the reconstructed observables, see appendix A.2. The mean muon number can be directly inferred from the reconstructed R_μ and E_{CR} by describing their correlation with a power-law $R_\mu(E_{\text{CR}}) = aE_{\text{CR}}^b$. The physical fluctuations $\sigma_{R_\mu}/\langle R_\mu \rangle$ can not be directly inferred from R_μ and E_{CR} as the variance of the reconstructed muon number $V(R_\mu)$ is a superposition of the physical fluctuations and contributions from the resolution in the reconstructed number of muon number $s_{R_\mu} = \sigma_{R_\mu}/R_\mu$ and energy $s_{E_{\text{CR}}} = \sigma_{E_{\text{CR}}}/E_{\text{CR}}$. With the latter, migration effects from higher energy showers containing more muons to lower energy showers with fewer muons and vice-versa are described. In Ref. [14], the physical fluctuations and reconstruction resolutions are introduced in a log-likelihood model for a power law describing the correlation between R_μ and E_{CR} , with which both observables are determined with great precision. Here, a simplified analysis strategy is followed: In discrete logarithmic bins, the mean of the normalized muon number $\mu(x)$ with $x \equiv R_\mu/(E/10 \text{ EeV})$ is calculated. The physical fluctuations $\sigma/\langle R_\mu \rangle$ are derived from the total relative variance of the muon number $V(x)/\mu(x)^2$ by subtracting the estimated resolutions of R_μ and E_{CR}

$$\sigma^2/\langle R_\mu \rangle^2 \approx V(x)/\mu(x)^2 - s_{R_\mu}^2 - s_{E_{\text{CR}}}^2. \quad (9.7)$$

The above equation, i.e., the contribution of the energy resolution to the total variance, assumes that the muon number scales (almost) linear with the energy, i.e. $b = 1$, which is not strictly correct for simulations while in data the estimated exponent is consistent with 1^4 [14]. The total relative variance as well as $s_{R_\mu}^2$ and $s_{E_{\text{CR}}}^2$ are shown in Fig. 9.6 for a random event set described by the maximum-rigidity scenario. Two things are apparent: First, at lower energies, the resolution in R_μ and E_{CR} can not account for the entire reconstructed variance, this is due to the physical fluctuations. Second, in the last bin the reconstructed variance is very low given the fact that the spectrum is dominated by iron nuclei which have a very low physical fluctuation. However, given the low statistics at those energies, the estimated resolution in R_μ and E_{CR} can, due to statistical uncertainties, exceed the reconstructed variance. Following Eq. (9.7), this equates to imaginary physical fluctuations which is nonphysical. The sensitivity to the statistical accuracy on the estimation of $s_{R_\mu}^2$ and $s_{E_{\text{CR}}}^2$ is a disadvantage of this analysis strategy.

For two random event sets composed of the QGSJetII-generated showers with a mass composition described by the maximum-rigidity and the photo-disintegration scenario respectively, and the event statistics expected in 10 years of RD-WCD measurements, the reconstructed mean number of muons (*top*) and their fluctuations (*bottom*) are shown in Fig. 9.7. Those simulated measurements are compared to theoretical predictions obtained from our CORSIKA simulations and the (actual) measurement of 289 high-quality air showers from hybrid-detections of the Fluorescence Detector and the WCD [14]. Comparison

⁴ Probably due to a change in the mass composition towards an increased abundance of heavier elements.

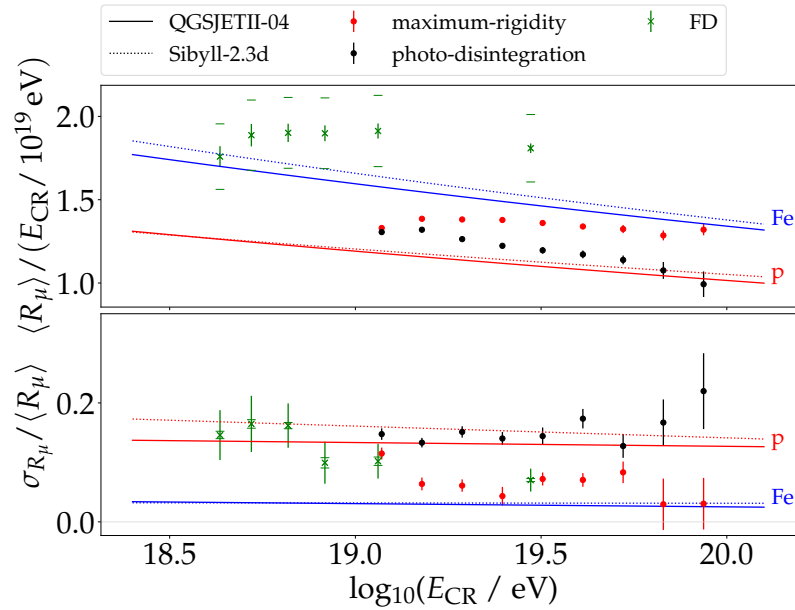


Figure 9.7.: Simulated measurement of the relative mean number of muons (*top*) and their physical fluctuations (*bottom*) with the WCD and RD for the two different mass-composition scenarios comprised of p, He, N, and Fe primaries for the QGSJetII-generated showers. The most recent measurements by the FD and WCD [14] and theoretical predictions for pure proton and iron compositions (see appendix A.2) are shown as well. The error bars illustrate the statistical uncertainty only and the error caps (only shown for FD-WCD, green) show the systematic uncertainty.

with the predictions for pure proton and iron compositions reveals that the reconstructed mean number of muons describes a mass composition which becomes heavier with energy for the maximum-rigidity scenario, and a mass composition which remains light also at higher energies for the photo-disintegration scenario. Similar conclusions can be drawn from the reconstructed physical fluctuations. The fact, that the reconstructed physical fluctuations for the photo-disintegration scenario can exceed the theoretical prediction of a pure proton composition is not a contradiction. For a mixed composition the difference in the mean muon number for different primaries increases the variance of the reconstructed distributions and thus the estimated fluctuations. Hence, the reconstructed observables qualitatively reproduce the injected composition, cf. Fig. 2.5.

The error bars represent the statistical uncertainties on the mean and the physical fluctuations, respectively. With both observables, $\mu(x)$ and $\sigma/\langle R_\mu \rangle$, the two mass-composition scenarios can be clearly distinguished, i.e., they are well-separated beyond their statistical uncertainties. However, this changes when taking into account systematic uncertainties as can be seen for the example of the measurements with the FD and WCD for which the systematic uncertainties are represented by the error caps. Considering those uncertainties, the interpretation of the reconstructed mean muon number is substantially impacted and a discrimination between the different mass composition scenarios is likely not possible anymore. However, the effect on the relative physical fluctuations is significantly less, as those fluctuations are rather flat in energy the uncertainty on the energy scale mostly

cancels out. Hence, a good discrimination is maintained even after including the systematic uncertainties on the energy scale.

We did not quantify the systematic uncertainty on the RD-reconstructed energy scale, however, preliminary studies for AERA estimate an uncertainty of 14% for the reconstruction of vertical air showers which is dominated by the detector calibration [66, Sec. 6.2.3]. The preliminary absolute antenna calibration of the RD has an uncertainty of about 10%. Hence, a similar uncertainty as for the FD-energy scale of 14% (see Sec. 3.1) is reasonable to assume.

9.5. Conclusion

We have studied the potential to enhance the capabilities of the observatory to measure the mass(-composition) of UHECRs with the AugerPrime Radio Detector. In particular, we have utilized the shower energy as reconstructed by the Radio Detector and the number of muons as reconstructed by the WCD from highly inclined air showers to: I) separate the proton- from iron-induced air showers, and II) measure the average mass composition of UHECRs. For the former, we achieved a figure of merit of $FOM \approx 1.6$ for a mixed proton-iron composition. The latter has been demonstrated for two different mass-composition scenarios. We were able to qualitatively recover the injected compositions and separate between the two reference scenarios.

The here-demonstrated separation power between proton- and iron-induced air showers has only limited relevance for the application on data to determine the mass of individual UHECRs, as their flux is most likely composed of a mixed composition which include intermediate mass cosmic rays. This makes a classification between them more challenging. However, it is an important characteristic to quantify the mass sensitivity of those hybrid measurements. The achieved separation is very promising and comparable or even slightly surpasses the separation with X_{\max} alone or that predicted for the universality reconstruction for the hybrid measurements of the WCD and SSD [5] of $FOM \approx 1.3 - 1.6$. Further improvements on the separation are likely only achievable with the combination of different anti-correlated observables like the R_{μ} and X_{\max} .

Hybrid measurements of these observables with the Fluorescence Detector and the water-Cherenkov detector have been shown to disagree with the theoretical predictions and hint at a heavier composition at the highest energies [24, 14]. However, the present FD - WCD data lack statistics at the highest energies due to the lower exposure of the FD. Thus, data of hybrid detections with the Radio Detector and WCD will increase the available statistics by more than one order of magnitude at energies above 10^{19} eV. Thereby, the found discrepancy between data and simulations can be tested at higher energies and with different systematically uncertainties and the mass-composition information inferred from the physical fluctuations can be used to constrain models for the prediction of the origin of UHECRs.

Part IV.
Summary

10. Summary

To improve our understanding of the nature of ultra-high-energy cosmic rays, and to identify their sources and acceleration mechanism(s), more, and more accurate data of their mass composition is required. The Pierre Auger Observatory is taking up this challenge by upgrading its large-aperture Surface Detector. As part of this upgrade, the AugerPrime Radio Detector will detect the electromagnetic radiation produced by inclined air showers within the 30 MHz to 80 MHz band. This will enable complementary measurements of the electromagnetic shower component with the RD and muonic shower component with the SD and thus provide a high sensitivity to the masses of ultra-high-energy cosmic rays.

For this work, I have simulated various sets of inclined air showers and the, by them, emitted radio emission. The simulation sets feature different high-energy hadronic interaction models, atmospheric conditions, and detector layouts. They enable the study of the nature of the radio emission, the development of reconstruction algorithms for the radio detection of inclined air showers, the investigation of the capabilities of the RD to detect and reconstruct those air showers, and the investigation of the mass sensitivity of hybrid measurements between the RD and SD, as conducted in this thesis.

Among the studies conducted in this thesis, I have investigated the **correlation between the strength of the radio emission, separated by its macroscopic emission mechanism, with the ambient conditions**, i.e., the air density at the shower maximum and the magnetic field orientation relative to the air shower arrival direction. I could verify the anti-correlation of the geomagnetic emission with the air density known from studies of more vertical air showers. However, for air showers with zenith angles $\gtrsim 82^\circ$, i.e., with air densities at their shower maxima of $\lesssim 0.2 \text{ kg m}^{-3}$, an unexpected residual correlation with the orientation to the geomagnetic field becomes apparent. For air showers arriving orthogonally to the magnetic field, the geomagnetic radiation energy starts decreasing with decreasing density. A possible explanation for this anti-correlation is a recently described transition from a time-varying transverse current regime to a regime in which synchrotron radiation is predominant. As a consequence of this, the coherence within the $\vec{v} \times \vec{B}$ polarization decreases. Investigating the (absolute strength of the) charge-excess emission, I found a correlation with the air density and proposed a simple qualitative explanation for this correlation. However, both observations need experimental confirmation. Furthermore, I studied **the radio-emission release as a function of the slant depth** with an adequate treatment of the coherence between the emission released early and later in the longitudinal development of the particle cascade. I found that the release of charge-excess emission arriving at the ground coherently follows closely the longitudinal profile of the excess electrons. While this has been predicted before, other literature had found a contradictory behavior, that the charge-excess emission originates from higher up in the atmosphere. I concluded that this contradictory result is due to an incorrect

treatment of the coherence within the radio emission emitted early and late in the shower development.

Another investigation focused on the propagation of the radio emission through the Earth's atmosphere. I found that in very inclined air showers with zenith angles $\gtrsim 80^\circ$, for which the "signal propagation" distance between the shower maximum and detector array is $\gtrsim 80$ km, **the refractive bending of electromagnetic waves displaces the coherent radio-emission footprint at the ground by up to ~ 1.5 km at about 85°** . This displacement can be quantitatively described with a simple numerical model of the refraction of a single electromagnetic wave using Snell's law. It is worth highlighting, that the displacement is caused by the refractive index gradient and not just by the non-unity refractive index of the atmosphere. In the context of this investigation, I verified the treatment of the refractivity in the propagation of the radio emission in CoREAS. Although in CoREAS, the propagation is calculated along straight lines, which at first glance seems to be in contradiction with the refractive displacement, the time delay in the (light-)propagation time introduced due to the refractive medium is correctly described (along those straight lines). The relative signal arrival timing between various signal sources and one observer, which governs the coherence in the radio emission, calculated along straight lines is found to properly reproduce the relative timing for curved trajectories within less than 0.1 ns, which is sufficient for the coherent emission in the sub-GHz frequency regime. The found displacement is crucial for the accurate modeling of the radio-emission footprints from highly inclined air showers as well as the interpretation of the reconstructed air shower position in hybrid measurements. In addition to this, a remaining displacement at lower zenith angles which is not correlated with the zenith angle and can not be described by refraction is apparent which requires further investigations.

Based on the insights gained from those studies, I have developed a **signal model for the radio-emission footprints from inclined air showers**, which can be utilized to accurately reconstruct the electromagnetic shower energy from inclined air showers detected by sparse antenna arrays. The signal model is composed of a description of the dominant geomagnetic emission with a symmetric (1-dimensional) LDF and of "asymmetries" to the symmetric emission which together constitute the total signal received in the $\vec{v} \times \vec{B}$ polarization. The asymmetries are associated with the superposition of the geomagnetic and the charge-excess emission as well as geometrical early-late imprints. With a parameterization of the charge-excess fraction, it is possible to reconstruct the LDF solely from measurements of the emission in the $\vec{v} \times \vec{B}$ polarization which is measured with a better signal-to-noise ratio in the presence of ambient noise as the signal in other polarizations. With this model, an *intrinsic* energy resolution of about 3 % to 5 % is achieved, depending on the zenith angle and without taking into account experimental or instrumental uncertainties. Furthermore, no reconstruction bias depending on the cosmic-ray mass is observed and systematic uncertainties due to the utilized hadronic interaction model or ambient conditions are within $\lesssim \pm 2\%$ on the absolute energy scale. It is found that the sensitivity to the depth of the shower maximum from the lateral shape of the signal distribution is minimal, given the fact that the shower maximum and detection plane are far apart.

Although the model has been developed to enable accurate reconstruction of the air shower observables with the RD, it can be useful for other experiments as well. However, a re-parameterization might be necessary depending on the particular experiment and its location.

An accurate determination of the depth of the shower maximum X_{\max} would improve the sensitivity of the Radio Detector to the masses of UHECRs. The anti-correlation between X_{\max} and the number of muons w.r.t. the cosmic-ray mass would strongly promote the separation of air showers induced by different primary particles. While this is not achieved for inclined air showers with traditional methods relying on the lateral shape of the signal amplitudes at the ground, a newly-proposed **interferometric reconstruction of X_{\max}** promises to provide an accurate reconstruction of X_{\max} , especially for very inclined air showers. To assess whether the application with the RD is possible or not, I evaluated the performance of this technique by considering realistic assumptions about experimental conditions and instrumental uncertainties. In particular, I simulated the effect of inaccurate time synchronization between wirelessly communicating antenna stations and a realistic shower sampling, i.e., signal multiplicity for realistically spaced antenna arrays. I conclude that the time synchronization between antennas has to be $\lesssim 1$ ns and the signal multiplicity $\gtrsim 20$. While the time synchronization of the RD is expected to be ~ 5 ns also the required signal multiplicity, which at the highest zenith angles is limited by the external WCD triggers, is hardly reached.

With the developed signal and reconstruction model, **the performance of the RD to detect and reconstruct inclined air showers** is investigated. To this end, I utilized Monte-Carlo simulations of air showers with the particular detector layout of the RD, performed a complete simulation of the RD instrumental response, i.e., the “detector simulation”, and reconstructed all relevant air showers observables. The simulation of the RD instrumental response as well as the reconstruction of the radio signals and air shower observables were performed with Offline. For this purpose, I have implemented the here-developed reconstruction model in Offline and improved the detector simulation.

For the simulation of the RD instrumental response, it is taken into account, that the response (i.e., sensitivity) of individual antenna stations is only known with an accuracy of 5% on the amplitude. Hence, to mimic variations in the actual response of individual antenna stations w.r.t. the one with which they are described, Gaussian smearing according to this uncertainty is applied. To realistically mimic measurements of air showers with the best possible accuracy, in-situ recorded noise is added to the simulated signals. Furthermore, for this work, a new approximation to determine the signal arrival direction at individual antennas to describe their direction-dependent antenna response is used.

With the reconstructed signals, the detection efficiency is derived for inclined air showers which have induced detectable signals in at least 3 antenna stations. I found that the RD will be detecting air showers with full efficiency for zenith angles above 70° and energies above $10^{18.8}$ eV. The aperture is calculated for detecting contained air showers with a 3000 km^2 array. For the detection of the highest-energy cosmic rays, the maximum aperture of $1612 \text{ km}^2\text{sr}$ is approached. With this, it is estimated, that in 10 years of operations, **the RD will collect over 3900 events with energies above 10^{19} eV and around 570 events for energies above 4×10^{19} eV** assuming the Auger-measured flux. Those results are,

within their statistical uncertainty, independent of the particular simulation setting, i.e., the selected hadronic interaction model, atmosphere conditions, and used particle thinning. Those results signify an improvement of more than one order of magnitude over the statistics of mass-sensitivity measurements with Fluorescence Detector at those energies and zenith angles. At the very highest energies $E \geq 4 \times 10^{19}$ eV, the result signifies an improvement to the statistic available with the Fluorescence Detector regardless of the zenith angle.

For air showers with signals in at least 4 antenna stations, the cosmic-ray arrival directions are reconstructed fitting a spherical shower front model to the reconstructed signals. The reconstruction is quantified with an angular resolution of 0.12° . A complete event reconstruction comprising a reconstruction of the lateral signal distribution, determination of the shower core, and electromagnetic energy is performed for air showers with zenith angles above 68° and signals in at least 5 antenna stations. For those showers, **the electromagnetic energy is reconstructed with an overall energy resolution of $\sim 6.2\%$** , and without any bias on the reconstructed electromagnetic energy for air showers induced by different primary particles. The energy resolution is found to improve with energy but is rather independent of the zenith angle. Furthermore, the fit-estimated resolution of the electromagnetic energy is found to underestimate the fluctuations w.r.t. the Monte-Carlo value. Hence, I parameterized a correction factor for the fit-estimated uncertainty on the electromagnetic energy. I also studied the systematic effects introduced from assumptions made in the detector simulation. In particular, if the sensitivity of individual antennas is only known with 10% accuracy. It causes the overall resolution to worsen to $\sim 9\%$ and introduces a -2% reconstruction bias. The reconstructed shower core position is found to exhibit a bias towards the incoming direction of the air showers as expected from the refractive displacement. However, the reconstruction is found to be very accurate with a resolution that scales with the zenith angle from about 20 m to about 80 m. Furthermore, the reconstruction is found to be very efficient.

With a simulation-derived calibration between the cosmic-ray and electromagnetic shower energy, the former can be reconstructed with no significant worsening in resolution. However, given that the primary particle type is unknown, the mass-independent calibration introduces a maximum mass-dependent bias of 3%.

With the RD-reconstructed cosmic-ray and electromagnetic shower energy and the SD-reconstructed number of muons, I have investigated **the potential to separate air showers induced by protons or iron nuclei as well as to measure the average mass composition of UHECRs**. Therefore, I have reweighted the simulated showers to obtain event sets that are representative of a 10-years measurement with the RD, i.e., in agreement with the Auger-measured flux, estimated RD exposure, and reference scenarios for the mass composition of UHECRs. **The separation for proton- and iron-induced air showers with zenith angles above 70° and electromagnetic energies above 10^{19} eV is quantified with a figure of merit $FOM \approx 1.6$** , based on an unrealistic 50%-50% proton-iron mixed composition. This discriminative power is very compatible with what can be achieved with fluorescence telescopes measuring X_{\max} or hybrid measurements of the WCDs and SSD. The simulated measurements of the average number of muons with the RD and SD for two different reference mass-composition scenarios, i.e., the maximum-

rigidity and photo-disintegration scenarios, were found to reproduce the injected mass compositions and hence carry the potential to extend measurements currently performed with the Fluorescence Detector and SD to higher energies and thus to distinguish between different astrophysical scenarios which describe the origin of the UHECRs.

With the work accomplished in the context of this thesis, the Pierre Auger Observatory is well-prepared for the advent of experiment data from the AugerPrime Radio Detector.

Part V.
Appendix

A. Appendix to Chap. 4

A.1. Extrapolating CoREAS pulses

The left panel in Fig. A.1 shows a pulse simulated for 400 ns in 3 polarizations. At the end of this time window, the electric field amplitudes have not regressed to 0. When zero padding those traces to, e.g., increase the frequency resolution of its Fourier-transform, a cut-off at the end of the simulated trace is introduced. In the band pass filtered trace, this cut-off introduces a second peak, cf. Fig. A.1 (right). Hence, to avoid introducing a cutoff, we fit an exponential to the last 50 ns of the simulated pulse in each polarizations and extrapolate based on this model the traces for 2 μ s. The exponential is indicated by the dashed lines. The assumption is made that, in each polarization, for the last 50 ns the pulse has already reached its maximum and is decaying exponentially. Appropriate warnings were introduced which alert the user when: 1) after or without the extrapolation of the pulses the RMS calculates over the last 20 ns and all 3 polarizations (quadratic sum) are larger than 50 μ V, 2) the fitted slope of the extrapolate model is at its upper boundary of -0.001 ns^{-1} for any polarization, and 3) if the integrated power in the pulse changed by more than 10% after the extrapolation while the energy fluence of the pulse (for all frequencies) is larger than 1 eV m^{-2} . The right panel of Fig. A.1 shows the 30 MHz to 80 MHz band-pass-filtered trace with and without the extrapolation. Without the extrapolation a second peak is found at the position of the cutoff.

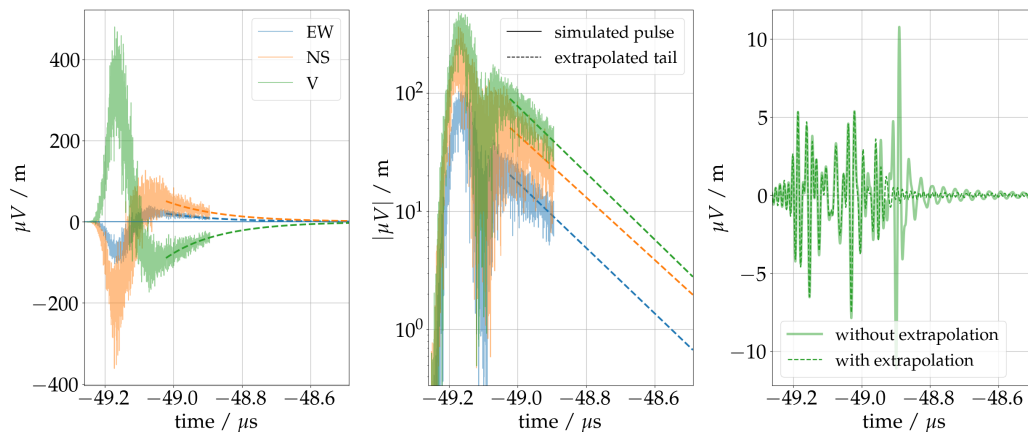


Figure A.1.: *Left & Middle:* Unfiltered simulated pulse with extrapolated “extension”. *Right:* Filtered pulse, with (dashed line) and without the extrapolation (solid transparent line). The cutoff in the non-extrapolated trace introduces a sharp peak at the position of the cutoff in the filtered trace.

A.2. Parameterizations of the mean number of muons and their fluctuations from simulated inclined air showers

The following parameterizations for a given energy were obtained with the indicated high-energy hadronic interaction model in combination with UrQMD and CORSIKA v7.74, cf. Chap. 4. See Fig. 4.2 for an example of the given parameterizations.

Table A.1.: $\langle R_\mu \rangle(E) = (E/a)^b$

Sibyll-2.3d, $E = E_{em}$		
	a / EeV	b
p	0.726	0.928
He	0.629	0.912
N	0.567	0.916
Fe	0.488	0.907

Sibyll-2.3d, $E = E_{CR}$		
	a / EeV	b
p	0.821	0.941
He	0.718	0.923
N	0.656	0.927
Fe	0.577	0.920

QGSJetII-04, $E = E_{em}$		
	a / EeV	b
p	0.734	0.918
He	0.661	0.920
N	0.588	0.918
Fe	0.510	0.911

QGSJetII-04, $E = E_{CR}$		
	a / EeV	b
p	0.829	0.931
He	0.751	0.930
N	0.679	0.928
Fe	0.603	0.925

Table A.2.: $\sigma(R_\mu/\langle R_\mu \rangle(E)) = a \log_{10}(E/10 \text{ EeV}) + b$

Sibyll-2.3d, $E = E_{em}$		
	a	b
p	-0.0120	0.1710
He	-0.0042	0.0984
N	-0.0021	0.0575
Fe	-0.0024	0.0332

Sibyll-2.3d, $E = E_{CR}$		
	a	b
p	-0.0198	0.1610
He	-0.0023	0.0912
N	-0.0004	0.0538
Fe	-0.0005	0.0318

QGSJetII-04, $E = E_{em}$		
	a	b
p	-0.0061	0.1426
He	-0.0077	0.0809
N	-0.0111	0.0503
Fe	-0.0073	0.0331

QGSJetII-04, $E = E_{CR}$		
	a	b
p	-0.0064	0.1334
He	-0.0056	0.0746
N	-0.0094	0.0470
Fe	-0.0054	0.0306

B. Appendix to Chap. 6

B.1. Alternative approach for the decomposition of the geomagnetic and charge-excess emission

As already discussed in section 6.2.3, the decomposition of the geomagnetic and charge-excess emission used in this work comes with the disadvantage that it breaks down for observers close to or on the $\vec{v} \times \vec{B}$ -axis. An alternative approach is outlined here. When assuming that both emission patterns are completely rotationally symmetric, one can, by inspecting the $\vec{v} \times \vec{B}$ -emission from opposite sides of the shower axis, estimate the strength of the geomagnetic emission and of the charge-excess emission (in this polarization). This relies on the idea that on opposite sides the charge-excess and geomagnetic emission interfere destructively and constructively in equal parts. With $f_{\text{vxB}}^\dagger(x, y) = f_{\text{vxB}}(-x, -y)$, one can determine the emission f_{geo} and f_{ce} as per:

$$f_{\text{geo}} = f_{\text{vxB}}^{\text{geo}} = \frac{1}{4} \left(\sqrt{f_{\text{vxB}}} + \sqrt{f_{\text{vxB}}^\dagger} \right)^2 \quad (\text{B.1})$$

$$f_{\text{vxB}}^{\text{ce}} = \frac{1}{4} \left(\sqrt{f_{\text{vxB}}} - \sqrt{f_{\text{vxB}}^\dagger} \right)^2 \quad (\text{B.2})$$

With the above $f_{\text{vxB}}^{\text{ce}}$ and $f_{\text{vxB}}^{\text{ce}} = f_{\text{vxB}}^{\text{ce}}$, the total charge-excess emission can be calculated $f_{\text{ce}} = f_{\text{vxB}}^{\text{ce}} + f_{\text{vxB}}^{\text{ce}}$. Using the mirror image of the radio emission $f_{\text{vxB}}^\dagger(x, y)$, strong shower-to-shower fluctuations of the charge-excess emission as reported in Ref. [122] distorted the estimation of the charge-excess fraction. Furthermore, the displacement of the core, as well as the early-late corrections, disturbs the concentric simulated antenna grids. This mandates to use interpolations to obtain the mirror image of the footprint which is not trivial for disturbed antenna grids.

B.2. Variation in the LDF parameters for different atmospheric conditions

As described in Sec. 4.1.1, we have simulated a subset of showers at lower energies with the artificial star-shaped antenna grid for different atmospheres. The atmospheres at the location of the Pierre Auger Observatory for February (summer), July (winter), and October correspond to the maximum, minimum, and yearly average for the refractivity at ground level, respectively. With the prediction of r_0 according to Eq. (4.4) depending on the atmospheric profile (refractive index at the shower maximum), the parameterization

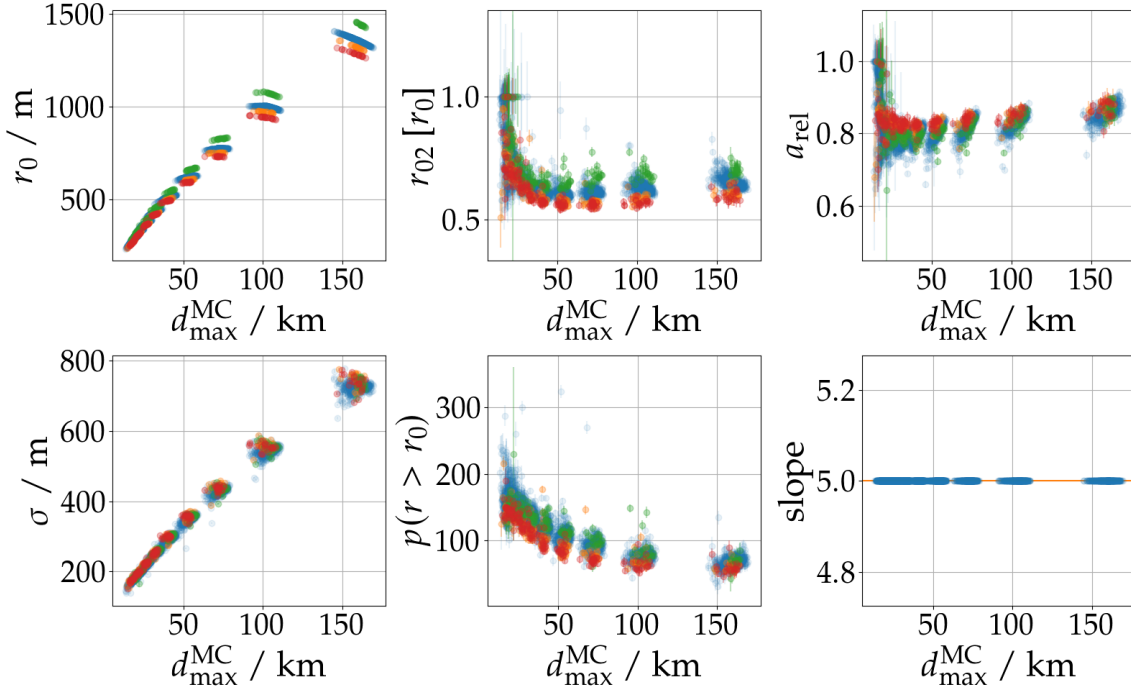


Figure B.1.: Parameters of f_{GS} extracted from simulations with different atmospheric conditions (same color mapping as in Fig. 6.5). The distributions correspond to the fit with all parameters free (besides the slope s and r_0) which explains the larger variations at lower d_{\max} w.r.t. Fig. 6.6.

of the LDF f_{GS} explicitly uses information from the atmosphere. The other parameters, however, are assumed to be universal, i.e., do not depend (significantly) on the simulated atmosphere. In Fig. B.1, the correlation of the parameters with d_{\max} , for the different simulated atmospheres is shown. Although the atmosphere influences the correlations of the parameters with d_{\max} , the variation is tolerable and the October atmosphere used for the parameterization indeed describes the mean reasonably well.

B.3. Refined lateral shape of the charge-excess fraction parameterization

Also, the “off-axis angle” $p_{\text{ce},0}$ term and the “exponential correction” $p_{\text{ce},1}$ term were refined w.r.t. [142] similarly as the “density scaling” $p_{\text{ce},2}$. Both terms were substituted and fitted with Eq. (6.11) to the previously found geomagnetic LDF f_{GS} . First the exponential correction was refined with $p_{\text{ce},1}$ while using the optimized expression of the density scaling and the fixed expression of the off-axis angle term from [142]. The results can be seen in Fig. B.2 (left). Finally, also the off-axis term is optimized. Instead of a constant factor a linear model with a slope depending on d_{\max} is found to describe the fitted distribution of $p_{\text{ce},0}$ better, Fig. B.2 (right).

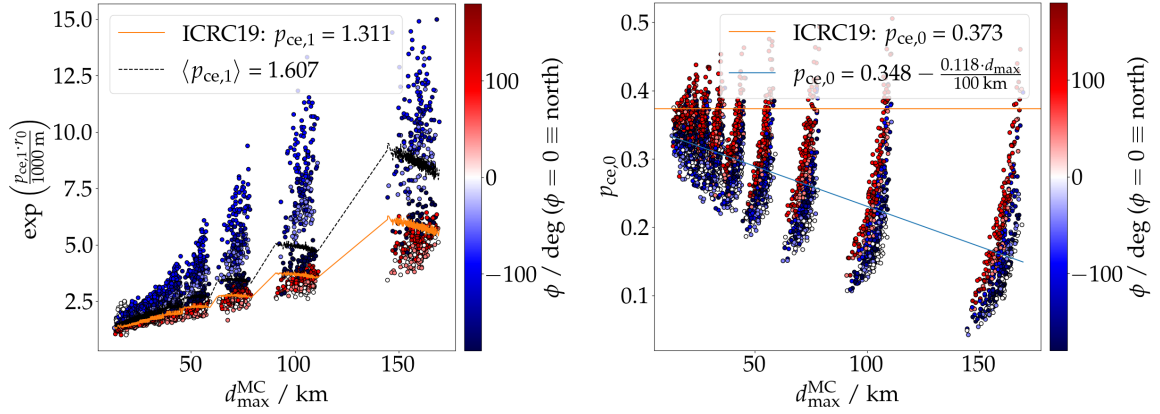


Figure B.2.: Optimized parameters of the lateral shape of the charge-excess fraction. All parameters are optimized by fitting the geomagnetic emission for each pulse determined via the parameterization Eq. (6.11) to the geomagnetic LDF of the shower f_{GS} .

B.4. Electromagnetic shower energy derived from CORSIKA simulations

The strength of the radio emission is strongly correlated with the energy in the electromagnetic particle cascade, i.e., the electromagnetic shower energy E_{em} . It should be stressed, that the fluorescence light measured by optical telescopes correlates with the total calorimetric energy E_{cal} (for which other particles like muons have a non-negligible contribution) and not E_{em} (although both observables have been confused in the past). We compute E_{em} with a sum over the longitudinal energy deposit table provided in the CORSIKA DATnnnnnnn.long file for gamma rays, electrons, and positrons (energy losses from ionization and when they are “cut” from the simulation), i.e.,

$$E_{em} = \sum_{i=0}^N E_i(\gamma) + E_i^{ioniz.}(e^+e^-) + E_i^{cut}(e^+e^-). \quad (\text{B.3})$$

It is worth mentioning, that this includes the energy deposit in the ground plane (which is accounted for in the two last rows of this table with the SLANT option).

B.5. Reconstructing the electromagnetic shower energy for showers generated with Sibyll-2.3d

Fig. B.3 shows the E_{em} reconstruction for showers generated with the Sibyll-2.3d high-energy interaction model. Out of 6199 showers with zenith angles greater than 68° and at least 5 simulated observers, 6185 showers were reconstructed with good quality. The results are very comparable to the ones achieved with the QGSJetII-04 showers: The S_{19} parameter decreased slightly by less than 2% and the resolution at lower zenith angles worsens slightly. It is worth stressing, that the model was developed solely with QGSJetII-04-generated showers, hence a small decrease in reconstruction quality for Sibyll-generated showers is

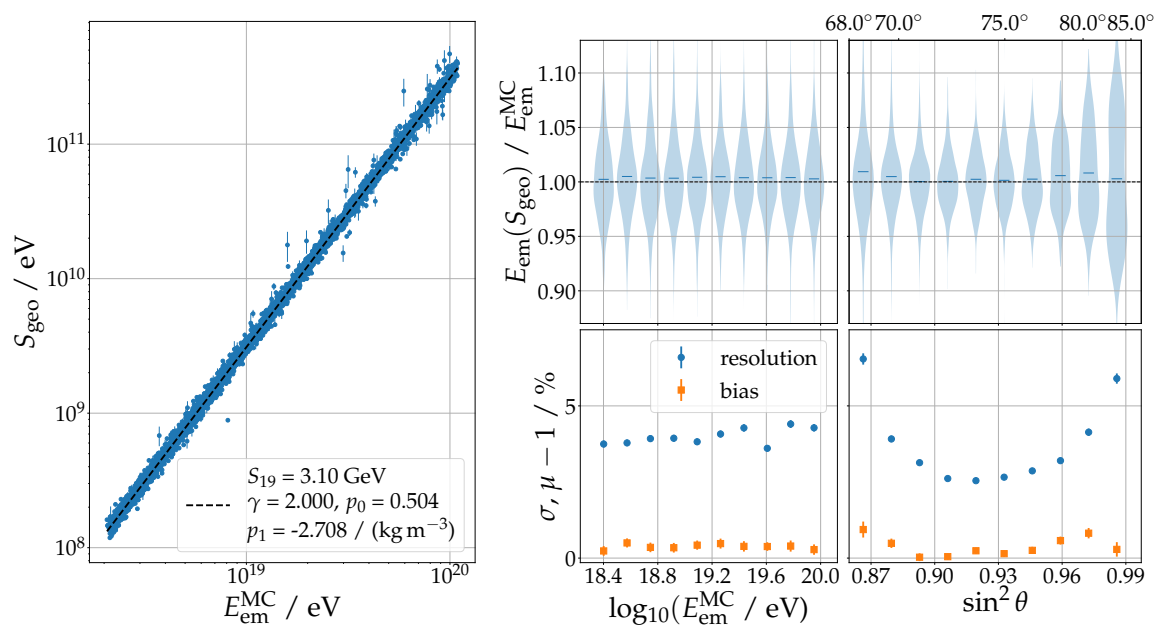


Figure B.3.: Reconstruction of the electromagnetic shower energy E_{em} for the showers generated with Sibyll-2.3d. *Left:* Scatter plot of the radio-reconstructed electromagnetic shower energy as a function of the true electromagnetic shower energy. Legend indicates fit parameters according to Eq. (6.17). Bias and resolution (bottom panels) of the reconstructed electromagnetic energy as a function of the true energy (*middle*) and zenith angle (*left*) are also shown. The full distributions are illustrated in the top panels.

not surprising. Furthermore, this result underlines the fact that the radio emission has little dependence on the underlying hadronic interaction model.

C. Appendix to Chap. 7

C.1. Calculation of the effective refractive index between two arbitrary locations in the atmosphere

From equation (4.1) it follows that the effective refractivity between two positions \vec{i} and \vec{j} is calculated via the integral along the line of sight with length $l_{i,j}$:

$$\overline{N}_{i,j} = \frac{N(0)}{\rho(0)} \frac{\int_i^j \rho(h(l)) dl}{l_{i,j}}. \quad (\text{C.1})$$

For sources with a zenith angle $\theta \lesssim 60^\circ$ the atmosphere can be approximated to be flat and the integral over dl can be substituted with $dl = dh/\cos(\theta)$. This simplifies the equation to

$$\overline{N}_{i,j} = \frac{N(0)}{\rho(0)} \frac{T_i - T_j}{\Delta h_{i,j}} \quad (\text{C.2})$$

with the analytically described mass-overburden $T_x = T(h_x)$. For more inclined geometries the curvature of the Earth has to be taken into account and the density along $l_{i,j}$ becomes a function of the zenith angle and distance from the ground. In that case, the integral in Eq. (C.1) cannot be solved analytically anymore and thus has to be solved numerically. This is computationally very demanding, and thus we use a pre-calculated table of the integrated refractivity¹. The table comprises the integrated refractivity as a function of the zenith angle at the Earth's surface at sea level (which is not identical to the zenith angle measured at higher altitudes along the line of sight) and the distance d between the Earth's surface and a point along the line of sight. For any two points in the atmosphere for which the line through both points also intersects with the spherical Earth the integrated refractivity between those points can then be determined directly from the pre-tabulated values. The grid points of the table are spaced in $\tan \theta$ and equidistant in distance d . The integrated refractivity for any arbitrary point in the atmosphere is determined by a bi-linear interpolation within this table. A python implementation of this table and the interpolation has been made publicly available at [178].

In Fig. C.1 we compare the effective refractivity determined with this model (pre-calculated table) to the exact numerical solution. The total light propagation time can be accurately calculated using the tabulated effective refractivity (cf. Fig. C.1 top panel). A minor zenith-angle-dependent bias is visible in the absolute residual (cf. middle panel), however, the deviation is negligible since it is below any coherence criteria for signals in the MHz regime. In addition to the bias, small *wiggles*, which originate from the non-physical, linear interpolation between zenith angle bins, are visible but also negligible.

¹ This is equivalent to the treatment introduced to CoREAS with version v7.7000.

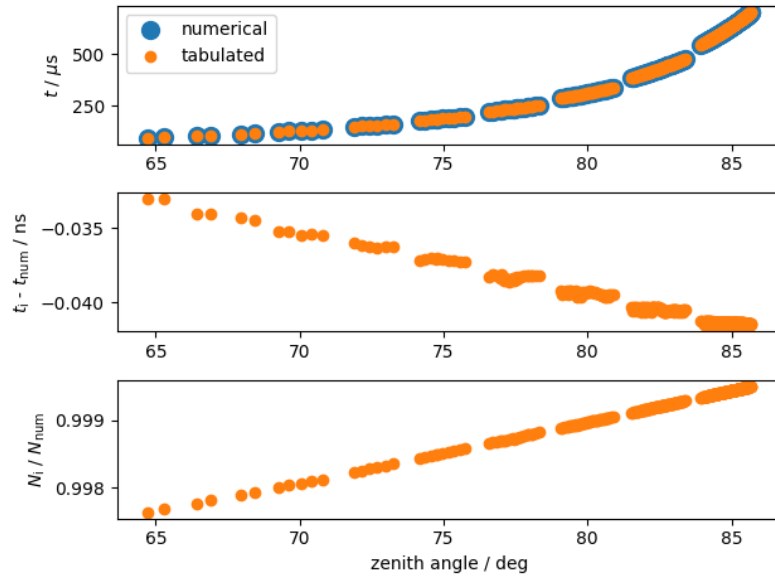


Figure C.1: *Top:* Total light propagation time for (9) different source positions and numerous observers. The x-axis denotes the zenith angle under which a source is seen by an observer. The propagation time is calculated along straight lines with the effective refractivity being calculated by very fine-grained piece-wise numerical integration or with the pre-calculated tables. *Middle:* Absolute difference of the light propagation time between numerical and tabulated calculation. *Bottom:* Relative agreement of the effective refractivity between numerical and tabulated calculation.

C.2. Parameterization of the Cherenkov radius for the interferometric reconstruction of inclined air showers with the Auger radio detectors

The parameterization introduced here is only used in Sec. 7.2. It describes a correction to Eq. (4.4) to prediction the Cherenkov angle. The equation to determine the “corrected” Cherenkov radius is given in Eq. (7.8). The correction is necessary to obtain the radius of a ring defined by the maximum energy fluence, cf. Sec 5.2.1.

Here we use the Cherenkov radii estimated from the geomagnetic emission from Chap. 5. In Fig. C.2 (*left*) the Cherenkov radii as derived from the showers with star-shaped antenna grids are shown as a function of d_{\max} . To derive a parameterization for this quantity it is better to express the radius in terms of the opening angle at the shower maximum and as a function of the density at the shower maximum (cf. Fig. C.2, *right*). Thereby, the dependency on the observation altitude vanishes and a continuous parameterization is possible. The opening angles are found to disagree with the Cherenkov angles calculated with Eq. (4.4). This may be due to two reasons: 1) The definition used to derive the Cherenkov radius from the simulations, namely that it is the axis distance at which the signal is strongest, is incorrect or 2) That the approximations made, i.e., a point source moving through the atmosphere with a homogeneous refractive index are not sufficiently fulfilled. Furthermore, it can be seen in that figure that the relationship between opening

angle and density is not unambiguous but that for a given density but different zenith angles the opening angle changes (cf. line structure for discrete zenith angle bins). To describe the derived Cherenkov angles (radii) we define a correction $A(d_{\max})$ for which Eq. (7.8) correctly describe the Cherenkov radii determined from the CoREAS simulations. The correction function $A(d_{\max})$ which was found to describe the simulation-derived radii best is:

$$A(d_{\max}) = 0.945 - \left(\frac{4.487 \text{ km}}{d_{\max}} \right)^{1.43} - \frac{d_{\max}}{2466.308 \text{ km}}. \quad (\text{C.3})$$

With this parameterization a good accuracy of $\sigma_{95}(|r^{\text{param}}/r^{\text{CoREAS}} - 1|) < 2.1\%$ is reached.

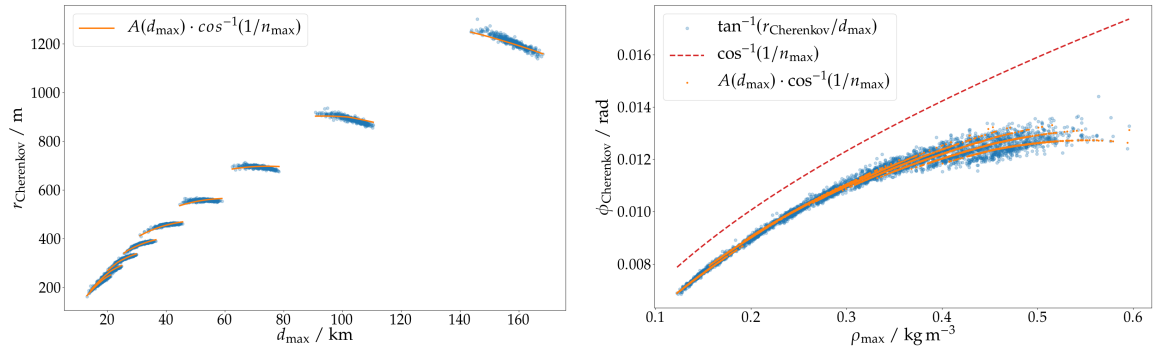


Figure C.2.: *Left:* Blue dots show the Cherenkov radii derived for the CoREAS simulations. Orange line shows the parameterization derived here, see text for details. *Right:* Cherenkov angles as a function of the atmospheric density at the shower maximum. Blue dots show the angles given the CoREAS derived Cherenkov radii. The dotted red line shows the expectation according to Eq. (4.4). Orange dots show the parameterization derived here.

C.3. Station multiplicity and event selection for the interferometric reconstruction of inclined air showers with the Auger radio detectors

Fig. C.3 (*left*) shows the (signal) station multiplicity for showers measured with a 1.5 km hexagonal grid using an energy-fluence threshold² of 5 eV m^{-2} [94] (blue) or a particle threshold, i.e., Offline-simulated WCD triggers (orange). It can be seen that for showers below 77.5° the radio emission is limiting the (signal) station multiplicity while for showers with greater zenith angles the particle component at the ground the limiting factor. This implies that for highly inclined showers measured with RD, triggered by the WCDs, we will lose a significant amount of stations.

In Fig. C.3 (*right*) the selection efficiency (cf. Sec. 7.2.2) for the RD simulations including WCD triggers (black curve) and several toy Monte-Carlo simulations (colored curves) are shown. The toy simulations estimate the efficiency for different array spacings purely

² The energy fluence is directly computed from the CoREAS-simulated electric field traces within 30 MHz to 80 MHz. No noise or any instrumental uncertainties are considered.

based on geometrical considerations, i.e., how many stations are within the defined annuli, but no signal threshold of any kind is required.

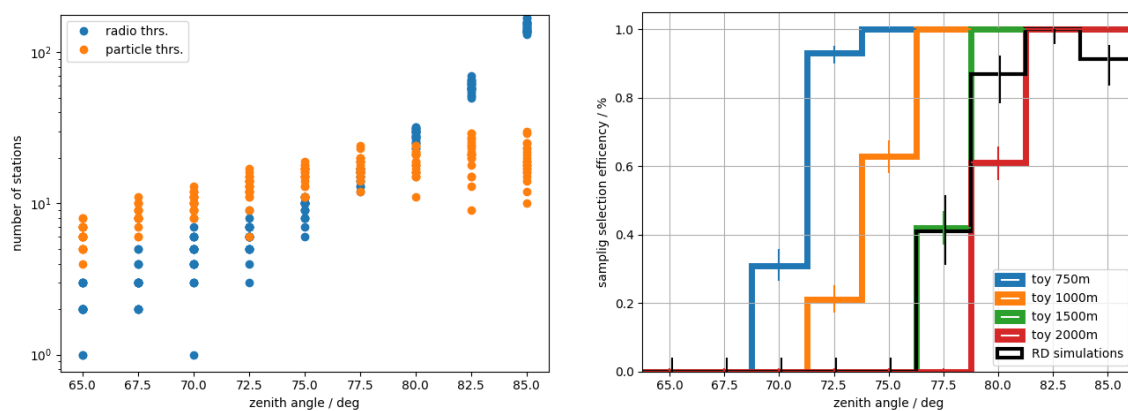


Figure C.3.: *Left:* Number of stations on a 1.5 km hexagonal grid, triggered from particles or the radio emission at ground as a function of the zenith angle for the 207 10 EeV proton showers. *Right:* Selection efficiency for the criterion described in Sec. 7.2.3 and different detector layouts as a function of the zenith angle. Black curve shows the selection efficiency all 207 RD showers from Sec. 7.2.3, the colored curves show the efficiency expected for different hexagonal grids with spacing between 500 m to 2000 m.

D. Appendix to Chap. 8

D.1. Simulation of the signal arrival direction at individual antennas

The two approximations to describe the signal arrival direction at each antenna station are illustrated with a comic in Fig. D.1 (*left*). The change in the sensitivity of single antennas between both approximations is illustrated in the example of a very inclined air shower in Fig. D.1 (*right*, the color coded is saturated, the maximum variations are on the level of $\sim \pm 40\%$). It shows the relative difference in the energy fluences when using one or the other approximation to describe the antenna response/sensitivity during the detector simulation but the same (plane-shower-front) approximation for reconstructing the electric field traces as otherwise the different sensitivities would cancel out again. The figure shows a strong early-late asymmetry introduced by the different approximations: The signals of early observers (positive y-axis) are increased as the antennas' sensitivities are described at lower zenith angles with the spherical-shower-front approximation and the antenna sensitivity decrease for increasing zenith angles at these inclinations. The variation introduced into the antenna sensitivities and reconstructed energy fluences, respectively, depend on the zenith angle. For lower zenith angles the difference decrease: at ~ 78 degree the maximum variation in energy fluence is $\sim 10\%$, for ~ 73 degree it is $\sim 5\%$.

If either approximation is used consistently in detector simulation and signal reconstruction, variations mostly cancel out. Only the effect of noise onto the reconstructed energy fluence might introduce large variations as noise affects less sensitive antennas more strongly. However, from simulations alone, it can not judge which approximation describes reality best. For measured data, the antenna sensitivity is only used for reconstructing the electric field traces. Hence, a miss modeling of the signal arrival directions, i.e., the antenna sensitivity, will imprint asymmetries into the signal distribution similar to what is observed in Fig. D.1 (*right*). To evaluate the effect on the reconstructed air shower observables when using the approximation inconsistently between the detector simulation and signal reconstruction (to illustrate a worse case scenario of miss modeling the arrival directions for data). We use the spherical-shower-plane approximation for the detector simulation but the plane-shower-front approximation in the signal reconstruction: We do not see a significant worsening of the achieved energy resolution, also not for very inclined air showers. The reason for that is simple: For contained, very inclined air showers with a large signal multiplicity, the shower footprint is well sampled and the additional early-late asymmetry increases the scatter of the data but does not change its mean which can still be found with good accuracy. However, we found that the reconstructed shower

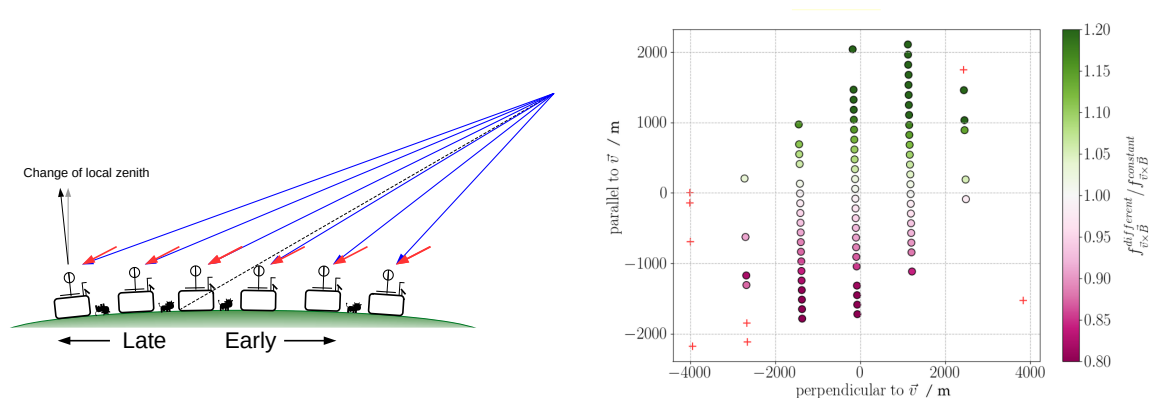


Figure D.1: *Left:* Comic of the two different approximations: constant signal arrival directions (plane-shower-front approximation, red) and differential signal arrival directions (spherical-shower-front approximation, blue). The latter also accounts for the curvature of the Earth’s surface, which causes a change in the local zenith (indicated by the black and gray arrow), while the former does not. Illustrated in between the upgraded Surface Detector stations: Wild cattle grazing in the Pampa. *Right:* Variation in energy fluence for a 84.7° air shower when using the two different approximations to describe the sensitivities of the antennas in the detector simulation. For reconstruction, a constant arrival direction is used. Please note, the variations at both ends of the color-scale are saturated. The maximum variations were found to be $\sim \pm 40\%$. Figure from [179, Slide 2]

core distribution exhibits a larger bias in the air shower incoming direction than what is expected from the refractive displacement alone.

D.2. Measured radio-frequency interference

Radio-frequency interference (RFI) or “noise” can significantly influence the detection of extensive air showers with radio antennas. We differentiate between different categories of RFI each influencing the radio detection or air showers differently: transient or non-transient, broadband or narrowband RFI. An example for a source of non-transient RFI is the galaxy which produced colored broadband radio emission. But also human-made RFI such as narrowband signals from TV or radio stations are sources of non-transient RFI. Those typically reduce the signal-to-noise ratio of air shower signals and thus govern the detection threshold of radio experiments. Sources of pulsed transient RFI are more difficult to identify and often due to human activity. For AERA, power lines and transformers have been identified as sources of transient RFI. This anthropogenic RFI typically exceeds the rate of air showers at energies above 10^{17} eV by several orders of magnitude and signifies a major challenge for self-triggering radio detection [180].

In this study, we use recorded data from 6 RD-EA antennas. The data was recorded during a special data-taking campaign for 15 days in December 2021 and January 2022. In this period, the RD stations were periodically readout with an interval of 15 min and the recorded ADC counts were written to a locally connected USB drive. This amounts in ~ 3620 recorded, $8.192 \mu\text{s}$ -long traces per antenna(-channel) and station. Alternatively, we

could have also used traces from T3 triggered data. This would have two benefits: more statistics and a larger period covered. However, there are also several disadvantages to it. Most obviously, those traces can contain actual air shower signals which, for the sake of this study would need to filter out. Furthermore, a “stationary” noise pulse is consistently found in triggered data appearing in the traces between 4000 ns to 5000 ns. Those pulses are likely caused by the onboard electronics during data taking (i.e., in coincidence with a trigger) and not found within the periodically triggered data, cf. Fig. D.2, *right bottom*. For air shower detection this is not a problem as the (triggered) signals from air showers typically occur before that at around 3400 ns and this area can be easily masked during reconstruction. However, in this study, to increase the available noise statistics, we want to augment the noise traces by randomly rolling them in time so that each trace can be used several times while a simulated signal peak is superposed with different noise each time.

The mean $\mu(\text{ADC})$ (top panel) and standard deviation $\sigma(\text{ADC})$ (bottom panel) for each of the recorded traces per station and antenna as a function of the UTC-time are shown in Fig. D.2 (*left*). The mean indicates a different baseline/pedestal for each antenna which can vary with time. The majority of noise traces have a $\sigma(\text{ADC}) \sim 2$, only traces from the EW antenna of station 31733 shows a significant deviation from this behavior. This antenna was operating with a broken low-noise amplifier (LNA) and hence the traces from both antennas of this station are not used in this work. Among the remaining stations, a temporal correlation of periods with high ADC counts can be observed. However, beyond a $\sigma(\text{ADC}) \gtrsim 7$ a second population of events emerges which shows not correlation in time. This second population is also clearly visible in the histogram of $\sigma(\text{ADC})$ shown in Fig. D.2 (*right, top*). A deeper investigation of this population of events showed repeated occurrences of strong pulses in the recorded traces which carry power mainly in 30 MHz to 35 MHz range [181]. As such a population was not found in triggered data, it is assumed that those traces are a special feature of the periodic data taking (with a manually connected USB drive and specific firmware) and hence each event with a $\sigma(\text{ADC}) > 7$ in any one of its both (antenna-)channels is rejected. It is also visible that the mean σ / ADC distribution for all stations slightly changed around the 6th of January 2022. This change can be connected to a change in power in the 65 MHz to 70 MHz range which is likely due to variation in the power from the transmission line of a local TV station [181].

D.3. Azimuthal dependency of the RD detection efficiency

The RD detection efficiency for four different energy bins (color-coded from $\log_{10}(E/\text{eV}) = 18.6 - 20.2$ in $\log_{10}(\Delta E/\text{eV}) = 0.4$) and the four lowest zenith angle bins (different panels) as a function of the azimuth angle is shown in Fig. D.3. The direction of the magnetic field is indicated with the vertical red line. While at low zenith angles and energies a correlation of the efficiency with the azimuth angle is visible, which follows in general the expectation, this correlation weakens with energy and for higher zenith angles. Above $\sim 67.5^\circ$ no correlation for the two highest energy bins is visible anymore while for the highest zenith angle bin no significant correlation is found regardless of the energy.

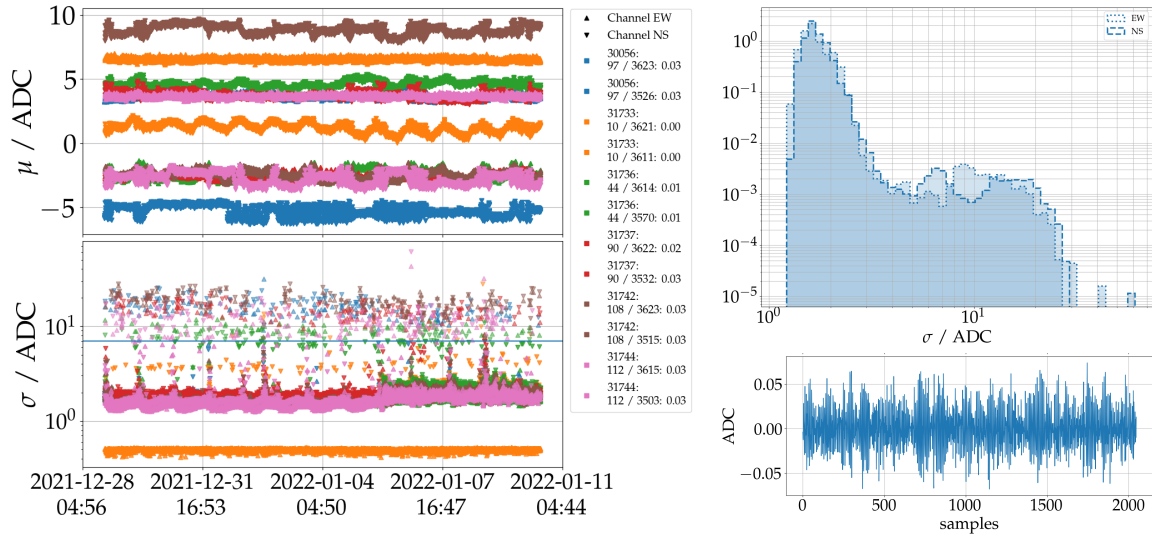


Figure D.2.: Statistic of periodically-taken background traces. *Left:* Mean (top) and standard deviation (bottom) of the ADC counts per trace as function of the UTC time. The markers indicate the different antenna channels/orientations, the colors the different stations. The EW antenna of station 31733 has a broken low-noise amplifier (LNA) and is thus excluded from all other plots. *Right:* Histogram of the standard deviation of all traces from all stations per antenna orientation. The y-axis shows the normalized frequency of each bin. A recovery of the frequency at $\sigma(\text{ADC}) \geq 7$ is visible in both antenna orientations with slight variations. The “averaged” traces of the NS antenna for all traces of all stations. No feature is visible which would hint for a stationary RFI pulse from, e.g., the station onboard electronics.

D.4. Goodness of the LDF fits with the RD

The goodness of the LDF fits performed for the RD can be described by the “reduced chi-square” χ^2/ndf , or, more adequate for events with a low number of degrees of freedom, the p-value. We show both quantities for a high-quality selection in Fig. D.4. The selection is equivalent to Tab. 8.5 with the exception, that no reduced chi-square cut was used.

With the χ^2/ndf and p-value the following hypothesis is tested: Is the data well described by the utilized LDF model under the assumption that the estimated uncertainties correctly describe the fluctuations within the data. If that is given, the p-value distribution is flat and the χ^2/ndf distribution exhibits a mean of 1. The distributions obtained for both quantities are shown in Fig. D.4 (*left*). It is clearly visible that the expectations for both quantities are not fulfilled. Hence, the hypothesis is rejected, or the assumption made for the uncertainties is not entirely fulfilled. Assuming that the LDF model is indeed correct, those distributions would indicate that the uncertainties are underestimated for at least a fraction of the showers with a p-value close to 0 and χ^2/ndf values much larger than 1. As we have seen, the selected LDF fits yield an accurate energy reconstruction, hence we argue that the used LDF model is adequate to describe the data and that the uncertainty model needs to be refined.

In both panels on the right side, the χ^2/ndf distribution as a function of the energy (*top*) and zenith angle (*bottom*) is shown. The orange lines indicate the 68%- and 95%-quantile.

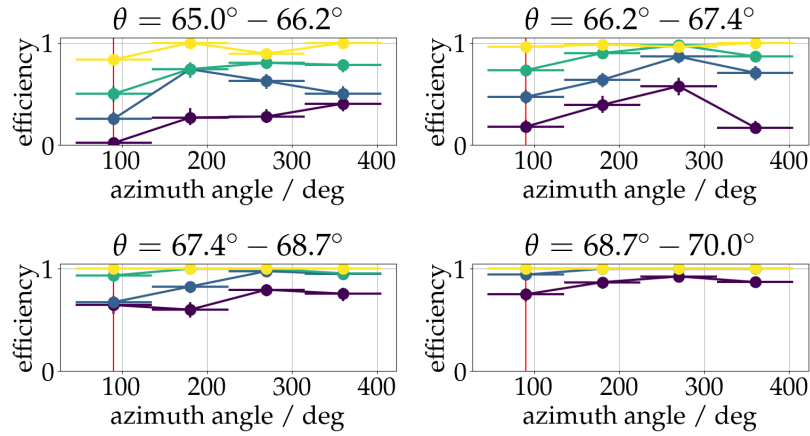


Figure D.3.: Detection efficiency for the RD as a function of the azimuth angle for different energy bins (color-coded in logarithmic bins) and zenith angles (different panels).

While with the energy no significant correlation is observed, the χ^2/ndf in generally improves for higher zenith angles.

Given that the signal multiplicity varies greatly with the zenith angle, the evaluation of the LDF fits via the “p-value” to select high fidelity events would be a better choice. However, given the general issues discussed here, we decide to use a soft $\chi^2/\text{ndf} < 10$ criterion and only reject the most prominent outliers.

D.5. Estimation of the uncertainty for the reconstructed electromagnetic shower energy

The statistical uncertainties for the geomagnetic radiation energy $\sigma_{E_{\text{geo}}}$ and distance to the shower maximum $\sigma_{d_{\text{max}}}$ are obtained directly from the χ^2 -minimization of the LDF fit. The uncertainty for the density at the shower maximum $\sigma_{\rho_{\text{max}}}$ is obtained by shifting d_{max} up and down by its uncertainty recalculating the density at those positions (using the reconstructed shower arrival direction without considering any uncertainty on it¹) and taking the average of the obtained up- and down-shift. For the uncertainty on $\sin \alpha$ the uncertainty on the reconstructed arrival directions is used while the uncertainty on the magnetic field orientation is omitted. The uncertainty of the electromagnetic shower energy is obtained using Gaussian error propagation while omitting any correlation between the different sources of uncertainties. This yields the following equations:

¹ The additional uncertainty in ρ_{max} due to the uncertainty in the reconstructed zenith angle is found to be negligible since the uncertainty is typically below 0.1° .

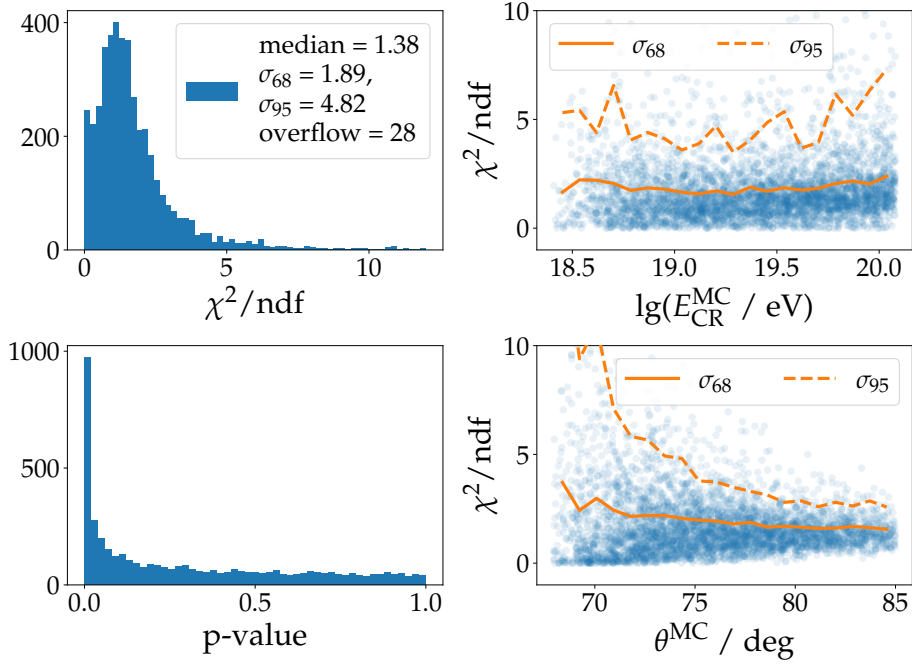


Figure D.4.: Goodness of the LDF fits evaluated with the χ^2/ndf and p-value. The histograms of the left side both indicate that the fitted model is not an adequate description of the data or the estimated uncertainties do not correctly reflect the fluctuations in the data. The right panels demonstrated no significant correlation of the reduced χ^2 with the energy but indicate an improvement with the zenith angle.

$$\sigma_{E_{\text{em}}} = \frac{10^{19} \text{ eV}}{\gamma S_{19}} \left(\frac{S_{\text{geo}}}{S_{19}} \right)^{1/(\gamma-1)} \sigma_{S_{\text{geo}}} \quad (\text{D.1})$$

$$\sigma_{S_{\text{geo}}} = S_{\text{geo}} \cdot \sqrt{\left(\frac{\sigma_{E_{\text{geo}}}}{E_{\text{geo}}} \right)^2 + \left(\frac{\sigma_{c(\rho_{\text{max}})}}{c(\rho_{\text{max}})} \right)^2 + \left(\frac{\sigma_{\sin \alpha}}{\sin^2 \alpha} \right)^2} \quad (\text{D.2})$$

$$c(\rho_{\text{max}}) = (1 - p_0 + p_0 \exp(p_1 [\rho_{\text{max}} - \langle \rho \rangle]))^{-2} \quad (\text{D.3})$$

$$\sigma_{c(\rho_{\text{max}})} = \frac{|-2p_0 p_1 \exp(p_1 [\rho_{\text{max}} - \langle \rho \rangle]) \sigma_{\rho_{\text{max}}}|}{(1 - p_0 + p_0 \exp(p_1 [\rho_{\text{max}} - \langle \rho \rangle]))^3} \quad (\text{D.4})$$

The uncertainty of S_{geo} from Eq. (D.2) is dominated by the uncertainty of E_{geo} .

D.6. Correction of the fit-estimated energy resolution

Fig. D.5 shows the parameterization of the correction for the estimated energy resolution Eq. (8.13). Table D.1 shows the selection applied to obtain the parameterization. Alongside the fitted parameterization is also shown a parameterization obtained using a more rigorous

Table D.1.: RD selection for parameterization of the energy resolution correction.

RD	N / 7972
min. 5 signal stations	4794 (60.1%)
Has LDF fit	4730 (98.7%)
min. 1 station < 1.5 r_0	4601 (97.3%)
Total	4601 (57.7%)

shower selection (similar to the one summarized in Tab. 8.5). The difference between both parameterization is small. The parameterization is sensitive to the signal uncertainty model of the energy fluence. When using an amplitude uncertainty of $\sigma_A = 10\%$ in the detector simulation and uncertainty model, i.e., Eq. (8.5), the difference between the estimated and true resolution decreased. However, the functional form for Eq. (8.13) is still adequate.

D.7. Estimating start values for the LDF fit

The start values for the LDF-fit parameters are derived partially from WCD-reconstructed observables. The core position is initial set to the WCD-reconstructed core. A first guess for the geomagnetic radiation energy is obtained using the WCD-reconstructed energy E_{WCD} and RD-reconstructed geomagnetic angle α_{RD} with the following equation

$$E_{\text{geo}}^{\text{guess}} = 26.86 \text{ MeV} \left(\frac{E_{\text{WCD}}}{1 \text{ EeV}} \right)^{1.989} \sin^2 \alpha_{\text{RD}}. \quad (\text{D.5})$$

This equation ignores additional dependencies on E_{geo} and is only suited to give a very rough estimate. To obtain an estimation for d_{max} we use the RD-reconstructed zenith angle, an X_{max} -estimation based on the E_{WCD} and a parameterization for the energy-dependent mean X_{max} [173]. We take the average between the parameterized X_{max} for protons and iron nuclei.

D.8. Offline configuration: Reconstruction sequence and modules

The WCD detector simulation is performed with the standard application *SdSimulationUpgrade*² application. The CoREAS-simulated radio pulses are stored alongside the simulated signals of the WCD and SSD in Offline ROOT files. Subsequently, with a second application, *RDSdHasSimulationReconstruction*, a WCD event reconstruction, RD detector simulation, and RD event reconstruction is performed. The Lst. D.1 describes the sequence of modules that were used to simulate and reconstruct events for the RD. Some comments are given describing the purpose of each module (the sequence can not be used 1:1 in Offline as a modules for reading and writing are missing). The Lst. D.2 shows the relevant configuration of the *RdHASLDFFitter* used in this work. This configuration does not coincide

² With minor modifications as explained in Chap. 8.

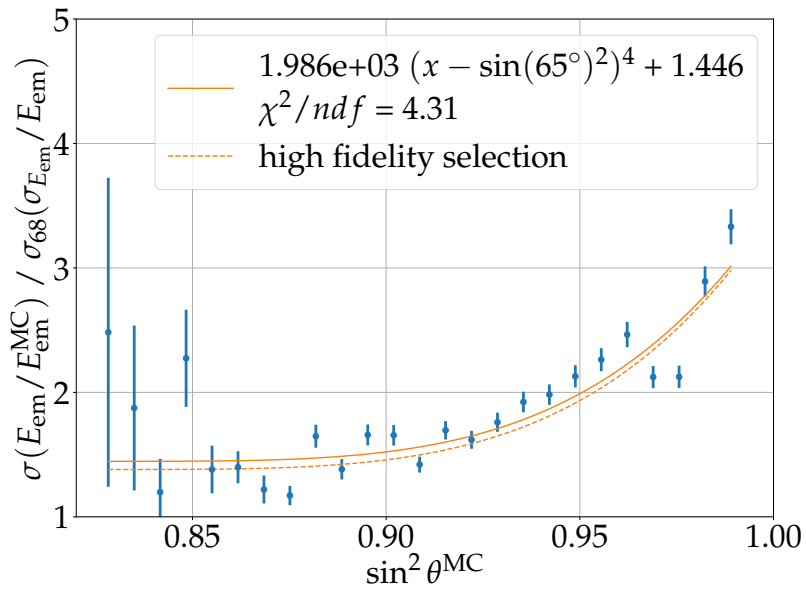


Figure D.5.: Parameterized correction for the fit-estimated resolution $\sigma_{E_{em}}$. Error bars correspond to the statistical uncertainty on $\sigma(E_{em}/E_{em}^{MC})$. The dashed line indicates a parameterization to data obtained with a more rigorous shower selection.

with the current default configuration of the module. When processing Sibyll-generated simulations, the hadronic interaction model for the X_{max} estimator is adapted.

Listing D.1: Module sequence for RD detector simulation and event reconstruction.

```

<!-- Radio Detector simulation -->
<module> RdStationAssociator </module>
<module> RdEventInitializer </module>

<!-- Converts electric field vector into voltage-response of antenna. -->
<module> RdAntennaStationToChannelConverter </module>

<!-- Applies antenna gain (LNA, cable, filter-amplifier). -->
<module> RdChannelResponseIncorporator </module>

<!-- Resamples & crops the simulated traces according to detector spec. -->
<module> RdChannelResampler </module>
<module> RdChannelTimeSeriesClipper </module>

<!-- Converts (analog) voltage trace into ADC counts -->
<module> RdChannelVoltageToADCConverter </module>

<!-- Apply a time jitter to mimic uncertainties in the
      (GPS) timing of the different stations. -->
<module> RdTimeJitterAdder </module>

<!-- Adds (measured) noise traces (ADC counts) to simulated signals. -->
<module> RdASCIINoiseImporterRD </module>

<!-- Radio reconstruction -->
<!-- Converts ADC counts into a voltage and upsamples trace. -->
<module> RdChannelADCToVoltageConverter </module>
<module> RdChannelUpsampler </module>

<!-- Remove the "baseline" of the measured traces. -->
<module> RdChannelPedestalRemover </module>

<!-- Remove the antenna gain (LNA, cable, filter-amplifier)
      from the signal trace. -->
<module> RdChannelResponseIncorporator </module>

<!-- Apply a Hann-window to "smooth" the edges of the trace. -->
<module> RdChannelTimeSeriesTaperer </module>

<!-- Convert the signal at the antenna output into a
      electric field vector. -->
<module> RdAntennaChannelToStationConverter </module>

<!-- Derive signal quantities from the electric field vector
      (energy fluence, signal time, SNR, ...). -->
<module> RdStationSignalReconstructor </module>

<!-- Perform a radio-based air shower reconstruction -->
<module> RdSphericalFit </module>
<module> RdHASLDFitter </module>

```

Listing D.2: Relevant configuration of the RdHASLDFitter used in this work (not the default config).

```

<!-- Skip event with too few signal stations. -->
<MinimumNumberOfStations> 5 </MinimumNumberOfStations>

<!-- Fit geometrical distance to Xmax (also requires at least 3 signal stations)-->
<FitDistanceToXmax> 1 </FitDistanceToXmax>

<!-- If the core position in the shower plane (also requires at least 4 (3)
      signal stations (without FitDistanceToXmax)) -->
<FitCore> 1 </FitCore>

<!-- The following two options allow to add "fudge" factors to the uncertainty
      in f_vxB in quadrature. This might help to mitigate the effect of artificial
      thinning artifacts on the simulated signals. -->
<!-- Add the lowest signal (f_vxB, classified as signal, e.g., with a SNR > 10)
      to uncertainty -->
<AddLowestSignalAsError> 0 </AddLowestSignalAsError>
<!-- Add a fraction (= value given here) of the parameterized max. geomagnetic
      energy fluence f_geo to the uncertainty in f_vxB. The parametrization is
      based on the MC energy and geometric distance to Xmax -->
<AddRelativeMaxSignalError> 0 </AddRelativeMaxSignalError>

<!-- Choose Xmax estimator to derive a start value to fit distance to Xmax:
      "MC": true value from SimShower
      "Param": Use param. of Xmax with SD energy.
               utl::PhysicalFunctions::XmaxParam::Mean, 50/50 proton iron mix.
               The hadronic interaction model is specified below.
      "Average": Fixed value of 750 g/cm2 -->
<XmaxEstimator> Param </XmaxEstimator>

<!-- Specify hadronic function for XmaxEstimator:
      Options: "Sibyll-2.3d", "EPOS-LHC", "QGSJETII-04". -->
<HadronicInteractionModel> QGSJETII-04 </HadronicInteractionModel>

<!-- Direction used in fit LDF:
      "Reference": ReferenceDirection specified in the RdEventInitializer,
      "Rd": As fitted by a radio wavefront model (e.g., RdSphericalFit) -->
<FitDirection> Rd </FitDirection>

<!-- If true, saturated stations are included in the fit.
      Be careful that does not mean that they are treated correctly. -->
<UseSaturatedStations> 0 </UseSaturatedStations>

<!-- Use parameterization of charge-excess fraction to estimate geomagnetic emission.
      If false, the emission in the vxvxB polarization is used to estimate
      the strength of charge-excess emission and thus the geomagnetic emission. -->
<UseParameterizationToDisentanglePolarisation> 1
</UseParameterizationToDisentanglePolarisation>

<!-- Use "soft" instead of "hard" exponent in LDF model (gauss+sigmoid model) -->
<UseSoftExponent> 1 </UseSoftExponent>

```

E. Appendix to Chap. 9

E.1. Selection for the discrimination between proton- and iron-induced air showers

An example for the energy spectrum of a reweighted event set composed solely out of protons and iron nuclei is shown in Fig. E.1 (*left*). The event set which contains 21812 events is based on only 3483 simulated proton- and iron-induced air showers with an energy above $10^{18.6}$ eV and the high-energy hadronic interaction model QGSJetII-04. Most of those events will be rejected in the subsequent shower selection which is detailed in Tab. E.1. The selection has a higher efficiency for proton- than for iron induced air showers. This is also apparent for 1000 random event sets, cf. Fig. E.1 (*right*). However, it should be noted that those event sets are not independent of each other as they share a lot of the same lower energy events. Therefore, it can not be excluded that the difference between proton and iron primaries is a statistical fluctuation due to the limited number of simulated air showers. For showers simulated with Sibyll-2.3d, such a difference is not found.

Table E.1.: Selection for proton and iron primaries for a random event sample following the RD energy spectrum.

	p	Fe	All
	10995	10817	21812
SdRecLvl ≥ 3	9650 (87.8%)	10725 (99.1%)	20375 (93.4%)
T4 & T5Has	9626 (99.8%)	10689 (99.7%)	20315 (99.7%)
$n_{\text{cand}} \geq 4$	9626 (100.0%)	10689 (100.0%)	20315 (100.0%)
$N_{19} \geq 0.6$	6187 (64.3%)	9529 (89.1%)	15716 (77.4%)
$\sigma_{N_{19}} < 50.0\%$	6187 (100.0%)	9522 (99.9%)	15709 (100.0%)
min. RD signal stations: 5	3279 (53.0%)	5660 (59.4%)	8939 (56.9%)
Has RD spherical fit	3244 (98.9%)	5518 (97.5%)	8762 (98.0%)
$\alpha_{\text{RD}} > 20.0^\circ$	3232 (99.6%)	5512 (99.9%)	8744 (99.8%)
$\theta_{\text{RD}} \geq 70.0^\circ$	3103 (96.0%)	5242 (95.1%)	8345 (95.4%)
$\sigma_{\theta_{\text{RD}}} < 0.3^\circ$	3102 (100.0%)	5223 (99.6%)	8325 (99.8%)
Has RD rec. LDF	3095 (99.8%)	5223 (100.0%)	8318 (99.9%)
$\lg(E_{\text{em}} / \text{eV}) \geq 19.0$	1015 (32.8%)	932 (17.8%)	1947 (23.4%)
$n_{\text{stat}}(r < 1.5r_0) > 0$	1014 (99.9%)	918 (98.5%)	1932 (99.2%)
$\sigma_{E_{\text{em}}} < 30.0\%$	1006 (99.2%)	918 (100.0%)	1924 (99.6%)
$\chi^2 / \text{ndf} < 10.0$	1006 (100.0%)	915 (99.7%)	1921 (99.8%)
fitted core at limit (1000m)	1005 (99.9%)	915 (100.0%)	1920 (99.9%)
$\angle(\hat{a}_{\text{RD}}, \hat{a}_{\text{WCD}}) < 1.50^\circ$	1005 (100.0%)	915 (100.0%)	1920 (100.0%)
Total	1005 (9.1%)	915 (8.5%)	1920 (8.8%)

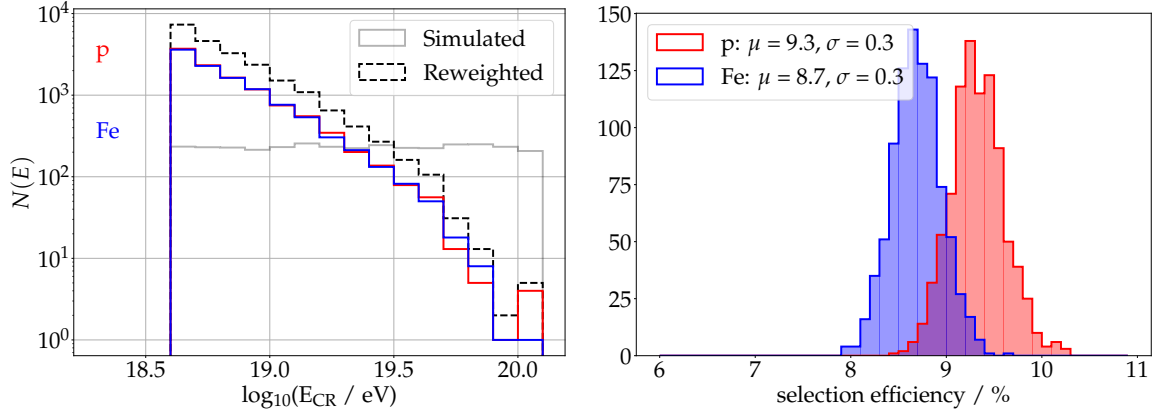


Figure E.1.: *Left:* Random event sample for a 50%-50% proton-iron mix following the expected RD energy spectrum (before any selection). In each primary and energy bin, the expected number of particles is drawn assuming Poisson fluctuations. *Right:* Proton and iron selection efficiency for 1000 random event samples after a selection as detailed in Tab. E.1.

E.2. Proton and iron separation with the depth of the shower maximum

To estimate the separation of proton- and iron-induced air showers with X_{\max} , we use the parameterization of the mean and standard deviation for different primaries and hadronic interaction models from Ref. [173]. The X_{\max} distributions for proton and iron, as predicted by the 3 different post-LHC hadronic interaction models are shown in Fig. E.2. The solid colored lines represent the $\langle X_{\max} \rangle$, the color-shaded areas $\sigma_{X_{\max}}$. To evaluate the separation between both primaries we adopt the figure of merit from Eq. (9.6). To account for a finite detector resolution, we add a σ_{det} in quadrature to $\sigma_{X_{\max}}$ for both primaries. The FOMs for different detector resolution scenarios are indicated by the black lines. It is apparent that the separation between proton and iron depends on the hadronic interaction model and the assumed detector resolution. The separation predicted with QGSJetII-04 is in general worse than with Sibyll-2.3d or EPOS-LHC. With a resolution of $\sigma_{\text{det}} = 15 \text{ g cm}^{-2}$, a $\text{FOM} \approx 1.5$ is obtained for Sibyll-2.3d depending only slightly on the energy.

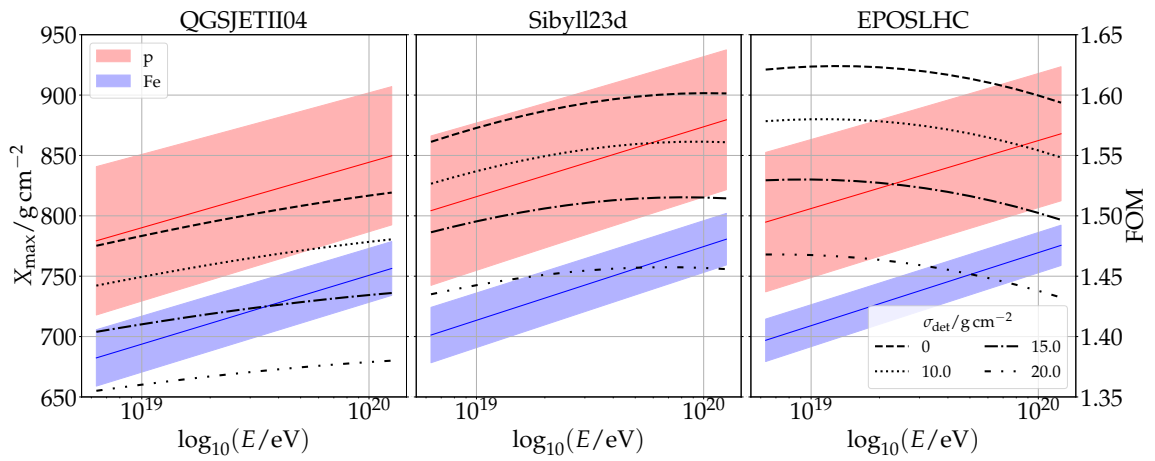


Figure E.2.: X_{\max} distributions for proton- and iron-induced air showers as a function of the energy for different high-energy hadronic interaction models. The separation between both primaries as a function of the energy is given by the *figure of merit* FOM (Eq. 9.6) for different assumptions of a Gaussian detector resolution by the black lines.

F. List of Publications

Published articles with significant personal contributions related to work performed in the context of this Ph.D. project.

Peer-reviewed journal article

F. Schlüter and T. Huege

"Expected performance of air-shower measurements with the radio-interferometric technique" [JINST 16 P07048 \(2021\)](#)

The author of this thesis is the corresponding author of this publication. The work was primarily performed by the author of this thesis. The text was written by the author of this thesis and was revised and copy-edited by the co-author of the publication.

F. Schlüter, M. Gottowik, T. Huege, and J. Rautenberg

"Refractive displacement of the radio-emission footprint of inclined air showers simulated with CoREAS" [Eur. Phys. J. C 80, 643 \(2020\)](#)

The author of this thesis is the corresponding author of this publication. The work was performed, and the text was written by him and M. Gottowik. The publication was revised and copy-edited by the other co-authors of the publication.

Unreviewed articles and conference proceedings

A. Coleman et al.

"Ultra-High-Energy Cosmic Rays: The Intersection of the Cosmic and Energy Frontiers" [arXiv:2205.05845](#)

The author of this thesis has contributed to this publication with a short review of the application of interferometric techniques for the detection of ultra-high-energy cosmic ray.

F. Schlüter and T. Huege

"Signal model and event reconstruction for the radio detection of inclined air showers" [arXiv:2203.04364](#) (Publication to JCAP in process)

The author of this thesis is the corresponding author of this publication. The work was primarily performed by the author of this thesis. The text was written by the author of this thesis and was revised and copy-edited by the co-author of the publication.

F. Schlüter for the Pierre Auger Collaboration

"Expected performance of the AugerPrime Radio Detector"

[PoS \(ICRC21\) 262](#)

The author of this thesis is the corresponding author of this publication. The work was primarily performed by the author of this thesis. The text was written by the author of this thesis and was revised and copy-edited by the co-author of the publication.

F. Schlüter and T. Huege

"Expected performance of interferometric air-shower measurements with radio antennas"

[PoS \(ICRC21\) 228](#)

The author of this thesis is the corresponding author of this publication. The work was primarily performed by the author of this thesis. The text was written by the author of this thesis and was revised and copy-edited by the co-author of the publication.

T. Huege and F. Schlüter

"Reconstructing inclined extensive air showers from radio measurements"

[PoS \(ICRC2021\) 209](#)

The author of this thesis performed the analysis and contributed figures to this publication. The text was written by the first author.

M. Gottowik, F. Schlüter, T. Huege and J. Rautenberg

"CoREAS simulations of inclined air showers predict refractive displacement of the radio-emission footprint"

[PoS \(ICRC2021\) 277](#)

The author of this thesis contributed to the analysis and figures of this publication. The text was written by the first author.

T. Huege, F. Schlüter and L. Brenk

"Symmetrizing the signal distribution of radio emission from inclined air showers"

[PoS \(ICRC2019\) 294](#)

The author of this thesis performed the analysis and contributed figures to this publication. The text was written by the first author.

T. Huege, L. Brenk and F. Schlüter

"A Rotationally Symmetric Lateral Distribution Function for Radio Emission from Inclined Air Showers"

[EPJ Web of Conferences 216, 03009 \(2019\)](#)

The author of this thesis contributed to this publication with copy-editing.

Internal publications

F. Schlüter and T. Huege

"Evaluating the Potential of radio-interferometric measurements with the Auger Radio Detectors" [GAP2020-055 \(2020\)](#), [Internal Document of the Pierre Auger Collaboration](#) *The author of this thesis is the corresponding author of this publication. The work was primarily performed by the author of this thesis. The text was written by the author of this thesis and was revised and copy-edited by the co-author of the publication.*

T. Huege, Julian Rautenberg, and Jörg Horandel

"The science case for the Radio Upgrade of the Pierre Auger Observatory" [GAP2020-004 \(2020\)](#), [Internal Document of the Pierre Auger Collaboration](#) *The author of this thesis has contributed to this publication with a study about the mass composition sensitivity of the Radio Upgrade. The text was revised and copy-edited by the author of this thesis*

G. Acknowledgment 🐾

First of all, I would like to thank Tim: Not only has it been a pleasure to work with you over the past almost four years, but you also had the confidence in me to offer me the job. I have learned and grown a lot working with you. Your motivation to pursue an academic career has reinforced my decision. So, a big thank you, Tim!

Of course, I would also like to thank my two supervisors, Ralph and Diego. Ralph, I would like to thank you for your great recognition and support of my work, not only in terms of my PhD project, but also in terms of my work in the collaboration. It has not only allowed me to assert myself as a budding scientist, but has also helped me to prepare myself for what is to come. Diego, thank you for our sometimes heated discussions, especially in the last months of my PhD.

To my good friend David, thank you for countless hours of discussions about physics, God and the world, for your advice and opinions, especially in difficult times. To my shifter buddy Alan, thank you for the great shifter and numerous (radio) discussions.

To my Auger Radio colleagues out there, especially Bjarni, Fabrizia and Marvin: it was always a fun and enjoyable time with you, especially at the workshops and collaboration meetings, thanks for that! Even if it's a big shame that I couldn't convince you of the superior taste of Kölsch and the perfectly sized glasses. Thanks also to all my other Auger colleagues. Auger is a really cool experiment, in no small part because of the collaboration, and it was a great experience working with you all and meeting you in Malargüe. Many thanks to Ana (and Joaquin) for translating my resume.

Last but not least, a big thank you to my family and friends and especially to my parents for putting up with my temper during (stressful) times. The last few years have been quite a ride with ups and downs. To everyone who stood by my side during this time, a big thank you!

Bibliography

- [1] John Linsley. “Evidence for a primary cosmic-ray particle with energy 10^{20} eV”. In: *Phys. Rev. Lett.* 10 (1963), pp. 146–148. DOI: [10.1103/PhysRevLett.10.146](https://doi.org/10.1103/PhysRevLett.10.146).
- [2] Thomas K. Gaisser, Ralph Engel, and Elisa Resconi. *Cosmic Rays and Particle Physics*. 2nd ed. Cambridge University Press, 2016. DOI: [10.1017/CB09781139192194](https://doi.org/10.1017/CB09781139192194).
- [3] Alexander Aab et al. “The Pierre Auger Cosmic Ray Observatory”. In: *Nucl. Instrum. Meth. A* 798 (2015), pp. 172–213. DOI: [10.1016/j.nima.2015.06.058](https://doi.org/10.1016/j.nima.2015.06.058). arXiv: [1502.01323](https://arxiv.org/abs/1502.01323) [[astro-ph.IM](#)].
- [4] A. Coleman et al. “Ultra-High-Energy Cosmic Rays: The Intersection of the Cosmic and Energy Frontiers”. In: (May 2022). arXiv: [2205.05845](https://arxiv.org/abs/2205.05845) [[astro-ph.HE](#)].
- [5] Alexander Aab et al. “The Pierre Auger Observatory Upgrade - Preliminary Design Report”. In: (2016). arXiv: [1604.03637](https://arxiv.org/abs/1604.03637) [[astro-ph.IM](#)].
- [6] Bjarni Pont. “A Large Radio Detector at the Pierre Auger Observatory - Measuring the Properties of Cosmic Rays up to the Highest Energies”. In: *PoS ICRC2019* (2019), p. 395. DOI: [10.22323/1.358.0395](https://doi.org/10.22323/1.358.0395).
- [7] E. M. Holt, F. G. Schröder, and A. Haungs. “Enhancing the cosmic-ray mass sensitivity of air-shower arrays by combining radio and muon detectors”. In: *Eur. Phys. J. C* 79.5 (2019), p. 371. DOI: [10.1140/epjc/s10052-019-6859-4](https://doi.org/10.1140/epjc/s10052-019-6859-4). arXiv: [1905.01409](https://arxiv.org/abs/1905.01409) [[astro-ph.HE](#)].
- [8] S. P. Swordy. “The Energy Spectra and Anisotropies of Cosmic Rays”. In: *The Astrophysics of Galactic Cosmic Rays*. Ed. by Roland Diehl et al. Dordrecht: Springer Netherlands, 2001, pp. 85–94. ISBN: 978-94-017-3239-0.
- [9] Oscar Adriani et al. “An anomalous positron abundance in cosmic rays with energies 1.5–100 GeV”. In: *Nature* 458 (2009), pp. 607–609. DOI: [10.1038/nature07942](https://doi.org/10.1038/nature07942). arXiv: [0810.4995](https://arxiv.org/abs/0810.4995) [[astro-ph](#)].
- [10] M. Aguilar et al. “First Result from the Alpha Magnetic Spectrometer on the International Space Station: Precision Measurement of the Positron Fraction in Primary Cosmic Rays of 0.5–350 GeV”. In: *Phys. Rev. Lett.* 110 (2013), p. 141102. DOI: [10.1103/PhysRevLett.110.141102](https://doi.org/10.1103/PhysRevLett.110.141102).
- [11] Victor F. Hess. “Über Beobachtungen der durchdringenden Strahlung bei sieben Freiballonfahrten”. In: *Phys. Z.* 13 (1912), pp. 1084–1091.
- [12] A. Aab et al. “Depth of maximum of air-shower profiles at the Pierre Auger Observatory. II. Composition implications”. In: *Phys. Rev. D* 90.12 (2014), p. 122006. DOI: [10.1103/PhysRevD.90.122006](https://doi.org/10.1103/PhysRevD.90.122006). arXiv: [1409.5083](https://arxiv.org/abs/1409.5083) [[astro-ph.HE](#)].

-
- [13] Alexander Aab et al. “Features of the Energy Spectrum of Cosmic Rays above 2.5×10^{18} eV Using the Pierre Auger Observatory”. In: *Phys. Rev. Lett.* 125.12 (2020), p. 121106. DOI: [10.1103/PhysRevLett.125.121106](https://doi.org/10.1103/PhysRevLett.125.121106). arXiv: [2008.06488](https://arxiv.org/abs/2008.06488) (astro-ph.HE).
- [14] Alexander Aab et al. “Measurement of the Fluctuations in the Number of Muons in Extensive Air Showers with the Pierre Auger Observatory”. In: *Phys. Rev. Lett.* 126.15 (2021), p. 152002. DOI: [10.1103/PierreAuger:2021qsd](https://doi.org/10.1103/PierreAuger:2021qsd). arXiv: [2102.07797](https://arxiv.org/abs/2102.07797) [hep-ex].
- [15] Vitor de Souza. “Testing the agreement between the X_{\max} distributions measured by the Pierre Auger and Telescope Array Observatories”. In: *PoS ICRC2017* (2018), p. 522. DOI: [10.22323/1.301.0522](https://doi.org/10.22323/1.301.0522).
- [16] Rasha Abbasi et al. “Joint analysis of the energy spectrum of ultra-high-energy cosmic rays as measured at the Pierre Auger Observatory and the Telescope Array”. In: *PoS ICRC2021* (2021), p. 337. DOI: [10.22323/1.395.0337](https://doi.org/10.22323/1.395.0337).
- [17] A. A. Watson. “Further evidence for an increase of the mean mass of the highest-energy cosmic-rays with energy”. In: *JHEAp* 33 (2022), p. 130. DOI: [10.1016/j.jheap.2021.11.001](https://doi.org/10.1016/j.jheap.2021.11.001). arXiv: [2112.06525](https://arxiv.org/abs/2112.06525) [astro-ph.HE].
- [18] P.A. Zyla et al. “Review of Particle Physics”. In: *PTEP* 2020.8 (2020), p. 083C01. DOI: [10.1093/ptep/ptaa104](https://doi.org/10.1093/ptep/ptaa104).
- [19] Alexander Aab et al. “Measurement of the cosmic-ray energy spectrum above 2.5×10^{18} eV using the Pierre Auger Observatory”. In: *Phys. Rev. D* 102.6 (2020), p. 062005. DOI: [10.1103/PhysRevD.102.062005](https://doi.org/10.1103/PhysRevD.102.062005). arXiv: [2008.06486](https://arxiv.org/abs/2008.06486) [astro-ph.HE].
- [20] A. Aab et al. “Large-scale cosmic-ray anisotropies above 4 EeV measured by the Pierre Auger Observatory”. In: *Astrophys. J.* 868.1 (2018), p. 4. DOI: [10.3847/1538-4357/aae689](https://doi.org/10.3847/1538-4357/aae689). arXiv: [1808.03579](https://arxiv.org/abs/1808.03579) [astro-ph.HE].
- [21] A. M. Hillas. “Can diffusive shock acceleration in supernova remnants account for high-energy galactic cosmic rays?” In: *J. Phys. G* 31 (2005), R95–R131. DOI: [10.1088/0954-3899/31/5/R02](https://doi.org/10.1088/0954-3899/31/5/R02).
- [22] Veniamin Berezhinsky, A. Z. Gazizov, and S. I. Grigorieva. “Dip in UHECR spectrum as signature of proton interaction with CMB”. In: *Phys. Lett. B* 612 (2005), pp. 147–153. DOI: [10.1016/j.physletb.2005.02.058](https://doi.org/10.1016/j.physletb.2005.02.058). arXiv: [astro-ph/0502550](https://arxiv.org/abs/astro-ph/0502550).
- [23] Alexey Yushkov. “Mass Composition of Cosmic Rays with Energies above $10^{17.2}$ eV from the Hybrid Data of the Pierre Auger Observatory”. In: *PoS ICRC2019* (2020), p. 482. DOI: [10.22323/1.358.0482](https://doi.org/10.22323/1.358.0482).
- [24] Alexander Aab et al. “Muons in Air Showers at the Pierre Auger Observatory: Mean Number in Highly Inclined Events”. In: *Phys. Rev. D* 91.3 (2015). [Erratum: *Phys.Rev.D* 91, 059901 (2015)], p. 032003. DOI: [10.1103/PhysRevD.91.032003](https://doi.org/10.1103/PhysRevD.91.032003). arXiv: [1408.1421](https://arxiv.org/abs/1408.1421) [astro-ph.HE].

- [25] Alexander Aab et al. “Depth of Maximum of Air-Shower Profiles at the Pierre Auger Observatory: Measurements at Energies above $10^{17.8}$ eV”. In: *Phys. Rev. D* 90.12 (2014), p. 122005. DOI: [10.1103/PhysRevD.90.122005](https://doi.org/10.1103/PhysRevD.90.122005). arXiv: [1409.4809](https://arxiv.org/abs/1409.4809) [astro-ph.HE].
- [26] P. A. Bezyazeev et al. “Reconstruction of cosmic ray air showers with Tunka-Rex data using template fitting of radio pulses”. In: *Phys. Rev. D* 97.12 (2018), p. 122004. DOI: [10.1103/PhysRevD.97.122004](https://doi.org/10.1103/PhysRevD.97.122004). arXiv: [1803.06862](https://arxiv.org/abs/1803.06862) [astro-ph.IM].
- [27] A. Corstanje et al. “Depth of shower maximum and mass composition of cosmic rays from 50 PeV to 2 EeV measured with the LOFAR radio telescope”. In: *Phys. Rev. D* 103.10 (2021), p. 102006. DOI: [10.1103/PhysRevD.103.102006](https://doi.org/10.1103/PhysRevD.103.102006). arXiv: [2103.12549](https://arxiv.org/abs/2103.12549) [astro-ph.HE].
- [28] B. Pont on behalf of The Pierre Auger Collaboration. “The depth of the shower maximum of air showers measured with AERA”. In: *PoS ICRC2021* (2021), p. 387. DOI: [10.22323/1.395.0387](https://doi.org/10.22323/1.395.0387).
- [29] W. D. Apel et al. “Ankle-like Feature in the Energy Spectrum of Light Elements of Cosmic Rays Observed with KASCADE-Grande”. In: *Phys. Rev. D* 87 (2013), p. 081101. DOI: [10.1103/PhysRevD.87.081101](https://doi.org/10.1103/PhysRevD.87.081101). arXiv: [1304.7114](https://arxiv.org/abs/1304.7114) [astro-ph.HE].
- [30] Ewa M. Holt. “Estimating the mass of cosmic rays by combining radio and muon measurements”. In: *EPJ Web Conf.* 216 (2019). Ed. by G. Riccobene et al., p. 02002. DOI: [10.1051/epjconf/201921602002](https://doi.org/10.1051/epjconf/201921602002).
- [31] Dennis Soldin. “Update on the Combined Analysis of Muon Measurements from Nine Air Shower Experiments”. In: *PoS ICRC2021* (2021), p. 349. DOI: [10.22323/1.395.0349](https://doi.org/10.22323/1.395.0349). arXiv: [2108.08341](https://arxiv.org/abs/2108.08341) [astro-ph.HE].
- [32] Johannes Albrecht et al. “The Muon Puzzle in cosmic-ray induced air showers and its connection to the Large Hadron Collider”. In: *Astrophys. Space Sci.* 367.3 (2022), p. 27. DOI: [10.1007/s10509-022-04054-5](https://doi.org/10.1007/s10509-022-04054-5). arXiv: [2105.06148](https://arxiv.org/abs/2105.06148) [astro-ph.HE].
- [33] S. Ostapchenko. “Nonlinear screening effects in high energy hadronic interactions”. In: *Phys. Rev. D* 74.1 (2006), p. 014026. DOI: [10.1103/PhysRevD.74.014026](https://doi.org/10.1103/PhysRevD.74.014026). arXiv: [hep-ph/0505259](https://arxiv.org/abs/hep-ph/0505259).
- [34] Eun-Joo Ahn et al. “Cosmic ray interaction event generator SIBYLL 2.1”. In: *Phys. Rev. D* 80 (2009), p. 094003. DOI: [10.1103/PhysRevD.80.094003](https://doi.org/10.1103/PhysRevD.80.094003). arXiv: [0906.4113](https://arxiv.org/abs/0906.4113) [hep-ph].
- [35] T. Pierog and K. Werner. “EPOS Model and Ultra High Energy Cosmic Rays”. In: *Nucl. Phys. B Proc. Suppl.* 196 (2009). Ed. by Jean-Noël Capdevielle, Ralph Engel, and Bryan Pattison, pp. 102–105. DOI: [10.1016/j.nuclphysbps.2009.09.017](https://doi.org/10.1016/j.nuclphysbps.2009.09.017). arXiv: [0905.1198](https://arxiv.org/abs/0905.1198) [hep-ph].
- [36] J. Biteau on behalf of The Pierre Auger Collaboration. “The ultra-high-energy cosmic-ray sky above 32 EeV viewed from the Pierre Auger Observatory”. In: *PoS ICRC2021* (2021), p. 307. DOI: [10.22323/1.395.0307](https://doi.org/10.22323/1.395.0307).

-
- [37] R. de Almeida on behalf of The Pierre Auger Collaboration. “Large-scale and multipolar anisotropies of cosmic rays detected at the Pierre Auger Observatory with energies above 4 EeV”. In: *PoS ICRC2021* (2021), p. 335. DOI: [10.22323/1.395.0335](https://doi.org/10.22323/1.395.0335).
- [38] E. Mayotte on behalf of The Pierre Auger Collaboration. “Indication of a mass-dependent anisotropy above $10^{18.7}$ eV in the hybrid data of the Pierre Auger Observatory”. In: *PoS ICRC2021* (2021), p. 321. DOI: [10.22323/1.395.0321](https://doi.org/10.22323/1.395.0321).
- [39] Kenneth Greisen. “End to the cosmic ray spectrum?” In: *Phys. Rev. Lett.* 16 (1966), pp. 748–750. DOI: [10.1103/PhysRevLett.16.748](https://doi.org/10.1103/PhysRevLett.16.748).
- [40] G. T. Zatsepin and V. A. Kuzmin. “Upper limit of the spectrum of cosmic rays”. In: *JETP Lett.* 4 (1966), pp. 78–80.
- [41] R. Aloisio et al. “Cosmogenic neutrinos and ultra-high energy cosmic ray models”. In: *JCAP* 10 (2015), p. 006. DOI: [10.1088/1475-7516/2015/10/006](https://doi.org/10.1088/1475-7516/2015/10/006). arXiv: [1505.04020](https://arxiv.org/abs/1505.04020) [astro-ph.HE].
- [42] R. Alves Batista et al. “Effects of uncertainties in simulations of extragalactic UHECR propagation, using CRPropa and SimProp”. In: *JCAP* 10 (2015), p. 063. DOI: [10.1088/1475-7516/2015/10/063](https://doi.org/10.1088/1475-7516/2015/10/063). arXiv: [1508.01824](https://arxiv.org/abs/1508.01824) [astro-ph.HE].
- [43] R. Aloisio et al. “SimProp: a Simulation Code for Ultra High Energy Cosmic Ray Propagation”. In: *JCAP* 10 (2012), p. 007. DOI: [10.1088/1475-7516/2012/10/007](https://doi.org/10.1088/1475-7516/2012/10/007). arXiv: [1204.2970](https://arxiv.org/abs/1204.2970) [astro-ph.HE].
- [44] Ariel Bridgeman. “Determining the Mass Composition of Ultra-high Energy Cosmic Rays Using Air Shower Universality”. PhD thesis. Universität Karlsruhe, 2018. URL: <https://inspirehep.net/files/fa126c087b8f6ea3a50c6aa3b7cbdb64>.
- [45] Ralph Engel, Dieter Heck, and Tanguy Pierog. “Extensive air showers and hadronic interactions at high energy”. In: *Ann. Rev. Nucl. Part. Sci.* 61 (2011), pp. 467–489. DOI: [10.1146/annurev.nucl.012809.104544](https://doi.org/10.1146/annurev.nucl.012809.104544).
- [46] D. Heck et al. “CORSIKA: A Monte Carlo Code to Simulate Extensive Air Showers”. In: *FZKA Report 6019, Forschungszentrum Karlsruhe* (1998). URL: <http://digbib.ubka.uni-karlsruhe.de/volltexte/fzk/6019/6019.pdf>.
- [47] W. Heitler. *The quantum theory of radiation*. Vol. 5. International Series of Monographs on Physics. Oxford: Oxford University Press, 1936.
- [48] J. Matthews. “A Heitler model of extensive air showers”. In: *Astropart. Phys.* 22 (2005), pp. 387–397. DOI: [10.1016/j.astropartphys.2004.09.003](https://doi.org/10.1016/j.astropartphys.2004.09.003).
- [49] T. Huege. “Radio detection of cosmic ray air showers in the digital era”. In: *Phys. Rept.* 620 (2016), pp. 1–52. DOI: [10.1016/j.physrep.2016.02.001](https://doi.org/10.1016/j.physrep.2016.02.001).
- [50] P. Allison et al. “Performance of two Askaryan Radio Array stations and first results in the search for ultrahigh energy neutrinos”. In: *Phys. Rev. D* 93.8 (2016), p. 082003. DOI: [10.1103/PhysRevD.93.082003](https://doi.org/10.1103/PhysRevD.93.082003). arXiv: [1507.08991](https://arxiv.org/abs/1507.08991) [astro-ph.HE].
- [51] S. W. Barwick et al. “Radio detection of air showers with the ARIANNA experiment on the Ross Ice Shelf”. In: *Astropart. Phys.* 90 (2017), pp. 50–68. DOI: [10.1016/j.astropartphys.2017.02.003](https://doi.org/10.1016/j.astropartphys.2017.02.003). arXiv: [1612.04473](https://arxiv.org/abs/1612.04473) [astro-ph.IM].

- [52] P. W. Gorham et al. “Constraints on the diffuse high-energy neutrino flux from the third flight of ANITA”. In: *Phys. Rev. D* 98.2 (2018), p. 022001. DOI: [10.1103/PhysRevD.98.022001](https://doi.org/10.1103/PhysRevD.98.022001). arXiv: [1803.02719](https://arxiv.org/abs/1803.02719) [[astro-ph.HE](#)].
- [53] J. A. Aguilar et al. “Design and Sensitivity of the Radio Neutrino Observatory in Greenland (RNO-G)”. In: *JINST* 16.03 (2021), P03025. DOI: [10.1088/1748-0221/16/03/P03025](https://doi.org/10.1088/1748-0221/16/03/P03025). arXiv: [2010.12279](https://arxiv.org/abs/2010.12279) [[astro-ph.IM](#)].
- [54] Clancy W. James. “Nature of radio-wave radiation from particle cascades”. In: *Phys. Rev. D* 105.2 (2022), p. 023014. DOI: [10.1103/PhysRevD.105.023014](https://doi.org/10.1103/PhysRevD.105.023014). arXiv: [2201.01298](https://arxiv.org/abs/2201.01298) [[astro-ph.HE](#)].
- [55] F. G. Schröder. “Radio detection of Cosmic-Ray Air Showers and High-Energy Neutrinos”. In: *Prog. Part. Nucl. Phys.* 93 (2017), pp. 1–68. DOI: [10.1016/j.pnpnp.2016.12.002](https://doi.org/10.1016/j.pnpnp.2016.12.002). arXiv: [1607.08781](https://arxiv.org/abs/1607.08781) [[astro-ph.IM](#)].
- [56] T. Huege, M. Ludwig, and C. W. James. “Simulating radio emission from air showers with CoREAS”. In: *AIP Conf. Proc.* 1535.1 (2013), p. 128. DOI: [10.1063/1.4807534](https://doi.org/10.1063/1.4807534).
- [57] E. Zas, F. Halzen, and T. Stanev. “Electromagnetic pulses from high-energy showers: Implications for neutrino detection”. In: *Phys. Rev. D* 45 (1992), pp. 362–376. DOI: [10.1103/PhysRevD.45.362](https://doi.org/10.1103/PhysRevD.45.362).
- [58] Jaime Alvarez-Muniz, Andres Romero-Wolf, and Enrique Zas. “Cherenkov radio pulses from electromagnetic showers in the time-domain”. In: *Phys. Rev. D* 81 (2010), p. 123009. DOI: [10.1103/PhysRevD.81.123009](https://doi.org/10.1103/PhysRevD.81.123009). arXiv: [1002.3873](https://arxiv.org/abs/1002.3873) [[astro-ph.HE](#)].
- [59] M. Ludwig and T. Huege. “REAS3: Monte Carlo simulations of radio emission from cosmic ray air showers using an ‘end-point’ formalism”. In: *Astropart. Phys.* 34 (2011), pp. 438–446. DOI: [10.1016/j.astropartphys.2010.10.012](https://doi.org/10.1016/j.astropartphys.2010.10.012). arXiv: [1010.5343](https://arxiv.org/abs/1010.5343) [[astro-ph.HE](#)].
- [60] C. W. James et al. “General description of electromagnetic radiation processes based on instantaneous charge acceleration in ‘endpoints’”. In: *Phys. Rev. E* 84 (2011), p. 056602. DOI: [10.1103/PhysRevE.84.056602](https://doi.org/10.1103/PhysRevE.84.056602). arXiv: [1007.4146](https://arxiv.org/abs/1007.4146) (physics.class-ph).
- [61] Konstantin Belov. “Radio emission from Air Showers. Comparison of theoretical approaches”. In: *AIP Conf. Proc.* 1535.1 (2013). Ed. by Robert Lahmann et al., p. 157. DOI: [10.1063/1.4807540](https://doi.org/10.1063/1.4807540). arXiv: [1303.3313](https://arxiv.org/abs/1303.3313) [[astro-ph.HE](#)].
- [62] K. Bechtol et al. “SLAC T-510 experiment for radio emission from particle showers: Detailed simulation study and interpretation”. In: *Phys. Rev. D* 105.6 (2022), p. 063025. DOI: [10.1103/PhysRevD.105.063025](https://doi.org/10.1103/PhysRevD.105.063025). arXiv: [2111.04334](https://arxiv.org/abs/2111.04334) [[astro-ph.IM](#)].
- [63] S. Buitink et al. “Method for high precision reconstruction of air shower X_{max} using two-dimensional radio intensity profiles”. In: *Phys. Rev. D* 90.8 (2014), p. 082003. DOI: [10.1103/PhysRevD.90.082003](https://doi.org/10.1103/PhysRevD.90.082003). arXiv: [1408.7001](https://arxiv.org/abs/1408.7001) [[astro-ph.IM](#)].
- [64] O. Scholten, K. Werner, and F. Ruydi. “A Macroscopic Description of Coherent Geo-Magnetic Radiation from Cosmic Ray Air Showers”. In: *Astropart. Phys.* 29 (2008), pp. 94–103. DOI: [10.1016/j.astropartphys.2007.11.012](https://doi.org/10.1016/j.astropartphys.2007.11.012). arXiv: [0709.2872](https://arxiv.org/abs/0709.2872) [[astro-ph](#)].

-
- [65] K. D. de Vries et al. “Coherent Cherenkov Radiation from Cosmic-Ray-Induced Air Showers”. In: *Phys. Rev. Lett.* 107 (2011), p. 061101. DOI: [10.1103/PhysRevLett.107.061101](https://doi.org/10.1103/PhysRevLett.107.061101). arXiv: [1107.0665](https://arxiv.org/abs/1107.0665) [astro-ph.HE].
- [66] Jens Christian Glaser. “Absolute energy calibration of the Pierre Auger observatory using radio emission of extensive air showers”. PhD thesis. RWTH Aachen U., 2017. DOI: [10.18154/RWTH-2017-02960](https://doi.org/10.18154/RWTH-2017-02960).
- [67] G. A. Askar’yan. “Excess negative charge of an electron-photon shower and its coherent radio emission”. In: *Zh. Eksp. Teor. Fiz.* 41 (1961), pp. 616–618. URL: <https://inspirehep.net/files/50aa3b9f4a1271a1476462d1635d96a7>.
- [68] Darko Verberic. Feb. 7, 2022. URL: https://web.iap.kit.edu/darko/auger/auger-array/auger_array-pdf/auger_array-small-topo.pdf.
- [69] David Schmidt. “Sensitivity of AugerPrime to the masses of ultra-high-energy cosmic rays”. 51.03.03; LK 01. PhD thesis. Karlsruher Institut für Technologie (KIT), 2019. 101 pp. DOI: [10.5445/IR/1000093730](https://doi.org/10.5445/IR/1000093730).
- [70] T. Huege and A. Haungs. “Radio Detection of Cosmic Rays: Present and Future”. In: vol. 9. JPS Conference Proceedings. Journal of the Physical Society of Japan, 2016. DOI: [10.7566/JPSCP.9.010018](https://doi.org/10.7566/JPSCP.9.010018). URL: <https://doi.org/10.7566/JPSCP.9.010018>.
- [71] Alexander Aab et al. “Observation of inclined EeV air showers with the radio detector of the Pierre Auger Observatory”. In: *JCAP* 1810.10 (2018), p. 026. DOI: [10.1088/1475-7516/2018/10/026](https://doi.org/10.1088/1475-7516/2018/10/026).
- [72] Pedro Abreu et al. “Techniques for Measuring Aerosol Attenuation using the Central Laser Facility at the Pierre Auger Observatory”. In: *JINST* 8 (2013), P04009. DOI: [10.1088/1748-0221/8/04/P04009](https://doi.org/10.1088/1748-0221/8/04/P04009). arXiv: [1303.5576](https://arxiv.org/abs/1303.5576) [astro-ph.IM].
- [73] Jean M Rüeger. “Refractive index formulae for radio waves”. In: *Proceedings of the FIG XXII International Congress, Washington, DC, USA*. Vol. 113. 2002.
- [74] P. Abreu et al. “Description of Atmospheric Conditions at the Pierre Auger Observatory using the Global Data Assimilation System (GDAS)”. In: *Astropart. Phys.* 35 (2012), pp. 591–607. DOI: [10.1016/j.astropartphys.2011.12.002](https://doi.org/10.1016/j.astropartphys.2011.12.002). arXiv: [1201.2276](https://arxiv.org/abs/1201.2276) [astro-ph.HE].
- [75] T. K. Gaisser and A. M. Hillas. “Reliability of the Method of Constant Intensity Cuts for Reconstructing the Average Development of Vertical Showers”. In: *International Cosmic Ray Conference*. Vol. 8. International Cosmic Ray Conference. 1977, p. 353.
- [76] A. Aab et al. “Data-driven estimation of the invisible energy of cosmic ray showers with the Pierre Auger Observatory”. In: *Phys. Rev. D* 100.8 (2019), p. 082003. DOI: [10.1103/PhysRevD.100.082003](https://doi.org/10.1103/PhysRevD.100.082003). arXiv: [1901.08040](https://arxiv.org/abs/1901.08040) [astro-ph.IM].
- [77] J. Abraham et al. “The Fluorescence Detector of the Pierre Auger Observatory”. In: *Nucl. Instrum. Meth. A* 620 (2010), pp. 227–251. DOI: [10.1016/j.nima.2010.04.023](https://doi.org/10.1016/j.nima.2010.04.023). arXiv: [0907.4282](https://arxiv.org/abs/0907.4282) [astro-ph.IM].
- [78] Bruce Dawson. “The Energy Scale of the Pierre Auger Observatory”. In: *PoS ICRC2019* (2020), p. 231. DOI: [10.22323/1.358.0231](https://doi.org/10.22323/1.358.0231).

- [79] I. Allekotte et al. “The Surface Detector System of the Pierre Auger Observatory”. In: *Nucl. Instrum. Meth. A* 586 (2008), pp. 409–420. DOI: [10.1016/j.nima.2007.12.016](https://doi.org/10.1016/j.nima.2007.12.016). arXiv: [0712.2832](https://arxiv.org/abs/0712.2832) [astro-ph].
- [80] J. Abraham et al. “Trigger and Aperture of the Surface Detector Array of the Pierre Auger Observatory”. In: *Nucl. Instrum. Meth. A* 613 (2010), pp. 29–39. DOI: [10.1016/j.nima.2009.11.018](https://doi.org/10.1016/j.nima.2009.11.018). arXiv: [1111.6764](https://arxiv.org/abs/1111.6764) [astro-ph.IM].
- [81] Alan Coleman. “Measurement of the Cosmic Ray Flux Above 100 PeV at the Pierre Auger Observatory”. PhD thesis. Penn State U., 2018.
- [82] X. Bertou et al. “Calibration of the surface array of the Pierre Auger Observatory”. In: *Nucl. Instrum. Meth. A* 568 (2006), pp. 839–846. DOI: [10.1016/j.nima.2006.07.066](https://doi.org/10.1016/j.nima.2006.07.066). arXiv: [2102.01656](https://arxiv.org/abs/2102.01656) [astro-ph.HE].
- [83] Alexander Aab et al. “Reconstruction of events recorded with the surface detector of the Pierre Auger Observatory”. In: *JINST* 15.10 (2020), P10021. DOI: [10.1088/1748-0221/15/10/P10021](https://doi.org/10.1088/1748-0221/15/10/P10021). arXiv: [2007.09035](https://arxiv.org/abs/2007.09035) [astro-ph.IM].
- [84] Alexander Aab et al. “Reconstruction of Inclined Air Showers detected with the Pierre Auger Observatory”. In: *JCAP* 08 (2014), p. 019. DOI: [10.1088/1475-7516/2014/08/019](https://doi.org/10.1088/1475-7516/2014/08/019). arXiv: [1407.3214](https://arxiv.org/abs/1407.3214) [astro-ph.HE].
- [85] Quentin Luce. “Data driven estimation of the Angular Resolution for vertical and horizontal air showers”. In: *Teleconferences of the Arrival Directions Task* (). URL: https://www.auger.unam.mx/AugerWiki/ArrivalDirections?action=AttachFile&do=get&target=AngularResolution_ADMeeting.pdf.
- [86] M. Ave et al. “Constraints on the ultrahigh-energy photon flux using inclined showers from the Haverah Park array”. In: *Phys. Rev. D* 65 (2002), p. 063007. DOI: [10.1103/PhysRevD.65.063007](https://doi.org/10.1103/PhysRevD.65.063007). arXiv: [astro-ph/0110613](https://arxiv.org/abs/astro-ph/0110613).
- [87] Ines Valino. “The flux of ultra-high energy cosmic rays after ten years of operation of the Pierre Auger Observatory”. In: *PoS ICRC2015* (2016), p. 271. DOI: [10.22323/1.236.0271](https://doi.org/10.22323/1.236.0271).
- [88] Alexander Aab et al. “Energy Estimation of Cosmic Rays with the Engineering Radio Array of the Pierre Auger Observatory”. In: *Phys. Rev. D* 93.12 (2016), p. 122005. DOI: [10.1103/PhysRevD.93.122005](https://doi.org/10.1103/PhysRevD.93.122005). arXiv: [1508.04267](https://arxiv.org/abs/1508.04267) [astro-ph.HE].
- [89] Marvin Gottowik. “Radio Hybrid Reconstruction and Analysis of Inclined Air Showers with AERA of the Pierre Auger Observatory - Measuring the Hadronic Shower Development and Cosmic Ray Mass Composition”. PhD thesis. Wuppertal U., 2021. DOI: [10.25926/21hw-wq22](https://doi.org/10.25926/21hw-wq22).
- [90] Stefan Jansen. “Radio for the masses: Cosmic ray mass composition measurements in the radio frequency domain”. PhD thesis. Nijmegen U., 2016. URL: <https://inspirehep.net/files/0bc7796a271c89620655446f35cfe053>.
- [91] Fabrizia Canfora. “Cosmic-Ray Composition Measurements Using Radio Signals”. PhD thesis. NIKEF, 2021. URL: https://www.nikhef.nl/pub/services/biblio/theses_pdf/thesis%5C_F%5C_Canfora.pdf.

-
- [92] Alexander Aab et al. “Calibration of the logarithmic-periodic dipole antenna (LPDA) radio stations at the Pierre Auger Observatory using an octocopter”. In: *JINST* 12.10 (2017), T10005. DOI: [10.1088/1748-0221/12/10/T10005](https://doi.org/10.1088/1748-0221/12/10/T10005). arXiv: [1702.01392](https://arxiv.org/abs/1702.01392) [astro-ph.IM].
- [93] Tim Huege. “Nanosecond-level time synchronization of AERA using a beacon reference transmitter and commercial airplanes”. In: *EPJ Web Conf.* 135 (2017). Ed. by S. Buitnik et al., p. 01013. DOI: [10.1051/epjconf/201713501013](https://doi.org/10.1051/epjconf/201713501013). arXiv: [1609.00630](https://arxiv.org/abs/1609.00630) [physics.ins-det].
- [94] M. Nowak. “Evaluierung von SALLA-Prototyp-Stationen für das Radio-Upgrade des Pierre-Auger-Observatoriums”. MA thesis. Karlsruher Institut für Technologie, 2019. URL: <https://web.i kp.kit.edu/huege/downloads/theses/2019-Nowak.pdf>.
- [95] H. Gemmeke. “New Antenna for Radio Detection of UHECR”. In: ICRC2009 (2009). URL: https://www.astro.ru.nl/lopes/_media/publications/icrc1232.pdf.
- [96] Pedro Abreu et al. “Antennas for the Detection of Radio Emission Pulses from Cosmic-Ray”. In: *JINST* 7 (2012), P10011. DOI: [10.1088/1748-0221/7/10/P10011](https://doi.org/10.1088/1748-0221/7/10/P10011). arXiv: [1209.3840](https://arxiv.org/abs/1209.3840) [astro-ph.IM].
- [97] P.A. Bezyazeev et al. “Measurement of cosmic-ray air showers with the Tunka Radio Extension (Tunka-Rex)”. In: *Nucl. Instrum. Meth. A* 802 (2015), pp. 89–96. DOI: [10.1016/j.nima.2015.08.061](https://doi.org/10.1016/j.nima.2015.08.061). arXiv: [1509.08624](https://arxiv.org/abs/1509.08624) [astro-ph.IM].
- [98] Jordan Roel et al Peter Dolron. *Optimization of the RD-SALLA - Privat communication*. 2022.
- [99] Giezen Metaal. *Producer of aluminum parts for the SALLA*. URL: <https://www.giezenmetaal.nl/>.
- [100] Roy Bakker et al. *Production Readiness Review - Radio Detector Mechanical parts/frame*. Mar. 3, 2021. URL: https://www.auger.unam.mx/AugerWiki/RD?action=AttachFile&do=get&target=RD_PRR_MEC3.pdf.
- [101] Roy Bakker et al. *Production Readiness Review - Radio Detector Electrical components*. Jan. 21, 2022. URL: https://www.auger.unam.mx/AugerWiki/RD?action=AttachFile&do=get&target=rd_prr_electr-Part2.pdf.
- [102] T. Fodran on behalf of The Pierre Auger Collaboration. “First results from the AugerPrime Radio Detector”. In: *PoS ICRC2021* (2021), p. 270. DOI: [10.22323/1.395.0270](https://doi.org/10.22323/1.395.0270).
- [103] Ugo Giaccari et al. *Simulations of RD antenna pattern with 4nec2*. 2021. URL: <https://indico.nucleares.unam.mx/event/1804/contribution/6/material/slides/0.pdf>.
- [104] B Pont, M Straub, et al. *Preparation for an Octocopter campaign for the calibration of the directional response pattern of the SALLA*. 2022. URL: <https://indico.nucleares.unam.mx/event/1853/contribution/1/material/slides/0.pdf>.

- [105] M Ishii and Y Baba. “Advanced computational methods in lightning performance. The Numerical Electromagnetics Code (NEC-2)”. In: *2000 IEEE Power Engineering Society Winter Meeting. Conference Proceedings (Cat. No. 00CH37077)*. Vol. 4. IEEE, 2000, pp. 2419–2424.
- [106] Sjoerd Timmer et al. *Monitoring algorithm on the RD-frontend FPGA - Privat communication*. 2022.
- [107] S. Argiro et al. “The Offline Software Framework of the Pierre Auger Observatory”. In: *Nucl. Instrum. Meth. A* 580 (2007), pp. 1485–1496. DOI: [10.1016/j.nima.2007.07.010](https://doi.org/10.1016/j.nima.2007.07.010). arXiv: [0707.1652](https://arxiv.org/abs/0707.1652) [astro-ph].
- [108] P. Abreu et al. “Advanced Functionality for Radio Analysis in the Offline Software Framework of the Pierre Auger Observatory”. In: *Nucl. Instrum. Meth. A* 635 (2011), pp. 92–102. DOI: [10.1016/j.nima.2011.01.049](https://doi.org/10.1016/j.nima.2011.01.049). arXiv: [1101.4473](https://arxiv.org/abs/1101.4473) [astro-ph.IM].
- [109] Jaime Alvarez-Muniz, Washington R. Carvalho Jr., and Enrique Zas. “Monte Carlo simulations of radio pulses in atmospheric showers using ZHAireS”. In: *Astropart. Phys.* 35 (2012), pp. 325–341. DOI: [10.1016/j.astropartphys.2011.10.005](https://doi.org/10.1016/j.astropartphys.2011.10.005). arXiv: [1107.1189](https://arxiv.org/abs/1107.1189) [astro-ph.HE].
- [110] Jaime Alvarez-Muñiz et al. “Radio pulses from ultra-high energy atmospheric showers as the superposition of Askaryan and geomagnetic mechanisms”. In: *Astropart. Phys.* 59 (2014), pp. 29–38. DOI: [10.1016/j.astropartphys.2014.04.004](https://doi.org/10.1016/j.astropartphys.2014.04.004). arXiv: [1402.3504](https://arxiv.org/abs/1402.3504) [astro-ph.HE].
- [111] Marvin Gottowik et al. “Determination of the absolute energy scale of extensive air showers via radio emission: systematic uncertainty of underlying first-principle calculations”. In: *Astropart. Phys.* 103 (2018), pp. 87–93. DOI: [10.1016/j.astropartphys.2018.07.004](https://doi.org/10.1016/j.astropartphys.2018.07.004). arXiv: [1712.07442](https://arxiv.org/abs/1712.07442) [astro-ph.HE].
- [112] *A tool package for cosmic-ray and neutrino radio detectors*. URL: <https://github.com/nu-radio/radiotools>.
- [113] B. Keilhauer M. Will D. Heck. “Monthly Average Profiles for CORSIKA and Offline Based on Data from the Global Data Assimilation System (GDAS)”. In: *Auger internal note GAP-2011-133* (2011). URL: <https://www.auger.org/gap-notes/download/3-gap-notes-2011/370-gap2011-133>.
- [114] M. Bleicher et al. “Relativistic hadron hadron collisions in the ultrarelativistic quantum molecular dynamics model”. In: *J. Phys. G* 25 (1999), pp. 1859–1896. DOI: [10.1088/0954-3899/25/9/308](https://doi.org/10.1088/0954-3899/25/9/308). arXiv: [hep-ph/9909407](https://arxiv.org/abs/hep-ph/9909407).
- [115] S. Ostapchenko. “Monte Carlo treatment of hadronic interactions in enhanced Pomeron scheme: QGSJet-II model”. In: *Phys. Rev. D* 83 (1 2011), p. 014018. DOI: [10.1103/PhysRevD.83.014018](https://doi.org/10.1103/PhysRevD.83.014018).
- [116] Felix Riehn et al. “Hadronic interaction model Sibyll-2.3d and extensive air showers”. In: *Phys. Rev. D* 102.6 (2020), p. 063002. DOI: [10.1103/PhysRevD.102.063002](https://doi.org/10.1103/PhysRevD.102.063002). arXiv: [1912.03300](https://arxiv.org/abs/1912.03300) [hep-ph].
- [117] M. Kobal. “A thinning method using weight limitation for air-shower simulations”. In: *Astropart. Phys.* 15 (2001), pp. 259–273. DOI: [10.1016/S0927-6505\(00\)00158-4](https://doi.org/10.1016/S0927-6505(00)00158-4).

-
- [118] D. Heck and T. Pierog. *Extensive Air Shower Simulation with CORSIKA: a User's Guide*. 2019. DOI: [10.1088/0954-3899/25/9/308](https://doi.org/10.1088/0954-3899/25/9/308). URL: <https://web.iikp.kit.edu/corsika/usersguide/usersguide.pdf> (visited on 05/01/2021).
- [119] H. P. Dembinski et al. "A phenomenological model of the muon density profile on the ground of very inclined air showers". In: *Astropart. Phys.* 34 (2010), pp. 128–138. DOI: [10.1016/j.astropartphys.2010.06.006](https://doi.org/10.1016/j.astropartphys.2010.06.006). arXiv: [0904.2372](https://arxiv.org/abs/0904.2372) [astro-ph.IM].
- [120] Tim Huege, Lukas Brenk, and Felix Schlüter. "A Rotationally Symmetric Lateral Distribution Function for Radio Emission from Inclined Air Showers". In: *EPJ Web Conf.* 216 (2019). Ed. by G. Riccobene et al., p. 03009. DOI: [10.1051/epjconf/201921603009](https://doi.org/10.1051/epjconf/201921603009). arXiv: [1808.00729](https://arxiv.org/abs/1808.00729) [astro-ph.IM].
- [121] Christian Glaser et al. "Simulation of Radiation Energy Release in Air Showers". In: *JCAP* 1609.09 (2016), p. 024. DOI: [10.1088/1475-7516/2016/09/024](https://doi.org/10.1088/1475-7516/2016/09/024).
- [122] Florian Lukas Briechle. "Measurement of the radiation energy release using radio emission from extensive air showers at the Pierre Auger Observatory". Ph.D. Thesis. RWTH Aachen University, 2021. DOI: [10.18154/RWTH-2022-01209](https://doi.org/10.18154/RWTH-2022-01209). URL: <https://publications.rwth-aachen.de/record/840356>.
- [123] Christian Glaser et al. "An analytic description of the radio emission of air showers based on its emission mechanisms". In: *Astropart. Phys.* 104 (2019), pp. 64–77. DOI: [10.1016/j.astropartphys.2018.08.004](https://doi.org/10.1016/j.astropartphys.2018.08.004).
- [124] O. Scholten et al. "Measurement of the circular polarization in radio emission from extensive air showers confirms emission mechanisms". In: *Phys. Rev. D* 94.10 (2016), p. 103010. DOI: [10.1103/PhysRevD.94.103010](https://doi.org/10.1103/PhysRevD.94.103010). arXiv: [1611.00758](https://arxiv.org/abs/1611.00758) [astro-ph.IM].
- [125] A. Corstanje. *A python module for interpolating 2D functions in polar coordinates, using Fourier series*. URL: https://github.com/acorstanje/interpolation%5C_fourier.
- [126] Simon Chiche et al. "Radio-Morphing: a fast, efficient and accurate tool to compute the radio signals from air-showers". In: *PoS ICRC2021* (2021), p. 194. DOI: [10.22323/1.395.0194](https://doi.org/10.22323/1.395.0194). arXiv: [2202.05886](https://arxiv.org/abs/2202.05886) [astro-ph.IM].
- [127] Jaime Álvarez-Muñiz et al. "The Giant Radio Array for Neutrino Detection (GRAND): Science and Design". In: *Sci. China Phys. Mech. Astron.* 63.1 (2020), p. 219501. DOI: [10.1007/s11433-018-9385-7](https://doi.org/10.1007/s11433-018-9385-7). arXiv: [1810.09994](https://arxiv.org/abs/1810.09994) [astro-ph.HE].
- [128] T. Huege. *CoREAS 1.4 User's Manual*. 2019. URL: <https://web.iikp.kit.edu/huege/downloads/coreas-manual.pdf> (visited on 03/29/2022).
- [129] Krijn D. de Vries, Olaf Scholten, and Klaus Werner. "The air shower maximum probed by Cherenkov effects from radio emission". In: *Astropart. Phys.* 45 (2013), pp. 23–27. DOI: [10.1016/j.astropartphys.2013.02.003](https://doi.org/10.1016/j.astropartphys.2013.02.003). arXiv: [1304.1321](https://arxiv.org/abs/1304.1321) [astro-ph.HE].
- [130] Marvin Gottowik. "Measurements of Inclined Air Showers with the Auger Engineering Radio Array at the Pierre Auger Observatory". In: *PoS ICRC2019* (2021), p. 274. DOI: [10.22323/1.358.0274](https://doi.org/10.22323/1.358.0274).

- [131] A. Corstanje et al. “The effect of the atmospheric refractive index on the radio signal of extensive air showers”. In: *Astropart. Phys.* 89 (2017), pp. 23–29. DOI: [10.1016/j.astropartphys.2017.01.009](https://doi.org/10.1016/j.astropartphys.2017.01.009). arXiv: [1701.07338](https://arxiv.org/abs/1701.07338) [astro-ph.HE].
- [132] Ewa M. Holt. “Recent Results of the Auger Engineering Radio Array (AERA)”. In: *PoS ICRC2017* (2018), p. 492. DOI: [10.22323/1.301.0492](https://doi.org/10.22323/1.301.0492).
- [133] P. Schellart et al. “Detecting cosmic rays with the LOFAR radio telescope”. In: *Astron. Astrophys.* 560 (2013), A98. DOI: [10.1051/0004-6361/201322683](https://doi.org/10.1051/0004-6361/201322683). arXiv: [1311.1399](https://arxiv.org/abs/1311.1399) [astro-ph.IM].
- [134] Tim Huege et al. “Ultimate precision in cosmic-ray radio detection – the SKA”. In: *EPJ Web Conf.* 135 (2017), p. 02003. DOI: [10.1051/epjconf/201713502003](https://doi.org/10.1051/epjconf/201713502003). arXiv: [1608.08869](https://arxiv.org/abs/1608.08869) [astro-ph.IM].
- [135] *A tool package for cosmic-ray and neutrino radio detectors*. Revision from 10.12.2019. URL: <https://github.com/nu-radio/radiotools>.
- [136] M.T. Dova, L.N. Epele, and Analisa G. Mariazzi. “The Effect of atmospheric attenuation on inclined cosmic ray air showers”. In: *Astropart. Phys.* 18 (2003), pp. 351–365. DOI: [10.1016/S0927-6505\(02\)00150-0](https://doi.org/10.1016/S0927-6505(02)00150-0). arXiv: [astro-ph/0110237](https://arxiv.org/abs/astro-ph/0110237).
- [137] Klaus Werner and Olaf Scholten. “Macroscopic Treatment of Radio Emission from Cosmic Ray Air Showers based on Shower Simulations”. In: *Astropart. Phys.* 29 (2008), pp. 393–411. DOI: [10.1016/j.astropartphys.2008.04.004](https://doi.org/10.1016/j.astropartphys.2008.04.004). arXiv: [0712.2517](https://arxiv.org/abs/0712.2517) [astro-ph].
- [138] D. Kuempel, K.-H. Kampert, and M. Risse. “Geometry reconstruction of fluorescence detectors revisited”. In: *Astropart. Phys.* 30 (2008), pp. 167–174. DOI: [10.1016/j.astropartphys.2008.08.003](https://doi.org/10.1016/j.astropartphys.2008.08.003). arXiv: [0806.4523](https://arxiv.org/abs/0806.4523) [astro-ph].
- [139] Anna Nelles et al. “A parameterization for the radio emission of air showers as predicted by CoREAS simulations and applied to LOFAR measurements”. In: *Astropart. Phys.* 60 (2015), pp. 13–24. DOI: [10.1016/j.astropartphys.2014.05.001](https://doi.org/10.1016/j.astropartphys.2014.05.001).
- [140] The Pierre Auger Collaboration. “The Pierre Auger Cosmic Ray Observatory”. In: *Nuclear Instruments and Methods in Physics Research Section A: Accelerators, Spectrometers, Detectors and Associated Equipment* 798 (2015), pp. 172–213. ISSN: 0168-9002. DOI: <https://doi.org/10.1016/j.nima.2015.06.058>.
- [141] Frank G. Schröder. “Science Case of a Scintillator and Radio Surface Array at IceCube”. In: *PoS ICRC2019* (2020), p. 418. DOI: [10.22323/1.358.0418](https://doi.org/10.22323/1.358.0418). arXiv: [1908.11469](https://arxiv.org/abs/1908.11469) [astro-ph.HE].
- [142] Tim Huege, Felix Schlüter, and Lukas Brenk. “Symmetrizing the signal distribution of radio emission from inclined air showers”. In: *PoS ICRC2019* (2021), p. 294. DOI: [10.22323/1.358.0294](https://doi.org/10.22323/1.358.0294). arXiv: [1908.07840](https://arxiv.org/abs/1908.07840) [astro-ph.IM].
- [143] Matt Newville et al. *lmfit/lmfit-py 1.0.2*. Version 1.0.2. 2021. DOI: [10.5281/zenodo.4516651](https://doi.org/10.5281/zenodo.4516651). URL: <https://doi.org/10.5281/zenodo.4516651>.
- [144] Hans Dembinski and Piti Ongmongkolkul et al. *scikit-hep/iminuit*. 2020. DOI: [10.5281/zenodo.3949207](https://doi.org/10.5281/zenodo.3949207). URL: <https://doi.org/10.5281/zenodo.3949207>.

-
- [145] Alexander Aab et al. “Probing the radio emission from air showers with polarization measurements”. In: *Phys. Rev. D* 89.5 (2014), p. 052002. DOI: [10.1103/PhysRevD.89.052002](https://doi.org/10.1103/PhysRevD.89.052002). arXiv: [1402.3677](https://arxiv.org/abs/1402.3677) [astro-ph.HE].
- [146] P. Schellart et al. “Polarized radio emission from extensive air showers measured with LOFAR”. In: *JCAP* 10 (2014), p. 014. DOI: [10.1088/1475-7516/2014/10/014](https://doi.org/10.1088/1475-7516/2014/10/014). arXiv: [1406.1355](https://arxiv.org/abs/1406.1355) [astro-ph.HE].
- [147] F. Schlüter et al. “Refractive displacement of the radio-emission footprint of inclined air showers simulated with CoREAS”. In: *The European Physical Journal C* 80.7 (2020). DOI: [10.1140/epjc/s10052-020-8216-z](https://doi.org/10.1140/epjc/s10052-020-8216-z). URL: <https://doi.org/10.1140/epjc/s10052-020-8216-z>.
- [148] F. Schlüter on behalf of The Pierre Auger Collaboration. “Expected performance of the AugerPrime Radio Detector”. In: *PoS ICRC2021* (2021), p. 262. DOI: [10.22323/1.395.0262](https://doi.org/10.22323/1.395.0262).
- [149] F. Schroeder et al. “Radio Detection of Cosmic Rays”. In: *SnowMass 2021 CF7* (2020). URL: <https://www.snowmass21.org/docs/files/summaries/CF/SNOWMASS21-CF7-CF0-NF4-NF0-IF10-IF0-118.pdf>.
- [150] H. Schoorlemmer and W. R. Carvalho Jr. *Radio interferometry applied to the observation of cosmic-ray induced extensive air showers*. 2020. arXiv: [2006.10348](https://arxiv.org/abs/2006.10348) [astro-ph.HE]. URL: <https://arxiv.org/pdf/2006.10348v1.pdf>.
- [151] H. Falcke et al. “Detection and imaging of atmospheric radio flashes from cosmic ray air showers”. In: *Nature* 435 (2005), pp. 313–316. DOI: [10.1038/nature03614](https://doi.org/10.1038/nature03614). arXiv: [astro-ph/0505383](https://arxiv.org/abs/astro-ph/0505383).
- [152] W. D. Apel et al. “The wavefront of the radio signal emitted by cosmic ray air showers”. In: *JCAP* 09 (2014), p. 025. DOI: [10.1088/1475-7516/2014/09/025](https://doi.org/10.1088/1475-7516/2014/09/025). arXiv: [1404.3283](https://arxiv.org/abs/1404.3283) [hep-ex].
- [153] W. D. Apel et al. “Final results of the LOPES radio interferometer for cosmic-ray air showers”. In: *The European Physical Journal C* 81.2 (2021), p. 176. ISSN: 1434-6052. DOI: [10.1140/epjc/s10052-021-08912-4](https://doi.org/10.1140/epjc/s10052-021-08912-4). URL: <https://doi.org/10.1140/epjc/s10052-021-08912-4>.
- [154] I. Jandt. “Beamforming with AERA”. MA thesis. Bergischen Universität Wuppertal, 2012. URL: <https://astro.uni-wuppertal.de/fileadmin/physik/astro/mainpage/publications/theses/Diplom/Jandt-Diplom.pdf>.
- [155] A. Romero-Wolf et al. “An interferometric analysis method for radio impulses from ultra-high energy particle showers”. In: *Astropart. Phys.* 60 (2015), pp. 72–85. DOI: [10.1016/j.astropartphys.2014.06.006](https://doi.org/10.1016/j.astropartphys.2014.06.006).
- [156] A. G. Vieregg et al. “A Ground-Based Interferometric Phased Array Trigger for Ultra-high Energy Neutrinos”. In: *PoS ICRC2017* (2018), p. 1013. DOI: [10.22323/1.301.1013](https://doi.org/10.22323/1.301.1013).
- [157] K. Hughes et al. “Towards Interferometric Triggering on Air Showers Induced by Tau Neutrino Interactions”. In: *PoS ICRC2019* (2020), p. 917. DOI: [10.22323/1.358.0917](https://doi.org/10.22323/1.358.0917).

- [158] F. G. Schröder et al. “New method for the time calibration of an interferometric radio antenna array”. In: *Nuclear Instruments and Methods in Physics Research Section A: Accelerators, Spectrometers, Detectors and Associated Equipment* 615.3 (2010), pp. 277–284. ISSN: 0168-9002. DOI: <https://doi.org/10.1016/j.nima.2010.01.072>. URL: <http://www.sciencedirect.com/science/article/pii/S016890021000166X>.
- [159] P. Allison et al. “Timing calibration and synchronization of surface and fluorescence detectors of the Pierre Auger Observatory”. In: *29th International Cosmic Ray Conference*. 2005. URL: <https://inspirehep.net/files/cfb05c7f4d3d1ab9c5bfbadb2dce8ced>.
- [160] A. Aab et al. “Nanosecond-level time synchronization of autonomous radio detector stations for extensive air showers”. In: *JINST* 11.01 (2016), P01018. DOI: [10.1088/1748-0221/11/01/P01018](https://doi.org/10.1088/1748-0221/11/01/P01018). arXiv: [1512.02216](https://arxiv.org/abs/1512.02216) [physics.ins-det].
- [161] T. Huege et al. “High-precision measurements of extensive air showers with the SKA”. In: *PoS ICRC2015* (2016), p. 309. DOI: [10.22323/1.236.0309](https://doi.org/10.22323/1.236.0309). arXiv: [1508.03465](https://arxiv.org/abs/1508.03465) [astro-ph.IM].
- [162] E. de Lera Acedo et al. “SKALA, a log-periodic array antenna for the SKA-low instrument: design, simulations, tests and system considerations”. In: *Experimental Astronomy* 39.3 (2015), pp. 567–594. ISSN: 1572-9508. DOI: [10.1007/s10686-015-9439-0](https://doi.org/10.1007/s10686-015-9439-0). URL: <https://doi.org/10.1007/s10686-015-9439-0>.
- [163] P. Mitra et al. “Reconstructing air shower parameters with LOFAR using event specific GDAS atmosphere”. In: *Astropart. Phys.* 123 (2020), p. 102470. DOI: [10.1016/j.astropartphys.2020.102470](https://doi.org/10.1016/j.astropartphys.2020.102470). arXiv: [2006.02228](https://arxiv.org/abs/2006.02228) [astro-ph.HE].
- [164] A. Aab et al. “Depth of maximum of air-shower profiles at the Pierre Auger Observatory. I. Measurements at energies above $10^{17.8}$ eV”. In: *Phys. Rev. D* 90 (12 2014), p. 122005. DOI: [10.1103/PhysRevD.90.122005](https://doi.org/10.1103/PhysRevD.90.122005). URL: <https://link.aps.org/doi/10.1103/PhysRevD.90.122005>.
- [165] A. Balagopal V. et al. “Search for PeVatrons at the Galactic Center using a radio air-shower array at the South Pole”. In: *Eur. Phys. J. C* 78.2 (2018). [Erratum: *Eur.Phys.J.C* 78, 1017 (2018)], p. 111. DOI: [10.1140/epjc/s10052-018-5537-2](https://doi.org/10.1140/epjc/s10052-018-5537-2). arXiv: [1712.09042](https://arxiv.org/abs/1712.09042) [astro-ph.IM].
- [166] Alexander Aab et al. “Deep-learning based reconstruction of the shower maximum X_{max} using the water-Cherenkov detectors of the Pierre Auger Observatory”. In: *JINST* 16.07 (2021), P07019. DOI: [10.1088/1748-0221/16/07/P07019](https://doi.org/10.1088/1748-0221/16/07/P07019). arXiv: [2101.02946](https://arxiv.org/abs/2101.02946) [astro-ph.IM].
- [167] S. Buitink et al. “Method for high precision reconstruction of air shower X_{max} using two-dimensional radio intensity profiles”. In: *Phys. Rev. D* 90 (8 2014), p. 082003. DOI: [10.1103/PhysRevD.90.082003](https://doi.org/10.1103/PhysRevD.90.082003). URL: <https://link.aps.org/doi/10.1103/PhysRevD.90.082003>.
- [168] P. A. Bezyazeev et al. “Reconstruction of cosmic ray air showers with Tunka-Rex data using template fitting of radio pulses”. In: *Phys. Rev. D* 97 (12 2018), p. 122004. DOI: [10.1103/PhysRevD.97.122004](https://doi.org/10.1103/PhysRevD.97.122004). URL: <https://link.aps.org/doi/10.1103/PhysRevD.97.122004>.

-
- [169] Harm Schoorlemmer and Washington R. Carvalho. “Radio interferometry applied to the observation of cosmic-ray induced extensive air showers”. In: *Eur. Phys. J. C* 81.12 (2021), p. 1120. DOI: [10.1140/epjc/s10052-021-09925-9](https://doi.org/10.1140/epjc/s10052-021-09925-9). arXiv: [2006.10348](https://arxiv.org/abs/2006.10348) [astro-ph.HE].
- [170] Ricardo Sato. “Signal timing studies”. In: *SDEU (Surface Detector Electronic Upgrade) task, Meeting on 27.05.2021* (2021). URL: https://www.auger.unam.mx/AugerWiki/SDEU_Front_Page?action=AttachFile&do=get&target=20210527_rsato_SignalTiming_analysis.pdf.
- [171] Jannis Pawlowsky. *Self trigger development for detecting inclined (photon) showers*. 2022. URL: <https://indico.nucleares.unam.mx/event/1853/contribution/13/material/slides/0.pdf>.
- [172] Marvin Gottowik. “Directional reconstruction of the radio signals with a spherical wavefront model”. In: *Auger internal note GAP-2020-055* (2020). URL: <https://www.auger.org/gap-notes/download/144-gap-notes-2020/5193-gap2020-055>.
- [173] Sergio Petrera. “Xmax parameterizations for post-LHC hadronic models”. In: *Auger internal note GAP-2020-058* (2020). URL: <https://www.auger.org/gap-notes/download/144-gap-notes-2020/5196-gap2020-058>.
- [174] Diego Ravnani. “The formulas of the angular resolution”. In: *Auger internal note GAP-2017-003* (2017). URL: <https://www.auger.org/gap-notes/download/104-gap-notes-2017/4382-gap2017-003>.
- [175] F. James. *MINUIT Function Minimization and Error Analysis: Reference Manual Version 94.1*. URL: <https://inspirehep.net/files/6dc93850d19776251caffa506d4e7c27>.
- [176] Felix Riehn. *Reconstruction of inclined showers: Efit vs. offlineHAS*. Apr. 22, 2021. URL: <https://www.auger.unam.mx/AugerWiki/FoundationsGeneralMeetings?action=AttachFile&do=get&target=HasVsEfit-22-apr-2021.pdf>.
- [177] Sangtae Ahn and Jeffrey A Fessler. “Standard errors of mean, variance, and standard deviation estimators”. In: *EECS Department, The University of Michigan* (2003), pp. 1–2. URL: <https://web.eecs.umich.edu/~fessler/papers/lists/files/tr/stderr.pdf>.
- [178] *A tool package for cosmic-ray and neutrino radio detectors*. Revision from 11.08.2020. URL: <https://github.com/nu-radio/radiotools>.
- [179] Sara Martinelli. *Using different arrival direction in the detector simulation*. Feb. 16, 2022. URL: <https://indico.nucleares.unam.mx/event/1853/contribution/29/material/slides/0.pdf>.
- [180] Anna Nelles et al. “A Survey of Narrowband and Broadband Radio-frequency Interference at AERA”. In: *Auger internal note GAP-2011-062* (2011). URL: <https://www.auger.org/gap-notes/download/3-gap-notes-2011/199-gap2011-062>.
- [181] Tomas Fodran. *AugerPrime Radio Detector: Update on performance and more...* Feb. 16, 2022. URL: <https://indico.nucleares.unam.mx/event/1853/contribution/16/material/slides/0.pdf>.